



Theses and Dissertations

2007-11-14

Counter-flow Ion Mobility Analysis: Design, Instrumentation, and Characterization

Nosa Agbonkonkon
Brigham Young University - Provo

Follow this and additional works at: <https://scholarsarchive.byu.edu/etd>



Part of the [Biochemistry Commons](#), and the [Chemistry Commons](#)

BYU ScholarsArchive Citation

Agbonkonkon, Nosa, "Counter-flow Ion Mobility Analysis: Design, Instrumentation, and Characterization" (2007). *Theses and Dissertations*. 1215.
<https://scholarsarchive.byu.edu/etd/1215>

This Dissertation is brought to you for free and open access by BYU ScholarsArchive. It has been accepted for inclusion in Theses and Dissertations by an authorized administrator of BYU ScholarsArchive. For more information, please contact scholarsarchive@byu.edu, ellen_amatangelo@byu.edu.

**COUNTER-FLOW ION MOBILITY ANALYSIS: DESIGN,
INSTRUMENTATION, AND CHARACTERIZATION**

by

Nosa Agbonkonkon

A dissertation submitted to the faculty of

Brigham Young University

in partial fulfillment of the requirements for the degree of

Doctor of Philosophy

Department of Chemistry and Biochemistry

Brigham Young University

December 2007

BRIGHAM YOUNG UNIVERSITY

GRADUATE COMMITTEE APPROVAL

of a dissertation submitted by

Nosa Agbonkonkon

This dissertation has been read by each member of the following graduate committee and by majority vote has been found to be satisfactory.

Milton L. Lee, Committee Chair

Date

David V. Dearden, Committee Member

Date

Matthew C. Asplund, Committee Member

Date

H. Dennis Tolley, Committee Member

Date

Daniel R. Maynes, Committee Member

Date

BRIGHAM YOUNG UNIVERSITY

As chair of the candidate's graduate committee, I have read the dissertation of Nosa Agbonkonkon in its final form and have found that (1) its format, citations, and bibliographical style are consistent and acceptable and fulfill university and department style requirements; (2) its illustrative materials including figures, tables, and charts are in place; and (3) the final manuscript is satisfactory to the graduate committee and is ready for submission to the university library.

Date

Milton L. Lee
Chair, Graduate Committee

Accepted for the Department

David V. Dearden
Graduate Coordinator

Accepted for the College

Thomas W. Sederberg, Associate Dean
College of Physical and Mathematical
Sciences

ABSTRACT

COUNTER-FLOW ION MOBILITY ANALYSIS: DESIGN, INSTRUMENTATION, AND CHARACTERIZATION

Nosa Agbonkonkon

Department of Chemistry and Biochemistry

Doctor of Philosophy

The quest to achieve high resolution in ion mobility spectrometry (IMS) has continued to challenge scientist and engineers in the field of separation science. The low resolution presently attainable in IMS has continued to negatively impact its utility and acceptance. Until now, efforts to improve the resolution have mainly focused on better instrumentation and detection methods. However, since the resolution of IMS is diffusion limited, it makes sense to address this limitation in order to attain high resolution. This dissertation presents a new IMS technique, which utilizes a high electric field and opposing high gas flow velocity with the aim to improve resolution. This approach essentially reduces the residence time of ions in the analyzer. This new technique is called “counter-flow ion mobility analysis” (CIMA). Theoretical modeling of this new technique predicted that a resolution of over 1000 is possible, which is over one order of magnitude better than that of conventional IMS techniques currently used. A wind tunnel was designed and constructed to produce a plug gas flow profile that is needed for CIMA. The test region of the wind tunnel was used as the CIMA analyzer region and was constructed from power circuit boards, PCBs, (top and bottom walls) and conductive plastic side walls. An inclined electric field was created by applying suitable voltages to multiple electrode traces on

the PCBs. This inclined field, when resolved into its x- and y-components, was used to oppose the counter-gas flow and transport the ions to the detector, respectively. The results obtained did not show an improvement over conventional IMS techniques because of a limitation in the voltage that could be applied to the analyzer region. However, the results predict that high resolution is possible if (1) the ratio of the electric fields in the horizontal (x direction) to the vertical (y direction) is within the range of 2–0.5, (2) very high electric field and high gas flow velocities are applied, and (3) wall effects in the counter-flow gas profile are eliminated. While the resolution obtained using the present instrumentation is far from what was predicted, the foundation for ultimately achieving high resolution has been laid. The use of a wind tunnel has made the instrumentation possible. As far as the author knows, this is the first time a wind tunnel has been used in chemical measurement instrumentation.

Chapter 5 of this dissertation, reports a method developed for predicting the reduced mobility constants, K_0 , of chemical compounds. This method uses a purely statistical regression analysis for a wide range of compounds which is different from similar methods that use a neural network. The calculated R^2 value for this method was 87.4% when calculated K_0 values were plotted against experimental K_0 values, which was close to the R^2 value for the neural network method (i.e., 88.7%).

ACKNOWLEDGMENTS

The author wishes to express profound gratitude to all of the individuals and organizations that have contributed to the success of this work. Their contributions, both financial and personal, including time and materials have been invaluable.

I wish to thank the Department of Chemistry and Biochemistry (Brigham Young University) for the opportunity granted me to pursue my aspiration of a graduate degree. Funding for this work was provided by the Defense Threat Reduction Agency (DTRA) and Torion Technologies. I also want to thank Robert M. Perry, Eric L. Bylund, Therin P. Garrett, Carolyn P. Carlton and other staff of the Brigham Young University Precision Machining Laboratory (PML) for their help in machining the parts that were used in this work, and Bart F. Whitehead of the Chemistry Department instrument shop for his work on the wind tunnel CIMA electronics, as well as other members of the instrument shop for their help in various ways.

I would like to thank Dr. Alan L. Rockwood for his continuous help and interest in this project. The CIMA idea was his; he spent considerable time explaining the new idea and was always ready to discuss and provide valuable suggestions while the technique was being developed. I am grateful to Dr. Edgar D. Lee, Randall W. Waite, Jeffery L. Jones and Kenneth D. Nemelka of Torion Technologies for the countless hours spent working with me on this project. I am indebted to them for their suggestions and, more importantly, for helping me refine my ideas. To James R. Oliphant, I say thank you for your help in modeling the CIMA concept at the onset of this research work.

I give special thanks to my committee members for their contributions; Dr. H. Dennis Tolley was very much involved with the modeling effort at the beginning, and in developing a

model for predicting reduced mobility constants, while Dr. Daniel R. Maynes guided my efforts in solving various fluid dynamics problems. I thank Dr Matthew C. Asplund and Dr. David V. Dearden for their valuable constructive evaluation of my work during the yearly progress reports.

My colleagues in the Lab, Jacolin Murray, Jesse Contreras, Aaron Nackos, Miao Wang, Yan Fang, Yuanyuan Li , Xin Chen, Xufei Sun, Yansheng Liu, Yun Li, John Edwards, and Tai Van Truong, played a vital part in the progress I made. Their help, including brainstorming through some ideas, has been great. To my friends and teachers, I thank you all for the ways your influence has shaped my life and led me to this point in my life.

I want to especially thank Dr. Milton L. Lee, my research adviser, for the opportunity he granted me to work on this project in his laboratory. His vision and excellence in his field will always remain a model for me. I hope to continue to imbibe his work ethics and professionalism in my own career. I will always be grateful to him for what I learned by working in his laboratory.

I am grateful for my parents, Imuetinyan and Esther Agbonkonkon, for the nurturing they gave me. They raised me to believe in myself and aspire to the heavens. Their love demonstrated by their sacrifices for me to achieve my desired goals will never be forgotten or taken lightly. I am indebted to them. To my siblings, I say thank you for all you are to me and what you mean to me; this achievement is for us all.

My wife, Christable, has stood solidly behind me through these years, both during times of success and the many difficult times when it felt like I would never make it. Her constant love and encouragement were and remain a source of strength. Her trust and belief in me gave me the confidence to move on. I am eternally grateful to her for her love and all that she is to me and our children. Her work at home gave me the opportunity to focus my time in school. My children,

Osatohamen, Osawese and Uyiosa, have brought so much comfort in otherwise turbulent times; I knew that no matter how frustrating the day had been, I could go home and they would make life wonderful. I thank you my little angels for your smiles and laughter that renew my life and my determination to succeed.

Finally, I am grateful to my Father in Heaven for the strength He has given me and for His love, which I feel everyday of my life. He alone made this and other blessings possible.

TABLE OF CONTENTS

TABLE OF CONTENTS.....	ix
LIST OF TABLES.....	xii
LIST OF FIGURES.....	xiv
Chapter 1 Ion Mobility Spectrometry	1
1.1 Historical Background.....	1
1.2 Theory and Principles.....	2
1.3 Instrumentation.....	3
1.4 Drift Tube.....	8
1.5 Temperature and Pressure Effects on Ion Mobility.....	14
1.6 IMS Resolution.....	15
1.7 IMS Hyphenated Techniques	17
1.8 Ion Mobility Spectrometry-Mass Spectrometry (IMS-MS).....	18
1.9 Applications of IMS	19
1.10 Other IMS Techniques	21
1.11 Limitations of Present IMS Techniques.....	29
1.12 Counter-flow Ion Mobility Analysis (CIMA).....	29
1.13 Previous Work on Using Opposing Forces to Manipulate Ions.....	31
1.14 References	38
Chapter 2 Counter-flow Ion Mobility Analysis	46
2.1 Introduction	46
2.2 Theory of CIMA.....	47

2.3 Numerical Calculations and Simulation	50
2.4 Results and Discussion	66
2.5 Conclusions	70
2.6 References	71
Chapter 3 Counter-flow Ion Mobility Analysis Using Concentric Cylinders.....	72
3.1 Introduction	72
3.2 Perforated Cylinder Design	72
3.3 Stacked Washer Design	75
3.4 Porous (Frit) Tube Design	79
3.5 Results from Tests Using the Concentric Tube Design	83
3.6 References	89
Chapter 4 Counter-flow Ion Mobility Analysis Using a Wind Tunnel	90
4.1 Introduction	90
4.2 Wind Tunnel Analyzer Design.....	92
4.3 Electrical and Electronic Components	99
4.4 Modeling of Gas Flow and Electrical Properties in the Analyzer Region	103
4.5 Experimental Characterization of the Analyzer Region Gas Flow	110
4.6 Performance Testing of the Prototype Wind Tunnel CIMA	116
4.7 Optimization of the CIMA Analyzer Electric Field.....	124
4.8 Effects of Different Counter Flow Gases and Test Samples	136
4.9 Simulation of CIMA Performance Using Actual Experimental Parameters.....	145
4.10 Ion Transient Time Determination	156
4.11 Ion Lifetime Determination	158

4.12 References	164
Chapter 5 Prediction of Gas-phase Reduced Ion Mobility Constants (K_0)	165
5.1 Introduction	165
5.2 Prediction Model	166
5.3 Results and Discussion	174
5.4 Conclusion.....	186
5.5 References	189
Chapter 6 Conclusions and Recommendations for Future Work	190
6.1 Conclusions	190
6.2 Recommendations for Future Work	191
6.3 Recommended Dimensions for a New Wind Tunnel CIMA Design	192
6.4 Diffuser and Fan	195
6.5 Number of Meshes	195
6.6 Materials and Machining	196
6.7 Ionization Source Chamber	196
6.8 Detection System.....	196
6.9 Electrical Parts and Electronics	197
Appendix A List of Acronyms and Symbols	198
Appendix B Definitions of Boundaries and Other Parameters Used in Fluent and Comsol Modeling	200
Appendix C Equations Used to Calculate Topological Descriptors	202

LIST OF TABLES

Table 4.1 Boundary conditions and other defining parameters used in the Fluent modeling. Some of these were default parameters selected by the program itself.....	104
Table 4.2 Parameters and boundary conditions used in Comsol for modeling the electric field in the analyzer test region.....	105
Table 4.3 Pitot tube voltage measurements and their conversion to pressures and gas flow velocities.....	113
Table 4.4 Voltage readings in the analyzer test region resulting from profiling (top to bottom) of the gas flow.....	117
Table 4.5 Voltages applied to the ends of the top and bottom plates of the prototype CIMA.....	122
Table 4.6 Electrode voltage and resultant potential difference across adjacent electrodes in the optimized wind tunnel CIMA.....	128
Table 4.7 Input parameters used in the modeling to simulate the actual experimental conditions.....	146
Table 4.8 Calculated electric field in the vertical y-axis of the wind tunnel CIMA as the “ground common” position is shifted and the field becomes more inclined.....	159
Table 4.9 Calculated velocity of acetone corresponding to the electric field in Table 4.9. This is the velocity of the ions as they travel from the injector to the detector.....	160
Table 4.10 Calculated transient time of acetone. This is the time it takes for acetone ions to reach the detector from when they enter the analyzer.....	161

Table 4.11 Transient times, reduced mobilities, and lifetimes analytes used in test experiments.....	163
Table 5.1 Experimental and predicted K_o values used in developing the prediction model ^a	169
Table 5.2 Grouping of compounds according to structure.....	173
Table 5.3 Estimated coefficients of parameters from regression analysis. ^{a,b}	175
Table 5.4 Estimated coefficients of parameters from regression analysis of the data used in Table 5.3 after elimination of data for chloroacetophenone and 3-xylyl bromide ^a	176
Table 5.5 R^2 Values for different groups ^a	185
Table 5.6 Unusual observations (residual for outliers).....	186
Table 5.7 Data for some compounds that show variation in measured K_o values.....	187
Table1 α based on covalent radius.....	201
Table2 Heteroatom valence δ values.....	203

LIST OF FIGURES

Figure 1.1 Schematic of a conventional IMS system showing three ions of different sizes in the reaction region and then migrating at different velocities in the drift region. The positions or speeds of the ions are directly related to their sizes (assuming they have the same charge).....	4
Figure 1.2 Example of a conventional stacked ring drift tube (CAD drawing) with metal rings separated by insulators. In this design, the insulator is a Teflon ring.....	9
Figure 1.3 Diagram showing the effect of increasing electric field on ion mobility. At low electric field, three ions all behave the same, but as the electric field is increased, the different ions are separated.	23
Figure 1.4 Schematic of a field ion spectrometer (FIS).	24
Figure 1.5 Schematic of the DMA, showing the sheath gas and electric field directions as ions transverse the analyzer.	28
Figure 1.6 Schematic description of CIMA showing the counter gas flow and electric field that acts on a selected sample of ions. The selected ions are directed to the detector while others are lost from the analyzer region.....	30
Figure 1.7 Schematic of an opposing flow analyzer. Zeleny used a simple instrument design as shown to demonstrate the manipulation of ion motion using a gas flow and opposing electric field.....	32
Figure 1.8 Loscertales and Tammet drift differential mobility analyzer schematic, showing the inclined electric field, the sheath gas flow and the motion and direction of ions.	34

Figure 1.9 Schematic representation of Flagen’s opposed migration aerosol classifier (OMAC) showing a porous wall with gas flow and opposing electric field as aerosol moves along the analyzer length.	36
Figure 1.10 Schematic representation of the orthogonal extraction ion mobility spectrometer proposed by Laiko. The analyzer channel is defined by grids through which the counter gas flows.	37
Figure 2.1 Perforated rectangular analyzer box used to describe the concept of CIMA. The perforation allows the counter-gas to flow into the analyzer. Samples are injected into the analyzer in the front end and are detected at the opposite end of the tube. There is an orthogonal force, F , (not shown) that is applied along the d direction that is used for transporting the ions from injection to detection. The sheets marked A, B, C, and D are explained later in the text.	52
Figure 2.2 Representation of a cross-section of the analyzer channel with perforated walls defining the CIMA drift region.	53
Figure 2.3 Injection profiles obtained by changing the numerical values of α and β in the beta-function. These were used to determine the initial spatial distribution of the ions as they entered the analyzer at time $t = 0$	55
Figure 2.4 Initial distribution of the ion sample as it enters the analyzer at $t = 0$. It is assumed to be a Gaussian distribution.	57
Figure 2.5 Hypothetical profiles of the sample concentration inside the analyzer drift region at different times, t , as the analyte moves from the injection point to the detector along the drift length. (A) $t = 0$, (B) $t = 0.01$, (C) $t = 0.02$, and (D) $t = 0.03$	62

Figure 2.6 Plots of concentrations vs. time showing the decay of sample.....63

Figure 2.7 Hypothetical peak or signal output for CIMA. This figure illustrates the narrow peak that is potentially achievable with the CIMA method. In this particular example, the gas flow is kept constant and the electric field is scanned.....64

Figure 2.8 Simulation of the sample behavior as it travels along the drift tube from the point of injection to the detector. Under the conditions of the simulation, the analytes are stopped from migrating to either wall by the opposing forces, while an orthogonal force is use to rapidly move the analyte to the detector before diffusion becomes significant.....67

Figure 2.9 Plot of concentration vs. time, depicting how much of the analyte reaches the detector versus how much is lost due to diffusion. The present conditions show that less than 0.1% was lost.....68

Figure 2.10 CIMA spectrum from the simulation showing baseline separation of two compounds with very close mobility constants.....69

Figure 3.1 Schematic of the perforated cylinder CIMA design. The placement of air amplifiers is shown, with arrows pointing in the direction of gas flow.74

Figure 3.2 Schematic (above) of an air amplifier showing the process of amplification and photograph (below) showing the actual air amplifiers used.76

Figure 3.3 Photograph of the actual stacked ring electrodes used. Both the inner and outer tubes are shown.....77

Figure 3.4 Schematic of the stacked washer CIMA design. The inner and outer stacked washers served also as electrodes to create an electric field. The baffle was used to even the flow around the outer stacked washers.78

Figure 3.5 Photograph close-up of the stacked arranged inside the metal housing, with the inner and outer tube visible. The space between them was the analyzer region.80

Figure 3.6 Photograph of the porous tubes used. These served both as electrodes and as uniform gas flow generator. As seen in the lower photograph, a section of the inner tube was nonporous. This part was attached to a high pressure source.82

Figure 3.7 Schematic of the porous tube CIMA analyzer design. The inner porous tube also served as an electrode. The outer electrode was made from a perforated cylinder.85

Figure 3.8 Fluent simulation of gas flow in the stack ring design. The flow in the analyzer region is non-uniform.86

Figure 3.9 Fluent simulation of gas flow using the porous tube design. Contours of the radial velocity show that there is appreciable variation of the flow along the tube, even when the pressure inside the porous tube was approximately 400 psi.87

Figure 3.10 A cross-section of the radial velocity of the analyzer region of the porous tube design. Flow variation within the region is evident.88

Figure 4.1 Schematic of a wind tunnel showing the three regions (contraction, analyzer and diffuser) with honeycomb and meshes.91

Figure 4.2 Photograph of the analyzer unit with PC boards on the top and bottom. The lower photograph shows the PC boards with conductive electrode traces.95

Figure 4.3 Preferred electrical schematic for the CIMA analyzer test region. The different positions where the voltage became zero as the voltage was increased are indicated by C to K.96

Figure 4.4 (A) Solid model drawing of the ionization chamber and (B) cross-section diagram of the ionization chamber and sampling system. The ionization chamber was designed such that the electric field created would help drive the ions into the analyzer test region.100

Figure 4.5 (A) model drawing and (B) actual photograph of the wind tunnel CIMA analyzer. The analyzer test region was connected to voltage sources through the wires shown. The drawing shows both the ion source on top and the detector at the bottom of the analyzer region.101

Figure 4.6 Schematic of the wind tunnel CIMA showing the various regions, gas flow direction, electric field components and other accessories.102

Figure 4.7 Modeled velocity contours in the contraction and analyzer regions of the wind tunnel. The converging features can be seen in the contraction region leading to uniform flow in the analyzer region. The direction of flow is indicated by arrows. The flow along the cross-section indicated by A and B is shown in Figure 4.8.107

Figure 4.8 Plug flow profile in the analyzer region at positions indicated in Figure 4.7. (A) Cross-section of the flow along the mid-section of the test region from top to bottom, and (B) cross-section at the downstream end of the test region.108

Figure 4.9 Electric field lines in the analyzer region. The inclined or tilted field lines are needed to transport the ions first against the gas flow, and then to the detector. The multi-electrode design helps to create straight field lines.109

Figure 4.10 Analyzer gas flow calibration setup showing the Pitot tube, fan, meshes, honeycomb and gas flow direction.112

Figure 4.11 Pressure transducer calibration.114

Figure 4.12 Calibration of the analyzer test region for gas flow velocity from fan voltage.
The R² value for this plot is 0.990.115

Figure 4.13 Plot of gas flow characteristics across the analyzer cross-section (bottom to top).118

Figure 4.14 Electrical configuration of the analyzer region. The two fixed “ground” electrodes on the top and bottom plates are indicated.120

Figure 4.15 CIMA detection of acetone ions. The voltage across the analyzer was scanned while the gas flow was kept constant.123

Figure 4.16 Ion intensity vs. fan voltage for detection of acetone ions. Peaks represent results obtained for increasing potential differences across electrodes. Higher electric fields require higher gas flows (i.e., the acetone ion peak shifts to the right as the potential difference is increased).125

Figure 4.17 Schematic of the modified electrical configuration of the CIMA analyzer region. V1 to V5 are power supplies, where V5 was connected to the transformer and used to create the inclined electric fields by increasing its voltage. This increase in voltage caused the position of “ground common” to move to the left as indicated.127

Figure 4.18 Visual representation of the change in ratio of horizontal field to vertical field from 4 to 0.5 as the "ground common" position is moved from position "C" to "J".130

Figure 4.19 Ion mobility spectra for 20 V potential difference across electrodes for electric field configurations depicted in Figure 4.18. Resolution values for (A) and (B) were not determined because the peaks were too small131

Figure 4.20 Ion mobility spectra for 30 V potential difference across electrodes for electric field configurations depicted in Figure 4.18. The resolution value for (A) was not determined because the peak was too small.....	132
Figure 4.21 Ion mobility spectra for 40 V potential difference across electrodes for electric field configurations depicted in Figure 4.18. The resolution value for (A) was not determined because the peak was too small.....	133
Figure 4.22 Ion mobility spectra for 50 V potential difference across electrodes for electric field configurations depicted in Figure 4.18. The resolution value for (A) was not determined because the peak was too small.....	134
Figure 4.23 Graph showing the trend toward increasing resolution as the electric field and gas counter gas flow increase with a decreasing ratio of horizontal electric field to vertical field.....	135
Figure 4.24 Representation of the effect of electric field and counter-gas flow on spectral peak width and ion volume. As values of the electric field strength and gas flow velocity increase, the ion volume shrinks, leading to narrower peak width and higher resolution.	137
Figure 4.25 Spectrum of benzyl alcohol obtained using nitrogen as carrier gas and helium as counter-flow gas.	139
Figure 4.26 Spectrum of methylene chloride obtained using nitrogen as carrier gas and helium as counter-flow gas.	140
Figure 4.27 Spectrum of chlorobenzene obtained using nitrogen as carrier gas and helium as counter-flow gas.	141

Figure 4.28 Spectrum of trichloroethane, toluene and ethylbenzene using nitrogen as carrier gas and helium as counter-flow gas.	142
Figure 4.29 Spectrum of trichloroethane, toluene, pyridine, ethylbenzene and chlorobenzene obtained using nitrogen as carrier gas and helium as counter-flow gas.	143
Figure 4.30 Example of the peak that appears when any of the test samples, either singly or in a mixture, was used in the presence of nitrogen as the counter flow gas.	144
Figure 4.31 Photograph of the "original" analyzer region design showing the "vectorial" electrodes and compensating end electrodes.	148
Figure 4.32 Electric field lines generated by the "vectorial" electrodes. Unexpectedly, the field lines were horizontal instead of inclined.	150
Figure 4.33 (A) Photograph of the wind tunnel CIMA and (B) drawing of the hypothetical analyzer used in the original CIMA simulation.	151
Figure 4.34 (A) Model of the initial simulation using the ideal conditions discussed in Chapter 2, which shows the concentration of the sample from the time it is injected at t_0 to when it is detected at t_d . (B) Model of the same process, but using the experimental parameters discussed in this chapter.	152
Figure 4.35 Plots of the amount of initial concentration of sample that reaches the detector as a function of time in the analyzer. While (A) takes 1 s to carry out the analysis, (B) takes 20 s. Diffusion is allowed to take place in (B) and most of the sample is lost before it reaches the detector, while in (A) less than 1% of sample is lost.	153

Figure 4.36 CIMA spectra from (A) original simulation using ideal conditions and (B) simulation using experimental conditions. Both reveal narrow peaks and, thus, high resolution. However, the intensities of the peaks in (B) relative to (A) are very small, indicating that while almost all of the sample introduced in (A) arrives at the detector, only about 5% in (B) reaches the detector.	154
Figure 4.37 Graphical representation of the trend in transient time in ms as the ratio between the horizontal and vertical fields approaches 0.5 and the voltage is increased across the analyzer.....	162
Figure 5.1 Plot of predicted K_0 vs experimental K_0 values using all compounds (Table 5.4 coefficients).	177
Figure 5.2 Plot of predicted K_0 vs experimental K_0 values after omitting data for chloroacetophenone and 3-xylylbromide (Table 5.5 coefficients).	178
Figure 5.3 Plot of predicted K_0 vs experimental K_0 values for groups 1 and 2 of Table 5.2.	179
Figure 5.4 Plot of predicted K_0 vs experimental K_0 values for groups 3 and 4 of Table 5.2.	180
Figure 5.5 Plot of predicted K_0 vs experimental K_0 values for groups 5 and 6 of Table 5.2.	181
Figure 5.6 Plot of predicted K_0 vs experimental K_0 values for groups 7 and 9 of Table 5.2.	182
Figure 6.1 Schematic showing the recommended analyzer design. This figure shows details including dimensions of the various components.	194

Chapter 1

Ion Mobility Spectrometry

1.1 Historical Background

Modern ion mobility spectrometry (IMS), as it is presently practiced, began in 1970 with the pioneering work of Karasek.¹ However, in 1969 at the Pittsburgh Conference on Analytical Chemistry and Applied spectroscopy,² it was Cohen who introduced it as plasma chromatography, erroneously implying that it was a form of chromatography. The contributions of these modern pioneers of IMS were preceded by over 100 years of work in ion transport phenomena.

According to Eiceman and Karpas,³ there were three specific developments in this early work that contributed to the recent advances in IMS. They include first, the theoretical treatment of mobility and practical experimentation by Langevin. Langevin recognized the collisional nature of mobility and the role of attractive forces on effective collision cross sections, and formed an early description of ion-molecule associations and the influence of ion-molecule interactions on mobility. The second development was pulsed ion injection into a drift tube using ion shutters of modern design, i.e., shutters with parallel wires. The third specific development of this period was an in-depth understanding of the effect of electric fields and gas pressure on the mobility of ions in gases. In this period, mobility was shown to be independent of the ratio of electric field to pressure, E/N , at low values and dependent on this ratio at high values.

Interest in IMS has been driven by attractive features sought after in analytical instrumentation and methodology, including high selectivity, high sensitivity, excellent detection limits (i.e., ppm to ppb), instrumentation simplicity, amenability to miniaturization and ruggedness for field operation.

1.2 Theory and Principles

IMS includes methods, principles and instrumentation used to characterize gas phase molecular ions on the basis of their velocities at atmospheric pressure and under the influence of a constant electric field.³ In IMS, an ionized gas is introduced into a drift region of constant electric field where separation of the packet of ions occurs based on several parameters such as mass, shape, orientation in space, and buffer gas. Separated ions are typically detected at the end of the flight distance by a Faraday detector. A mobility spectrum is produced by plotting the detector current (in pA or nA) vs. drift time, t_d (usually in ms).⁴

IMS analysis is based on measuring the drift time an ion takes to move along a drift tube of defined length in an electric field. Ion mobility, K , which is characteristic of an ion, is determined from the ion drift velocity, v_d , and is inversely proportional to the electric field strength, E

$$K = \frac{v_d}{E} \quad (1.1)$$

where K is in $\text{cm}^2 \text{V}^{-1} \text{s}^{-1}$, v_d is in cm s^{-1} and E is in V cm^{-1} .

Ion mobility measurements are often carried out at ambient pressure and elevated temperature. However, mobility is generally reported as reduced mobility, K_0 , to standardize measurements carried out at different temperatures and pressures. The relationship between K and K_0 is

$$K_0 = K \left(\frac{273}{T} \right) \left(\frac{P}{760} \right) \quad (1.2)$$

where P is pressure measured in torr and T is temperature measured in Kelvin.⁵

1.3 Instrumentation

An ion mobility spectrometer is made up of three parts: an ionization region (reaction region), a drift region and a detection region (see Figure 1.1). Each of these regions and how each contributes to IMS technology are discussed in the following sections. Efforts to improve their effectiveness are also described.

Sample Introduction. In IMS, there are several methods used to introduce the sample to be analyzed into the reaction region. The goal is to produce gas phase molecules in low enough concentration to minimize the incidence of clustering, which is a major problem in IMS. Thus, solid and liquid samples must be introduced in such a way that they are allowed to vaporize easily in the reaction region.

A method for determining volatile and semi volatile compounds in liquids or solids is to deposit the sample solution (solids are dissolved or suspended in a solvent) onto a platinum wire attached to a glass rod. The solvent is allowed to evaporate in the air; the wire is then inserted into a heated gas flow near the ion source, and the desorbed vapor is swept into the reaction region by the gas flow.³

Some modern IMS instrumentation uses a membrane inlet to aid sample introduction. Membranes help to eliminate moisture, dust, and interfering chemicals from entering the reaction region. A commonly used membrane is composed of polydimethylsiloxane (PDMS).

Other sampling methods that have been successfully used include headspace vapor,⁶ an electrospray needle, and direct introduction of solids through laser desorption. The choice of inlet system significantly affects analytical performance. Factors that impact the choice of inlet system include the type of sample, matrix, and concentration level, as well as practical constraints such as cost, size, weight and power consumption.³

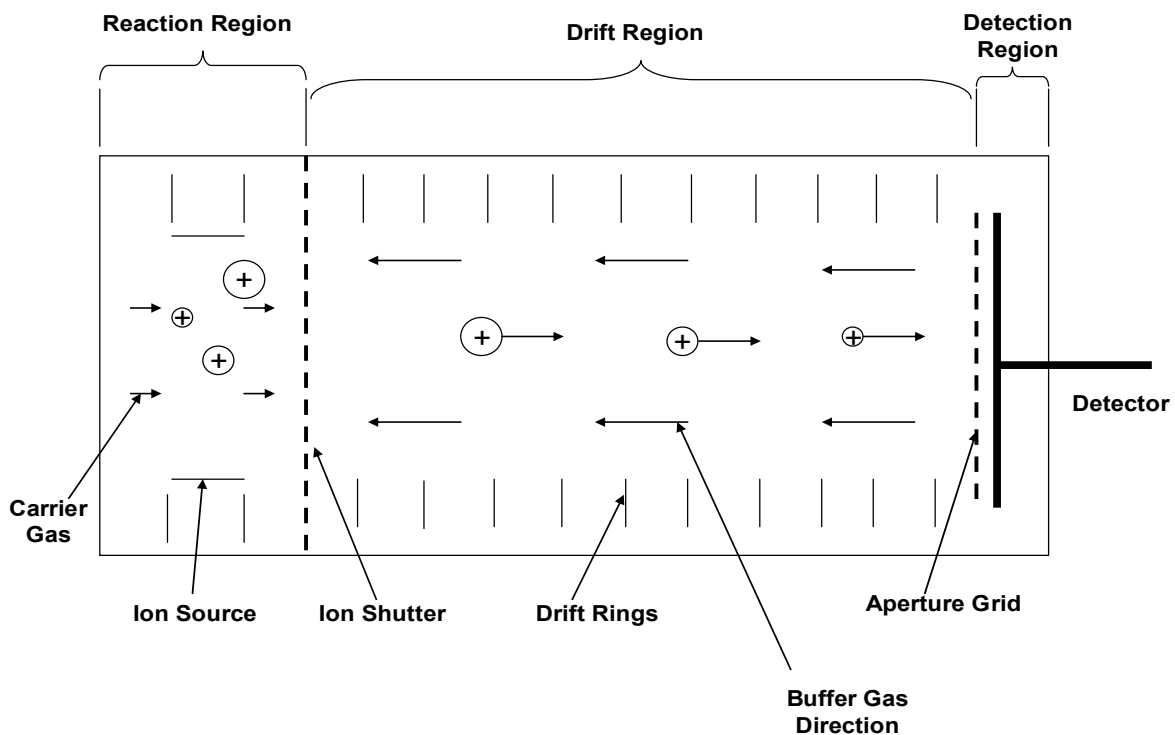


Figure 7.1 Schematic of a conventional IMS system showing three ions of different size in the reaction region and then migrating at different velocities in the drift region. The positions or speeds of the ions are directly related to their sizes (assuming they have the same charge).

Other important components of the sample introduction system are the carrier and reagent gases. The carrier gas is used to sweep the sample mixture into the ionization region and, subsequently, aids in moving the ionized molecules into the drift tube. This is generally an inert gas such as air, water vapor or nitrogen. The reagent gas is used to aid ionization. It can either suppress unwanted ions or help to selectively ionize analytes of interest. The reagent gas is carefully selected according to ionization potential so that it does not compete with the analyte during ionization. In some cases, the reagent gas is allowed to ionize and, through ion-molecule reactions, ionize the analyte. Unfortunately, the reagent gas does not always provide efficient sample ionization or good resolution, which has led some to propose the use of an alternative reagent gas such as halide ions.⁷

Ionization. Ionization of the sample is vital to the success of the entire process of sample separation and identification in IMS. This process ultimately determines the effectiveness of the IMS method. Both positive and negative ions can be monitored in an IMS system.

Traditionally, Nickel-63 has been the ionization source of choice. One reason for this is that the energy range of an electron emitted from a standard 10 mCi ⁶³Ni source (i.e., 0-67 keV) is able to ionize most organic compounds. The noise-free operation,³ stability and the reliability of the ionization chemistry are additional reasons for the choice of Nickel-63. This method also does not require an external power supply, and has no moving parts or maintenance requirements. The most common design is a thin layer of ⁶³Ni coated on a metal strip, generally nickel or gold. The average electron energy is approximately 17 keV. Other radioactive isotopes such as americium and tritium have also been investigated. Despite the attractive features of radioisotopes, their utility has declined due to regulatory requirements and safety issues.

The physics of the phenomenon called corona discharge (CD) are well known.⁹ CD can be characterized as a self-maintained electrical gas discharge in which a Laplacian electrical field confines the primary ionization process to regions close to high-field electrodes or insulators. A CD source consists of high-field curved/sharp electrodes in an ionization region where free charges are produced, a low-field drift region where charged particles drift and react, and a low field passive electrode that collects the charge.¹⁰ The low field collector is a plane or a ring.

The CD source is a continuous current-regulated discharge from a DC power supply. To form a CD, a sharp needle or thin wire is placed 2 to 8 mm from a metal plate or discharge electrode, with a potential difference of 1 to 3 kV between needle and plate. An electrical discharge develops in the gas between the needle and the plate; ions are formed within the gap, similar to what occurs in a ⁶³Ni source. These ions subsequently are available for ion-molecule reactions with the sample ions.³

Negative ions can be formed using a CD by changing the polarity of the power supply. The challenge of adapting CD ionization for negative mode IMS is the formation of NO₂⁻ and NO₃⁻ related cluster ions.¹¹ The reaction pathways to these species are not well understood, but their existence is a well established fact.⁸

The use of a CD as a replacement for ⁶³Ni is rapidly becoming a popular option. The most prevalent mode is operating the power supply in a continuous current mode; however, recently a new design was introduced that makes use of a pulsed mode called pulsed CD ionization. This approach yields IMS responses in both positive and negative modes. The pulsed CD is attractive due to the reduced power required to operate the corona.⁸ Interest in CD is due to the fact that it is not radioactive and the design is simple to build, operate and maintain. It is also applicable to liquid samples.³

Electrospray ionization (ESI) has been used for IMS studies of biomolecules such as peptides and proteins. ESI is a soft ionization technique that is used to transfer ions directly from solution into the gas phase. ESI-IMS was first described in 1972 by Gieniec *et al.*, when they modified a plasma chromatograph from Franklin GNO. They replaced the sample entrance and ^{63}Ni ion source with an electrospray chamber.¹²

The principles, theory and mechanism of ESI have been described elsewhere.¹³ Gas phase ions are formed when a sample in liquid form containing the ions of interest is passed through a needle held at high voltage (as high as 10 kV) relative to the plate or grid that is a few millimeters away. As the sample escapes the tip of the needle, the high voltage and electric field at the tip pass the charge to the aerosol. The aerosol undergoes evaporation as it migrates to the counter plate, creating a high charge density on the shrinking aerosol. The resulting space charge leads to the breakup of the aerosol. This process is repeated until the liquid sample is converted to a gas.

In addition to the three prominent ionization sources described above that are used in IMS, other forms of ionization can be used, depending on the particular application. Surface ionization in the positive mode is one of these. Analytes that are placed on a heated ionization surface in the reaction region of the spectrometer dissociate by losing a hydrogen atom, H, or an alkyl group, R. The remaining portion of the molecule can then be ionized to form product ions. Surface ionization offers unique features such as simplicity, reliability, and extended dynamic range. In addition, it does not respond to most small molecules such as H_2O , CO_2 , CO , N_2 , and O_2 present in air and, thus, it does not produce the typical background ions that are a problem with other ionization sources.¹⁴ Photo-ionization is another method of ionization that has been used in IMS. In photo-ionization, photo-discharge lamps and lasers are used to ionize neutral

molecules in air at ambient pressure. Photo-discharge lamps emit photons from electrically excited gas filled lamps.³

1.4 Drift Tube

The drift tube is the heart of an IMS instrument; it is where separation and differentiation of ions takes place *en route* to the detector. Its design, including the type of material used, is critical to achieving optimum performance. Low sensitivity, poor resolution and memory effects can result from a poorly designed drift tube. A conventional drift tube consists of an ion source and reaction region where ions are formed, a drift region where ion separation based on mobility takes place, and a detector where ions are collected and measured. A shutter grid separates the ionization region from the drift region, while an aperture grid further separates the drift region from the detection region (see Figure. 1.1).

Conventionally, the design of the drift region consists of a set of stacked electrodes (see Figure 1.2) that establishes a uniform axial electric field along the length of the drift region, which is used to drive ions through the drift region to the detection region. A packet of ions introduced into the drift region by the shutter grid moves along the length at drift velocities and diffusion rates determined by the nature of the ions, the buffer gas, the electric field strength and the buffer gas pressure and temperature.¹⁵ However, a continuous guard ring made from a resistive material has been shown to work just as well as the stacked-electrode drift tube, which virtually eliminates the inherent non-uniformity from the fringing fields at the interfaces between the electrodes and insulators in the stacked ring design.¹⁶ Another advantage of the continuous ring approach is that it is simple to design and construct.¹⁷ Others have constructed the drift tube from resistively coated ceramic material that also creates a uniform electric field.

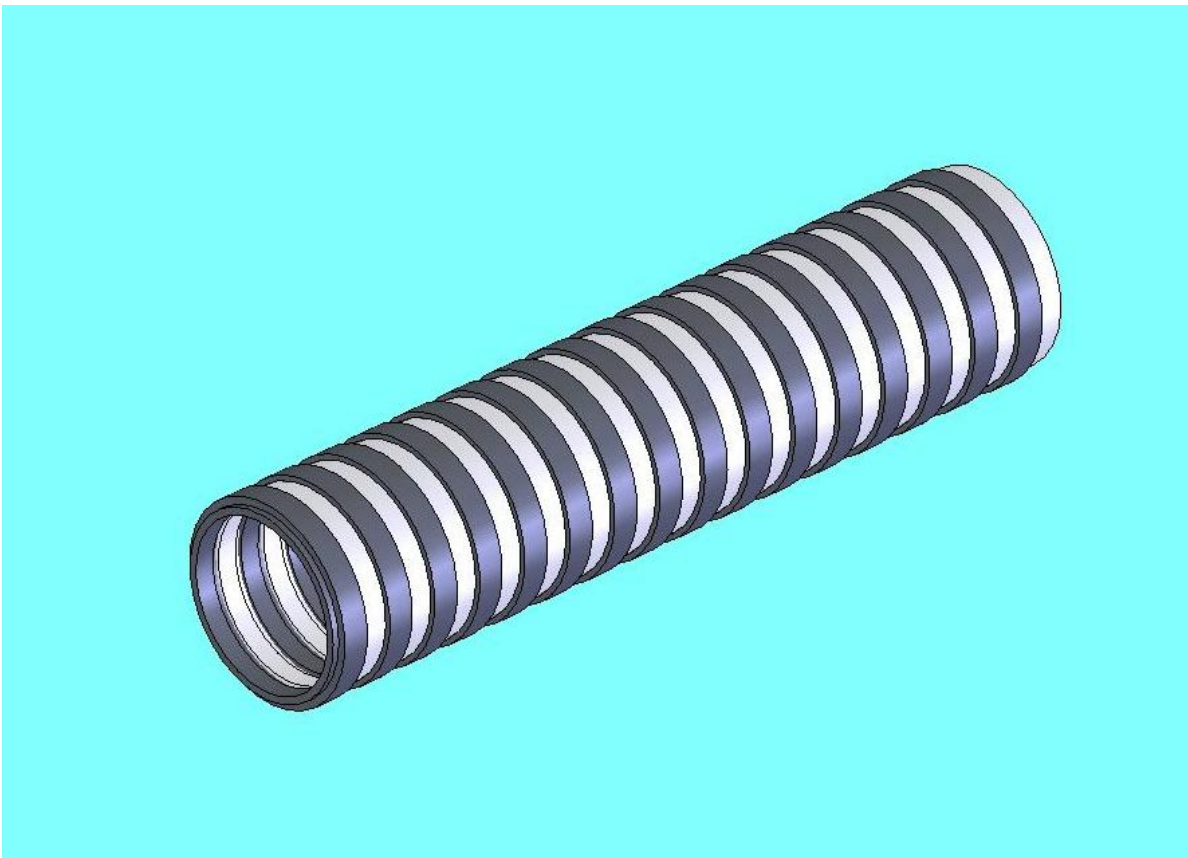


Figure 7.2 Example of a conventional stacked ring drift tube (CAD drawing) with metal rings separated by insulators. In this design, the insulator is a Teflon ring.

Carrier and Drift Gases. In IMS, the carrier gas can be the same as the drift gas, or it can be different depending on the application. The carrier gas, as the name suggests, is used to transport the ionized sample from the ionization region to the drift region. Typically, the carrier gas is nitrogen or air, although other reagent gases have been reported.

The drift gas, or buffer gas, is the gas that fills the drift region. It is the gas through which the ions move, which determines their mobility or rate of migration along the length of the drift tube. The mobility can be determined from the following equation

$$K = \left(\frac{3q}{16N} \right) \left(\frac{2\pi}{\mu kT} \right)^{\frac{1}{2}} \left(\frac{1}{\Omega_D} \right) \quad (1.3)$$

where q is the charge of the ion, N is the density of the drift gas molecule, k is the Boltzmann constant, T is the temperature of the drift tube, and Ω_D is the collision cross-section. The reduced mass, μ , of the ion or drift gas molecule is given by

$$\mu = \frac{mM}{(m + M)} \quad (1.4)$$

where m is the mass of the ion or molecule and M is the mass of the buffer gas. This equation reveals how the nature and type of buffer gas affects the mobility constant, K , of the ions. Scientists have used this to their advantage to improve the selectivity of the IMS instrument. Instead of using nitrogen or air, some have experimented with He, Ar, CO₂, SF₆ and other heavier and lighter gases to deliberately change the selectivity of IMS.^{18,19}

Using different drift gases to change the mobility constant led to a new parameter for identification, or figure of merit, called the separation factor (α), which is the ratio of mobility measurements for two different drift gases

$$\alpha = \frac{K_1}{K_2} \quad (1.5)$$

where K_1 is the mobility constant for analyte in gas 1, and K_2 is for the same analyte in gas 2.

Another way of changing the separation factor will be discussed later.²⁰

Ion Shutter or Gate. The ion source and drift region are separated by an ion shutter gate. The primary function of this gate is to help in the delivery of ions from the ion source region to the drift region in a controlled manner. The most common ion gate is the Bradbury-Nielson design, which is made up of thin wires that are parallel, coplanar and equally spaced. Alternate wires are mechanically and electrically isolated and usually held with a nonconductive support.³ By applying different voltages to the alternate wires, the grid can be either opened to allow ions to pass through or closed to prevent their passage. The opening and closing of the shutter gate is synchronized with the applied electric field in the drift region to optimize the available ions in the region. The synchronization controls the sampling rate (ion injection rate), thus allowing an ion packet time to reach the aperture gate or detector before a new packet is introduced.

Aperture Grid. To maintain spectral resolution from a single-scan or signal-averaged spectrum in IMS, an aperture grid is typically positioned approximately 1 mm in front of the ion collector or detector. This grid could be the same Bradbury-Nielsen type as used in the ion shutter mechanism, or it could be a fine wire mesh. Appropriate voltages are applied to the mesh to maintain the drift field close to the collector plate. One of the earlier problems of the IMS design was the capacitive coupling of the charges on the ions as they approach the collector, which affects the field close to the detector. The aperture grid was introduced to capacitively

decouple the ion packet. Without the aperture grid, there is broadening of the spectral peaks as the detector, sensing induced current from the approaching ion packets some distance away from it, begins to respond as if the ions are actually at the detector. The grid helps to neutralize the charge on the leading ions in the packet until the packet arrives and is allowed to pass through, thus helping to achieve a tighter packet of ions at the detector.²¹ This, however, results in a loss in sensitivity.

Detection, Signal Acquisition and Processing. A Faraday plate is the most common detector used in traditional IMS. This is simply a conductive plate or cup made from either aluminum or stainless steel, connected to the inverting input of an operational amplifier (op-amp) that is connected to virtual ground, which measures the current from ions that impinge onto the plate.³ Current in the nano-and pico-ampere range is measured and converted to voltage. The size of the detector and the aperture grid are critical to the quality of the ion mobility spectrum recorded. While a large plate leads to good sensitivity, it also leads to broadening of the peaks which degrades the spectral resolution. Thus, a smaller Faraday plate with an accompanying aperture grid is usually preferable. The potential between the aperture grid and the detector affects both the shape of the spectral peaks and the ion intensities. These factors must be optimized to give the best results.

The ion mobility spectrum in a constant electric field is usually a plot of ion intensity (or ion current) as a function of drift time. There are five modes of signal recording and acquisition. These include single scan, signal averaging, moving second gate, Fourier transform²² and a nonlinear mode as reported by Blanchard,²³ each with their advantages and disadvantages. Using the single scan mode, the entire ion mobility spectrum is acquired from one entrance pulse gate, while the exit gate is held open for the entire scan time. This mode is used to monitor ion

concentrations that vary rapidly with time, however, the speed of data collection leads to a sacrifice in sensitivity. In signal averaging, successive scans are stored and then averaged to produce a single ion mobility spectrum. This gives enhanced signal-to-noise ratio (S/N) and is the fastest way to obtain mobility spectra. The Fourier transform (FT) mode utilizes a square-wave generator capable of producing a linear frequency ramp, or chirp, to drive the entrance and exit gates simultaneously. The amplified output is then digitized and subjected to Fourier transform. Although the FT mode produces only a modest S/N compared to the signal averaging mode, it does not show as much peak broadening. In the nonlinear mode, an ion packet is allowed through the entrance gate, and when the selected ion almost reaches the aperture gate, the electric field direction is reversed. The ions move back to the entrance gate where additional ions are allowed into the drift tube from the ionization region. This operation is repeated over a period of time, enriching the ion of interest in the swarm. This mode enhances the sensitivity and selectivity, as well as the resolution of the instrument. The nonlinear mode also helps to trap ions for subsequent ion fracturing. The resulting daughter ions are then detected.²⁵

Electric Field Considerations. The nature of the electrical field²⁶ in the drift region of the IMS, as well as the characteristics of the neighboring reaction and detection regions, affect the overall operation and performance of the system. There have been several studies in this regard,²⁷ all conducted to improve IMS instrument performance. These fields have a bearing on the mobility and diffusion of gaseous ions and, thus, on the resolution produced by the instrument.

Eiceman and coworkers performed an evaluation of the electrical parameters in the different regions of an IMS instrument to determine which regions had the greatest influence on spectral peak shape and ion current.²⁸ The study found that electric fields between the aperture

grid and the detector and between neighboring wires in the ion shutter had the greatest influence. Electric fields on other components had little or no influence on the IMS results. Additionally, the size and position of the detector and the aperture grid also affected the performance. A small detector plate positioned along the axis of the drift tube yielded the best resolution.

In another study, Soppart and Baumbach found that improving the electric field homogeneity within the drift tube improved the resolution. This was shown through both simulation and experiments.²⁹ They found, as was always assumed, that ions drifting close to the walls of the drift tube experienced successive strong and weak accelerations and changes in direction. In comparison, ions drifting close to the axis of the drift tube followed a more direct path with a more uniform velocity. The effect of the metallic housing was also studied, as well as the length of the drift tube. The results indicated that a shorter drift tube yielded better results, probably because of a higher attainable electric field, while a larger enclosure reduced the effects of wall perturbations of the field in the drift tube.

1.5 Temperature and Pressure Effects on Ion Mobility

In IMS, the mobility values are usually corrected for temperature and pressure to give a reduced mobility value according to Equation 1.2. The underlying assumption is that the reduced mobility, K_0 , is unaffected by operational parameters, such as temperature and pressure, unlike the drift time. However, K_0 is actually influenced by temperature^{3,30} even after it has been corrected to a standard temperature of 273 K.

Karpas and coworkers studied the effect of temperature on mobility between 87 and 250°C for a series of ions in helium, air, CO₂ and SF₆. They found that the reduced mobility varies considerably. In helium, the reduced mobility was found to decrease as the temperature was raised, due to an increase in the collision cross section, and was approximately proportional

to $T^{-1/2}$. In CO_2 , where clustering takes place at low temperatures, raising the temperature led to an increase in the reduced mobility, mainly due to the breakdown of clusters and decrease in the effective masses of the ions.³¹

Tabrizchi has done considerable work on the effect of temperature and pressure on mobility measurements and resolution.³² He concluded that drift time varies linearly with pressure, but not with temperature. He attributed this to the different impacts they have on clustering.³² Temperature and pressure both affect the neutral density of the drift gas, which leads to a change in the collision frequency, however, temperature changes the identities of the ions by affecting the clustering equilibria. Therefore, a non-linear behavior is observed for temperature versus mobility.

Operating IMS at elevated temperature decreases the resolution, but improves declustering. Therefore, IMS is frequently operated at elevated temperature to assist in declustering and cleaning of the drift tube, even though some resolution is sacrificed. In contrast, negative ion mobility spectra are better resolved at elevated temperatures.³³ Declustering (for negative ions) at elevated temperature leads to a change in the identities of the ions, which results in faster drift times.

1.6 IMS Resolution

As in any spectral method, IMS resolution is critical to its utility. Unfortunately, this has been the key reason IMS has not attained wider acceptance. Resolution in IMS, often referred to as resolving power, has been investigated throughout its history, with different definitions based on mass separation, separation of a pair of peaks, or a single-peak-based quotient. The now generally accepted single-peak-based measurement of IMS resolving power³⁴ is

$$R = \frac{t_d}{W} \quad (1.6)$$

where t_d is the ion drift time and W is the ion pulse duration at the detector measured at half of its maximum intensity. Probably, because of its history, some practitioners continue to measure resolution using the standard two peak definition of resolution normally used in chromatography

$$R_s = \frac{t_{d2} - t_{d1}}{(w_{b1} + w_{b2})/2} \quad (1.7)$$

or

$$R_s = \frac{t_{d2} - t_{d1}}{w_{bavg}} \quad (1.8)$$

where R_s is the resolution, t_{d1} and t_{d2} are the drift times of two consecutive peaks w_b is the width of a peak at its base, and w_{bavg} is the average base peak width of the two consecutive peaks. In the absence of reactions with time constants on the order of, or greater than, the drift time, IMS typically produces Gaussian peaks (assuming a narrow pulse width applied to the shutter grid). Mobility theory relates the drift time, t_d , to the drift length, l_d , and the voltage, V , applied to the drift tube by the equation

$$t_d = \frac{l_d^2}{KV} \quad (1.9)$$

where K ($\text{cm}^2 \text{V}^{-1} \text{s}^{-1}$) is the mobility of the ion.³⁵

The resolution of IMS is often described as diffusion limited resolution³⁶ because the broadening of the peaks is due to the diffusion of ions as they transverse the drift tube. Other factors that contribute to peak broadening include (1) the initial pulse width and shape, (2) coulombic repulsion, (3) capacitive coupling between approaching ions and the collector plate, (4) field gradient uniformity, (5) temperature gradient, (6) gate depletion/dynamic leakage, (7)

pressure fluctuations, and (8) ion-molecule reaction in the drift space.²¹ Additional broadening has been attributed to the construction of the IMS drift tube and the parallelism (or lack thereof) that exists between the aperture grid and ion collector. Still another is the so called distribution of the electric field to bias the drift tube. If the electric field in the aperture/collector region is less than in the shutter/aperture region, apparent or “real” peak broadening can occur.³⁷

1.7 IMS Hyphenated Techniques

Hyphenating IMS to other instrumental methods such as gas chromatography (GC) and mass spectrometry (MS) has exponentially increased the utility of IMS. While IMS was mistakenly called a chromatographic^{38,39} method at the beginning of its development, it has since been successfully interfaced to GC, which is a real chromatographic technique. Karasek and his colleagues demonstrated the first coupled IMS-GC system.⁴⁰ The beauty of hyphenated techniques is that a second dimension of analysis is added, thus enhancing accuracy and positive identification of analytes. In some cases, the second dimension is used to characterize the IMS instrument.

In GC-IMS, the IMS can be regarded as a detector. Effluent from the GC column is introduced directly into the reaction region before the drift tube, where it is ionized and directed into the drift region for mobility measurement. In 1972, Karasek and coworkers again, while working on the characterization of musk ambrette,⁴¹ reported the first experimental results showing successful coupling of GC to IMS.

Most early work in interfacing GC to IMS, from 1972 to 1980, was not very successful because column technology was not as advanced as at present. This seriously limited the analytical capability of the method.⁴²⁻⁴⁹ The introduction of capillary columns and their accompanying lower flow rates and more stable stationary phases in the late ‘70s and early ‘80s

led to advances in GC-IMS systems. Hill and Biam in 1982 further advanced GC-IMS methods when they successfully solved the problem of residence time and band broadening in the drift tube.⁵⁰

The successful interfacing of capillary GC to IMS led to the development of new instruments, including the environmental vapor monitor (EVM)⁵¹⁻⁵³ and volatile organic analyzer (VOA).^{54,55} One very useful GC-IMS system that found application in the U.S. Army was a pyrolysis-GC-IMS system developed by Snyder *et al.*⁵⁶⁻⁵⁹ This coupled system was operated as a field GC-IMS for the analysis of pyrolysis products of bacteria spores.

Interfacing IMS to other chromatographic techniques such as liquid chromatography (LC) and supercritical fluid chromatography (SFC) has resulted in little to moderate success due to the excessive volume of vaporized effluent.^{60,61} Recent advances in LC have renewed interest in these methods.⁶²⁻⁶⁴ The large volume of gases produced from supercritical and liquid effluents when converted to vapor is the challenge.⁶⁵⁻⁷² However, modern micro-electrospray ionization (ESI) techniques facilitate this interfacing.

1.8 Ion Mobility Spectrometry-Mass Spectrometry (IMS-MS)

IMS-MS is growing to be a powerful hyphenated technique. From the earliest development of IMS technology, MS has been used to identify⁴⁰ and quantify the separated ions. IMS-MS is a powerful analytical tool that has gained popularity within the last 10 years, because even when IMS successfully separates ions, these ions oftentimes must be positively identified. MS methods are used to positively identify ions through their fragmentation characteristics. This becomes especially important when mobility constants of different analytes are close to each other or the same.^{73,74} MS has been used to assign masses to separated peaks in the mobility spectrum.⁷⁵ It has also been used to study the type and behavior of an electrospray ion in the

IMS.^{76,77} This has been particularly valuable in the study of biological samples with atmospheric pressure ionization methods such as MALDI and ESI mentioned above, and time-of-flight mass spectrometry.⁷⁸

In interfacing IMS to MS, a major problem is encountered, i.e., how to interface two instruments that work in different pressure regimes. While IMS works at atmospheric and higher pressures, MS operates in a vacuum. The challenge is to transport ions from high pressure to vacuum without losing ions or the integrity of the ions. When ions in the gas phase move through a pinhole or orifice between ambient pressure and high vacuum, ions and molecules of the supporting atmosphere undergo supersonic expansion, resulting in unregulated and unpredictable changes in their internal energies and in the composition of the cluster between the core ion and its surrounding neutral molecules.⁷⁹

There are two types of interfaces between IMS and MS, depending on user preference and other parameters such as pump speed and ion efficiency. These are the pinhole orifice, with a diameter of 20 to 50 μm , or skimmer cone with a diameter of 100 μm as part of a differentially pumped design in which the ions pass through two or more pressure regions.³ The main consideration in designing an interface region is the configuration of the electric field so that ions can pass from the drift tube, through the interface, and into the mass analyzer without electrical potential barriers. Thus, the orifice or skimmer are electrically isolated from the vacuum housing and raised in potential above the mass analyzer.

1.9 Applications of IMS

IMS has found application in many areas of current interest, including environmental monitoring, airport security, chemical and biological warfare agent detection, detection of illicit

drugs, pharmaceutical development and screening, biological studies and general laboratory analysis.

IMS has been in the forefront of chemical and biological warfare agent detection. Its simple instrumentation coupled with its speed of operation makes it ideal when conducting tests in a war environment. Its light weight makes it easy to carry by military personnel. In an era where developments in IMS seemed dormant, the military continued to work on improving the performance of IMS. The military considered the limitations in IMS to be mostly technological and engineering, rather than problems with the underlying principles. Although most of this work carried out by both the British and U.S. was classified, nevertheless, considerable strides in miniaturization of this technology were made. Their efforts led to two first-generation handheld chemical warfare detectors: the chemical agent monitor (CAM) and chemical agent detector (CAD).⁸⁰ The CAM was actually deployed during the 1991 Gulf War.

Other applications of IMS being pursued include the detection of explosives and illicit drugs. IMS instruments can easily be seen in airports today where they are used routinely to screen passengers. IMS can detect nitro-organic explosives at detection limits in the nanogram range. Its high sensitivity allows the explosive to be detected in complex samples without any sample pretreatment or pre-separation.^{3, 81-83} Furthermore, scientists have been using IMS to develop a methodology to separate and detect combinations of illicit drugs. This is useful for forensic scientists to establish a chain of evidence and link criminals to crime scenes.^{84,85}

In the area of environmental monitoring, IMS has been used either as a stationary device at a specific location to monitor the quality of the air, or has been deployed in the field to determine levels of degradation products from chemical warfare agents in areas where they have been stockpiled.⁸⁶ The instrument of choice has been the Rapid Alarm and Identification

Detector (RAID 1). In Germany, a new IMS was developed that uses a dimethylsilicon rubber membrane to reduce interferences so that air can be used both as carrier gas and drift gas, thus reducing the intensity of the reactant ion peak (RIP) and improving the selectivity of the IMS instrument so that incidents of false positives are reduced, if not eliminated.⁸⁷

1.10 Other IMS Techniques

High Field Asymmetry Waveform Ion Mobility Spectrometry (FAIMS). In traditional IMS, as has been discussed, there is a linear relationship between the drift velocity, v , and the electric field, E , in a low electric field strength, as depicted in Equation 1.1. Studies have shown that as the electric field in a drift tube increases, this linear relationship breaks down. This leads to ion behavior that cannot be explained nor represented by the simple mobility equation. A new set of equations and treatment of ions in this new environment are needed to understand and predict system behavior.

This behavior has been known for as long as IMS has been studied,¹⁵ but not until recently has it been thoroughly investigated to ascertain its usefulness and application. Rasulev and coworkers⁸⁸ were the first to take a fresh look at this old idea, and to develop it and find applications for it. Their efforts led to the introduction of a method and technique now called high-field asymmetric waveform IMS, better known as FAIMS. Since their defining work in 1993, attention and interest in this technique has constantly increased.

In a region of high electric field, e.g., $10,000 \text{ V cm}^{-1}$, the ion drift velocity as stated above (Equation 1.1) is no longer directly proportional to the electric field; instead, it becomes nonlinear. This general behavior can be represented by

$$K_h(E/n) = K(E=0) \left(1 + \alpha_1 (E/n)^2 + \alpha_2 (E/n)^4 + \dots \right) \quad (1.10)$$

At low electric fields, the second and third terms in the bracket go to zero and are not applicable, while at high electric fields they dominate the ion behavior. The α_i variables are the specific coefficients of even powers of the electric field and are ion species dependent. Figure 1.3 depicts this behavior for three different ions. What is observed in this figure is that at low electric field, it appears that there is one ion in the system. By increasing the electric field, it becomes evident that three different ions are actually in the field and they behave differently. This leads to improvement in selectivity which is the power of FAIMS. The dependence of K_h on the applied electric field is the basis of the development of FAIMS. Carnahan and coworkers were the first to successfully introduce a commercial FAIMS instrument; they called it a field ion spectrometer (FIS).⁸⁹ It has also been called a transverse field compensation sensor (TFC).⁹⁰ The FIS or TFC shown schematically in Figure 1.4 consisted of an ionization region and a spectrometer section, which was comprised of an ion filter and an ion collector. These were housed in an enclosure that had an inlet and outlet for gas flow. A pump attached to the outlet was used to move gas through the ionization region where the sample in the gas stream was ionized by beta-radiation. These ions were carried by the bulk gas flow into the spectrometer region.

The ion filter consisted of two parallel plates; hence, it was called a parallel plate style TFC. One of the plates was held at circuit common (virtual ground), while the other was driven by a time varying voltage, $V_{dis}(t)$, known as the dispersion voltage.

When an ion enters the analyzer region, it is subjected to a high electric field that varies at a fast rate. As the ions oscillate in the space between the plates, they gradually move toward one of the plates, depending on their mobility ratios. To reverse this trend, a compensation voltage is superimposed on the asymmetric waveform field. When this happens, the ions change their direction. When the asymmetric and compensation fields are carefully fine-tuned to balance

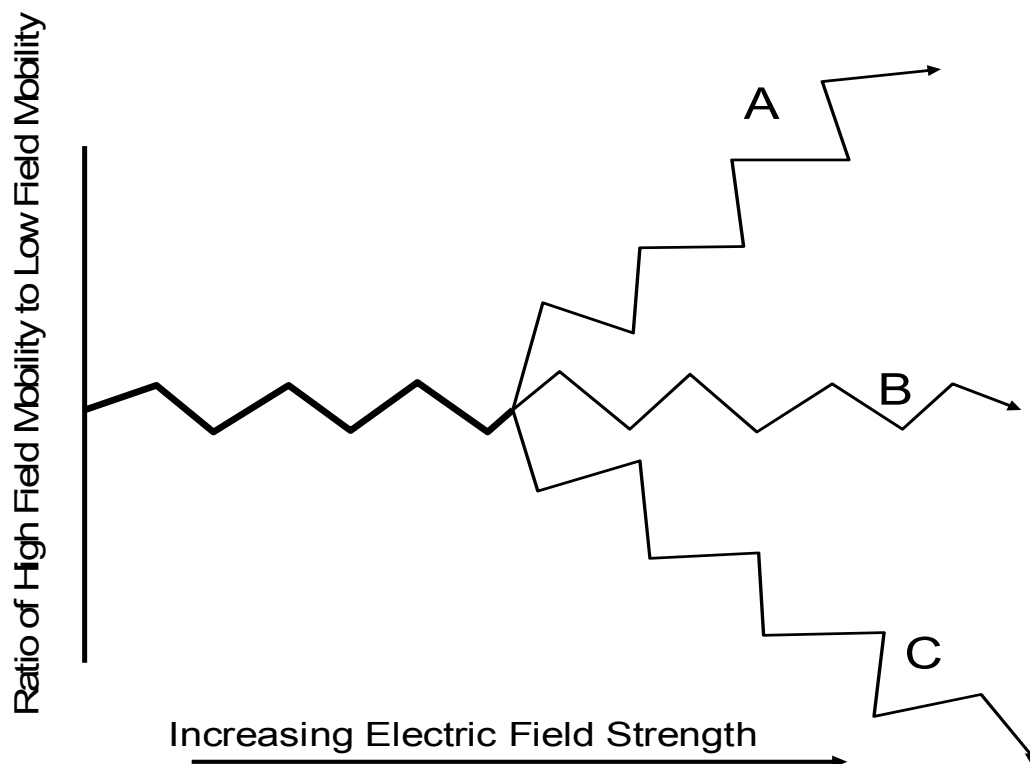


Figure 7.3 Diagram showing the effect of increasing electric field on ion mobility. At low electric field, three ions all behave the same, but as the electric field is increased, the different ions are separated.

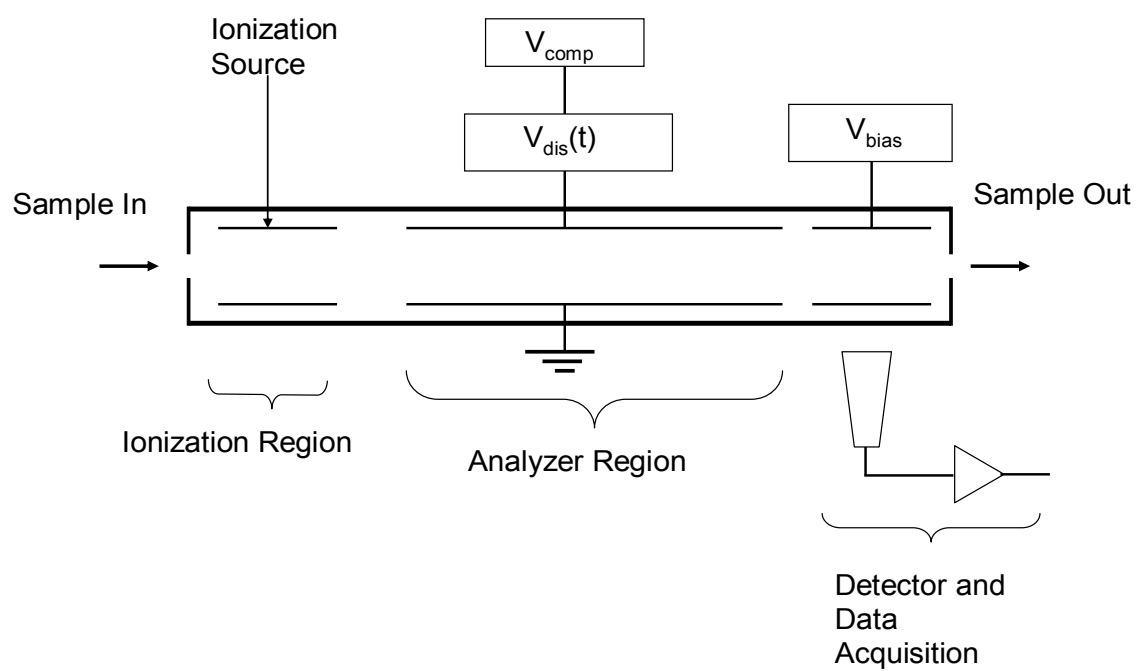


Figure 7.4 Schematic of a field ion spectrometer (FIS).

each other, specific ions can move through the filter without colliding with either plate. When the compensation voltage is scanned, different ions can be allowed to pass through the filter, and a spectrum is generated of ion intensity as a function of compensation voltage.

Further improvement and refinement were later introduced with the development of the cylindrical tube style FAIMS.⁹¹ In this design, the spectrometer has three coaxial cylinders. Two of the cylinders lie horizontally end to end inside the third larger cylinder. The shorter of the two smaller tubes defines the sensor inlet, while the longer inner and outer cylinders form the spectrometer analytical volume. The outer cylinder is grounded while the compensation and dispersion voltages are applied to the longer inner tube. This design was introduced to overcome some of the shortcomings observed in the parallel plate design, which had to do with gas introduction and humidity of the gas.

The concentric cylinder design imparted, among other things, higher sensitivity; however, the identities of the peaks that appeared in the FAIMS spectra were not positively confirmed until Guevremont successfully characterized a FAIMS spectrometer using MS.⁹²

He and his colleagues successfully interface a cylindrical style FAIMS to MS, thereby introducing the first FAIMS-MS system. This study led to other interesting and compelling possibilities, among them being the ability to focus⁹³ ions at atmospheric pressure, which before was not possible in MS. The nature of the field in a cylindrical geometry and the asymmetric waveform were responsible for this focusing of ions. Guevremont *et al.* further improved on the Carnahan *et al.* design by introducing a hemispherical end at the detector end of the spectrometer,⁹³ which caused the ions to converge and focus into the aperture that led to the MS.

The effect of the carrier gas in FAIMS has been evaluated.⁹⁴ Its impact on the ratio of high to low field mobility was studied, and the behaviors of ions from other ionization sources

such as ESI⁹⁵ were evaluated. Additionally, Guevremont *et al.* exploited the possibility of using other types of geometric configurations in an effort to improve on the performance of FAIMS. They included the use of spherical and oval configurations.^{96,97}

Recently, the planar configuration was reintroduced as a micromachined device.⁹⁸ It became possible to miniaturize the planar configuration through microfabrication for handheld devices and other micromachined instruments.⁹⁹ This has subsequently led to the development of high performance planar field-asymmetric ion mobility spectrometry (PFAIMS) for target chemical compound detection.¹⁰⁰ This instrument has been successfully used to monitor volatile organic compounds (VOC) in ambient air, both in and outside buildings.¹⁰¹⁻¹⁰³

Despite the interest that FAIMS has generated within the last few years, its performance as a high resolution instrument is still lacking. The resolution is worse than that of traditional IMS, being so poor that it is rarely mentioned in the literature. Practitioners try to highlight its strongest advantage, which is high selectivity. To improve resolution, the FAIMS technique is being extensively characterized to understand how the various components work together and how they affect the resolution and selectivity of the technique.¹⁰⁴ This is being done by modeling the resolution and selectivity. Simulation of FAIMS under realistic conditions is helping to provide understanding to the method.¹⁰⁵ The feasibility of using higher-order components in the FAIMS equations is also being studied.¹⁰⁶

Differential Mobility Analysis (DMA). Another analytical technique that uses the principles of IMS is differential mobility analysis (DMS). This technique is very common and popular among environmentalists, especially for measuring and determining aerosol particle sizes in the atmosphere. This technique is older than the FAIMS approach described above.

In DMA, particles or ions are separated in space by the combination of an electric field and a flow field orthogonal to each other. Only a narrow mobility range is sampled and detected. This is different from conventional IMS in which separation occurs in time. DMA is most often used to determine particles in the sub micrometer range. The first step is to apply an electrical charge to the particles. It is difficult to put more than one charge on a small particle; as a result, most particles either remain uncharged or have a single charge. Only the positively charged particles are sorted by the DMA; all of the others are lost.¹⁰⁷

A simplistic description of DMA is that it consists of two charged concentric cylinders with an inlet slit and a sampling slit. Aerosol particles for sizing are introduced into the annular region between the two cylinders at the inlet slit (see Figure 1.5). They are carried by flowing clean air through the annular region while the electric field draws them toward the inside cylinder. Particles with mobilities in a certain narrow range are sampled at the sampling slit. Then, an inversion calculation is done to specify the size distribution; of course, sizing depends on certain adjustable parameters such as voltage and flow rate.¹⁰⁸ Similar to the other IMS techniques, the DMA is also challenged with issues of selectivity and resolution. The inability to measure multiply charged particles is also a major limitation to its use, unlike conventional IMS where multiply charged ions give higher resolution.

The resolution issue is also troublesome to DMA. Like traditional IMS, DMA resolution is a diffusion limited resolution, so that any effort to improve resolution must focus on ways to minimize the diffusion of particles to the walls of the analyzer. The effect of this Brownian diffusion on resolution is well documented.¹⁰⁹ One way scientists have sought to reduce the diffusion rate is by increasing the sheath gas flow velocity.¹¹⁰ At high gas velocity, peak broadening is greatly reduced if done in conjunction with a shorter drift tube.¹¹¹

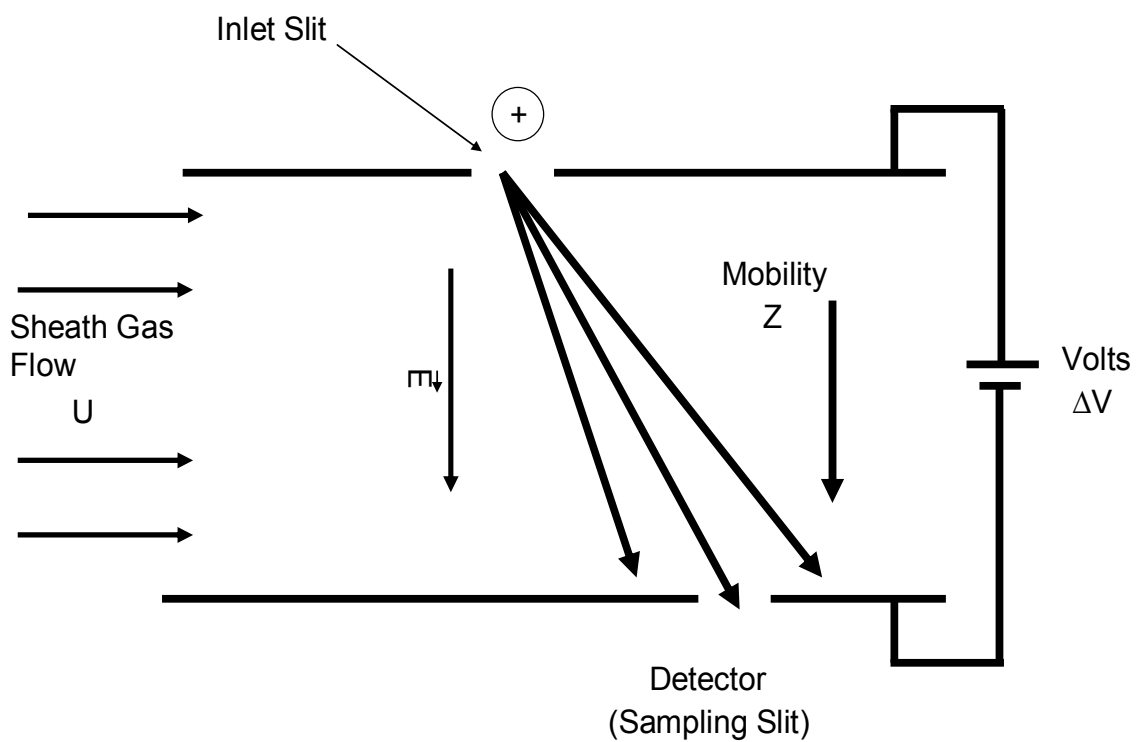


Figure 7.5 Schematic of the DMA, showing the sheath gas and electric field directions as ions transverse the analyzer.

1.11 Limitations of Present IMS Techniques

As discussed above, all of the IMS techniques suffer from low resolution and, hence, low selectivity which is due to gas diffusion that competes with the ion mobility transport process. This low resolution has affected the utility and acceptance of IMS. If IMS is to achieve its full potential, the resolution limitation must be overcome. The work described in this dissertation addresses an attempt to improve IMS resolution by utilizing a high velocity gas flow counter to the ion drift direction imposed by the electric field. This technique has been named “counter-flow ion mobility analysis (CIMA)”

1.12 Counter-flow Ion Mobility Analysis (CIMA)

In conventional IMS, the velocity of an ion is determined in part by the electric field that is used. A relatively low velocity buffer gas is oftentimes used to clean the drift tube and help with declustering of ions. This buffer gas has little to no effect on the drift velocity of the ions. In CIMA, the flow rate of the counter-flow buffer gas is increased to a point that its force on the ions is close to the force of the electric field. The electric field must be high so that ions will travel at high speeds to reduce their residence time in the analyzer and minimize diffusion, and the velocity of the buffer gas must be greatly increased, so that it is able to reverse the direction of ion motion. When these two velocities or forces balance each other, ions of a particular mobility are stopped in space while other ions of lesser or greater mobility move along the direction of the gas flow or electric field, respectively, and are lost (see Figure 1.6). These selected ions are quickly moved to the detector before diffusion takes place.

CIMA utilizes the basic principles of IMS, but with modification to achieve higher resolution and, hence, better selectivity than conventional IMS. To achieve high resolution, a high electric field (over 2500 V cm^{-1}) and high counter-gas velocity (over 10 m s^{-1}) provide

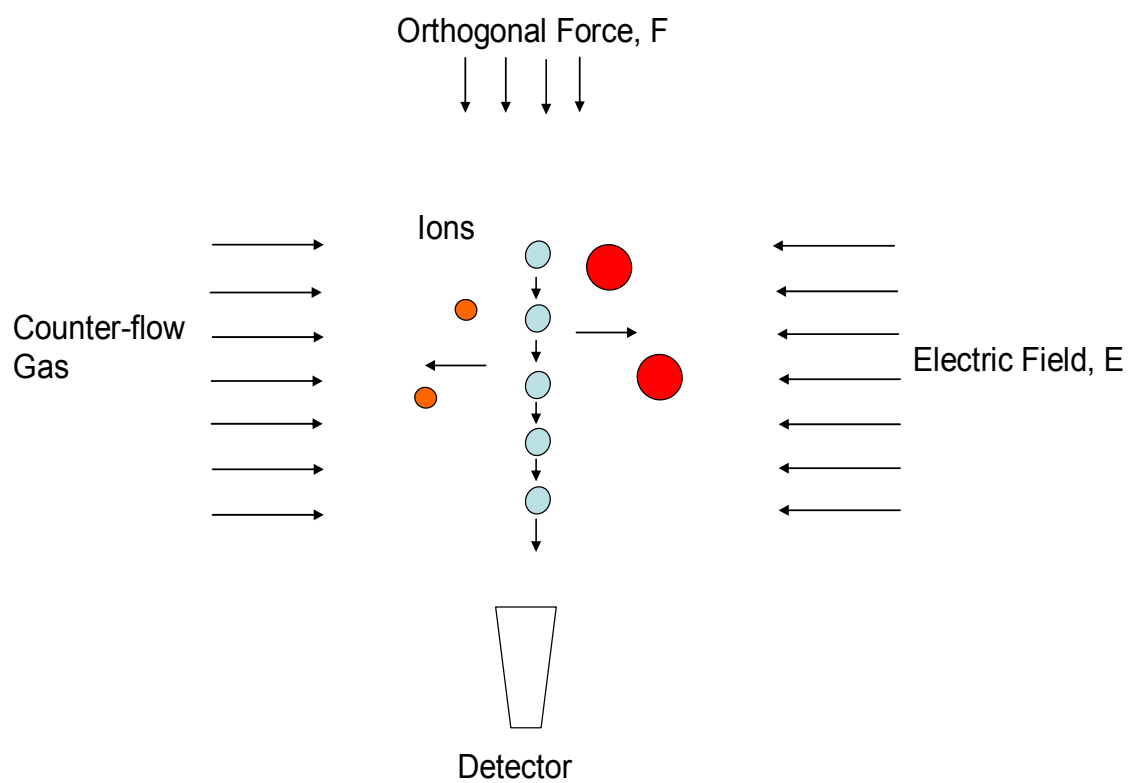


Figure 7.6 Schematic description of CIMA showing the counter gas flow and electric field that acts on a selected sample of ions. The selected ions are directed to the detector while others are lost from the analyzer region.

opposing forces to stop the motion of the ions in space. A third force, which is stronger than either of the opposing forces is used to quickly move the ions to the detector. This third force is orthogonal to both the opposing electric field and gas flow. This third force can be either an electric field or gas flow. In CIMA, the key is in the use of the opposing electric field and gas flow to select analyte ions and to use a stronger orthogonal force or field to transport them to the detector or to use a drift tube of short length.

1.13 Previous Work on Using Opposing Forces to Manipulate Ions

In 1898, Zeleny used a similar approach to CIMA to investigate the ratio of velocities of two ion species produced in gases by Roentgen radiation.¹¹² He used two wire meshes (A and B) that were separated by a distance, d , with a voltage, V applied across them (See Figure 1.7). Ions were created by Roentgen radiation between the plates. The electric field created by the applied voltage moved the ions to one mesh or the other depending on their polarities. He then introduced a flow of gas through the wire meshes from A to B at a uniform velocity. Depending on the voltage applied across the meshes, the gas flow velocity and the nature of the ions, he was able to stop the ions, or even move them in the opposite direction when the gas velocity was larger than the ion drift velocity.

It appears that Zeleny was the first to manipulate the motion of ions by using two opposing forces. In his work, he did not measure ion mobilities or perform separation and detection, but measured the velocities of charged species. Interestingly, he faced the same issues associated with CIMA today, namely, how to generate a uniform gas flow.

Most of the recent work directed at improving the resolution of IMS using the concept of opposing forces, was done by environmentalists using a modified differential mobility analyzer (DMA) to sample aerosols. As described above, in DMA, the electric field is established

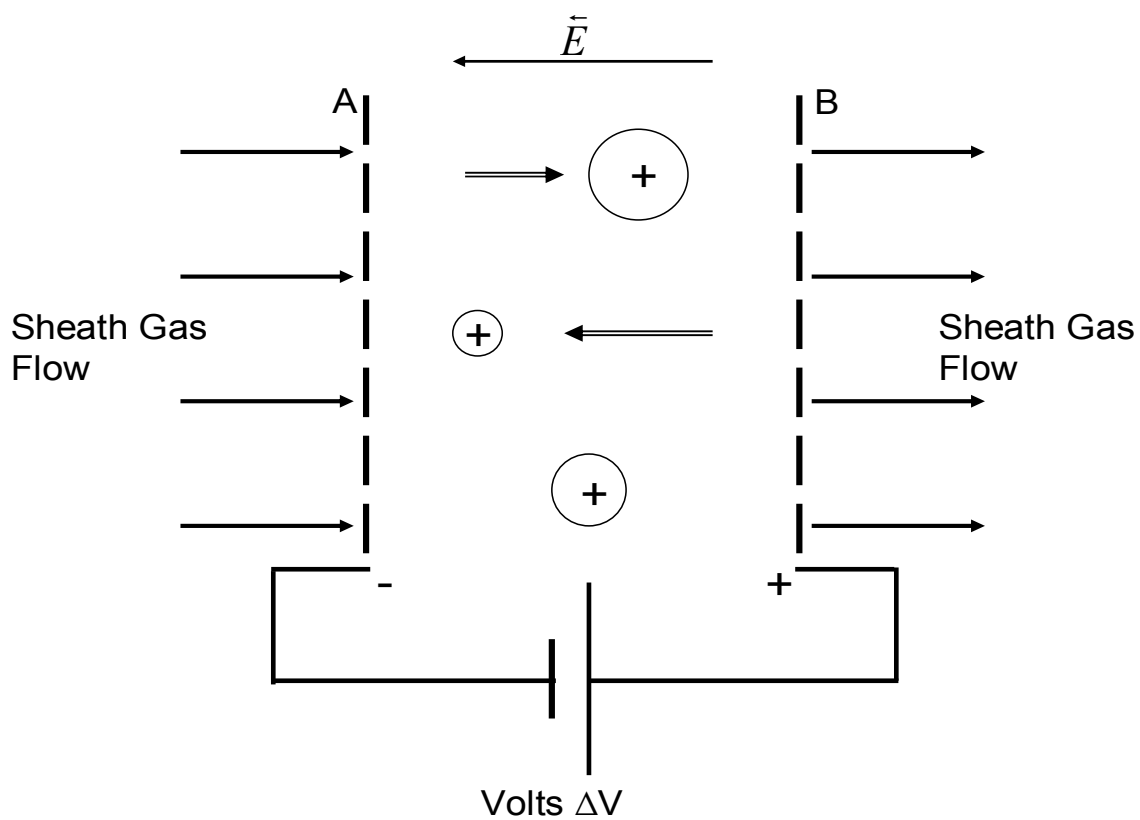


Figure 7.7 Schematic of an opposing flow analyzer. Zeleny used a simple instrument design as shown to demonstrate the manipulation of ion motion using a gas flow and opposing electric field.

between two plates (or electrodes) and ions or particles are injected through a slit in one electrode. As the ions drift in the field toward the other electrode, they are carried in the direction parallel to the plates by a flow of clean ion-free gas moving perpendicularly to the slit.

Loscertales and coworkers found that they could minimize the diffusive broadening of ultrafine particles by using large flows with Reynolds numbers still within the laminar flow region.¹¹³ In addition, they found that diffusional broadening can be further reduced if the ratio between the DMA length and the separation between its electrodes is roughly between 0.5 and 2.

Approximately 3 years later, Loscertales found that the resolution could be further improved, at least theoretically, when the axial electric field was superimposed on the classical radial field in addition to increasing the flow rate of the sheath gas.¹¹⁴ The resulting instrument was a combination of both IMS and DMA, which he called a drift differential mobility analyzer (DDMA). The concept of DDMA allows the resolution of IMS to be increased by a factor of approximately 3, and allows for a continuous feed instrument (unlike IMS) which is pulsed.¹¹⁵

A year earlier, i.e., 1997, Tammet produced a working model that Loscertales used to explain his proposed idea. As depicted in Figure 1.8, Tammet's model¹¹⁶ consisted of two flat plates, parallel to each other, separated by a constant distance, h , with a sheath gas flowing between the plates. It was assumed for the sake of simplicity that the flow was of the plug type, i.e., a constant gas velocity, v_g , between the plates. The aerosol entered and left the analyzer through two slits located at an axial distance, l_0 , from each other. The aerosol flow rate was assumed negligible compared with the sheath gas flow rate. The plates were not equipotential and the electric field was not perpendicular to the sheath gas, as in the classical DMA; instead the electric field was inclined but uniform.

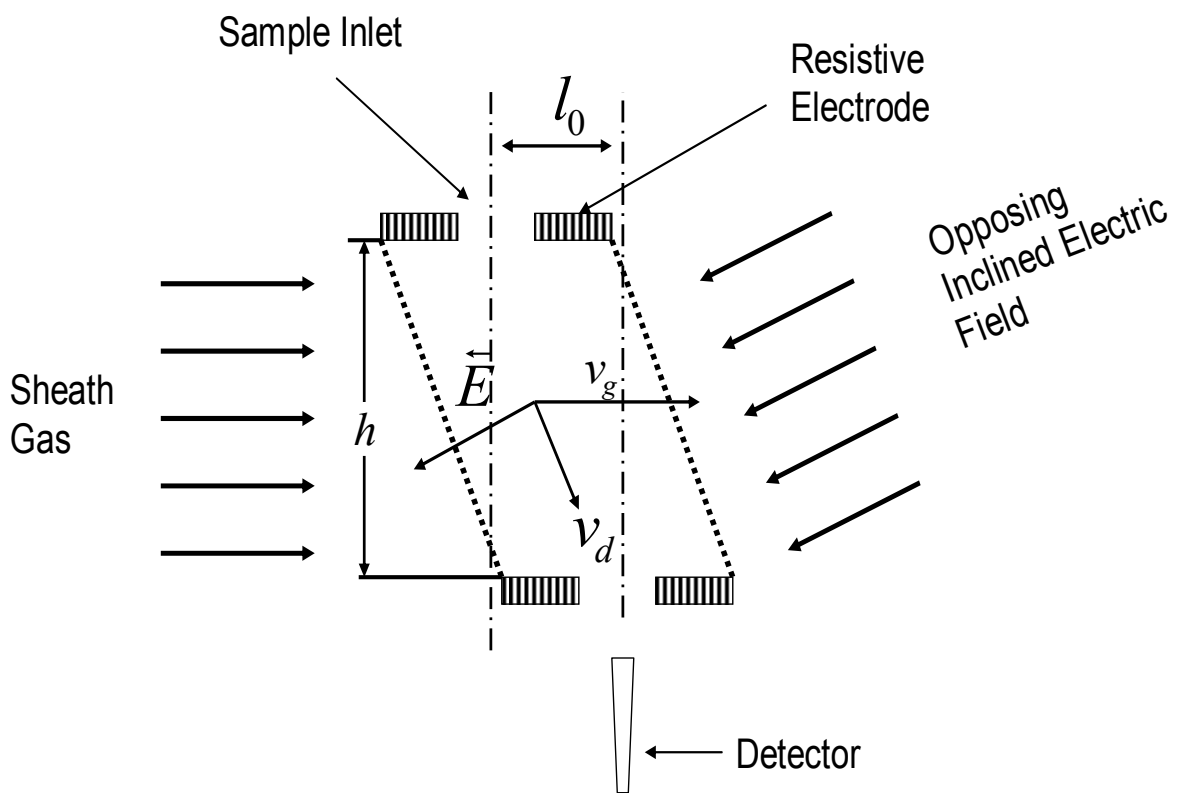


Figure 7.8 Loscertales and Tammet drift differential mobility analyzer schematic, showing the inclined electric field, the sheath gas flow and the motion and direction of ions.

In another design, Tammet proposed the use of an inclined grid.¹¹⁷ This is because of the technical difficulty in realizing the Loscertales proposed design due to the non-equipotential electrodes. In the inclined grid, shown in Figure 1.8, the driving voltage was applied between the grids, creating an inclined electric field relative to the sheath gas flow direction. Tammet further showed that the optimum length¹¹⁸ of the analyzer produces a ratio of the electric fields in the horizontal and vertical directions of between 0.5 and 2

$$\frac{E_x}{E_y} = L_o \quad (1.11)$$

where L_o is the Loscertales ratio with values of 0.5 to 2.

Flagan,^{119,120} in a yet to be developed cross-flow differential migration classifier, which was also called an opposed migration aerosol classifier (OMAC), described his approach to using opposing forces. The general principle is the same as described above, with applications to aerosol particles. His instrument classified aerosol particles in a channel flow between porous (or screen) electrodes (see Figure 1.9). In his design, gravitational and centrifugal forces could be used in place of the cross flow gas. Using a Monte-Carlo algorithm, he simulated a technique closely related to field flow fractionation, FFF. Interestingly, his modeled cross-flow between the electrodes was a parabolic flow, which is different from the plug flow others have used.

Laiko recently described a system similar to what is presented in this dissertation. He called his method orthogonal extraction IMS (Figure 1.10). He used a Monte-Carlo three-dimensional numerical simulation to predict that a resolution of approximately 600 would be achievable for this yet to be built instrument.¹²¹

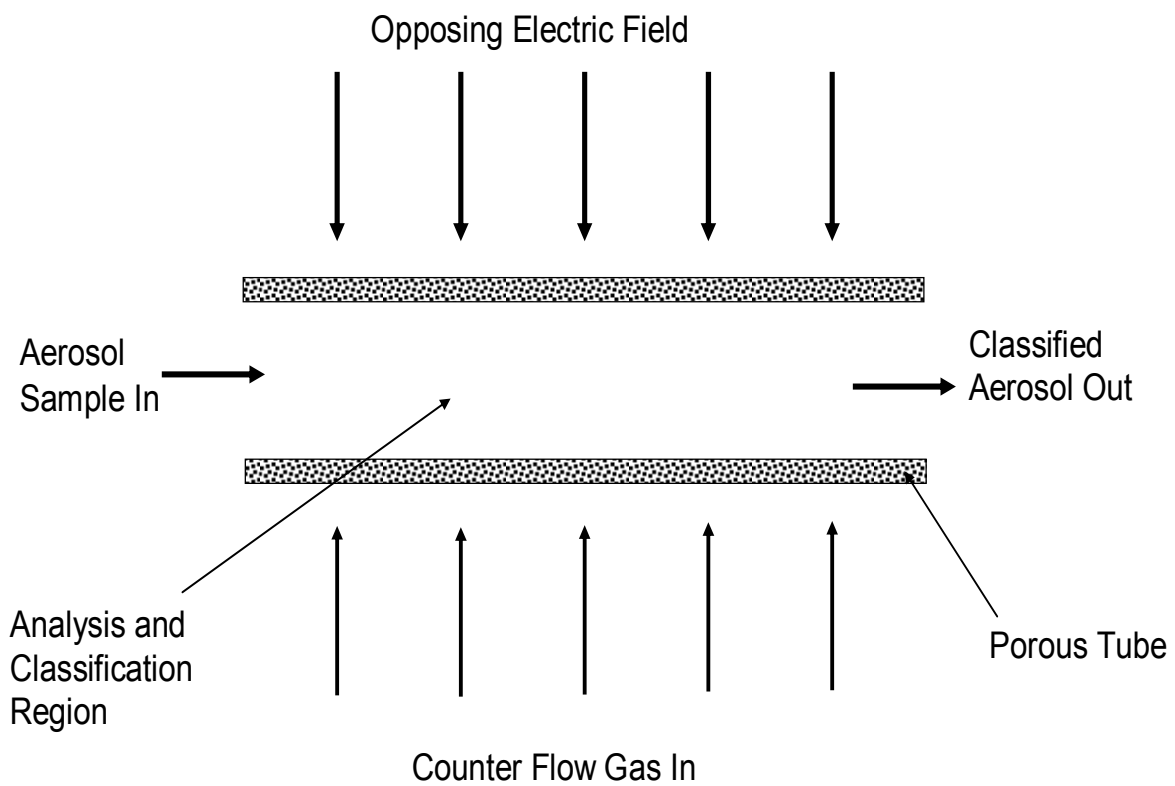


Figure 7.9 Schematic representation of Flagen's opposed migration aerosol classifier (OMAC) showing a porous wall with gas flow and opposing electric field as aerosol moves along the analyzer length.

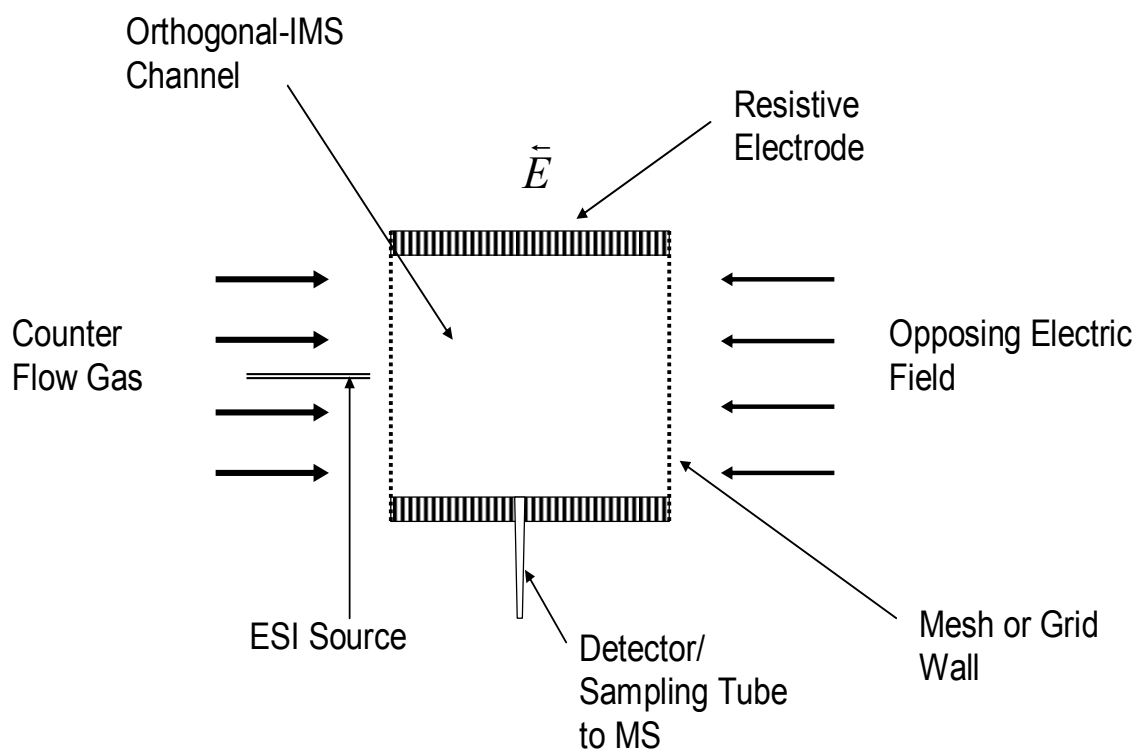


Figure 7.10 Schematic representation of the orthogonal extraction ion mobility spectrometer proposed by Laiko. The analyzer channel is defined by grids through which the counter gas flows.

1.14 References

1. Cohen, M.J.; Karasek, F.W. *J. Chromatogr. Sci.* **1970**, 8, 300-337.
2. Cohen, M.J. *Pittsburgh Conference on Analytical Chemistry and Applied Spectroscopy*, March **1969**.
3. Eiceman, G.A.; Karpas, Z. *Ion Mobility Spectrometry*, CRC Press: Boca Raton, FL, **2005**.
4. Eiceman, G.A. *Crit. Rev. Anal. Chem.* **1991**, 22, 17-36.
5. Griffin, G. W.; Dzidic, I.; Carroll, D. I.; Stillwell, R. N.; Horning, E. C. *Anal. Chem.* 1973, 45, 1204-1209.
6. Pozzi, R.; Pinelli, F.; Bocchini, P.; Galletti, G. C. *Anal. Chim. Acta* **2004**, 504, 313-317.
7. Proctor, C. J.; Todd, J. F. *J. Anal. Chem.* **1984**, 56, 1794-1797.
8. Hill, C. A.; Thomas, I. P. *Analyst* **2003**, 128, 55-60.
9. Loeb, L. B. *Electrical Coronas*, University of California Press: Berkeley and Los Angeles, CA, 1965.
10. Carreño, F.; Barbabeu, E. *J. Phys. D: Appl. Phys.* **1994**, 27, 2136-2144.
11. Tabrizchi, M.; Abedi, A. *J. Phys. Chem. A* **2004**, 108, 6319-6324.
12. Doug, W.; Yong, H. C.; Luckenbill, B. K.; Hill, H. H. Jr., *Anal. Chem.* **1994**, 66, 2348-2355.
13. Gross, J. H. *Mass Spectrometry: A textbook*, Springer, Heidelberg, **2004**.
14. Wu, C.; Hill, Jr.; Rasulev, U. K.; Nazarov, E. G. *Anal. Chem.* **1999**, 71, 273-278.
15. Mason, E. A.; McDaniel, E. W. *Transport Properties of ions in Gases*, John Wiley & Sons, NY, 1988.
16. Iinuma, K.; Takebe, M.; Satoh, Y.; Seto, K. *Rev. Sci. Instrum.* **1982**, 53, 845-850.
17. Carrico, J. P.; Sickenberger, D. W.; Spangler, G. E.; Vora, K. N. *J. Phys. E: Sci. Instrum.*, **1983**, 16-25.

18. Karpas, Z.; Berant, Z. *J. Phys. Chem.* **1989**, 93, 3021-3025.
19. Li-Aravena, F.; Saporoschenko, M. *J. Chem. Phys.* **1993**, 98, 8888-8891.
20. Asbury, G. R.; Hill, Jr., H. H. *Anal. Chem.* **2000**, 72, 580-584.
21. St. Louis, R. H.; Hill, H. H. Jr., *Crit. Rev. Anal. Chem.* **1990**, 21, 321-355.
22. Knorr, F. J., Eatherton, R. L.; Sims, W. F.; Hill, H. H. Jr., *Anal Chem.* **1985**, 57, 402-408.
23. Blanchard, W. C.; *Res. Dev.* **1998**, 50-55.
24. Hill, H. H. Jr.; Siems, W. F.; St. Louis, R. H.; McMinn, D. G. *Anal. Chem.* **1990**, 62, 1201A-1209A.
25. Blanchard, W. C. *Int. J. Mass Spectrom. Ion Processes* **1989**, 95, 199-210.
26. Viehland, L. A.; Mason, E. A. *Ann. Phys.* **1975**, 91, 499-533.
27. Viehland, L. A.; Mason, E. A. *J. Chem. Phys.* **1975**, 63, 2913-2915.
28. Eiceman, G. A.; VAnduver, V. J.; Chen, T.; Rico-Martinez, G. *Anal. Instrum.* **1989**, 18, 227-242.
29. Soppart, O.; Baumbach, J. I. *Meas. Sci. Technol.* **2000**, 11, 1473-1479.
30. Eiceman, G. A.; Wang, Y. F.; Rodriguez, J. E.; Nazarov, E. *The 8th International Conference on Ion Mobility Spectrometry*, Buxton, UK, August 8-12, **1999**.
31. Karpas, Z.; Berant, Z.; Shahal, O. *J. Am. Chem. Soc.* **1989**, 111, 6015-6018.
32. Tabrizchi, M.; Rouholahnejad, F. *J. Phys. D: Appl. Phys.* **2005**, 38, 857-862.
33. Tabrizchi, M. *Talanta*, **2004**, 62, 65-70.
34. Reid, G.; Hill, H. H. Jr. *J. Chromatogr. A*, **2000**, 902, 433-437.
35. Siems, W. F.; Wu, C.; Traver, E. E.; Hill, H. H. Jr.; Laesen, P. R.; McMinn, D. G. *Anal. Chem.* **1994**, 66, 4195-4207.
36. Revercomb, H. E.; Mason, E. A. *Anal. Chem.* **1975**, 47, 970-983.

37. Spangler, G. E. *Int. J. Mass Spectrom.* **2002**, 220, 399-418.
38. Karasek, F. W. *Anal. Chem.* **1974**, 46, 710A-720A.
39. Carr, T. W. *Plasma Chromatography*, Plenum Press, New York, 1984.
40. Cohen, M. J.; Karasek, F. W., *J. Chromatogr. Sci.* **1970**, 8, 330-337.
41. Karasek, F. W.; Keller, R. A. *J. Chromatogr. Sci.* **1972**, 10, 626-628.
42. Cram, S. P.; Chesler, S. N. *J. Chromatogr. Sci.* **1973**, 11, 391-401.
43. Ithakissios, D. S. *J. Chromatogr. Sci.* **1980**, 18, 88-92.
44. Hagen, D. F., *Anal. Chem.* **1979**, 51, 872-874.
45. Ramstad, T.; Nestruck, T. J.; Tou, J. C., *J. Chromatogr. Sci.* **1978**, 16, 240-245.
46. Karasek, F. W.; Hill, H. H. Jr.; Kim, S. H.; Rokushika, S., *J. Chromatogr. Sci.* **1977**, 15, 329-339.
47. Keller, R. A.; Metro, M. M., *J. Chromatogr. Sci.* **1974**, 12, 673-677.
48. Karasek, F. W.; Kim, S. H., *J. Chromatogr. Sci.* **1974**, 99, 257-266.
49. Metro, M. M.; Keller, R. A., *J. Chromatogr. Sci.* **1973**, 11, 520-524.
50. Baim, M. A.; Hill, H. H. Jr., *Anal. Chem.* **1982**, 54, 38-43.
51. Arnold, N. S.; Dworzanski, J. P.; Sheya, S. A.; McClennen, W. H.; Meuzelaar, H. L. C., *Field Anal. Chem. Technol.* **2000**, 4, 219-238.
52. Snyder, A. P.; Harden, C. S.; Brittain, A. H.; Kim, M-G.; Arnold, N. S.; Meuzelaar, H. L. C., *Anal. Chem.* **1993**, 65, 299-306.
53. McClennen, W. H.; Arnold, N. S.; Meuzelaar, H. L. C., *TrAC: Trends Anal. Chem.*, **1994**, 13, 286-293.
54. Limero, T.; Reese, R.; Trowbridge, J.; Hohmann, R., *33rd International Conference on Environmental Systems*, San Antonio, TX, July 2002.

55. Limeró, T.; Reese, E., *Int. J. Ion Mobility Spectrom.* **2002**, 5, 27-30.
56. Snyder, A. P.; Thornton, S. N.; Dworzanski, J. P.; Meuzelaar, H. L. C. *Field Anal. Technol.* **1996**, 1, 49-59.
57. Snyder, A. P.; Maswadeh, W. M.; Tripathi, A.; Dworzanski, J. P. *Field Anal. Chem. Technol.* **2000**, 4, 11-126.
58. Dworzanski, J. P.; McClennen, W. H.; Cole, P. A.; Thornton, S. N.; Meuzelaar, H. L. C.; Arnold, N. S.; Snyder, A. P. *Field Anal. Chem. Technol.* **1997**, 1, 295-305.
59. Snyder, A. P.; Tripathi, A.; Maswadeh, W. M.; Ho, J.; Spence, M. *Field Anal. Chem. Technol.* **2001**, 5, 190-204.
60. Issenberg, P.; Essigmann, J. *Pittsburgh Conference of Analytical Chemistry and Applied Spectroscopy*, Cleveland, OH, March 1972.
61. Karasek, F. W.; Denney, D. W. *Anal. Lett.* **1973**, 6, 993-1002.
62. Shumate, C. B.; Hill, H. H. Jr. *Anal. Chem.* **1989**, 61, 601-606.
63. Hill, H. H. Jr.; Siems, W. F.; Eatherton, R. L.; St. Louis, R. H.; Morrissey, M. A. *Instrum. Trace Org. Monit.* **1992**, 49-64.
64. McMinn, G. G.; Kinzer, J. A.; Shumate, C. B.; Siems, W. F.; Hill, H. H. Jr. *J. Microcolumn Sep.* **1990**, 2, 188-192.
65. Eatherton, R. L.; Morrissey, M. A.; Hill, H. H. Jr. *Anal. Chem.* **1988**, 60, 2240-2243.
66. Huang, M. X.; Markides, K. E.; Lee, M. L. *Chromatographia* **1991**, 31, 163-167.
67. Morrissey, M. A.; Widmer, H. M. *J. Chromatogr.* **1991**, 552, 551-561.
68. Eatherton, R. L.; Morrissey, M. A.; Hill, H. H., Jr. *J. High Resolut. Chromatogr./Chromatogr. Commun.* **1986**, 9, 154-160.
69. Rokushika, S.; Hatano, H.; Hill, H. H., Jr. *Anal. Chem.* **1987**, 59, 8-12.

70. Morrissey, M. A.; Siems, W. F.; Hill, H. H., Jr. *J. Chromatogr.* **1990**, 505, 215-225.
71. Hannan, R. M.; Hill, H. H., Jr. *J. Chromatogr.* **1991**, 547, 393-401.
72. Hallen, R. W.; Shumste, C. B.; Siems, W. F.; Tsuda, T.; Hill, H. H., Jr. *J. Chromatogr.* **1989**, 480, 233-245.
73. Kim, S.H.; Spangler, G. E. *Anal. Chem.* **1985**, 57, 567-569.
74. Karpas, Z.; Stimac, R.M.; Rappoport, Z. *Int. J. Mass Spectrom. Ion Process*, **1988**, 83, 163-175.
75. Griffin, G. W.; Dzidic, I.; Carroll, D.I.; Stillwell, R.N.; Horning, E.C. *Anal. Chem.* **1973**, 45, 1204-1209.
76. Fernandez de la Mora, J.; Thomson, B. A.; Gamero-Castano, M. *J. Am. Soc. Mass Spectrom.* **2005**, 16, 717-732.
77. Clowers, B.H.; Dwivedi, P.; Steiner, W. E.; Hill, H.H. Jr.; Bendiak, B. *J. Am. Soc. Mass Spectrom.* **2005**, 16, 660-669.
78. Stiener, W.E.; Clowers, B.H.; English, W.A.; Hill, H. H. Jr. *Rapid Commun. Mass Spectrom.* **2004**, 18, 882-888.
79. Spangler, G.E.; *Int. J. Mass Spectrom.* **2001**, 208, 169-191.
80. [http:// 63.89.158.169/products /Default.asp?product=7](http://63.89.158.169/products/Default.asp?product=7)
81. Spangler, G.E.; Lawless, P.A. *Anal. Chem.* **1978**, 50, 884-892.
82. Ewing, R.E.; Ewing, G.J.; Atkinson, D.A.; Eiceman, G.A. *Talanta*, **2001**, 54, 515-529.
83. http://www.geindustrial.com/ge-interlogix/iontrack/prod_itemiser.html
84. Ochoa, M.L.; Harrington, P.B. *Anal. Chem.* **2004**, 76, 985-991.
85. Wu, C.; Siems, W.F.; Hill, H.H. Jr. *Anal. Chem.* **2000**, 72, 396-403.
86. Sohn, H.; Steinhanses, J. *IJIMS*, **1998**, 1, 1-14.

87. Adler, J.; Döring, H.R.; Starrock, V.; Wülfing, E. *Proc. 4th Int. Symp. Protection Against Chemical Warfare Agents*, Stockholm, Sweden 8-12 June **1992**.
88. Buryakov, I.A.; Krylov, E.V.; Nazarov, E.G.; Rasulev, U.Kh. *Int. J. Mass Spectrom. Ion Processes* **1993**, 128, 143-148.
89. Carnahan, B. L.; Tarassov, A. S. Ion Mobility Spectrometer. U.S. Patent 5,420,424, May 30, 1995.
90. Carnahan, B.; Day, S.; Kouznetsov, V.; Matyjaszczyk, M.; Tarassov, A. *41st Annual Analysis Division Spring Symposium*, Framingham, MA, April 21-24, **1996**.
91. Carnahan, B.; Day, S.; Kouznetsov, S.; Tarassov, A. *Proceedings: 4th International Workshop on Ion Mobility Spectrometry*, August 6-9, **1995**.
92. Purves, R.W.; Guevremont, R. *Rev. Sci. Instrum.* **1998**, 69, 4094-4105.
93. Guevremont, R.; Purves, R.W. *Rev. Sci. Instrum.* **1999**, 70, 1370-1383.
94. Barnett, D. A.; Ells, B.; Guevremont, R.; Purves, R. W.; Viehland, L. A. *J. Am. Soc. Mass Spectrom.* **2000**, 11, 1125-1133.
95. Guevremont, R.; Barnett, D. A.; Purves, R. W.; Vandermeij, J. *Anal. Chem.* **2000**, 72, 4577-4584.
96. Guevremont, R.; Purves, R.; Barnett, D. Tandem high Field Asymmetric Waveform Ion Mobility Spectrometry (FAIMS) Tandem Mass Spectrometry. U.S. Patent 0,226,965 January 30, 2003.
97. <http://www.ionanalytics.com/en/technology/faims.shtml>
98. Miller, R. A.; Eiceman, G.A.; Nazarov, E. G.; King, A. T. *Sens. and Actuators B* **2000**, 67, 300-306.

99. Eiceman, G. A.; Nazarov, E. G.; Miller, R. A.; Krylov, E. V.; Zapata, A. M. *Analyst*, **2002**, 127, 466-471.
100. Miller, R. A.; Zapata, A.; Nazarov, E. G.; Krylov, E. Eiceman, G. A. *Mat. Res. Soc. Symp. Proc.* **2002**, 729, 139-147.
101. Krylova, N.; Krylov, E.; Eiceman, G. A.; Stone, J. A. *J. Phys. Chem. A* **2003**, 107, 3648-3654.
102. Eiceman, G. A.; Nazarov, E. G.; Tadjikov, B.; Miller, R. A. *Field Anal. Chem. Technol.* **2002**, 4, 297-308.
103. Eiceman, G. A.; Tarassov, A.; Funk, P. A.; Hughs, S. E.; Nazarov, E. G.; Miller, R. A. *J. Sep. Sci.* **2003**, 26, 585-593.
104. Shvartsburg, A. A.; Tang, K.; Smith, R. D. *J. Am. Soc. Mass Spectrom.* **2004**, 15, 1487-1498.
105. Shvartsburg, A. A.; Tang, K.; Smith, R. D. *J. Am. Soc. Mass Spectrom.* **2005**, 16, 1447-1455.
106. Shvartsburg, A. A.; Mashkevich, S. V.; Smith, R. D. *J. Phys. Chem. A* **2006**, 110, 2663-2673.
107. Flagan, R. *Aerosol Sci. Technol.* **1998**, 28, 301-380.
108. Reischl, G. P. *J. Aerosol Sci.* **1991**, 22, 297-312.
109. Kousaka, Y.; Okuyama, K.; Adachi, M.; Mimura, T. *J. Chem. Eng. Jpn.* **1986**, 19, 401-407.
110. Rosell-Llompart, J.; Locertales, D.; Bingham, D.; Fernández de la Mora, J. *J. Aerosol Sci.* **1996**, 27, 695-719.
111. Loscertales, I. G. *J. Aerosol Sci.* **1998**, 29, 1117-1139.
112. J. Zeleny, *Philos. Mag.*, **1898**, 46, 120-154.

113. Rosell-Llompart, J.; Loscertales, I. G.; Bingham, D.; Fernandez, de la Mora, J. *J. Aerosol Sci.* **1996**, *27*, 695-719.
114. Loscertales, I. G. *J. Aerosol Sci.* **1998**, *29*, S1241-S1242.
115. Loscertales, I. G. *J. Aerosol Sci.* **1998**, *29*, 1117-1139.
116. Tammet, H. IPST, Jerusalem, 1970.
117. Tammet, H. *Proc. 11th Int. Conf. Atmos. Electr.*, NASA, MSFC, Alabama, 1999, 626-626.
118. Tammet, H. *J. Aerosol Sci.* **1998**, *29*, S63-S64
119. Flagan, F, C. Cross-flow Differential Migration Classifier. US Patent 6,905,029 B2 June 14, 2005.
120. Flagan, F. C. *Aerosol Sci. Technol.* **2004**, *38*, 890-899.
121. Laiko, V. V. *J. Am. Soc. Mass Spectrom.* **2006**, *17*, 500-507.

Chapter 2

Counter-flow Ion Mobility Analysis

2.1 Introduction

Both IMS acceptance and utility have been limited by relatively poor resolution due to diffusion.¹ Recent attempts to achieve higher resolution in traditional IMS have focused on improving the drift tube or detector system, with little to moderate success. Although the theory of IMS predicts a resolution of approximately 300, which is low, a value of only 70 has been attained by laboratory built units.^{2,3} With the aid of powerful detectors that sample only a few molecules from the packet of ions, a resolution of over a 100 has been reported.⁴

It is well known that if IMS is to reach its full potential, the resolution must be improved. In order to increase the resolution of IMS, the time available for gas-phase dispersion (diffusion) of ion packets must be reduced. The fundamental laws of diffusion place a limit on the attainable IMS resolution due to ion residence time; the current instrumentation allows diffusion to dominate ion transport processes as a result of the relatively long time that the ions spend in the drift tube. From the Einstein equation, diffusion and mobility are directly related and are affected by the same physical conditions, such as temperature

$$K = \frac{eD}{kT} \quad (2.1)$$

where e is the ion charge, k is the Boltzmann constant, T is the gas temperature, and D is the diffusion coefficient. Elevated temperature used in conventional IMS further accelerates the diffusion process.

It is reasonable that any effort to improve the resolution of IMS must make diffusion a less dominant process by reducing the ion residence time in the drift tube. This objective can be accomplished by using a shorter drift tube and higher electric field. Such a technique is counter-flow ion mobility analysis (CIMA) in which two opposing forces act on the ions, effectively shortening the drift tube and residence time, thus making the ions reach the detector rapidly before diffusion becomes significant.

2.2 Theory of CIMA

Theoretically, CIMA predicts a much higher resolution than the other mobility-based separation techniques discussed in Chapter 1. To greatly improve resolution, CIMA uses a high electric field and high gas flow that oppose each other and are orthogonal to the direction of ion motion toward the detector. To achieve high resolution, CIMA can be viewed as using a very high electric field in a very long drift tube. However, a short drift tube is actually used, because a high velocity gas flow in the opposite direction of ion migration is used, which effectively increase the length of the drift tube. A third orthogonal force (possibly another gas flow or electric field), which is stronger than either of the opposing forces, is then used to quickly move the ions to the detector. Modeling results, discussed later, suggest that the use of an electric field of approximately 3000 V cm^{-1} and a gas flow velocity that is over 10 m s^{-1} reduce the required drift tube length and thus, drift time, effectively resulting in a theoretical resolution in excess of 1000. A resolution of 100 has been reported for a drift tube that was 44.3 cm long, when an electric field of 500 V cm^{-1} was used.⁵

To examine how analyte is transported through out the CIMA device, we consider the device in three dimensions with points in three dimensions denoted as $x = (x, y, z)$ and the three dimensional velocity denoted as $V = (V_x, V_y, V_z)$. Let D denote the diffusion coefficient

implicitly defined in equation 2.1. Then, letting $c(x,t)$ denote the concentration at the point x at time t , the flux equation⁶ for three dimensions is given by

$$\frac{\partial c(x,t)}{\partial t} = D\nabla^2 c(x,t) - V \cdot \nabla c(x,t) \quad (2.2)$$

Here ∇ is the gradient operator,

$$\nabla c = i \frac{\partial c}{\partial x} + j \frac{\partial c}{\partial y} + k \frac{\partial c}{\partial z}$$

and ∇^2 is the Laplacian operator,

$$\begin{aligned} \nabla^2 c &= \nabla \cdot (\nabla c) \\ &= \frac{\partial^2 c}{\partial x^2} + \frac{\partial^2 c}{\partial y^2} + \frac{\partial^2 c}{\partial z^2} \end{aligned}$$

Rewriting, the flux equation is thus given by

$$\frac{\partial c(x,t)}{\partial t} = D \left(\frac{\partial^2 c}{\partial x^2} + \frac{\partial^2 c}{\partial y^2} + \frac{\partial^2 c}{\partial z^2} \right) - \left(V_x \frac{\partial c}{\partial x} + V_y \frac{\partial c}{\partial y} + V_z \frac{\partial c}{\partial z} \right) \quad (2.3)$$

For the CIMA model, the axes are as follows. The length of the drift tube is parallel to the z -axis with $z = 0$ corresponding to the point of injection and $z = d$ corresponding to the point at which the detector is located. The direction of the electric field effect and the counter-flow gas are parallel to the x direction with $x = -\frac{L}{2}$ corresponding to the wall where the counter-flow gas starts and moves toward the wall at $x = \frac{L}{2}$. The wall at $x = \frac{L}{2}$ corresponds to the wall where the electric field originates, creating a field towards the wall at $x = -\frac{L}{2}$. The y -axis represents the height of the CIMA device ranging from $y = 0$ to $y = h$.

To examine the proposed CIMA device, we can simulate the behavior of an injected compound at point $z = 0$ by using the flux equation above. Classically, examination of the flow

of material down a dominant axis, in our case the z -axis, is the primary axis modeled with often the transport in the x and y directions considered to be ignorable. The primary justification for this is that it is usually assumed that the only transport, laterally, is due to lateral diffusion. Put in symbols, this is essentially the same as assuming the V_x and V_y are both zero in the equation 2.3 above. In this case the resolution and efficiency of an IMS is determined by considering mainly the flux equation in the z -axis, only.

In the current case however, there are opposing transport forces in the x -axis direction. Specifically, the velocity in the x -direction, V_x , is the sum of v_g and v_d , where v_g is the counter-gas flow velocity and v_d is the drift velocity created by the electric field for ions with a mobility coefficient of K , i.e., $v_d = KE$.

On the other hand, the y -axis direction has no opposing forces other than diffusion. Since the method of injection is a slit running in the direction of the y -axis, it is reasonable to assume that transport in the y -axis direction is in steady state throughout the experiment and is often ignored.

Transport in the z -axis direction from injection to detection follows equation 2.3. However, the detector works as an accumulator in that the signal is essentially accumulated over time. Consequently, any “band broadening” of the injected analyte in the z -axis direction, or any differential transport time in the sample will have no effect on the aggregate signal. Although it is possible for the drift time and the band broadening to be so large in the z -axis direction as to reduce the signal relative to the noise to the point that detecting and accumulating a signal is problematic, this difficulty was not encountered on this project.

As a consequence of these points, the main concern in analyzing the behavior of an analyte is determination of the transport in the x -axis direction. The CIMA design makes the V_x

component the dominant component of equation 2.3. By increasing the counter-flow gas velocity, v_g , and simultaneously increasing the opposing electric field, it is possible to decrease the time necessary for ions with mobilities other than the target mobilities to be eliminated from the sample. Thus the simulation of the flux equation will be applied to the dynamic behavior of the ions in a sample induced by the counter-flow gas velocity and the opposing electric field in the x -axis direction.

Equation 2.3 indicates that the concentration of ions that reach the detector is dependent on diffusion and the flow velocity within the analyzer. In a traditional IMS where the velocities of the buffer gas and ion packet are low, diffusion is the dominant cause of band broadening. The counter forces in CIMA create a type of “filtering” process, where ions of different mobilities are detected as either the electric field or gas flow velocity is scanned.

Another feature of CIMA is the ability to perform continuous sampling which is an advantage over conventional IMS where pulsed sampling is utilized. Conventional IMS requires elevated temperature to help in declustering ions and cleaning the drift tube. CIMA simplifies the instrument design by performing the same function with a high velocity counter-flow gas and high electric field at room temperature.

2.3 Numerical Calculations and Simulation

Numerical analysis of CIMA was carried out in two ways: first, by solving Equation 2.3 as it applies to CIMA (i.e., using appropriate parameters) with diagrams to illustrate the technique, and second, modeling (simulating) CIMA using a hypothetical analyzer and conditions to see the predicted results.

To simplify the calculations and numerical simulation, the flowing assumptions were made:

1. All ions are singly charged.
2. Ions are assumed to be free from clusters (from water vapor and nitrogen in the ionization process).
3. Ions do not interact with one another, so that interactions resulting from space charging do not occur.
4. Only velocity of the counter flow gas is important; the type of counter-flow gas is unimportant.
5. Ions are created immediately upon entering the analyzer.
6. The type of ionization method is not important.
7. Reactant ions and product ions are not present in the system.
8. The type and geometry of the detector is undefined.

A hypothetical analyzer is diagramed in Figure 2.1. It is a rectangular tube with perforated sides (or grids), W_1 and W_2 , that allow the counter-flow gas to pass through. These walls define the analytical volume. The analyzer is made from conducting material for voltage application. The walls, W_1 and W_2 , have a height, h , in the y -axis direction; the analyzer width, L , is in the x -axis direction, and the length, d , is in the z -axis direction. Ions are introduced through the slit on the front end and move along the length of the tube in the z -axis to the detector situated at the back.

A cross-section of the analyzer showing the analyzer channel is depicted in Figure 2.2. This diagram shows an analytical region between two perforated walls. For simplicity, a rectangular analyzer between two parallel perforated walls was assumed; however, this region could have been formed between two grids or between two perforated or porous cylinders.

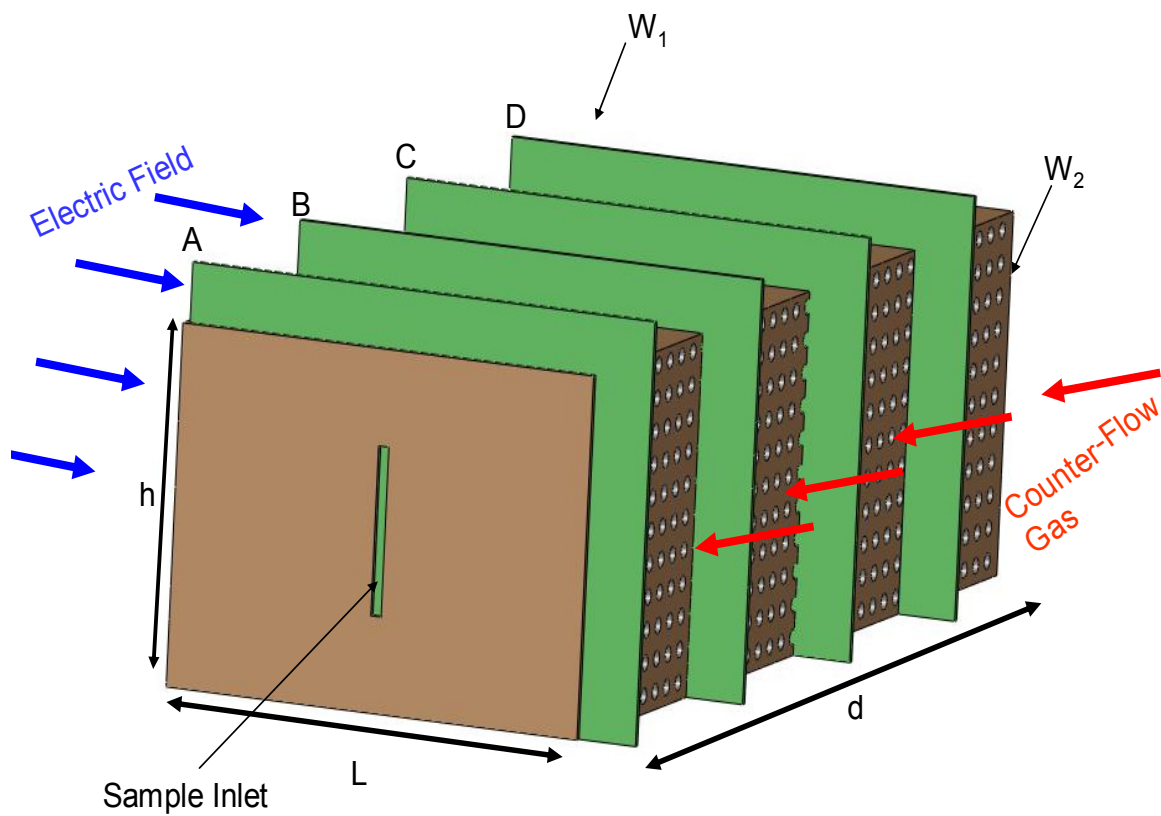


Figure 8.1 Perforated rectangular analyzer box used to describe the concept of CIMA. The perforation allows the counter-gas to flow into the analyzer. Samples are injected into the analyzer in the front end and are detected at the opposite end of the tube. There is an orthogonal force, F , (not shown) that is applied along the d direction that is used for transporting the ions from injection to detection. The sheets marked A, B, C, and D are explained later in the text.

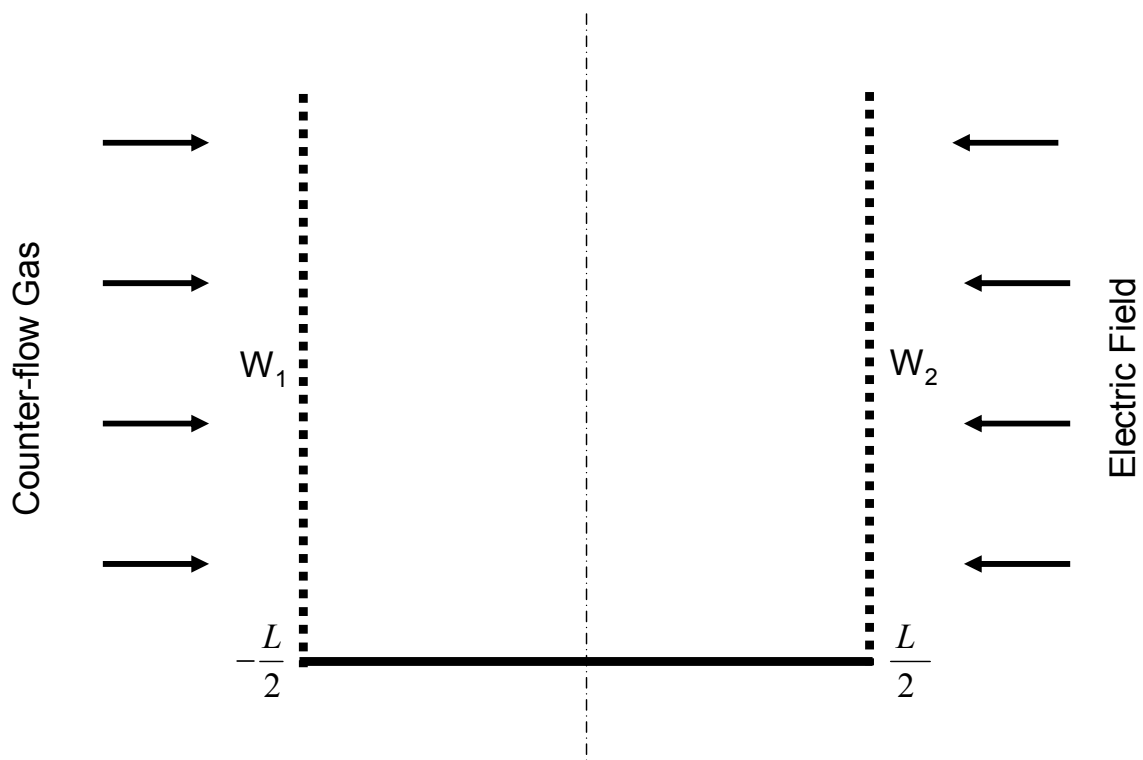


Figure 8.2 Representation of a cross-section of the analyzer channel with perforated walls defining the CIMA drift region.

The same general principles would apply to a cylindrical configuration. The analyzer channel dimensions provided the boundary conditions used to solve Equation 2.3 and model the performance of CIMA.

In CIMA, the initial ion sample concentration spatial distribution in the x -axis at the entrance of the analyzer is very important. Therefore, different entrance geometries were modeled. The shapes of ion samples as they enter the analyzer (called “injection profiles” in this dissertation) are depicted in Figure 2.3. A sample with concentration, c , is introduced at the sample inlet at time $t = 0$ at one end in the z -axis direction. Immediately, the electric field pushes the analyte ions toward the wall W_2 , and the counter-flow gas pushes against the ions until they are balanced in the middle of the analyzer. An orthogonal force is used to transport the ions down the drift tube to the other end where the detector is situated. As the ions migrate, they diffuse in all directions, only the diffusion in the x -axis direction is important in CIMA consideration. If counter-flow gas is maintained at a constant velocity while the opposing electric field is programmed to gradually increase, ions of different mobilities are allowed to pass through the analyzer to the detector. If the orthogonal force is high enough to transport the ions to the detector before diffusion in the x -axis takes place, the ion mobility spectrum recorded by the detector will result in a high resolution spectrum. At the wall of the drift region, c is zero, since ions are lost when they hit the wall.

The above description of CIMA provides the boundary conditions used to solve Equation 2.3., thus reducing equation 2.3 to a one dimensional equation with interest only in the x -axis direction, the new equation is

$$\frac{\partial c(x,t)}{\partial t} = D \frac{\partial^2 c}{\partial x^2} - V \frac{\partial c}{\partial x} \quad (2.4)$$

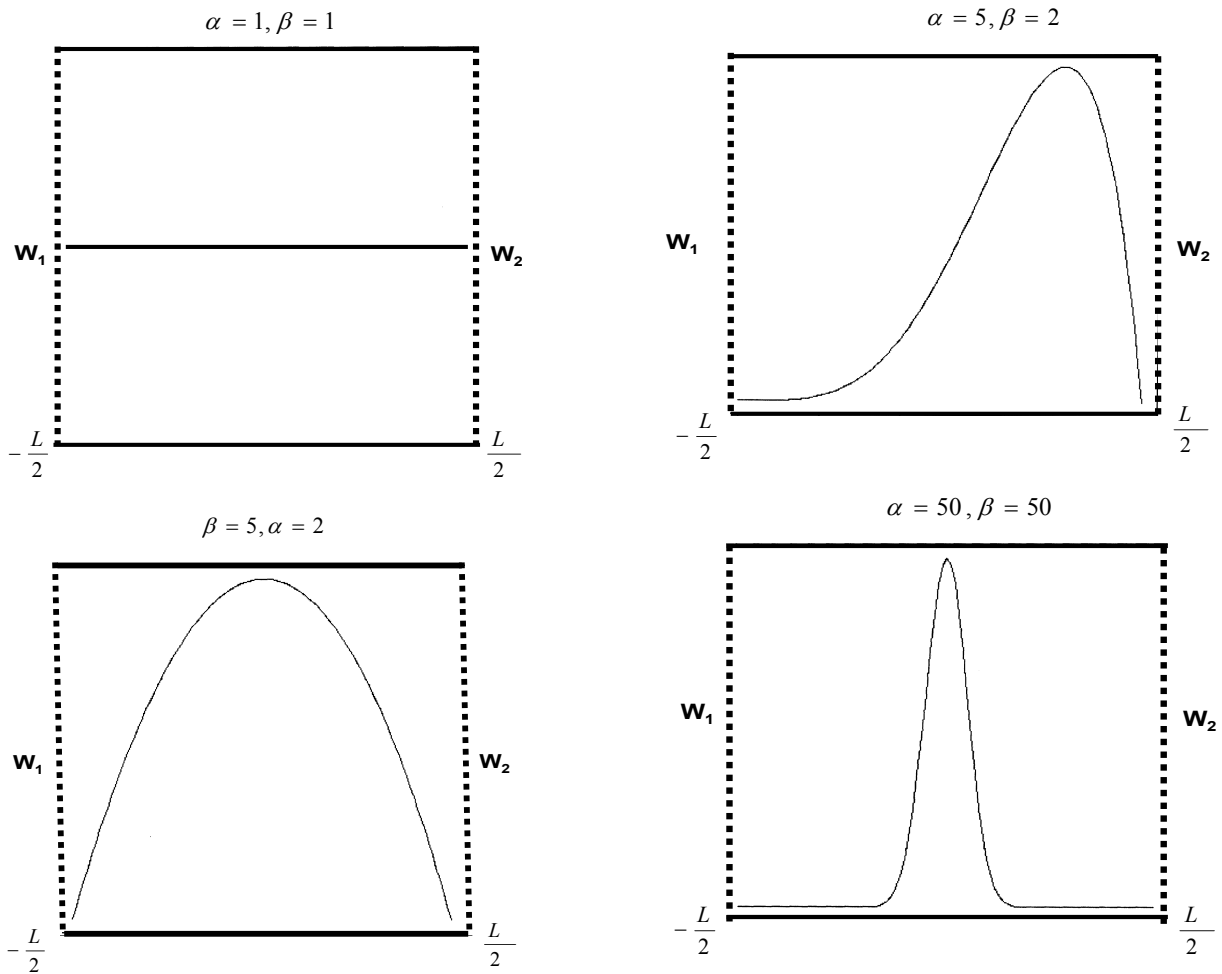


Figure 8.3 Injection profiles obtained by changing the numerical values of α and β in the beta-function. These were used to determine the initial spatial distribution of the ions as they entered the analyzer at time $t = 0$.

A method of separation of variables was used to solve equation 2.4, and various functions were randomly selected and tested to determine which function will satisfy equation 2.4 and be a solution, hence the solutions are called “trial solutions”. Two trial solutions were obtained: F_n and G_n solutions, also known as the “cosine” and “sine” solutions, respectively

$$F_n(x, t) = e^{\left(-\frac{v^2}{2D} - \frac{4D\pi^2}{L^2}\right)(n-0.5)t} e^{\frac{v}{2D}x} \cos\left(2\pi \frac{(n-0.5)}{L}x\right) \quad (2.5)$$

and

$$G_n(x, t) = e^{\left(-\frac{v^2}{2D} - \frac{4D\pi^2}{L^2} - n^2\right)t} e^{\frac{v}{2D}x} \sin\left(2\pi \frac{n}{L}x\right) \quad (2.6)$$

where n is the number of waveforms between the boundaries defined by walls W_1 and W_2 , t is the time it takes the ions to reach the detector, and x is the position of the ions along the analyzer channel with width L . Within the gap, the concentration of the analyte can be expressed as

$$c(x, t) = \sum A_n F_n(x, t) + \sum B_n G_n(x, t) \quad (2.7)$$

The initial sample ion concentration profile was fitted or approximated to the selected injection profiles in Figure 2.3.

At $t = 0$, when the sample is injected into the analyzer, the spatial distribution of the ion concentration, c , in the analyzer is assumed to be a Gaussian distribution shown in Figure 2.4, and can be represented as

$$c_0(x) = \sum A_n F_n(x, t = 0) + \sum B_n G_n(x, t = 0) \quad (2.8)$$

The challenge is to solve the above equation for all values of A_n and B_n , which when summed together approximate the original or actual sample concentration profile. Finding all values of A_n and B_n , whose summation reproduces the assumed profile in Figure 2.4, is an optimization

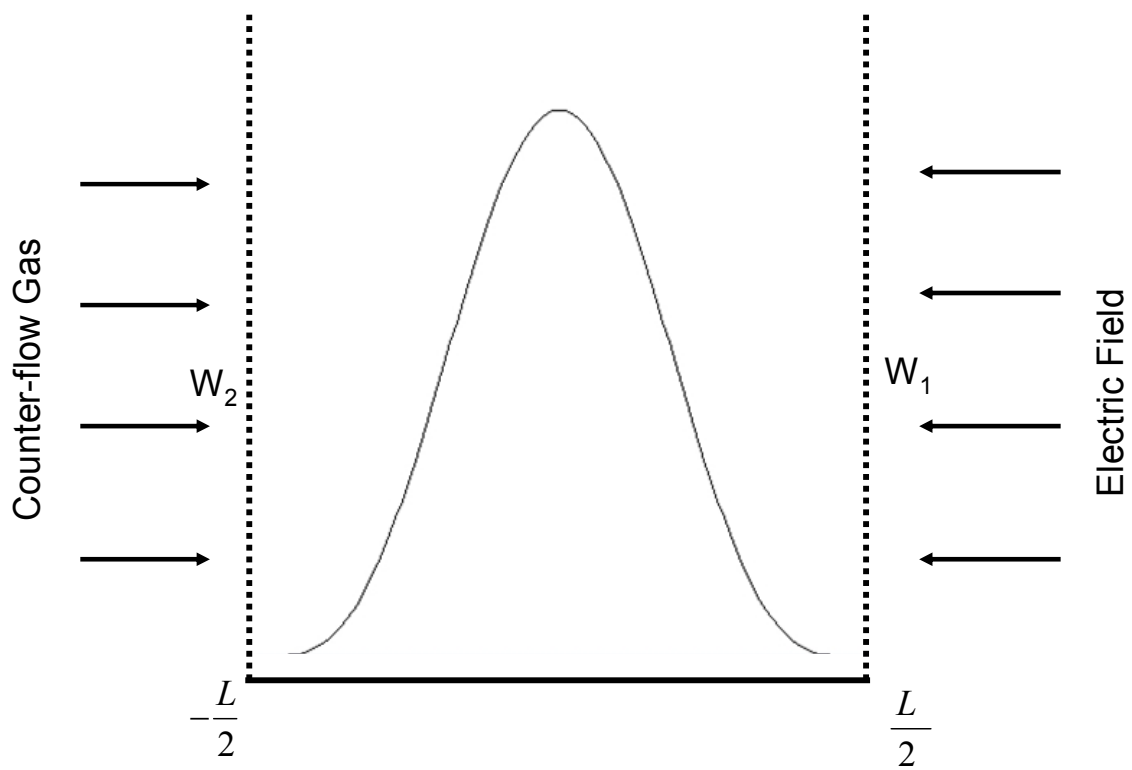


Figure 8.4 Initial distribution of the ion sample as it enters the analyzer at $t = 0$. It is assumed to be a Gaussian distribution.

problem for a non-orthogonal basis functions, A_n and B_n with weights F_n and G_n , respectively; thus, they must be solved to determine the initial sample ion concentration. The calculation/derivation that follows solves for A_n and B_n . First, F_n and G_n are solved for at $t = 0$ when the sample just enters the analyzer. Equations 2.5 and 2.6 become

$$F_n = e^{\frac{v}{2D}x} \cos(2\pi(\frac{n-0.5}{L})x) \quad (2.9)$$

and

$$G_n = e^{\frac{v}{2D}x} \sin(2\pi \frac{n}{L}x) \quad (2.10)$$

respectively. Substituting Equations 2.9 and 2.10 into Equation 2.8 yields

$$c_0(x) = \sum A_n e^{\frac{v}{2D}x} \cos(2\pi \frac{(n-0.5)}{L}x) + \sum B_n e^{\frac{v}{2D}x} \sin(2\pi \frac{n}{L}x) \quad (2.11)$$

To determine A_n and B_n , Equation 2.11 must be transformed into a form that can be solved as a Fourier series by multiplying both sides of the equation by

$$e^{-\frac{v}{2D}x} \cos(2\pi \frac{(k-0.5)}{L}x) \quad (2.12)$$

to obtain

$$\begin{aligned} c_0(x) e^{-\frac{v}{2D}x} \cos(2\pi \frac{(k-0.5)}{L}x) = \\ \sum A_n \cos(2\pi \frac{(n-0.5)}{L}x) \cos(2\pi \frac{(k-0.5)}{L}x) \\ + \sum B_n \sin(2\pi \frac{n}{L}x) \cos(2\pi \frac{(k-0.5)}{L}x) \end{aligned} \quad (2.13)$$

Taking the integral of both sides within the limits of $\pm \frac{L}{2}$ (the analyzer width), gives

$$\begin{aligned}
& \int_{-\frac{L}{2}}^{\frac{L}{2}} c_0(x) e^{-\frac{v}{2D}x} \cos\left(2\pi \frac{(k-0.5)}{L}x\right) dx = \\
& + \sum \int_{-\frac{L}{2}}^{\frac{L}{2}} A_n \cos\left(2\pi \frac{(n-0.5)}{L}x\right) \cos\left(2\pi \frac{(k-0.5)}{L}x\right) dx \\
& + \sum \int_{-\frac{L}{2}}^{\frac{L}{2}} B_n \sin\left(2\pi \frac{n}{L}x\right) \cos\left(2\pi \frac{(k-0.5)}{L}x\right) dx
\end{aligned} \tag{2.14}$$

In equation 2.14 we assumed that we can rearrange the order on integration with the infinite sum. This is justified by assuming that the summations in equation 2.14 are absolutely convergent. In integrating the right hand side of equation 2.14 by orthogonality, note that if $k \neq n$ then

$$\int_{-\frac{L}{2}}^{\frac{L}{2}} \cos\left(2\pi \frac{(n-0.5)}{L}x\right) \cos\left(2\pi \frac{(k-0.5)}{L}x\right) dx = 0$$

Also, for all values of n and k orthogonality of cosine and sine functions results in

$$\int_{-\frac{L}{2}}^{\frac{L}{2}} \sin\left(2\pi \frac{(n-0.5)}{L}x\right) \cos\left(2\pi \frac{(k-0.5)}{L}x\right) dx = 0$$

Applying these two results to equation 2.14 we obtain

$$\int_{-\frac{L}{2}}^{\frac{L}{2}} c_0(x) e^{-\frac{v}{2D}x} \cos\left(2\pi \frac{(k-0.5)}{L}x\right) dx = \int_{-\frac{L}{2}}^{\frac{L}{2}} A_k \left[\cos\left(2\pi \frac{(k-0.5)}{L}x\right) \right]^2 dx \tag{2.15}$$

Therefore, A_k can be solved by

$$A_k = \frac{\int_{-\frac{L}{2}}^{\frac{L}{2}} c_0(x) e^{-\frac{v}{2D}x} \cos\left(2\pi \frac{(k-0.5)}{L} x\right) dx}{\int_{-\frac{L}{2}}^{\frac{L}{2}} \cos^2\left(2\pi \frac{(k-0.5)}{L} x\right) dx} \quad (2.16)$$

Similarly, the sine solution gives B_k as

$$B_k = \frac{\int_{-\frac{L}{2}}^{\frac{L}{2}} c_0(x) e^{-\frac{v}{2D}x} \sin\left(2\pi \frac{k}{L} x\right) dx}{\int_{-\frac{L}{2}}^{\frac{L}{2}} \sin^2\left(2\pi \frac{k}{L} x\right) dx} \quad (2.17)$$

where k takes values from 1 to infinity. The sum of A_k and B_k with weights F_n and G_n is the original concentration, $c_0(x)$, i.e.,

$$c_0 = \sum A_n F_n(x, t) + \sum B_n G_n(x, t) \quad (2.18)$$

where $A_k = A_n$ and $B_k = B_n$.

The next step is to solve for the concentration at different times, i.e., from $t = 0$ (sample is injected) to $t = t_d$, detected at a distance, S , from the injection point

$$c(x, t) = \sum A_n e^{\left(-\frac{v^2}{2D} - \frac{4D\pi^2}{L^2}\right)(n-0.5)t} e^{\frac{v}{2D}x} \cos\left(2\pi \frac{(n-0.5)}{L} x\right) + \sum B_n e^{\left(-\frac{v^2}{2D} - \frac{4D\pi^2}{L^2}\right)t} e^{\frac{v}{2D}x} \sin\left(2\pi \frac{n}{L} x\right) \quad (2.19)$$

The solution of this equation gives the concentration profile at different times, t , from the time of injection to the time of detection. Changes in the concentration of the sample from its original profile as it moves from the point of injection to detection under the influence of the opposing fields in the x -axis direction as it travels along the length of the drift tube (marked A, B, C, and D in Figure 2.1) can be represented by “decay profiles” as depicted in Figure 2.5. These results can be applied to an analyte of fixed mobility constant, K , with a varying electric field, E , (i.e., scanning) and constant counter-flow gas velocity, or for constant electric field, E , with a varying counter-flow gas velocity.

This procedure is continued until a flat profile is obtained to indicate that the diffusion process is complete. This is useful for determining the placement of the detector (i.e., the analyzer length) and the analysis time (to limit diffusion). Next, the concentration of each profile is calculated by taking the integral of the profile, i.e., $\int c dx = \text{area under the curve}$. Plots are made of $\int c dx$ vs. time, t , as the E-field is changed or scanned. This is shown in Figure 2.6. As time elapsed during analysis, the concentration of analyte was reduced due to loss at the wall.

From the drift velocity, v_d , and distance, d , between the point of injection to the point of detection, the drift time, t_d , can be calculated

$$t_d = \frac{d}{v_d} \quad (2.20)$$

Plotting various t_d values as the E-field is scanned gives the scanned signal output registered at the detector. This is the output signal, which is similar to that depicted in Figure 2.7.

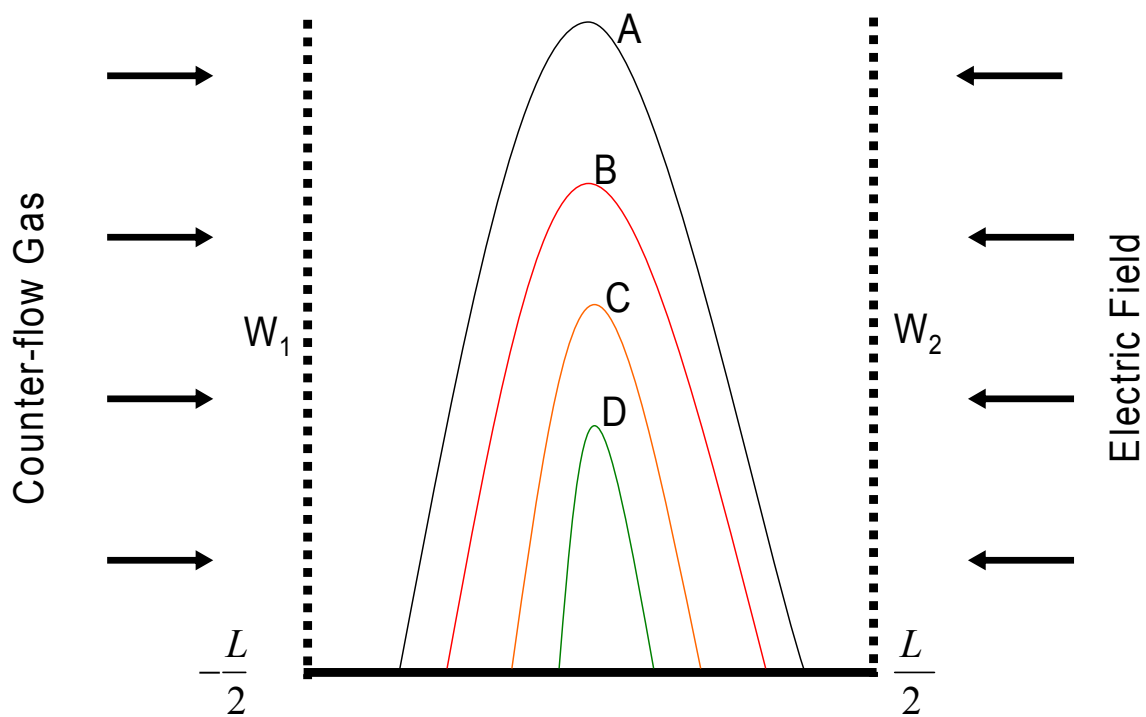


Figure 8.5 Hypothetical profiles of the sample concentration inside the analyzer drift region at different times, t , as the analyte moves from the injection point to the detector along the drift length. (A) $t = 0$, (B) $t = 0.01$, (C) $t = 0.02$, and (D) $t = 0.03$.

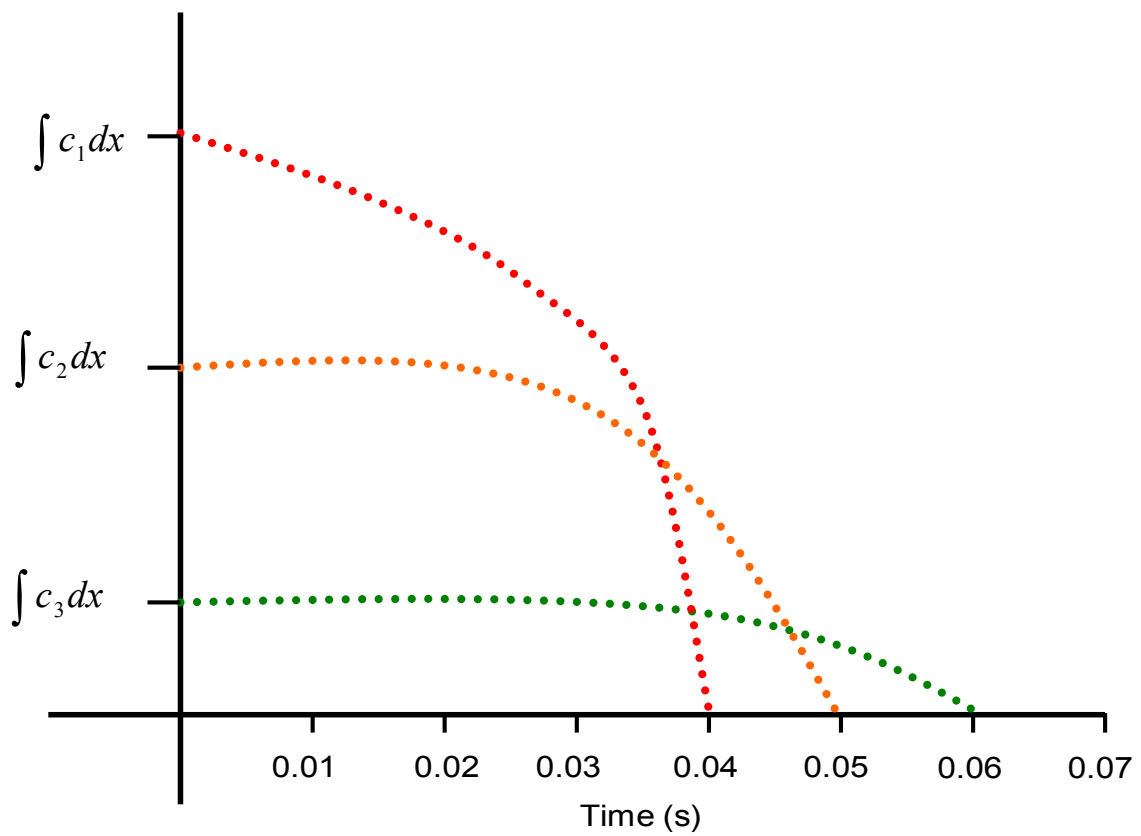


Figure 8.6 Plots of concentrations vs. time showing the decay of the sample.

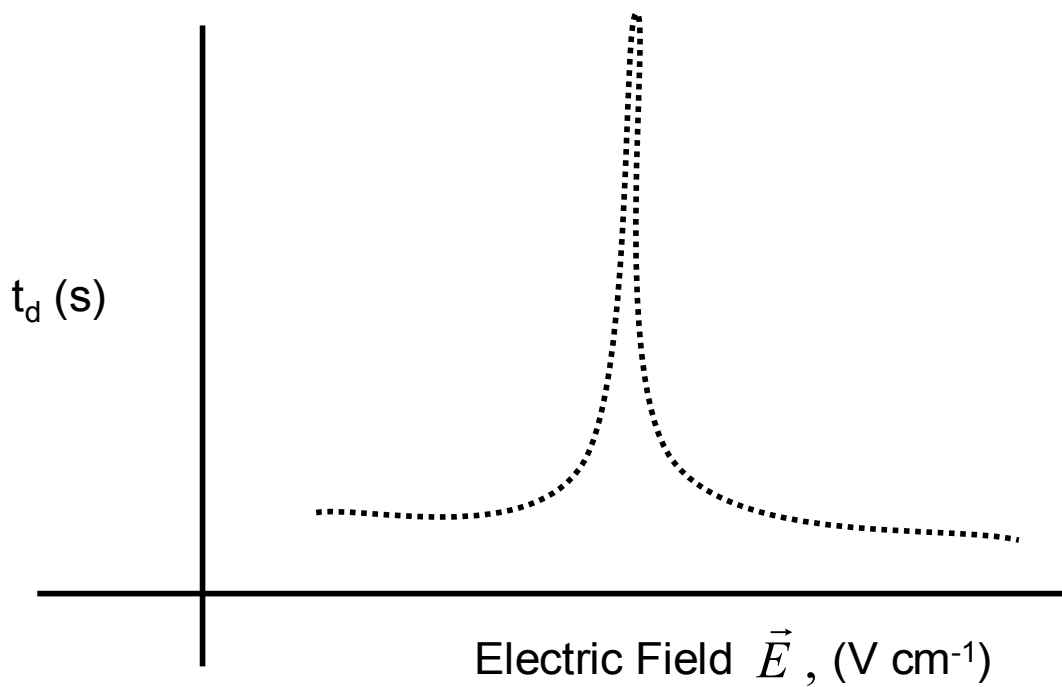


Figure 8.7 Hypothetical peak or signal output for CIMA. This figure illustrates the narrow peak that is potentially achievable with the CIMA method. In this particular example, the gas flow is kept constant and the electric field is scanned.

The second part of the numerical work involved simulating the above solution from the partial differential equation. Simulation was done using a statistical program called R.⁸ In modeling CIMA, four compounds with reduced mobility values close to each other were chosen: methylamine, 2.65; ethylamine, 2.36; formamide, 2.45; dimethylamine, 2.46; and isopropylamine, 2.20. Formamide and dimethylamine were of special interest because of the closeness of their reduced mobility constants.

Equal amounts of these compounds were used in the simulation. Other parameters included analyzer gap distance, 3 cm; drift tube length, 10 cm; counter-flow gas velocity, 10 m s⁻¹; voltage across the drift tube, 10 KV; and drift time, 1 s. Thus, the ions moved across the analyzer at a velocity of 0.1 m s⁻¹. Additional simulations using different gap widths, voltages and drift times were also done to determine the interactions of the various parameters and how they influence the resolution and selectivity.

Using the following beta function, the injection profiles were determined

$$c(x, t = 0) = \left(\frac{1}{2} + \frac{x}{L} \right)^{\alpha-1} \left(\frac{1}{2} - \frac{x}{L} \right)^{\beta-1} \frac{1}{L} \frac{\gamma(\alpha + \beta)}{\gamma(\alpha)\gamma(\beta)} \quad (2.21)$$

where $\alpha > 0$, $\beta > 0$, and $\gamma(\alpha + \beta)$ is a gamma function defined as

$$\gamma(\alpha) = \int_0^{\infty} x^{\alpha-1} e^{-x} dx \quad (2.22)$$

Different combinations of α and β values gave different injection profiles (as previously described in Figure 2.3). These different injection profiles help establish a relationship between the shape of sample inlet and the final spectral output recorded by the detector. This enables us to ascertain which injection inlet contributes to optimum results and enhanced resolution.

The final task was to plot the sample concentration with respect to the electric field applied to the drift tube. This plot is a modeled separation of the sample analytes.

2.4 Results and Discussion

The simulation results are illustrated in Figures 2.8-2.10. Figure 2.8 shows how the ion concentration profile varies as the ions move along the drift tube. In this figure, t_0 is at injection, and t_d is at detection. This figure shows that the sample ions are situated in the middle of the analyzer, held in place by the opposing forces of counter-gas flow and electric field. The high electric field strength and high counter-gas flow velocity were able to stop the motion of specific ions to either wall, while the orthogonal force is used to move the ions until detection at time t_d at a velocity of 0.1 m s^{-1} . Therefore, ions reach the detector before diffusion becomes significant.

Figure 2.9 shows the ion transmission performance expected of CIMA. It is a plot of ion sample concentration with respect to drift time along the length of the drift tube. Approximately 0.1% of the sample is lost to the walls from diffusion which implies that 99.9% of the sample reaches the detector. The fast analysis time gives diffusion little time to occur.

As can be seen in Figure 2.10, there is baseline resolution of all four peaks. The second and third peaks have reduced mobilities of 2.45 and $2.46 \text{ V cm}^{-2} \text{ s}^{-1}$, respectively. The resolution of these peaks is over 1000, which is the most important figure of merit for this new technique. Other IMS techniques cannot resolve compounds with such close mobilities because the low electric field applied makes these ions reach the detector at approximately the same time and appear as one single broad peak. One key parameter to note is the electric field strength. In conventional IMS, the electric field typically ranges from 100 to 500 V cm^{-1} , while in this system, the field can be over 3000 V cm^{-1} . The higher field is used to discriminate ions by amplifying the difference in mobilities; while some are stopped by the opposing counter gas flow, others are pushed in different directions by the opposing forces. The high orthogonal force is used to rapidly move the ions to the detector before diffusion becomes significant.

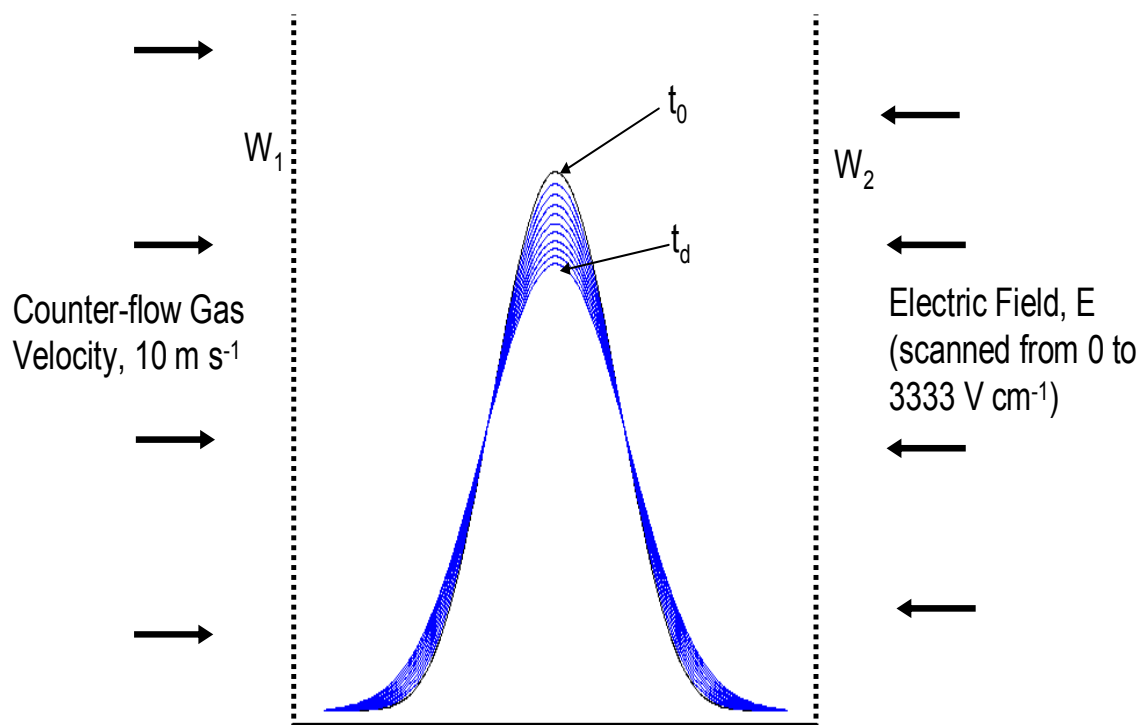


Figure 8.8 Simulation of the sample behavior as it travels along the drift tube from the point of injection to the detector. Under the conditions of the simulation, the analytes are detected before diffusing to the walls.

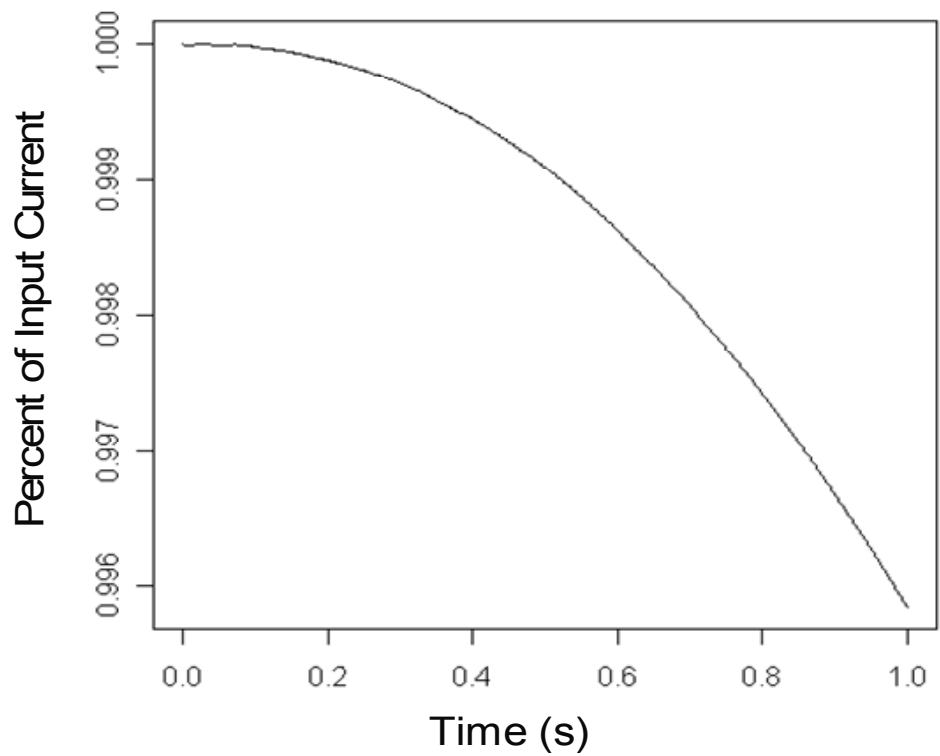


Figure 8.9 Plot of percent of input current vs. time, depicting how much of the analyte reaches the detector versus how much is lost due to diffusion. The present conditions show that less than 0.1% is lost.

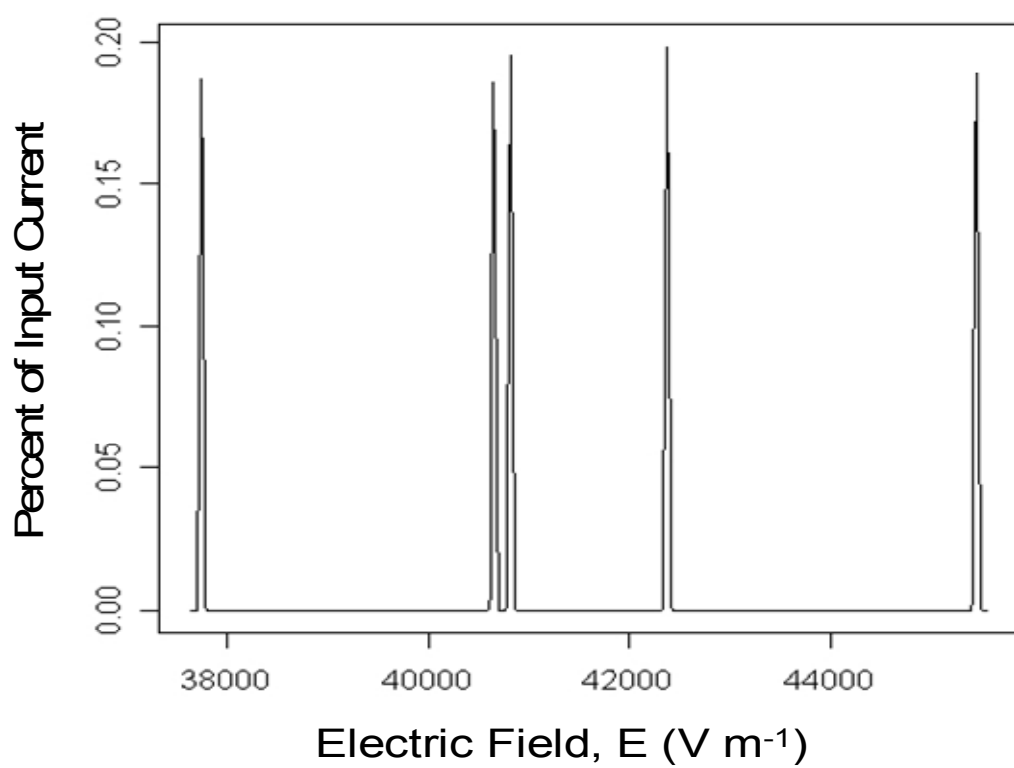


Figure 8.10 CIMA spectrum from the simulation showing baseline separation of two compounds with very close mobility constants.

As impressive as these results seem, they should be taken within the context of the assumptions used in the simulation outlined earlier. A real system under actual laboratory or field conditions will no doubt give a different result. How much these assumptions affect the final result must be investigated.

2.5 Conclusions

In this work, a new technique for ion mobility analysis is introduced. This method helps to overcome the diffusion limited resolution issues that impact traditional IMS techniques by essentially reducing the amount of time ions spend in the analyzer. This is done using two opposing forces to stop the motion of the ions and move them rapidly to the detector before diffusion becomes significant. CIMA simulation results predict a resolution that is over one order of magnitude higher than traditional IMS methods, which improves the sensitivity and selectivity of IMS techniques. CIMA allows the use of very high voltages and electric fields that are not possible in conventional IMS. The use of high gas flow rates makes it possible to employ room temperature in CIMA, further simplifying the instrumentation. Furthermore, this technique allows the use of continuous sampling methods instead of pulsed injection used in conventional IMS systems.

2.6 References

1. Dugourd, Ph.; Hudgins, D. E.; Clemmer, D. E.; Jarrold, M. F. *Rev. Sci. Instrum.* **1997**, 68, 1122-1129.
2. Wu, C.; Siems, W. F.; Asbury, G. R.; Hill, Jr. H. H. *Anal. Chem.* **1998**, 70, 4929-4938.
3. Tang, K.; Shvartsburg, A. A.; Lee, H.; Prior, D. C.; Buschbach, M. A.; Li, F.; Tolmachev, A. V.; Anderson, G. A.; Smith, R. D. *Anal. Chem.* **2005**, 77, 3330-3339.
4. Denton, M. B.; Sperline, R. P.; Gillig, K. J. "Recent Advances in Ion Mobility Detectors and Analyzers", presented at the Pittsburgh Conference, Chicago, IL, Feb.-Mar. 2007
5. Watts, P.; Wilders, A. *Int. J. Mass Spectrom. Ion Processes* **1992**, 112, 179-190.
6. Mason, E. A.; McDaniel, E. W. *Transport Properties of ions in Gases*, John Wiley & Sons, NY, 1988.
7. Rockwood, A. L.; Lee, E. D.; Agbonkonkon, N.; Lee, M. L. Cross-flow ion mobility analyzer, US Patent 7,199,362 B2, April 3, 2007.
8. www.r-project.org

Chapter 3

Counter-flow Ion Mobility Analysis Using Concentric Cylinders

3.1 Introduction

In this chapter, initial efforts to design a CIMA instrument are described. In determining the design of the analyzer, the following issues were considered: (1) how to generate a gas flow of uniform velocity (i.e., plug flow), (2) how to ionize and introduce the sample ions, including whether or not the sample is ionized inside or outside the analyzer region, (3) how to transport the ions along the analyzer region from the injector to the detector, and (4) how to detect the ions. The gas flow issue was the most critical. All of the other considerations were dependent on how the uniform gas flow was generated.

Several unsuccessful attempts at designing the analyzer revealed the challenge of achieving uniform gas flow. Three analyzers based on a concentric tube design were constructed and tested; however, they failed to achieve the required flow characteristics. Even though these attempts were for the most part unsuccessful, important concepts and characteristics were learned. These analyzers are described in the following sections and include: (1) perforated hollow cylinders, (2) stacked washers or rings, and (3) porous (frit) tubes.

3.2 Perforated Cylinder Design

The gas velocity and flow profile through a perforated tube will depend on the volume and pressure of the gas being introduced on the inside, as well as on the structure of the perforated tube. High pressure and high volume gas or fluid forced through small holes or pores was predicted to result in a uniform fluid flow.

The porous tube design was machined and fabricated by the BYU Precision Machining Laboratory (PML) as were all other analyzer components used in this work. Electrical discharge machining (EDM) was used to drill the holes in the tube. This design consisted of two concentric cylinders with tiny holes to make them porous. The inner cylinder was 6" x 2" while the outer cylinder was 8" x 4". The 1" gap between the cylinders was the analyzer region. These two cylinders also served as electrodes between which an electric field was established. The middle 4" length of both cylinders had approximately 2600 holes of approximately 0.0128" in diameter drilled through them. These holes were evenly spread around the cylinders to make them perforated. Each cylinder was 0.0625" thick. The front end of the inner cylinder had a hemispherical end cap with a 0.0394" lens located 0.236" between the hemispherical end cap and the inner cylinder. The back end was attached to an air amplifier.

The air amplifiers used in this work were variable air amplifiers from Air Research Technology Company (ATRX)¹, Cincinnati, OH (models 98008 and 15015). As can be seen in a schematic diagram (Figure 3.1), the air amplifier held the inner and outer cylinders in place at the back end, allowing alignment of the holes. The front end of the outer cylinder was cup shaped. This negative hemispherical geometric design provided space between it and the inner tube to create a region for ionization and secondary ion reaction. The shape also provided a focusing effect so the ions were not dispersed when they entered the analyzer region. The detector, which was a Faraday cup, was positioned between the ends of the two cylinders.

In operation, a large volume of gas was introduced into the inside of the inner tube, creating a pressurized system. As the gas escaped through the holes in the cylinder, it passed through the space between the concentric tubes, generating a uniform gas flow.

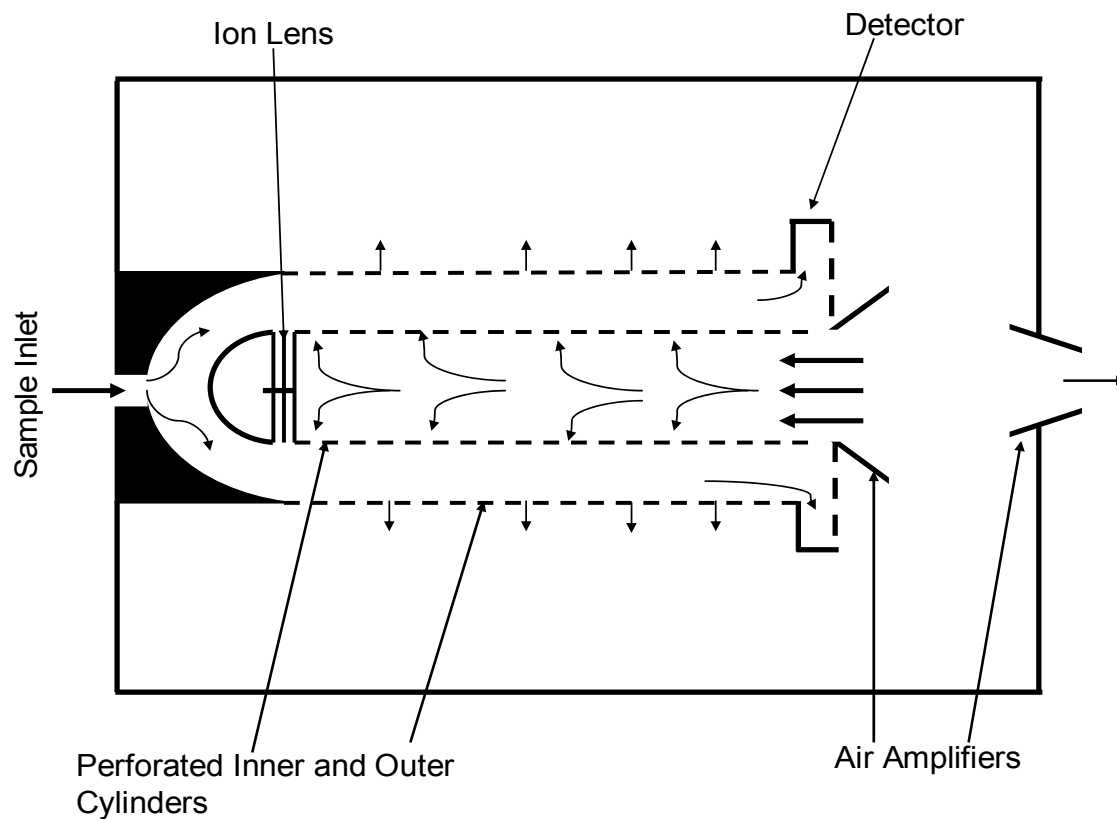


Figure 9.1 Schematic of the perforated cylinder CIMA design. The placement of air amplifiers is shown, with arrows pointing in the direction of gas flow.

As the name implies, an air amplifier is a device that is used to amplify the air velocity and volume, in some cases as high as 25 times. A small amount of compressed air enters the annular orifice of the air amplifier (see Figure 3.2). The compressed air accelerates to sonic speed along the exit wall, creating a low pressure area (vacuum area) in the center that draws additional air through the amplifier and out the exit. The air flow is amplified by utilizing the free ambient air to create a large flow.¹

3.3 Stacked Washer Design

The second design that was tried is the stacked washer design. Similar to the previous design, the objective was to achieve uniform gas flow across the space between the cylinders. In this design, two sets of washers were assembled into cylindrical electrodes. The inner electrode was made from washers with OD of 0.750” and ID of 0.500”. The outer electrode was made from washers with OD of 2.125” and ID of 1.500”. All of the washers had a thickness of 0.03125” and were made from the same material, aluminum. The inner electrode washers were held in place by three rods, and the washers were separated from one another by very tiny spacers that were approximately 0.0005” thick. This created the spacing through which the gas flowed. The larger washers were held in place by 6 rods of the same size, and were again separated by the same tiny spacers (see Figure 3.3).

When the smaller cylinder was placed inside the larger cylinder, they formed an analyzer unit with the space between them serving as the analyzer region (see Figure 3.4). A Faraday detector made from a circular plate was positioned between the two electrodes at one end of the analyzer unit. In this system, nickel-63 was employed as the ionization source. The spacing between the washers was small, so as to create a pressure on the inside of the inner electrode

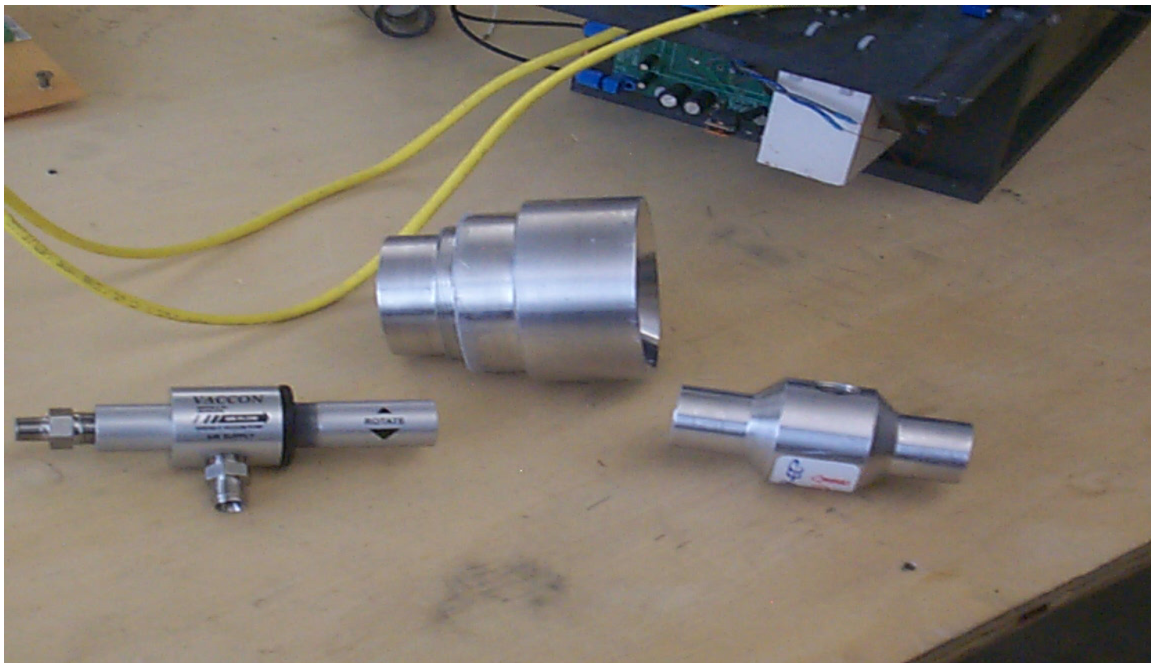
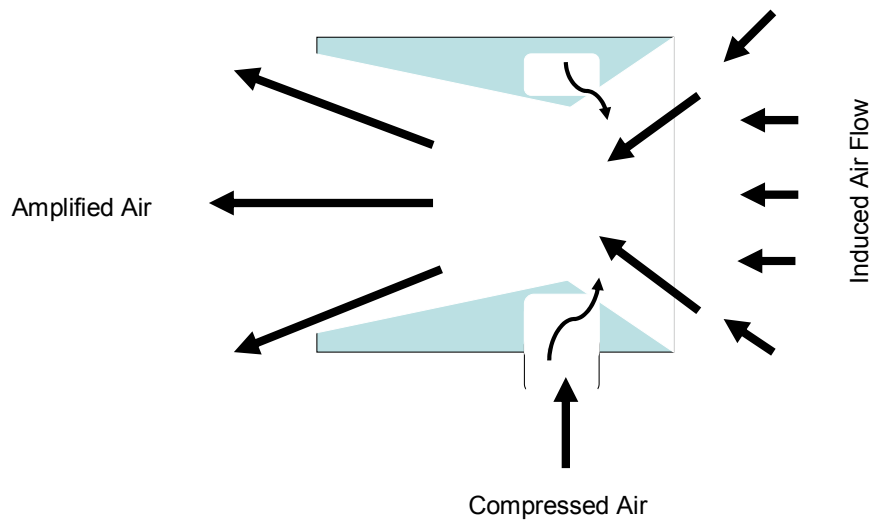


Figure 9.2 Schematic (above) of an air amplifier showing the process of amplification and photograph (below) showing the actual air amplifiers used.

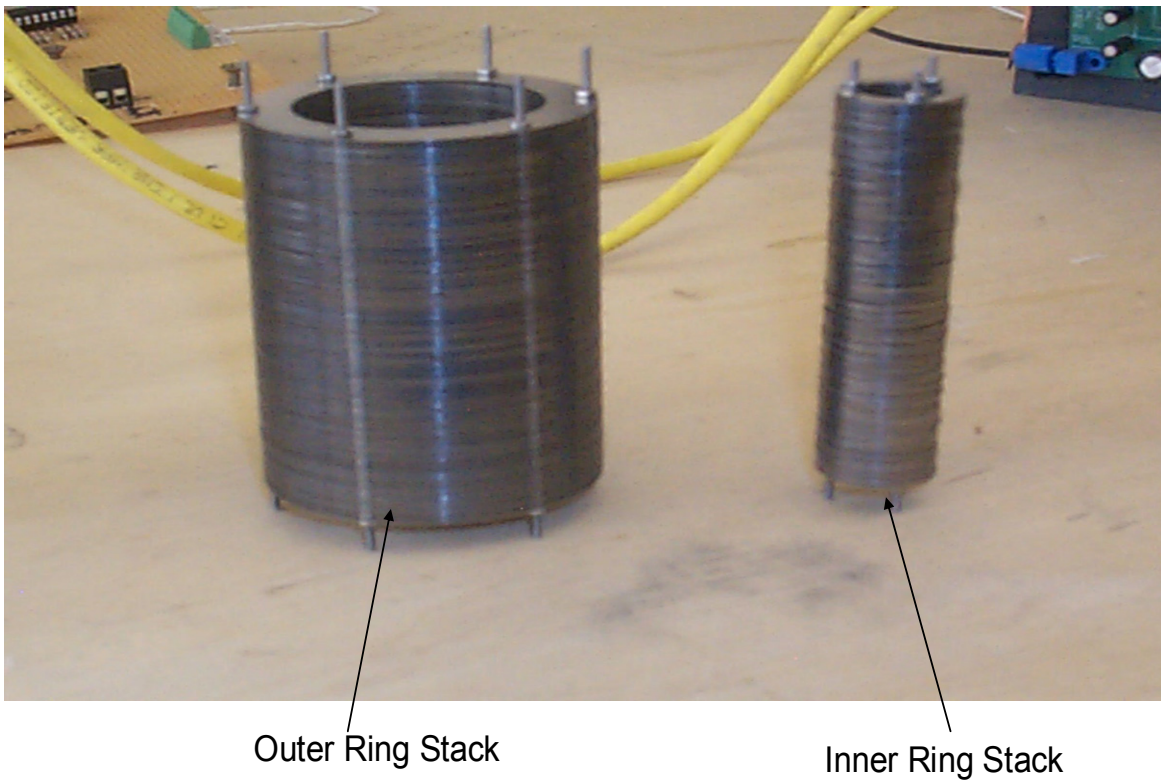


Figure 9.3 Photograph of the actual stacked ring electrodes used. Both the inner and outer tubes are shown.

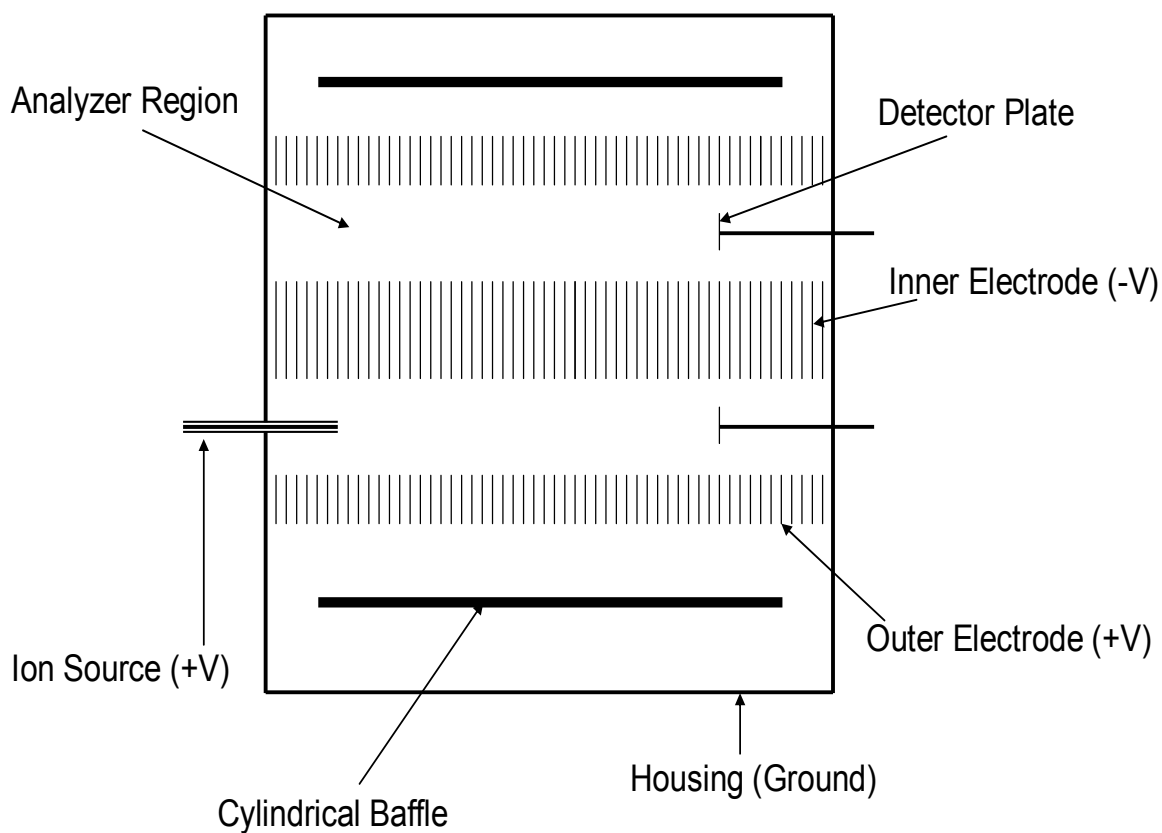


Figure 9.4 Schematic of the stacked washer CIMA design. The inner and outer stacked washers served also as electrodes to create an electric field. The baffle was used to even the flow around the outer stacked washers.

cylinder. This led to a pressure drop across the smaller cylinder when high-pressure gas was introduced into the inside of the smaller cylinder.

An ionization chamber was made from a Swagelok union connector; the inside was lined with a nickel-63 foil. The side attached to the analyzer gave the needed constriction to slow down the gas flow and allow the sample time to be ionized as it passed by the nickel-63 to the analyzer. A carrier gas carried the ionized sample into the annular region where it immediately experienced the opposing forces. The idea was to use the opposing forces to balance and center the ions in the middle portion of the annular region (i.e., analyzer space). The carrier gas flow that was used to transport the sample ions into the analyzer was also used to generate a flow vector along the analyzer length to transport the ions to the detector.

Voltages were applied to the electrodes to create an electric field pointing radially toward the inner stacked washers. This electric field was designed to push the sample ions in that same direction, while the opposing gas flow pushed them back. If the forces on the ions were equal and opposite, the ions would be transported along the length of the analyzer to the detector

The entire length of the stacked washers was 3.00". This drift tube was housed in a metal housing that was 6.00" square and 3.00" long, with a 5.00" cylindrical baffle around the outside of the larger stacked washers; this was to help even out the gas flow around the drift tube (see Figures 3.5).

3.4 Porous (Frit) Tube Design

Porous metal tubes used in this design were fabricated by Mott Corporation, Farmington, CT, from metal powders with precise particle distribution. The strictly controlled sintering process enabled the production of uniformly sized and distributed pores in media grades ranging from 0.2 to 100 micron particle sizes, thus ensuring even porosity throughout the tubes.

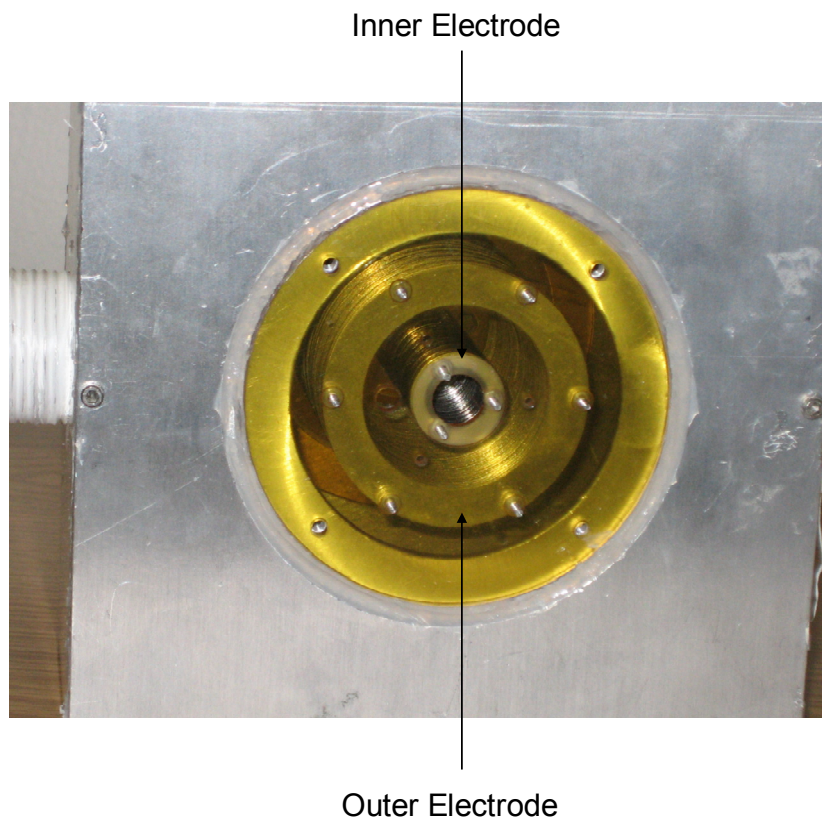


Figure 9.5 Photograph close-up of the stacked washer CIMA arrangement inside the metal housing, with the inner and outer tubes visible. The space between them was the analyzer region.

By definition, a porous medium is composed of solid regions and pores through which the fluid flows. The choice of porous metal for this application was decided from the uniform gas flows observed in other applications.² Flows in porous media are described by Darcy's law,³ which states that the volumetric flow rate, Q , of a liquid through a porous material is proportional to the hydrostatic pressure difference, ΔP , across the material, inversely proportional to the length, L , of the material, and directly proportional to the cross sectional area, A

$$Q = \frac{kA\Delta P}{L} \quad (3.1)$$

where k is the permeability of the material. Rearranging the above equation gives

$$\frac{Q}{A} = \frac{k\Delta P}{L} \quad (3.2)$$

This is the linear velocity, which is proportional to the pressure drop, ΔP , across the thickness of the material.

The porous metal allows pressurization of the inside of the tube to obtain a uniform gas flow velocity through the walls. For this work, different media grades of 5, 10 and 20 microns were used, giving porosities of 30, 32 and 45%, respectively. The porous metal tubes were 3" long with an ID of 0.375" and an OD of 0.500". One end of the tube was sealed and the other end was connected to a non-porous tube to facilitate connecting to the gas supply (see Figure 3.6).

The outer perforated tube was made from stainless steel. Approximately 1000 holes 0.0032" in diameter were uniformly drilled through the wall. The perforated tube was also 3" long with an ID of 1.00" and an OD of 1.030" (see Figure 3.6). A plastic housing was used to enclose the instrument for protection from high voltage. The gas pressure inside the annular

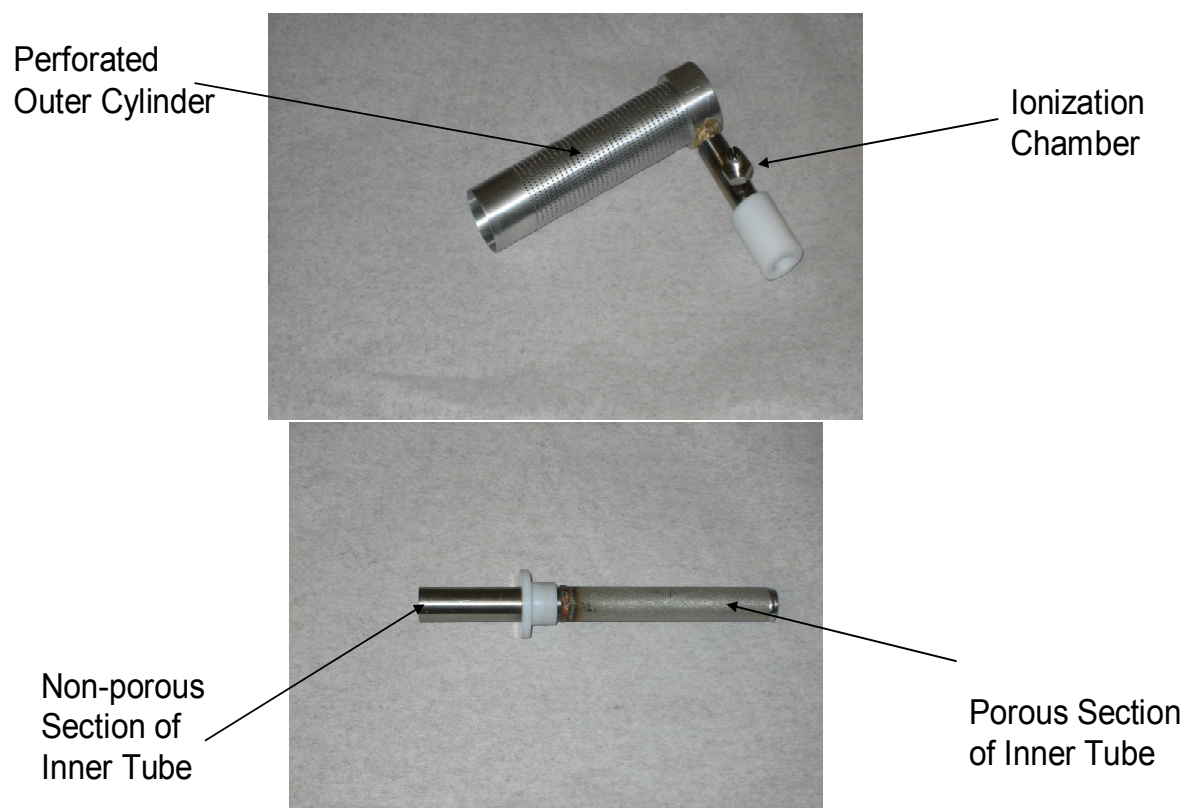


Figure 9.6 Photograph of the porous tubes used. These served both as electrodes and as uniform gas flow generator. As seen in the lower photograph, a section of the inner tube was nonporous. This part was attached to a high pressure gas source.

region, i.e., the space between the two cylinders (see Figure 3.7), was near atmospheric pressure. This pressure could be calculated easily by an equation supplied by the porous metal tube manufacturer.⁴ The operation of this design was similar to the stacked washer design.

3.5 Results from Tests Using the Concentric Tube Design

None of the concentric tube designs worked as hoped. The required uniform plug flow was not achieved with any of the three designs. In the perforated tube type, it was not possible to pressurize the inner tube to a uniform pressure under the gas pressure and flow conditions that were used. The same results were obtained with the stacked washer design. The spacers used were too large; therefore, non uniform pressure on the inside of the tube was obtained. Using the porous frit design, considerable pressure was achieved inside the inner tube; however, the particle arrangement made it impossible to have a uniform direction of gas flow out of the wall. Another problem was experienced with the ion introduction system used. Ions were created outside the analyzer and a carrier gas was used to carry them into the analyzer. The carrier gas velocity was only a tenth of the counter-flow gas velocity and the sample was carried along with the counter flow gas, never reaching the detector.

Figures 3.8 to 3.10 are fluent simulation results for the stacked ring and the porous tube designs. In Figure 3.8, the stacked ring flow pattern from the velocity contours indicate that the flow in the analyzer region was non-uniform. Figure 3.9 is a velocity contour representation of the flow inside the porous tube and in the analyzer region. While the flow pattern is an improvement over the stacked ring design, a detailed investigation of the contour plots shows that there is considerable variation in the gas velocity inside the analyzer region. Figure 3.10 is a plot of the cross-section flow velocity of the analyzer region from the inner porous tube to the

outer perforated tube. This figure indicates substantial variation of flow velocity as the gas moves from the porous tube to the outer cylinder.

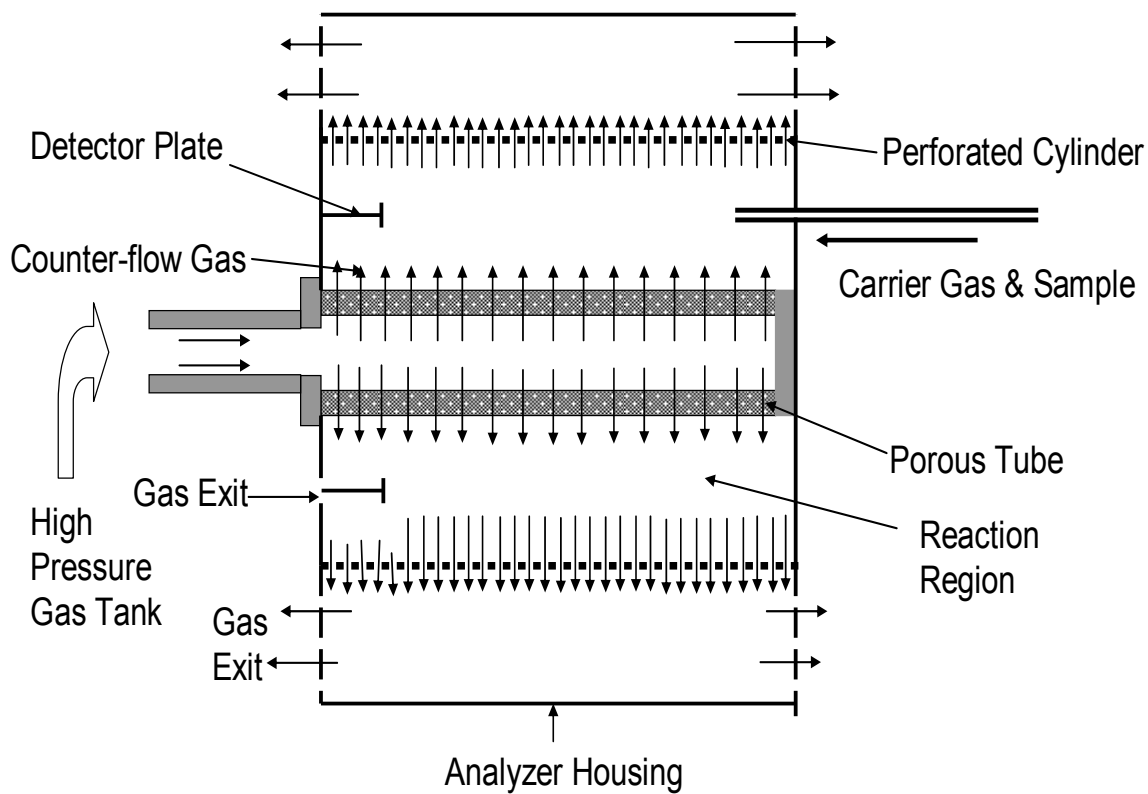


Figure 9.7 Schematic of the porous tube CIMA analyzer design. The inner porous tube also served as an electrode. The outer electrode was made from a perforated cylinder.

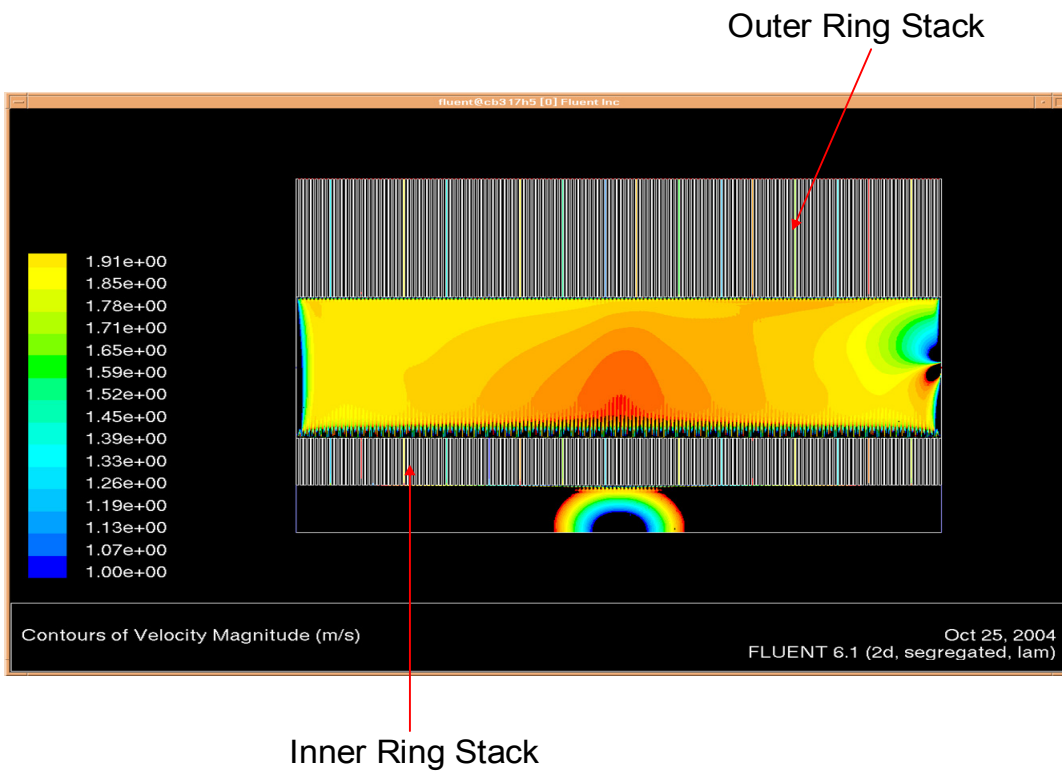


Figure 9.8 Fluent simulation of gas flow in the stacked ring design. The flow in the analyzer region is non-uniform.

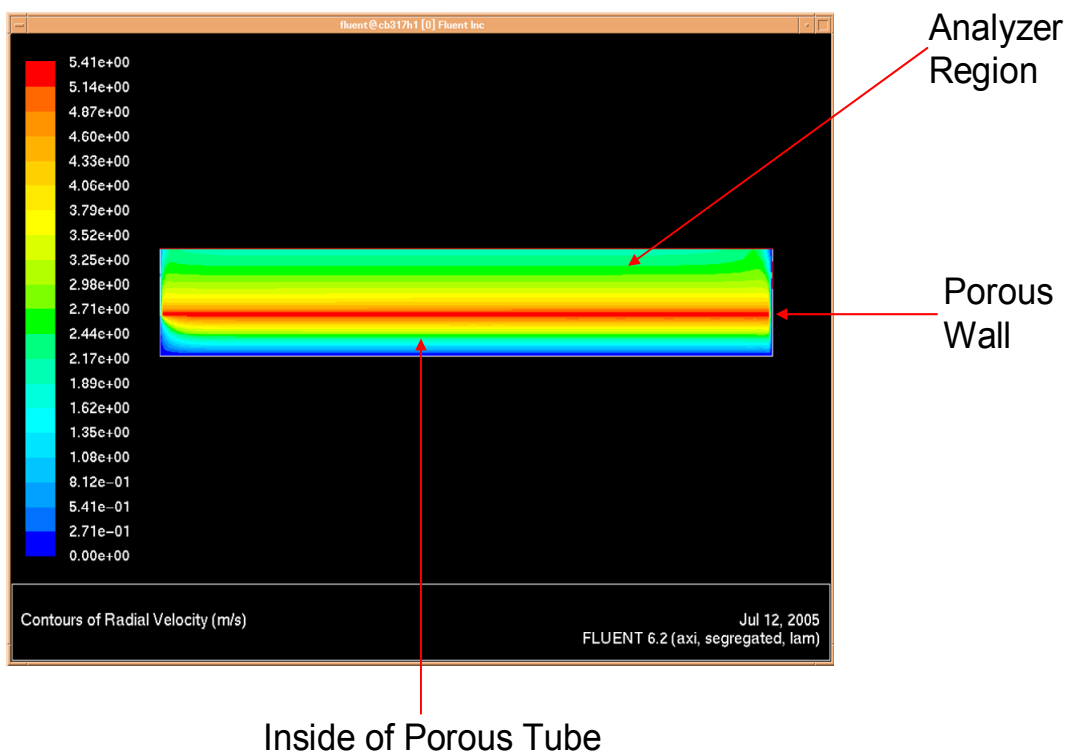


Figure 9.9 Fluent simulation of gas flow using the porous tube design. Contours of the radial velocity show that there is appreciable variation of the flow along the tube, even when the pressure inside the porous tube was approximately 400 psi.

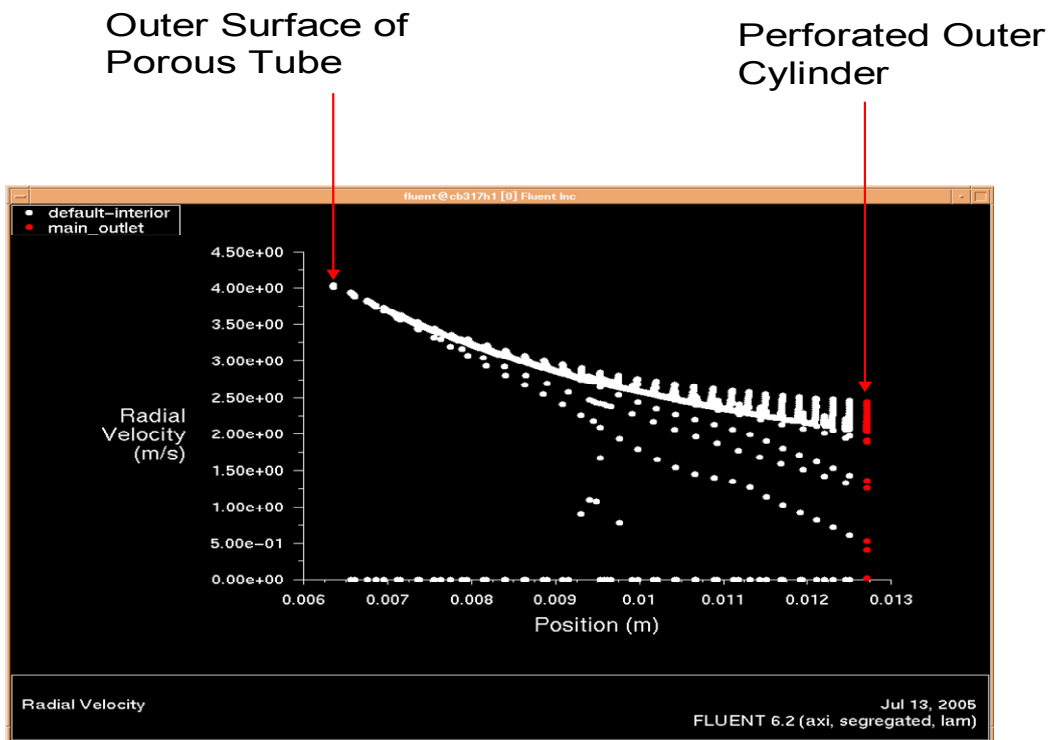


Figure 9.10 A cross-section of the radial velocity of the analyzer region of the porous tube design. Flow variation within the region is evident.

3.6 References

1. www.airtxinternational.com/catalog/air_amplifiers
2. <http://www.cmse.ed.ac.uk/MSE3/Topics/MSE-permeability.pdf>
3. Floyd, D. *Porvair Fuel Cell Technology*. 2000.
4. www.mottcorp.com

Chapter 4

Counter-flow Ion Mobility Analysis Using a Wind Tunnel

4.1 Introduction

For CIMA to function as an ion mobility analyzer, the counter-gas flow profile must be plug flow. Chapter 3 described unsuccessful attempts to use concentric cylinders to achieve a flow profile with uniform velocity. In this chapter, efforts to solve this problem using a wind tunnel are described. The test region of the wind tunnel where plug flow exists served as the CIMA analyzer region. The wind tunnel was designed to avoid many of the problems experienced with previous designs, including the ability to achieve a plug flow profile, the ability to construct an analyzer region without “defining” grids, meshes, or perforated walls as described in Chapter 3, the ability to have complete control over the gas flow, and the capacity to determine accurately the flow properties and relate them to other physical properties such as pressure, temperature and viscosity.

A wind tunnel is a converging flow device that is used in the automotive and aeronautics industries. It is a proven way of generating uniform gas flow and has been used for over a hundred years. A wind tunnel consists of essentially three parts: a contraction region with a characteristic bell-shaped mouth, a test (analyzer) region, and a diffuser region (Figure 4.1). These three regions are related and dependent on each other, both in design and functionality.¹

The goal in this work was to convert a wind tunnel from its natural use in fluid dynamics analysis to a chemical analyzer used for separation, detection and measurement. This may be the first time that a wind tunnel has been used in chemical measurement instrumentation. In this system, the test region became the analyzer region. The test region of most fluid dynamic

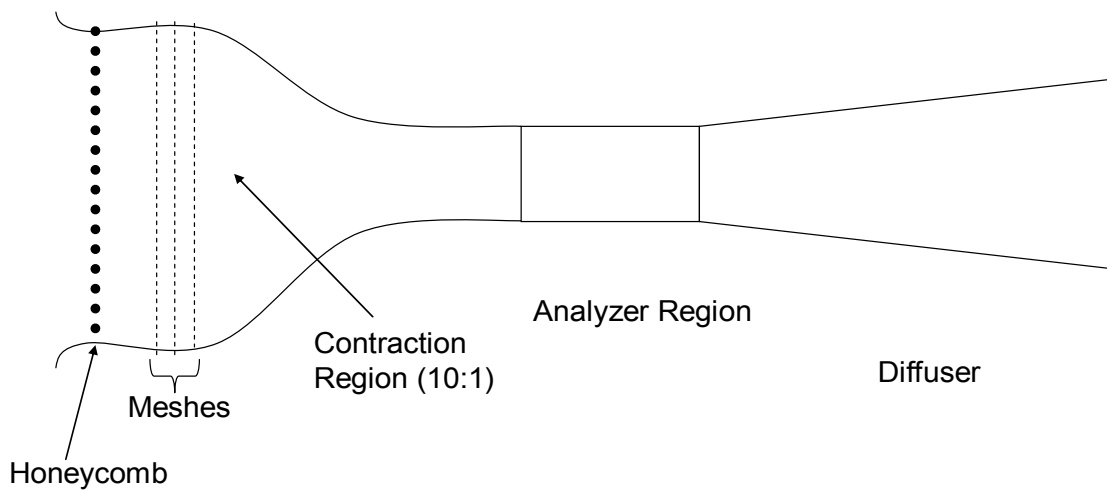


Figure 10.1 Schematic of a wind tunnel showing the three regions (contraction, analyzer and diffuser) with honeycomb and meshes.

wind tunnels are either square-cubic or rectangular in shape, the one described in this chapter was rectangular to create a geometry that minimized the “wall” or “edge” effect on the flow in one of the dimensions orthogonal to the gas flow.

The objective of this chapter is to describe the wind tunnel CIMA design, construction and experimental results. An in-depth description of the wind tunnel, its components and their functionality is followed by results obtained from utilizing the wind tunnel in a laboratory prototype CIMA instrument. First, the design and results from modeling the gas flow and electric field in the analyzer region are presented. This is followed by experimental calibration of the gas flow in the wind tunnel analyzer region, which enabled establishment of the relationship between the velocity of the gas in the analyzer region and the voltage used to operate the fans. Next, results obtained using the prototype CIMA instrument are presented and discussed.

4.2 Wind Tunnel Analyzer Design

General Considerations. The design of the wind tunnel began by considering the requirements of the analyzer region, primarily the flow velocity range that was needed in that region. This was used to determine the area as well as the volume of the region, which ultimately determined the dimensions of the other two regions, i.e., contraction and diffuser. Next the fan to be used was selected. In addition to the volume flow rate of the fan, the fan bearings had to be constructed such that no outgassing of chemical vapors would occur. In chemical analysis, impurities and contamination from a gas source must be avoided. A fan with a brushless motor system and non-grease bearing design was selected.

The gas flow velocity desired in this region was in the range of 5.00-15.0 m s⁻¹. A ratio of 1:2 height to width was selected for the cross-sectional area of the analyzer region; this ratio was the minimum ratio of height to width that would minimize the wall effects. Wall effects

occur as a result of viscous drag of a fluid flow at a surface, giving rise to a boundary layer region where the fluid velocities is not uniform (the same effect is experienced by electrostatic fields in which field lines near a wall become distorted, while away from the wall they are straight). The dimensions of the analyzer used were 4.00”x 2.00”. These dimensions combined with the desired gas velocity determine the volumetric flow rate in the analyzer.

Mehta and Bradshaw² provided detailed design information and dimensional relationships of the various parts of the wind tunnel. Their design rules were followed in the design of the CIMA wind tunnel. They gave additional information on criteria for selecting components such as honeycomb and meshes.

Contraction Region. The contraction region in the CIMA design produced a 10:1 contraction between the inlet and the exit, which is better than most industrial wind tunnel designs (typical industrial designs have a 9:1 contraction ratio). It had a bell-shaped entrance that contained a honeycomb and screens (meshes) as shown in Figure 4.1. Care was taken to ensure that no flow separation occurred inside the inlet, and that the resulting flow was uniform.

Honeycomb and Screens. Placing a honeycomb structure in the wind tunnel gas flow stream affected the flow uniformity, and screens controlled the turbulence intensity in the analyzer region. The area of the contraction region dictated the size of the honeycomb. The honeycomb was used to remove swirl and lateral mean velocity variations,² thereby straightening the flow. Its cells were hexagonal in shape. For this application, a 3/16” cell width with 1.00” height cut to fit the bell-shaped contraction region was used. Five meshes of different open areas were used. The honeycomb was sandwiched between two meshes with 67.4% open area, followed by three more separated by approximately 2.00” each in descending order of 64.8%, 62.7% and 59.1% open areas, respectively.

Analyzer Region. The analyzer region is the most important component of the wind tunnel CIMA instrument. In this region, the gas flow must be uniform and non-turbulent, representing a plug flow. The material used in the analyzer region must be fabricated from a highly resistive material with a surface that is slightly conductive to dissipate the space charge. As mentioned earlier, the shape of the analyzer region was rectangular in order to eliminate wall effects that would impact both the gas flow and electrical field inside the region. The size of the analyzer region was 4.00”x 2.00” with a total length of 8.27” (21.0 cm).

The analyzer region was made from four assembled parts. The top and bottom walls were made from a power circuit board (fiber glass) and the side walls (in the x and z axes) were made from polyetherimide (PEI), a conductive plastic material. The side walls were insulated from the top and bottom walls with Kapton (polyimide) tape of 10.0 k Ω resistance. The inside of the top and bottom walls had parallel conductive traces that were 0.0400” thick and separated by a spacing of 0.00800” for a total number of 145 traces on the middle 7.09” (18.00 cm) portion of the plates (see Figure 4.2). The trace through 1.25” off-center of the bottom (see Figure 4.3) was grounded; the trace at the same position on the top plate was at common ground and connected to a transformer that was attached to a power supply (V5). The position of the common ground on the top board varied along the length of the board (in the x-axis) depending on the voltage set by the transformer. As this common ground position moved to one side or the other, an inclined electrical field was produced inside the analyzer. The angle of inclination was dependent on how much voltage was applied. The traces were connected to each other with resistors so that a potential gradient (i.e., constant electric field) was established from one end of the analyzer to the other. The traces at the ends of the PCB boards were used as input points where the voltages

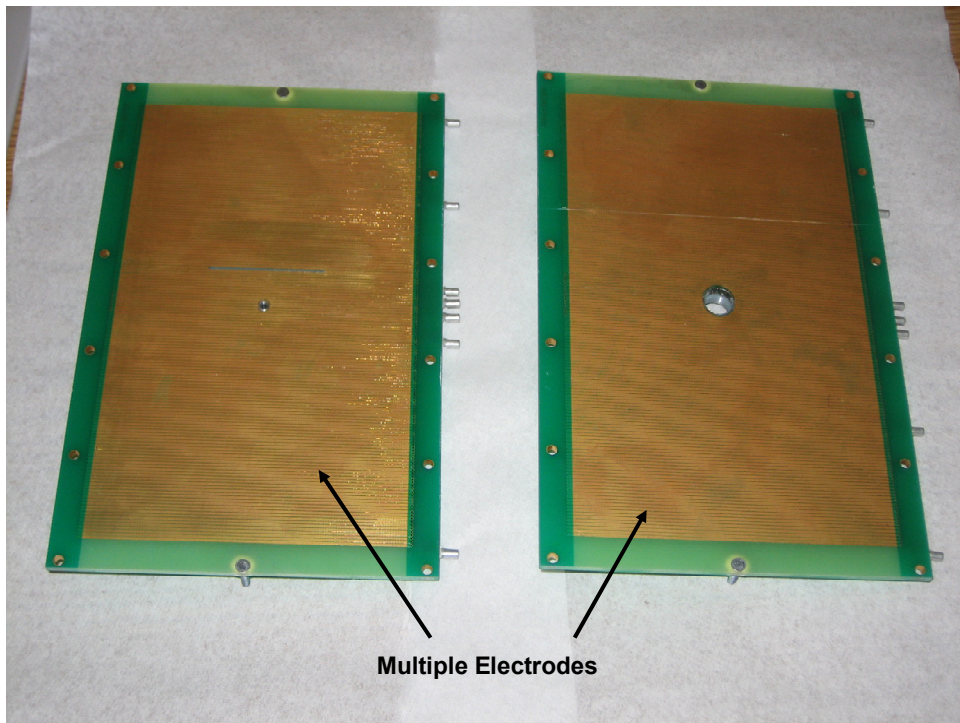
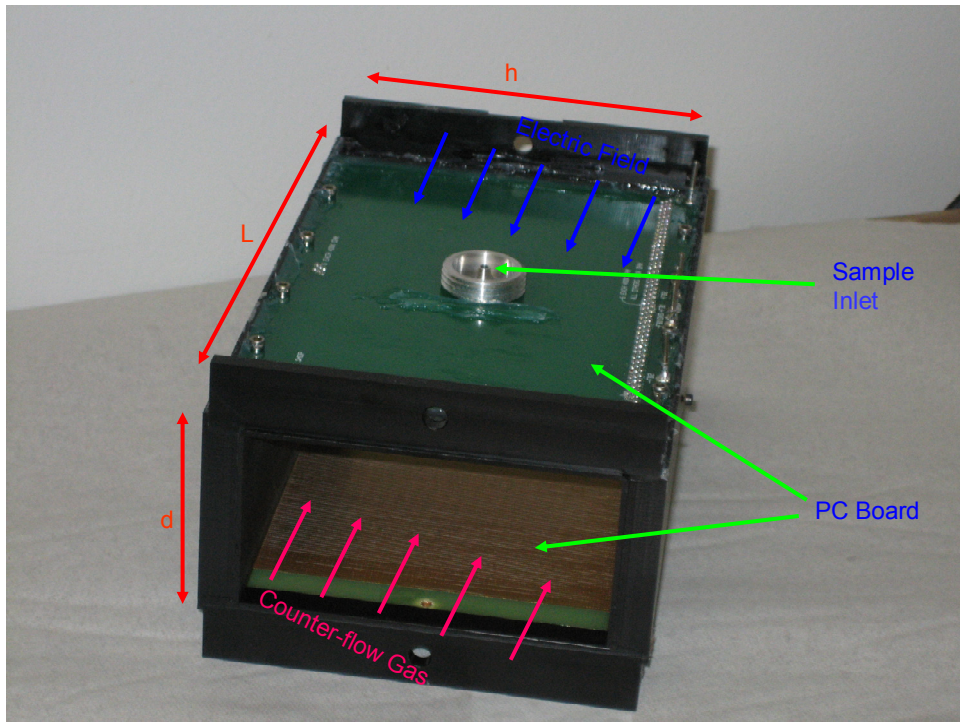


Figure 10.2 Photograph of the analyzer unit with PC boards on the top and bottom. The lower photograph shows the PC boards with conductive electrode traces.

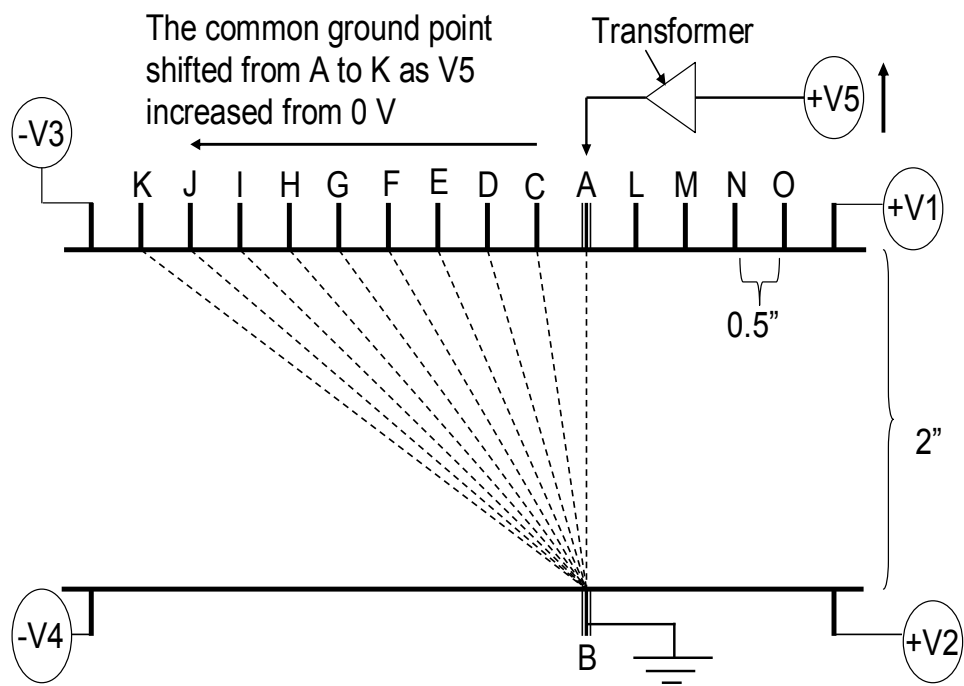


Figure 10.3 Preferred electrical schematic for the CIMA analyzer test region. The different positions where the voltage became zero as the voltage was increased are indicated by C to K.

(V1 to V4) were applied. A read-back system was used to read the voltages along the length of the plates to verify that the voltages were correct as desired.

The 1.25" position off-center of the top and bottom plates had holes. The bottom plate hole was used to introduce the detector, while the upper plate hole was used for sample introduction. There were feed-back points every half inch along the boards.

Diffuser and Fan. The diffuser is the third component of the wind tunnel analyzer. Its shape and dimensions were critical to the flow properties in the preceding test region. In this design, the diffuser was 18.0" long and was a rectangular shaped cone. The adjacent walls were angled at 4.60° and 8.80°. The end attached to the analyzer region was 4.00"x 2.00" and the end attached to the fans was 9.51"x 4.92". The diffuser angle prevented boundary layer separation of the gas flow in the analyzer region. This ensured that the flow properties in the analyzer region were maintained throughout.

The fans used in this design were specially selected, not only for the range of voltages that could be used to operate them or for the volume flow capacity, but more importantly for the type of bearing system. Chemical contamination of the analyte sample and counter-flow gas was of major concern. Therefore, all parts used for construction of the analyzer were designed such that they would not introduce contamination into the system. The fan used had a brushless motor system that did not require oil or grease lubrication. The fans were DC voltage rotary fans from Sunon, Brea, CA. The Sunon model KDE2412PMV1 fan has a magnetic levitation motor with a "vapo" bearing system. It is rated at 24 VDC, but operated with approximately 3 volts. Its dimensions are 4.720"x 4.72" x 1.50", with maximum air flow of 145 CFM at 0.320-inch water. In this design, six fans were used (two parallel sets with each set containing three fans in series).

The Sunon MagLev fan design is based on magnetic principles and forces that not only propel the fan, but also ensure stable rotation over an entire 360 degrees of movement.³ Utilizing the attraction of the magnetic levitation force, it eliminates wobbling and shaking characteristics of traditional motor fans (a needed feature for gas flow stability in the analyzer region). The MagLev fan propeller is suspended in air during rotation so that the shaft and bearing do not come into direct contact with each other to create friction. Additionally, the bearing system in this fan is what is called the “vapo” bearing. Unlike traditional ball or sleeve bearing systems, this type of bearing uses gas or air that surrounds the shaft. When used in conjunction with the MagLev, it creates a spring function, which helps the fan motor operate efficiently. This new system removes the use of oil rings and washers. Additionally, the shaft inside the bearing bore experiences friction only with air.

A honeycomb of the same general specifications as the one used in the contraction region was sandwiched between two meshes and then placed between the fans and the diffuser at the end of the wind tunnel. This helped to straighten the gas flow coming through the diffuser. As gas was moved by the fan blades, it tended to follow the blade swirling motion. To prevent this motion from propagating back to the test region, honeycomb and meshes were used. The fan was oriented such that it pulled air or gas through the wind tunnel. This helped to ensure that the gas passing through the contraction region was a stable gas flow with very little or no turbulence from the fan.

Ion Sampling and Ionization Chamber. A corona discharge was used as the ion source, and head space above a liquid sample was introduced into the ion source for ionization and testing in the wind tunnel analyzer. The ionization chamber was carefully designed and constructed so as to maximize the ionization process as well as to help in ion transport. As can be

seen in Figure 4.4, the inside of the ion source chamber was designed to create a converging electric field so that ions would be pushed through the opening into the analyzer. The concave shape of the floor of the chamber and the convex shape of the middle section of the chamber was used for this purpose. The corona needle was positioned approximately 2.00 mm from the exit, creating a point to ring effect,⁴ where the ions were made. The carrier gas also aided the electric field in transporting ions into the analyzer.

Assembled Wind Tunnel Analyzer. The wind tunnel contraction and diffuser components were constructed from aluminum and stainless steel while, as indicated earlier, the analyzer region was made from conductive plastic and PC boards. When the three components were assembled together, the entire system looked like the solid model drawing shown in Figure 4.5(A). Figure 4.5(B) shows a photograph of the CIMA; it had an overall length of approximately 56.0” and was housed in a large metal housing that measured 76.0”x 38.0”x 38.0”. Figure 4.6 is a schematic of the assembled system with electric field and gas flow directions indicated.

4.3 Electrical and Electronic Components

The electrical and electronic components of the CIMA system were equally important as the mechanical design. The electrical components can be viewed in three categories, the PCB components of the analyzer hardware, the detector data collection and amplifier system, and the control system which includes manipulation of the power supplies and other electrical components. The PCB components were described earlier. The detector system consisted of a metal hemisphere that operated like a Faraday plate and an integrating amplifier. This dome-shaped stainless steel surface was rounded for easy gas flow around and above it. The amplifier was a basic reset-and-integrate measurement type. It operated by acquiring data every 16 ms

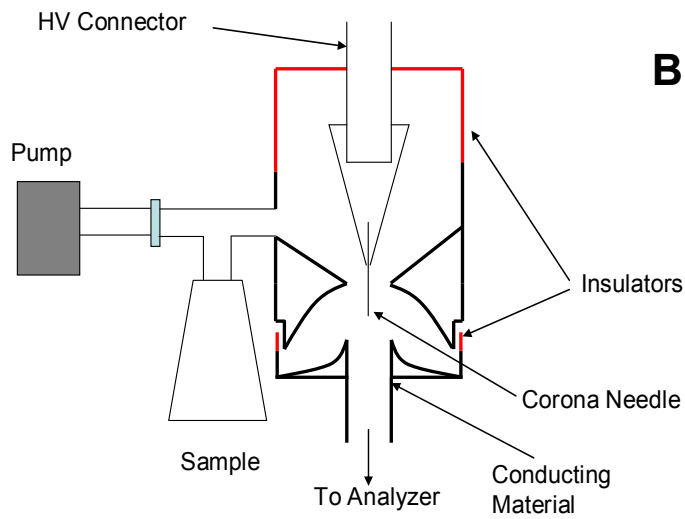
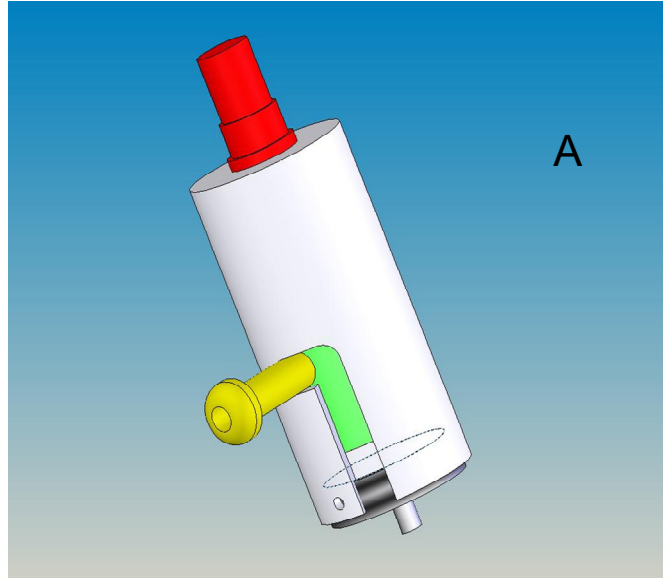


Figure 10.4 (A) Solid model drawing of the ionization chamber and (B) cross-section diagram of the ionization chamber and sampling system. The ionization chamber was designed such that the electric field created would help drive the ions into the analyzer test region.

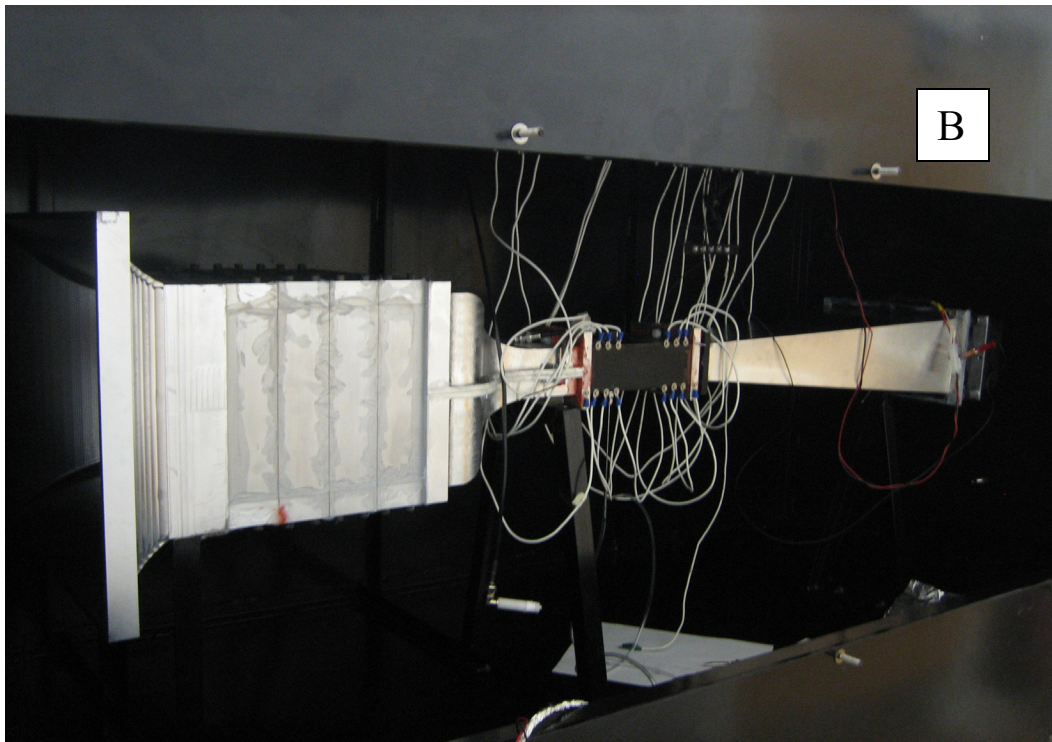
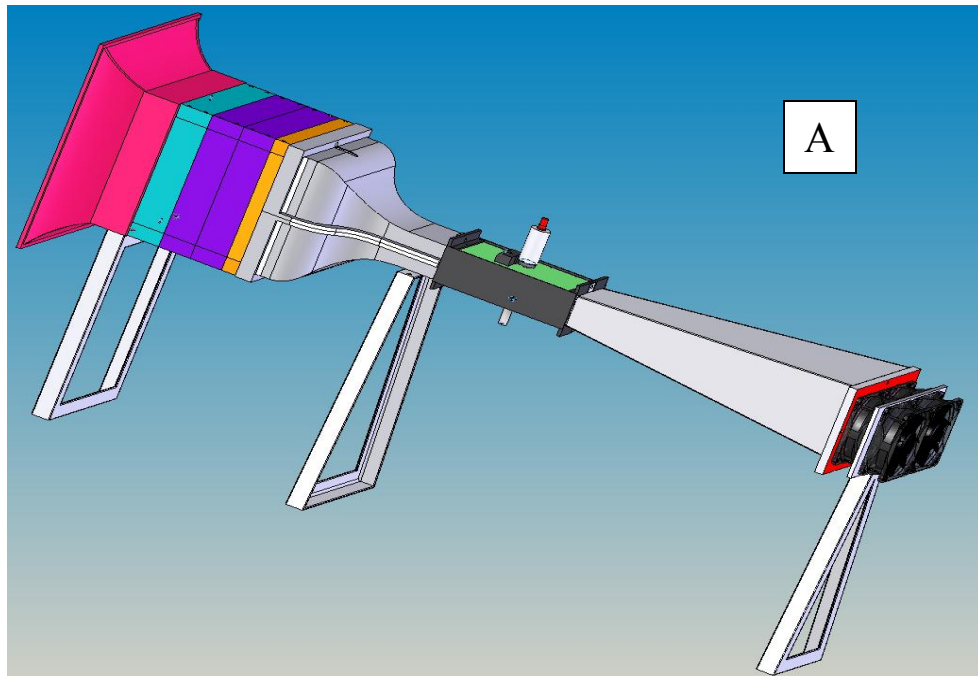


Figure 10.5 (A) model drawing and (B) actual photograph of the wind tunnel CIMA analyzer. The analyzer test region was connected to voltage sources through the wires shown. The drawing shows both the ion source on top and the detector at the bottom of the analyzer region.

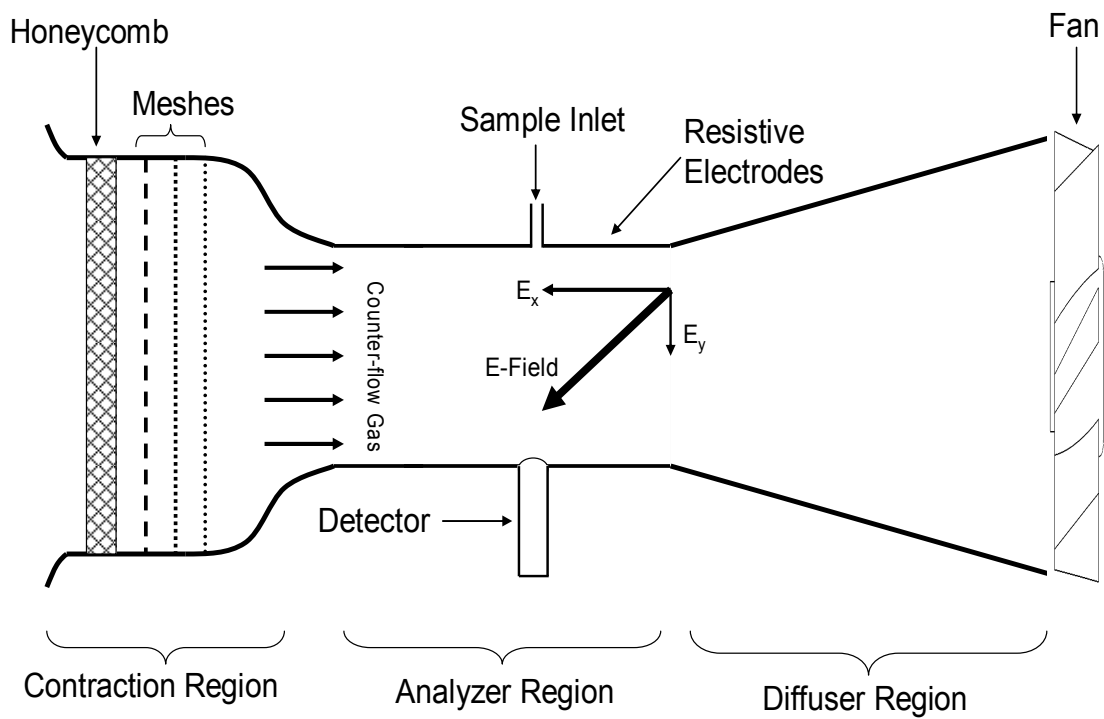


Figure 10.6 Schematic of the wind tunnel CIMA showing the various regions, gas flow direction, electric field components and other accessories.

with a 16 ms reset time. This type of amplifier was chosen to overcome the capacitive coupling that results from both electric fields changing close to the detector and from ions approaching the detector. This amplifier was operated at 60.0 Hz to filter away the 60 Hz noise. A control box contained all of the power supplies, amplifier, and other electrical peripherals, such as the Labview DAQ board, control features for the fans, mass flow controller, and pumps.

4.4 Modeling of Gas Flow and Electrical Properties in the Analyzer Region

Objectives. The objective of this modeling effort was to simulate the gas flow and electric field in the analyzer region. The simulations, using experimental operating conditions, were used to predict gas flows and electric field lines in the analyzer region, and how these properties interact with analytes.

Modeling Software and Boundary Conditions. Fluent⁵ and Comsol⁶ simulation software were used. Fluent is a computational fluid dynamics (CFD) computer program used for simulating fluid flow, and heat and mass transfer behavior in both reactive and non-reactive systems. Comsol, on the other hand, uses a finite element method (FEM) to find approximate solutions of partial differential equations as well as integral equations that describe physical phenomena such as fluid flow and electrical properties. The analyzer dimensions as well as the operating conditions anticipated in an actual experiment were used. Tables 4.1 and 4.2 present the boundary and other parametric conditions used in these simulations.

Analytical Procedure. Fluent was used to model the gas flow behavior in the contraction and analyzer regions. First, a 2-D model outline of the analyzer with the actual dimensions of the two regions was created with Gambit,⁵ a preprocessor of the Fluent program, and the model was then “meshed”. The various parts were defined and labeled, and the flow boundary conditions

Table 10.1 Boundary conditions and other defining parameters used in the Fluent modeling. Some of these were default parameters selected by the program itself.

Boundary Conditions		Solver Parameters		Others	
Zone	Type	Solver Parameters	Segregated	Viscous Mode Used	Laminar*
Default interior	Interior	Formulation	implicit	Material	Air
Face	Fluid	Space	2D	Density	1.25 kg m ⁻³
Gas-withdrawal	Pressure outlet	Time	Steady	Viscosity	1.7894E-5 kg m ⁻¹ s ⁻¹
Inlet	Pressure inlet	Velocity formulation	Absolute		
Outlet	Pressure outlet	Gradient option	Cell based		
Sample inlet	Pressure inlet	Porous formulation	Superficial velocity		
Sample outlet	Pressure outlet				
Walls	Wall				

* k-epsilon was used when turbulent flow was modeled

Table 10.2 Parameters and boundary conditions used in Comsol for modeling the electric field in the analyzer test region.

Physics-subdomain Setting		Physics-boundary Condition Setting		Other	
Material	Electrical Conductivity	Electrodes	Potential (V)*	Space Dimension	3D
Plastic	10E-10 S m ⁻¹	Plastic Walls	Inward Current Flow	Application Mode	Comsol Multiphysics
Electrode	3.77E9 S m ⁻¹			Electromagnetic Mode	Conductive Media DC
Air	10E-7 S m ⁻¹				

* V is the voltage of a particular electrode

were defined in Gambit (see Appendix B for explanation of the various boundary conditions and other parameters used in the modeling). The meshed model was then imported into Fluent, the values of the boundary conditions were set, and Fluent was allowed to determine the flow characteristics. The boundary conditions included defining all of the solid wall surfaces; the bell-shaped mouth of the contraction region where the counter-flow gas entered the analyzer was defined as the pressure inlet, the end of the analyzer region where the counter-flow gas exited was defined as the pressure outlet, the inside of the analyzer was defined as the interior, and the fluid was air. All other parameters listed in Table 4.1 were default parameters set by the program based on the type of solver selected. Boundary conditions in addition to those in Table 4.1 were gas flow velocity of 10.0 m s^{-1} at ambient pressure (101,325 Pa) in the analyzer region.

In the Comsol modeling, a 3-D model was used; a drawing of the actual analyzer region using the exact dimensions was made. The various parts were labeled either as electrodes or plastic walls; they were differentiated by their electrical conductivity. The electrodes were set to a boundary condition of “potential” while the plastic walls were set to “inward current.” The solver selected was the conductive media DC type. The various electrodes were set to their appropriate potentials, the figure was “meshed” and the program was allowed to solve the electrostatic problem. The solver was then instructed to present the results as electric field lines as in Figure 4.9. The voltage boundary conditions are listed in Table 4.2. This simulation was used to determine the electrostatic field components vital to this design.

Modeling Results and Discussion. Figures 4.7 to 4.9 present the modeling results. Figure 4.7 is a velocity contour plot of the gas flow in the contraction and analyzer regions of the modeled instrument. Converging of the gas flow is evident as it moves from the contraction region to the analyzer region. The analyzer region is one color (blue), indicating that the velocity

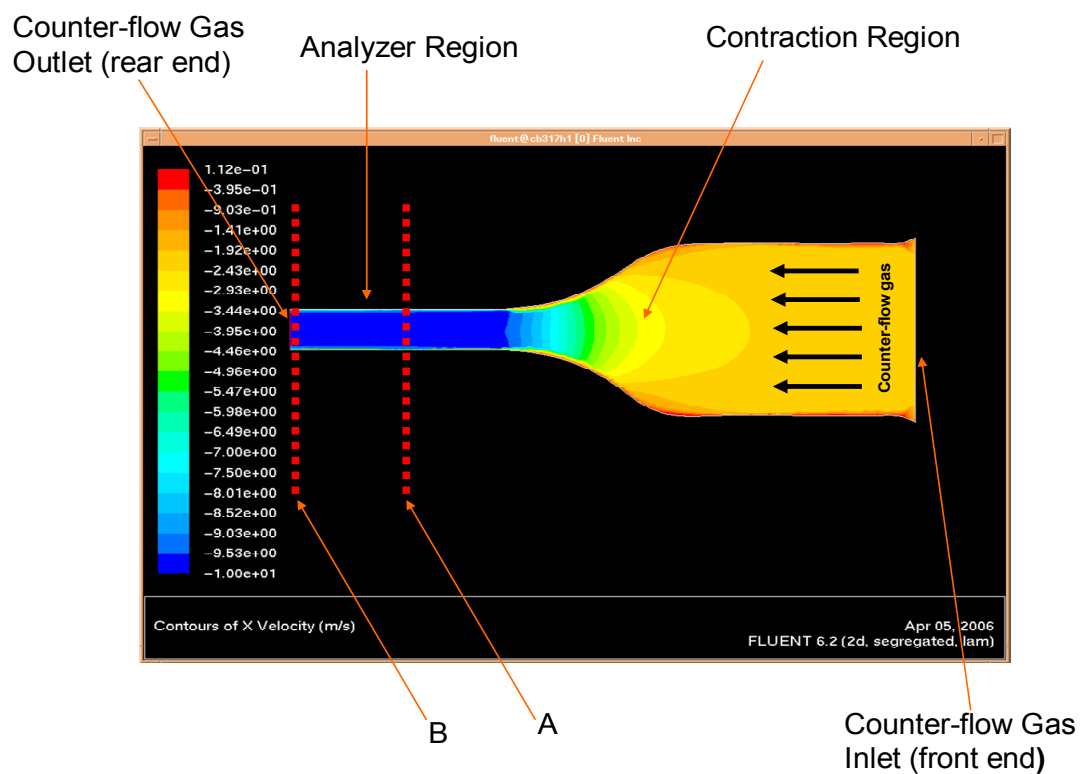


Figure 10.7 Modeled velocity contours in the contraction and analyzer regions of the wind tunnel. The converging features can be seen in the contraction region leading to uniform flow in the analyzer region. The direction of flow is indicated by arrows. The flow along the cross-section indicated by A and B is shown in Figure 4.8.

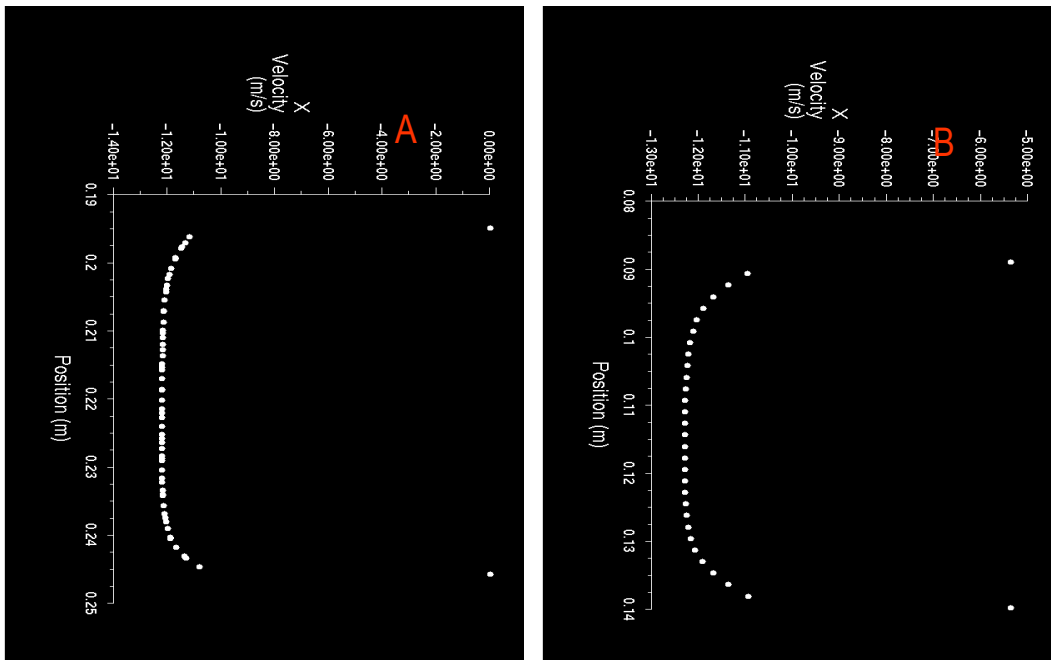


Figure 10.8 Plug flow profile in the analyzer region at positions indicated in Figure 4.7. (A) Cross-section of the flow along the mid-section of the test region from top to bottom, and (B) cross-section at the downstream end of the test region.

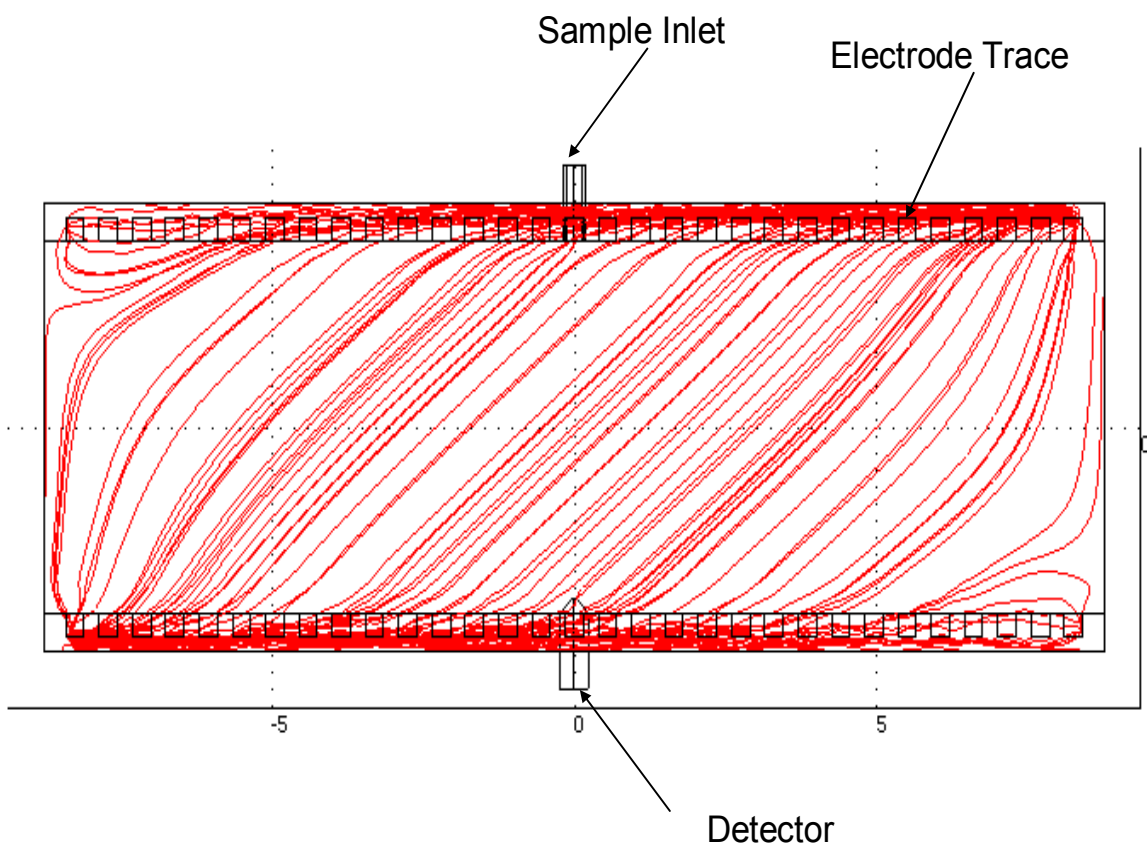


Figure 10.9 Electric field lines in the analyzer region. The inclined or tilted field lines are needed to transport the ions first against the gas flow, and then to the detector. The multi-electrode design helps to create straight field lines.

in that entire region is the same or nearly the same (i.e., uniform). Figure 4.8 further illustrates the gas flow velocity cross-section through the middle [Figure 4.7(A)] and end [Figure 4.7(B)] positions of the analyzer region. The gas flow velocity in the middle is more flat (plug flow like) than the end near the exit, indicating that the optimum position of the ion source and detector should be near the middle section of the analyzer region. Here, the ions would interact with a gas velocity that is uniform across the analyzer.

Figure 4.9 displays the inclined electric field in the analyzer region. This is the type of field that was desired. When this field is resolved into its horizontal and vertical components, the horizontal or x-component of the electric field moves the ions in a direction opposing the gas flow while the vertical or y-component transports the separated ions to the detector at the other side of the analyzer region. The multiple electrodes, or electrode traces should help to straighten the field lines and aid in the ion transport process. The sample inlet device and detector situated on top and at the bottom of the analyzer, respectively, do not appear to affect the electric field. This non-distortion of the electric field by the detector and sample inlet preserves the uniform field throughout the inside of the analyzer.

4.5 Experimental Characterization of the Analyzer Region Gas Flow

Objectives. Experiments described in this section were performed to characterize the actual gas flow in the analyzer region of the wind tunnel CIMA. Specifically, (1) the relationship between the fan operating voltage and gas flow velocity at the center of the analyzer region was determined, and (2) the gas flow along the vertical direction of the analyzer was measured to ascertain whether or not plug flow was achieved.

Material and Instruments. The wind tunnel CIMA instrument with fans attached as previously described was equipped with a voltage control device to operate the fan. A 1/16”

Pitot-static pressure probe from United Sensor (Amherst, NH) connected to a PX138 ± 0.3 PSI digital pressure transducer from Omega (Stamford, CT) was used to measure the gas pressure in the analyzer. The Pitot-static probe was connected to the digital transducer using hollow tubing. The digital transducer was powered by an 8.00 V DC power supply. The transducer output voltage was 3.50 V at atmospheric pressure. The output voltage was read by a voltmeter in millivolts to detect small pressure variations.

Experimental Procedure. The wind tunnel analyzer was assembled as shown in Figure 4.10, with the fans attached to the diffuser. A static Pitot pressure probe was inserted through a hole at the center of the analyzer region. In the first characterization experiment, the Pitot probe elbow arm was placed 1.00” into the middle portion of the analyzer, enabling measurements of gas pressure at that point. Voltages ranging from 3.00-24.0 VDC were applied to the fans at 1.00 V increments and the pressure transducer readings were measured in millivolts using a voltmeter. Table 4.3 list the results of these measurements along with the conversion to volts, pressure (Pa) and velocity (m s^{-1}). Information from the fan manufacturer and the calibration curve in Figure 4.11 were used to convert the pressure transducer measurements in volts to pressure (Pa). The pressure results were converted to volumetric flow using

$$v = \sqrt{\frac{2\Delta P}{\rho}} \quad (4.1)$$

where ΔP is the pressure difference measured by the Pitot tube in Pa, and ρ is the gas density in kg m^{-3} . The volumetric flow was divided by the area of the analyzer (2.00” x 4.00”) to determine the gas linear velocity in m s^{-1} . The result of this calibration was plotted as shown in Figure 4.12.

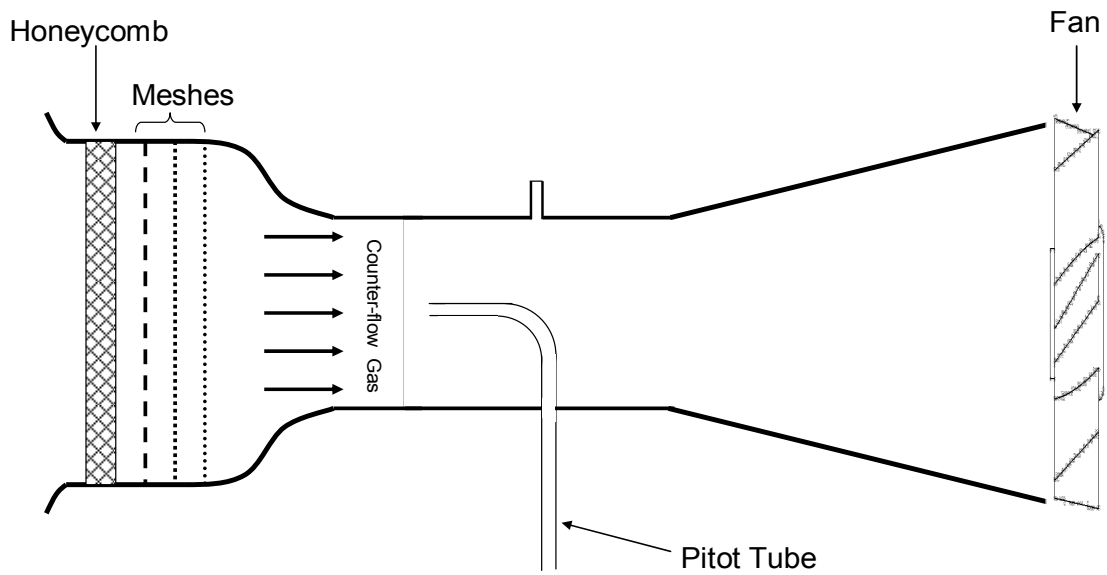


Figure 10.10 Analyzer gas flow calibration setup showing the Pitot tube, fan, meshes, honeycomb and gas flow direction.

Table 10.3 Pitot tube voltage measurements and their conversion to pressures and gas flow velocities.

Fan Voltage (V)	Pressure Transducer Reading on Pitot Tube					Counter-gas Flow Parameters			
	Min (mV)	Max (mV)	Range (mV)	Ave (mV)	Volts (V)	Volts (V)	Pressure (psi)	Pressure (pa)	Velocity (m s ⁻¹)
3.00	.0240	0.830	0.590	0.670	6.70E-04	3.50	8.04E-05	0.550	1.05
4.00	1.98	2.58	0.600	2.24	2.24E-03	3.50	2.68E-04	1.85	1.92
5.00	3.52	3.91	0.390	3.68	3.68E-03	2.50	4.12E-04	3.05	2.47
6.00	5.42	5.78	0.330	5.59	5.59E-03	3.51	6.71E-04	4.63	3.04
7.00	8.12	8.55	0.430	8.33	8.33E-03	3.51	10.0E-03	6.89	3.71
8.00	11.1	11.9	0.750	11.5	1.15E-02	3.51	1.38E-03	9.54	4.36
9.00	15.4	16.6	1.18	16.0	1.60E-02	3.52	1.92E-03	13.3	5.14
10.0	21.2	22.7	1.45	21.8	2.18E-02	3.52	2.61E-03	18.0	5.99
11.0	27.2	29.4	2.20	28.3	2.83E-02	3.53	3.39E-03	23.4	6.83
12.0	33.0	38.7	5.66	36.1	3.61E-02	3.54	4.34E-03	29.9	7.73
13.0	45.0	48.9	3.80	46.7	4.67E-02	3.55	5.61E-03	38.7	8.79
14.0	56.1	58.4	2.30	57.3	5.73E-02	3.56	6.87E-03	47.4	9.73
15.0	65.9	68.1	3.23	66.3	6.63E-02	3.57	7.96E-03	57.9	10.5
16.0	72.1	78.1	5.99	75.9	7.59E-02	3.58	9.11E-03	62.8	11.2
17.0	83.7	88.5	4.77	86.4	8.64E-02	3.59	1.04E-02	71.5	12.0
18.0	93.5	99.9	6.40	96.3	9.63E-02	3.60	1.15E-02	79.7	12.6
19.0	104	106	2.50	106	1.06E-01	3.61	1.28E-02	87.9	13.3
20.0	114	118	3.40	116	1.16E-01	3.62	1.39E-02	95.8	13.8
21.0	123	130	6.60	126	1.26E-01	3.63	1.51E-02	104	14.4
22.0	130	135	6.00	133	1.33E-01	3.63	1.60E-02	110	14.8

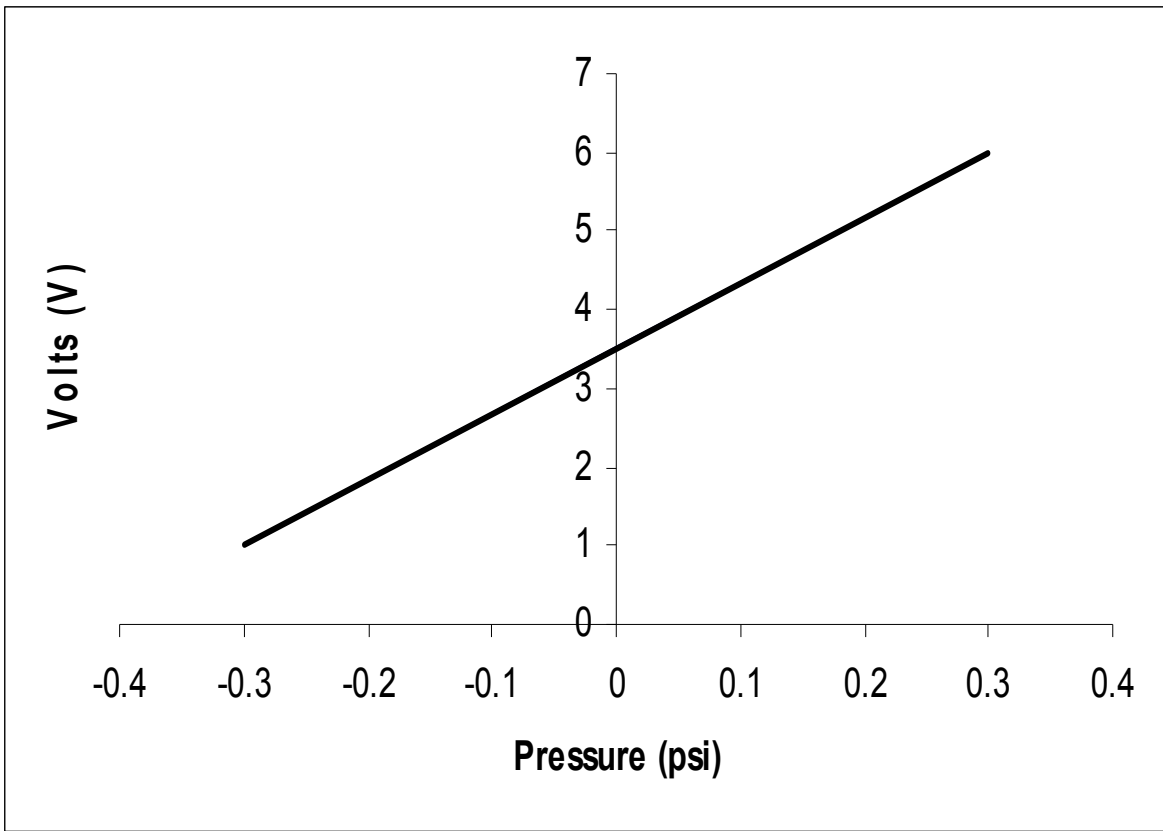


Figure 10.11 Pressure transducer calibration.

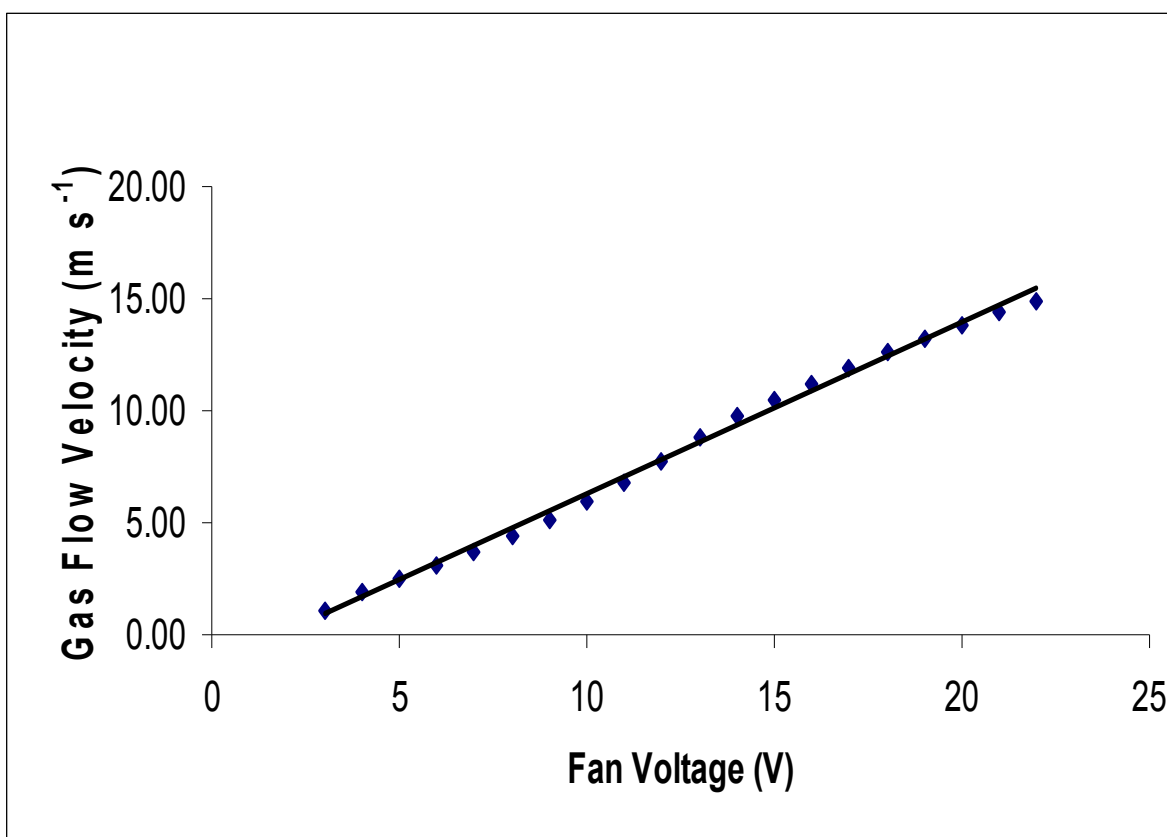


Figure 10.12 Calibration of the analyzer test region for gas flow velocity from fan voltage. The R^2 value for this plot is 0.990.

In the second characterization experiment, the elbow arm of the Pitot probe was first rested on the bottom wall while measurements were taken. Subsequent measurements were obtained as the Pitot probe was moved vertically upward every 0.500 cm until it touched the top wall. This gave a vertical flow profile from the bottom to the top of the analyzer. The data acquired are presented in Table 4.4. The fan was set at 18.0 V.

Results. Flow calibrations were done for both air and nitrogen gases and, as expected, the difference was small. A calibration plot of fan voltage versus gas velocity was made, and a flow profile plot for analyzer cross-section (top to bottom) was also made as depicted in Figures 4.12 and 4.13, respectively. The relationship between fan voltage and gas flow velocity in the analyzer region (Figure 4.12) is nearly linear. A linear fit of the data allows one to determine the gas flow at any voltage. Perhaps the most interesting result of these experiments is the cross-section flow profile in the analyzer region. As stated previously, the ideal flow profile is plug flow. Figure 4.13 shows that plug flow was achieved with only minor wall effects.

Conclusions. A significant achievement toward producing a working CIMA instrument was the attainment of a plug gas flow. Calibration of the gas flow in the analyzer region allowed control of the gas velocity in the analyzer.

4.6 Performance Testing of the Prototype Wind Tunnel CIMA

Objective. The prototype wind tunnel CIMA instrument was tested to determine if ions could be detected and mobility measured.

Materials and Instrumentation. The CIMA wind tunnel analyzer was assembled with an electrical box for control of the electronics and data acquisition as stated earlier. The electrical control box contained the power supplies, specially designed PC board containing control IC's, resistors, amplifiers, transformers, etc. A Labview⁷ program was used to operate the analyzer and

Table 10.4 Voltage readings in the analyzer test region resulting from profiling (top to bottom) of the gas flow.

Distance from Bottom Wall (cm)	Min (mV)	Max (mV)	Range [Deviation (mV)]	Ave (mV)
0.00	7.04	13.6	6.51	9.89
0.50	27.7	37.0	9.30	31.7
1.00	49.1	54.7	5.63	52.5
1.50	49.6	56.0	6.44	53.5
2.00	50.8	55.27	4.93	53.5
2.50	49.9	55.3	5.39	53.2
3.00	50.7	56.2	5.45	53.3
3.50	49.7	55.8	6.04	53.4
4.00	49.0	54.6	5.59	52.8
4.50	4.66	8.37	3.71	6.24

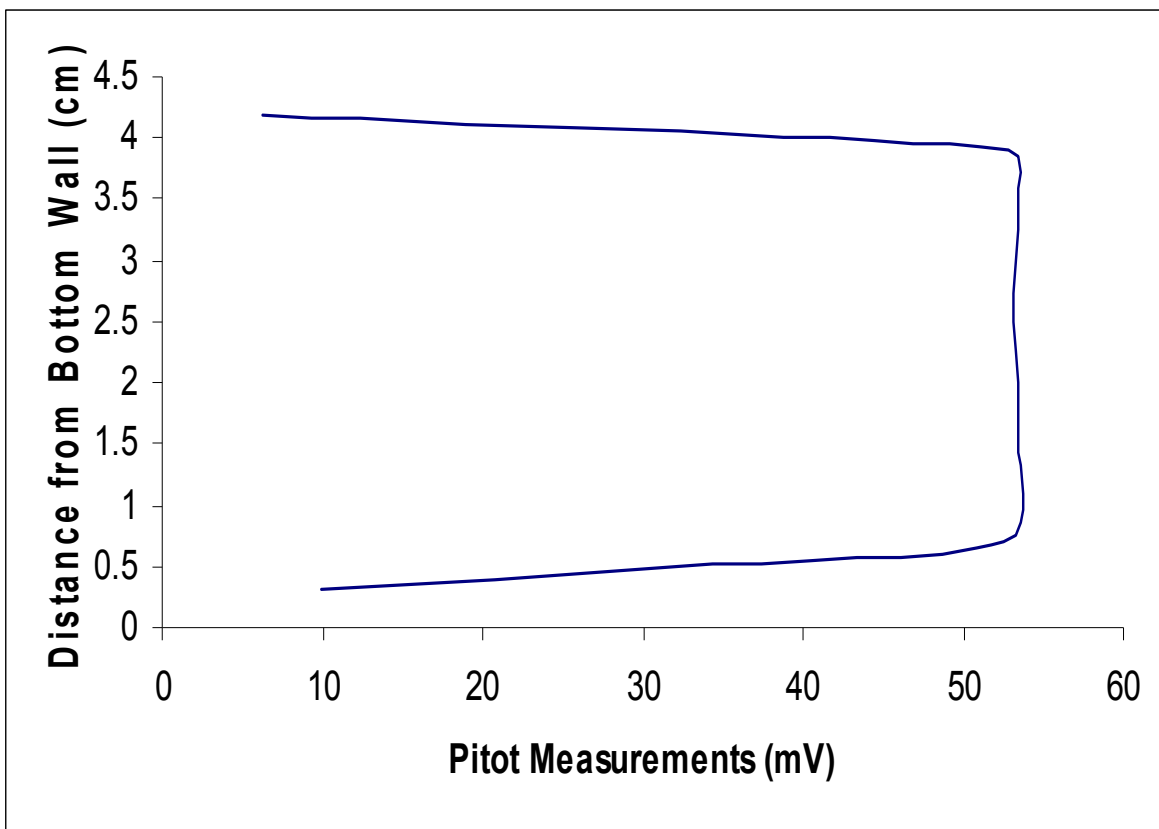


Figure 10.13 Plot of gas flow characteristics across the analyzer cross-section (bottom to top).

acquire data. Mass flow controllers (Sierra Instruments, Monterey, CA) calibrated for nitrogen at flow rates between 0-50.0 SLPM (standard liters per minute) were used to control gas flow into the system. Technical grade acetone (Mallinckrodt Chemicals, Phillipsburg, NJ) was used as test analyte.

As stated earlier, the bottom PC board had a total of 153 electrodes with the middle electrode set at zero potential or ground, and 76 electrodes on each side. The 76 electrodes on the right side of the ground towards the +V2 (see Figure 4.14) were connected to a positive power supply and the ones on the left to a negative power supply, -V4. The top board had 88 electrodes on the right side connected to the positive power supply, +V1, the 89th electrode connected to ground and the remaining 64 electrodes on the left connected to a negative power supply, -V3. The electrode connected to ground on the top plate was 0.500" off center. The electrodes that were connected to ground on both the top and bottom boards were positioned with respect to each other at an angle of 14° to the perpendicular cross-section, inclined to the left (see Figure 4.14).

Experimental Procedure. The voltages applied to the electrodes, fan voltages, discharge needle voltage, and the mass flow controller used to control the carrier gas flow rate were all controlled using Labview. Labview additionally was capable of recording data both in the static and scanning modes of operation. In the static mode, ion signal was measured and recorded as a DC current when the analyzer voltage and gas flow were set at constant values. In the scanning mode, the ion signal was recorded either as a function of changing voltage across the electrodes at constant gas flow, or as a function of changing gas flow velocity at constant potential across the electrodes. Plotting either of these data sets would produce a peak if ions were present and the system was operating as predicted.

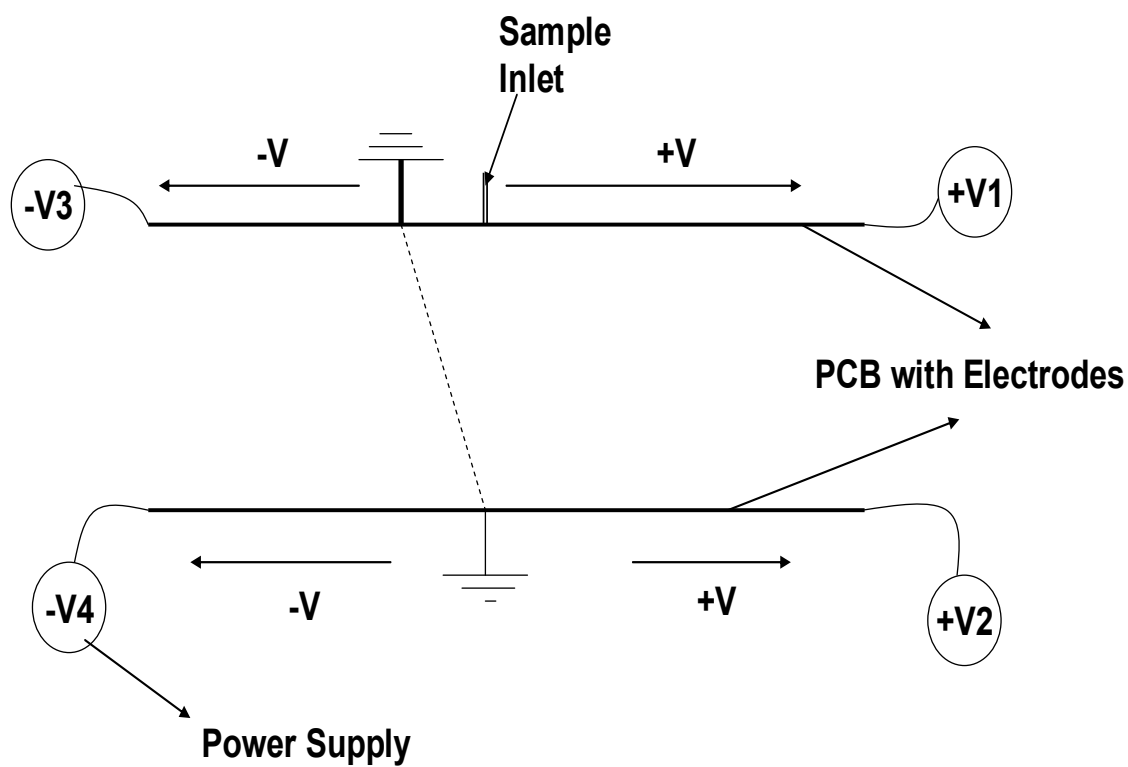


Figure 10.14 Electrical configuration of the analyzer region. The two fixed “ground” electrodes on the top and bottom plates are indicated.

Acetone (80.0 mL) was placed in a 100 mL bottle, leaving approximately 20.0 mL of headspace. The headspace was allowed to saturate with acetone vapor at room temperature [see Figure 4.4(B) for a schematic diagram of the system]. Nitrogen (carrier gas) flowing at 3 mL s^{-1} was then used to sweep the saturated vapor into the ionization chamber where a corona discharge (CD) needle was set at approximately 3000 V.

Table 4.5 lists the voltages used in this experiment. The potential differences across adjacent electrodes during a test were always the same. A different potential difference was used with each new run or test. By increasing the potential across the electrodes, the overall electric field in the analyzer was also increased. Table 4.5 lists the potential differences across electrodes and the voltages at the ends of the analyzer where the voltages were applied to the boards. With the discharge needle set at 3000 V and carrier gas (which carried the sample into the ionization area) flowing at approximately 3.00 mL s^{-1} , the electrode voltages were set at constant values and the fan voltage was scanned from 3.00-24.0 VDC at a rate of 0.840 V s^{-1} to produce a changing counter-flow gas velocity. Later, the fan voltage was set at 13.0 V to generate a constant gas velocity of approximately 6 m s^{-1} , while the electric field was scanned from 82.2 to 460 V cm^{-1} at a rate of $15.1 \text{ V cm}^{-1} \text{ s}^{-1}$. During these experiments, the detector response was monitored and recorded.

Results and Discussion. A schematic of the arrangement of the prototype CIMA used in this experiment is shown in Figure 4.6. Also shown are the directions of the electric field and gas flow, as well as the placement of the ion (sample) inlet and the detector. Figure 4.15 shows the detection of acetone ions obtained by setting the gas flow at 6 m s^{-1} and scanning the electric field from 82.2-460 V cm^{-1} . The centroid of the spectral peak is at 270 V cm^{-1} corresponding to a

Table 10.5 Voltages applied to the ends of the top and bottom plates of the prototype CIMA.

Potential ΔV Across Electrodes	Top Right Voltage (V) 88 Electrodes	Top Left Voltage (V) 64 Electrodes	Bottom Right Voltage (V) 76 Electrodes	Bottom Left Voltage (V) 76 Electrodes	Electric Field (V/cm^{-1})
10.0	880	-640	760	-760	82.2
20.0	1760	-1280	1520	-1520	164
30.0	2640	-1920	2280	-2280	247
40.0	3520	-2560	3040	-3040	329
50.0	4400	-3200	3800	-3800	411
56.0	4928	-3584	4256	-4256	460

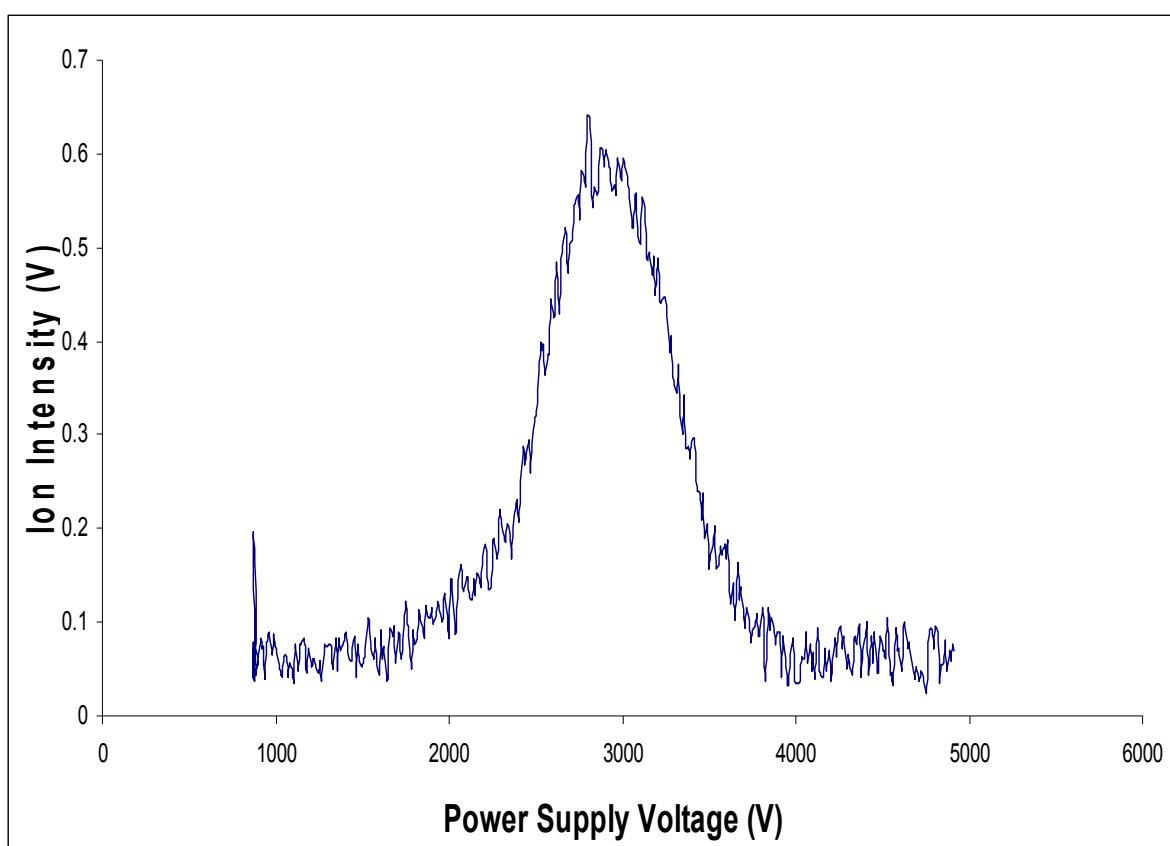


Figure 10.15 CIMA detection of acetone ions. The voltage across the analyzer was scanned while the gas flow was kept constant.

mobility constant of $2.22 \text{ cm}^2 \text{ V}^{-1} \text{ s}^{-1}$, which is close to $2.13 \text{ cm}^2 \text{ V}^{-1} \text{ s}^{-1}$ and $2.20 \text{ cm}^2 \text{ V}^{-1} \text{ s}^{-1}$ which others have measured and calculated, respectively, for acetone.^{8,9}

For Figure 4.16, the electric field was kept constant while the gas flow was increased from 1.00 m s^{-1} to about 11.0 m s^{-1} at a rate of 0.400 m s^{-2} . The different peaks represent measurements for different fixed potential differences across the electrodes. Increasing the potential difference across the electrodes (i.e., the total electric field) required a corresponding increase in the gas flow velocity to detect the ions (Figure 4.16).

While these initial results indicate that CIMA using a wind tunnel basically functioned, the ion peak widths were too broad to be useful without further improvement. One possible contribution to the broad peaks was that the electric field direction, strength and angle of inclination were not optimized. When the electric field was resolved into its horizontal and vertical components, the ratio of the horizontal to vertical fields was 4, which is too high. As discussed in Chapter 1, the ratio must be between 0.5-2 to achieve high resolution. The next section describes the modifications that were made to achieve this optimal electric field configuration.

Conclusions. The results presented above demonstrate that the wind tunnel CIMA approach, with its inclined electric field lines, should be feasible, and ions can be detected and their mobility constants determined using this system. Further efforts should be directed toward narrowing the spectral peaks in an attempt to improve the resolution which is necessary in order to achieve acceptable performance.

4.7 Optimization of the CIMA Analyzer Electric Field

Objectives. The objective of this work was to improve the wind tunnel CIMA resolution (i.e., narrow the spectral peaks). By increasing the inclination angle of the electric field, the ratio

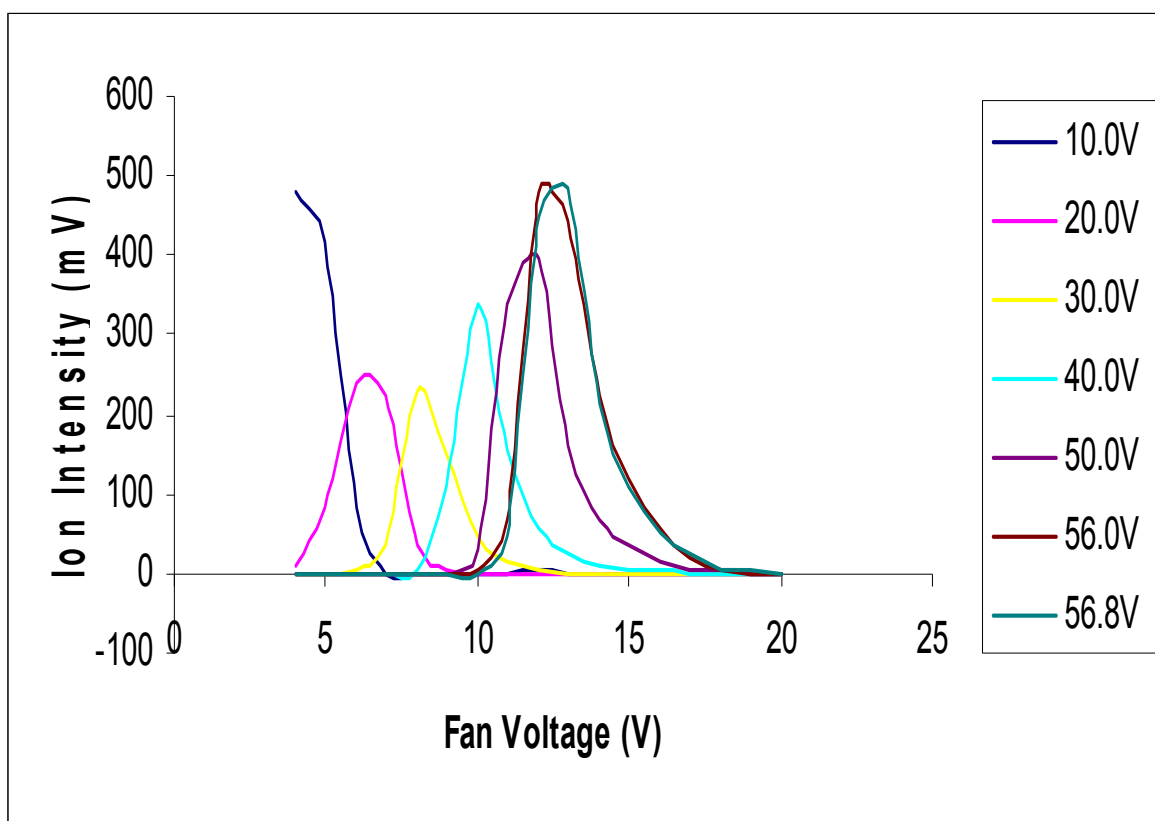


Figure 10.16 Ion intensity vs. fan voltage for detection of acetone ions. Peaks represent results obtained for increasing potential differences across electrodes. Higher electric fields require higher gas flows (i.e., the acetone ion peak shifts to the right as the potential difference is increased).

between the horizontal and vertical components of the inclined field were adjusted to fall between 0.5-2. The electric field in the vertical direction, which is used to transport ions from the point of injection to the detector, was increased so that ions would travel faster to the detector.

Experimental Procedure. The same materials and instrumentation were used for these experiments as described in the preceding section, except the position of the “ground common” on the top plate was moved by half inch intervals toward the negative power supply, -V3, as shown in Figure 4.17. The “ground common” position was moved by either increasing the voltage on the transformer or by increasing the voltage of the power supply, +V1, and decreasing the voltage of the power supply, -V3, by the same amount.

The operating procedures were the same as described above. The sample was acetone with a nitrogen carrier gas at the same flow rate. The ionization source was set at 3000 V and the voltage on the fans was scanned from 3.0 V to 22.0 V.

In this particular set of experiments, the transformer was not used. The power supplies were calibrated to provide 0 V at the locations marked A, C, D, E, F, G, H, I, J, and K in Figure 4.17 (these positions were exactly half an inch from each other) when the potential differences between the electrodes were 10, 20, 30, 40 and 50 V for different sets of experiments. These values are listed in Table 4.6.

With the potential difference set at the values stated above, measurements were recorded for every position as the “ground common” was moved to the left (Figure 4.16). Eight readings, corresponding to the eight different “ground common” positions were taken for potential difference of 20 and 30 V, respectively. Five and four readings were taken for the 40 and 50 V potential differences, respectively; less than eight readings were taken because the power supplies reached their maximum voltage outputs at 5000 V.

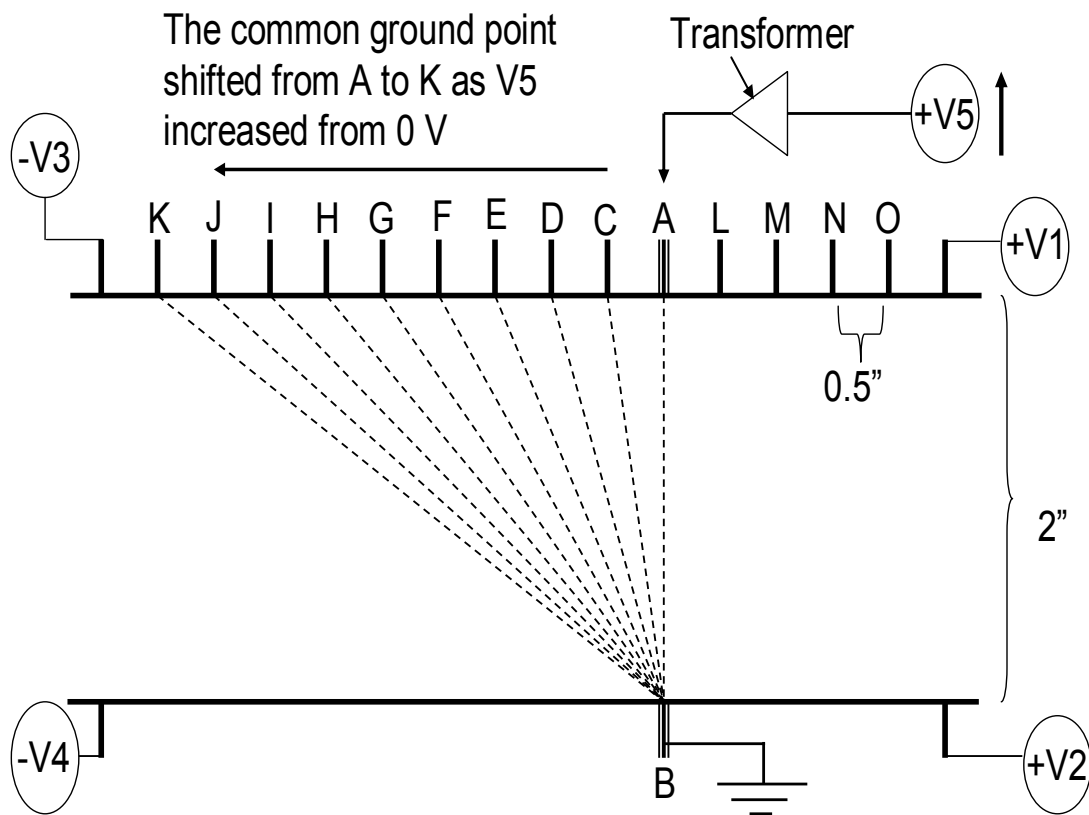


Figure 10.17 Schematic of the modified electrical configuration of the CIMA analyzer region. V1 to V5 are power supplies, where V5 was connected to the transformer and used to create the inclined electric field by increasing its voltage. This increase in voltage caused the position of “ground common” to move to the left as indicated.

Table 10.6 Electrode voltage and resultant potential difference across adjacent electrodes in the optimized wind tunnel CIMA.

		Calibrated Voltages from Power Supplies on Top Plate (V)								
Potential (ΔV) Across Electrodes		A Com. Grd.	C 0.500"	D 1.00"	E 1.50"	F 2.00"	G 2.50"	H 3.00"	I 3.50"	J 4.00"
10	V1 (+)	410	520	640	740	870	980	1090	1190	1280
	V3 (-)	-1030	-920	-800	-680	-550	-440	-330	-230	-140
20	V1 (+)	820	1050	1280	1520	1720	1950	2160	2350	2530
	V3 (-)	-2060	-1830	-1600	-1360	-1090	-860	-650	-460	-280
30	V1 (+)	1230	1575	1920	2290	2650	3190	3560	3815	4105
	V3 (-)	-3090	-2745	-2400	-2030	-1670	-1130	-740	-455	-260
40	V1 (+)	1640	2090	2570	3270	4130	4620			
	V3 (-)	-4120	-3670	-3190	-2490	-1630	-1140			
50	V1 (+)		2625	3475	4175	4950				
	V3 (-)		-4575	-3725	-2425	-1620				

Results and Discussion. Figure 4.18 shows the changing ratios of the horizontal electric field to the vertical field as the position of the “ground common” was moved every half inch toward the $-V_3$ power supply of Figure 4.17. Corresponding ion mobility spectra are shown in Figures 4.19 to 4.22. These figures also indicate the resolution that was calculated for each peak using the single peak measurement method calculated using the fan voltage

$$R = \frac{V}{\Delta V} \quad (4.2)$$

V is the voltage at the centroid of the peak and ΔV is the voltage difference at half peak height. The data reported here do not show a clear trend; however, there seems to be an increase in the R values as the voltage across the electrodes are increased (from 20 V to 50 V) with a corresponding decrease in the ratio of the horizontal electric field to the vertical electric field from 2 to 0.5. Although the literature suggests^{10, 11} that an increased resolution would result as the ratio of the horizontal to vertical electric fields is decreased from 2 to 0.5, the results obtained show a slight increase. Unfortunately, because of the limited data that were obtained (due to the limit in the power supply maximum voltage), establishing a reliable trend was not possible at this time.

An obvious trend observed was that as the potential difference between the electrodes increased (and by implication the electric field), the resolution also increased, as shown in Figure 4.23. The reason for an increase in resolution as the angle of inclination increased is that the vertical component of the electric field increased with it. The vertical electric field component is what drives the ions to the detector. A stronger vertical field means a higher ion drift velocity and, therefore, less time for diffusion to occur.

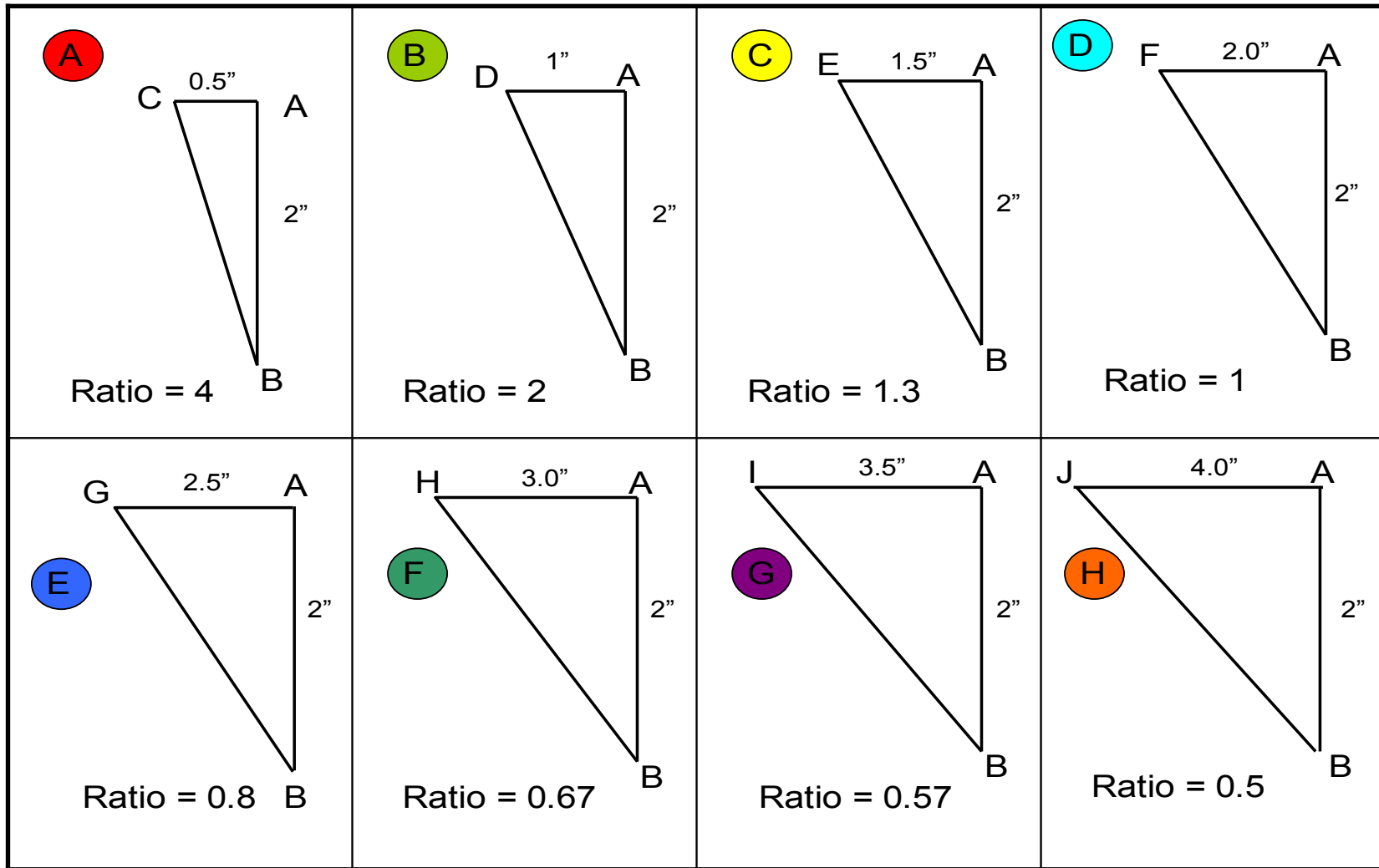


Figure 10.18 Visual representation of the change in ratio of horizontal field to vertical field from 4 to 0.5 as the "ground common" position is moved from position "C" to "J".

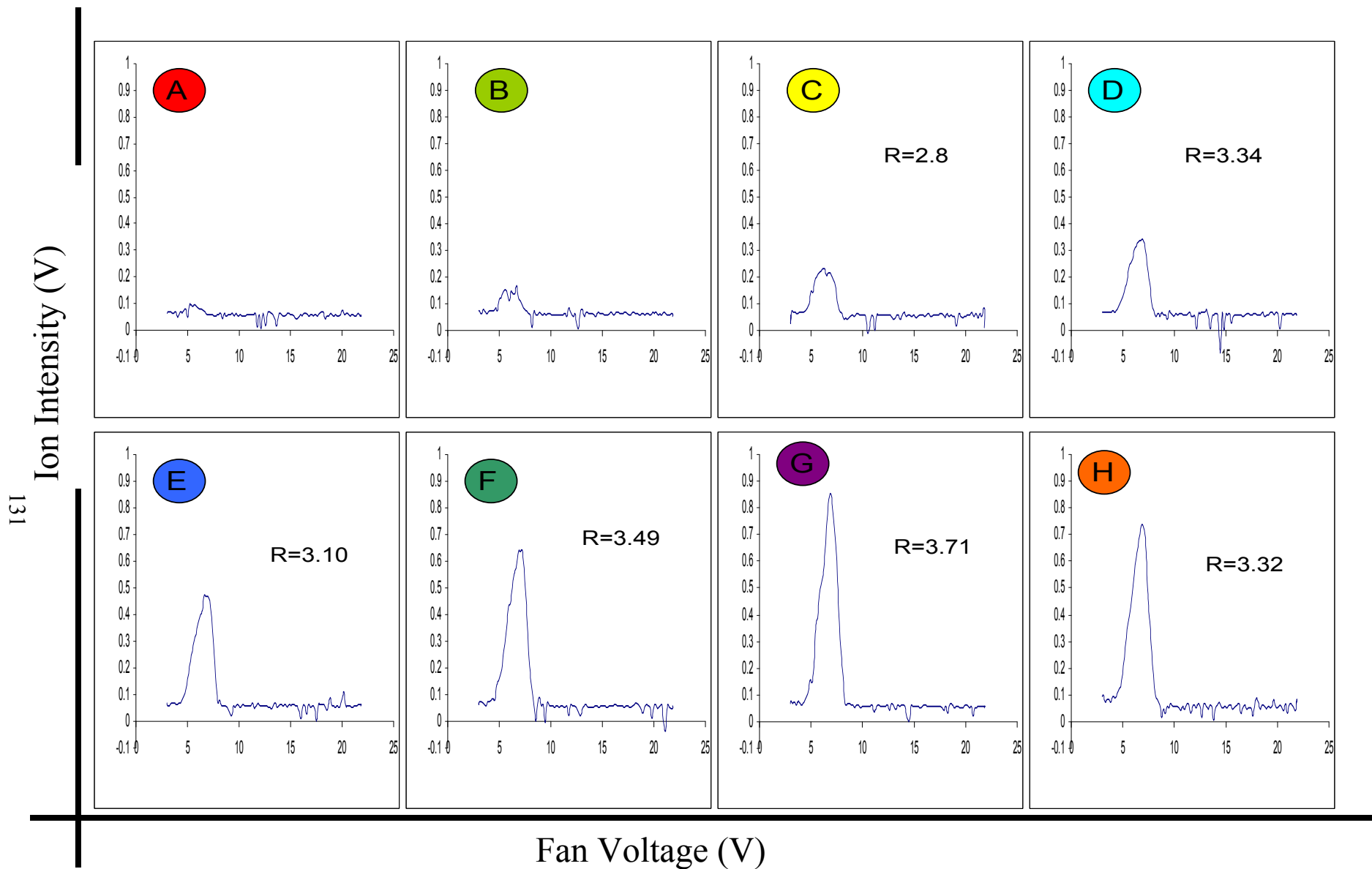


Figure 10.19 Ion mobility spectra for 20 V potential difference across electrodes for electric field configurations depicted in Figure 4.18. Resolution values for (A) and (B) were not determined because the peaks were too small

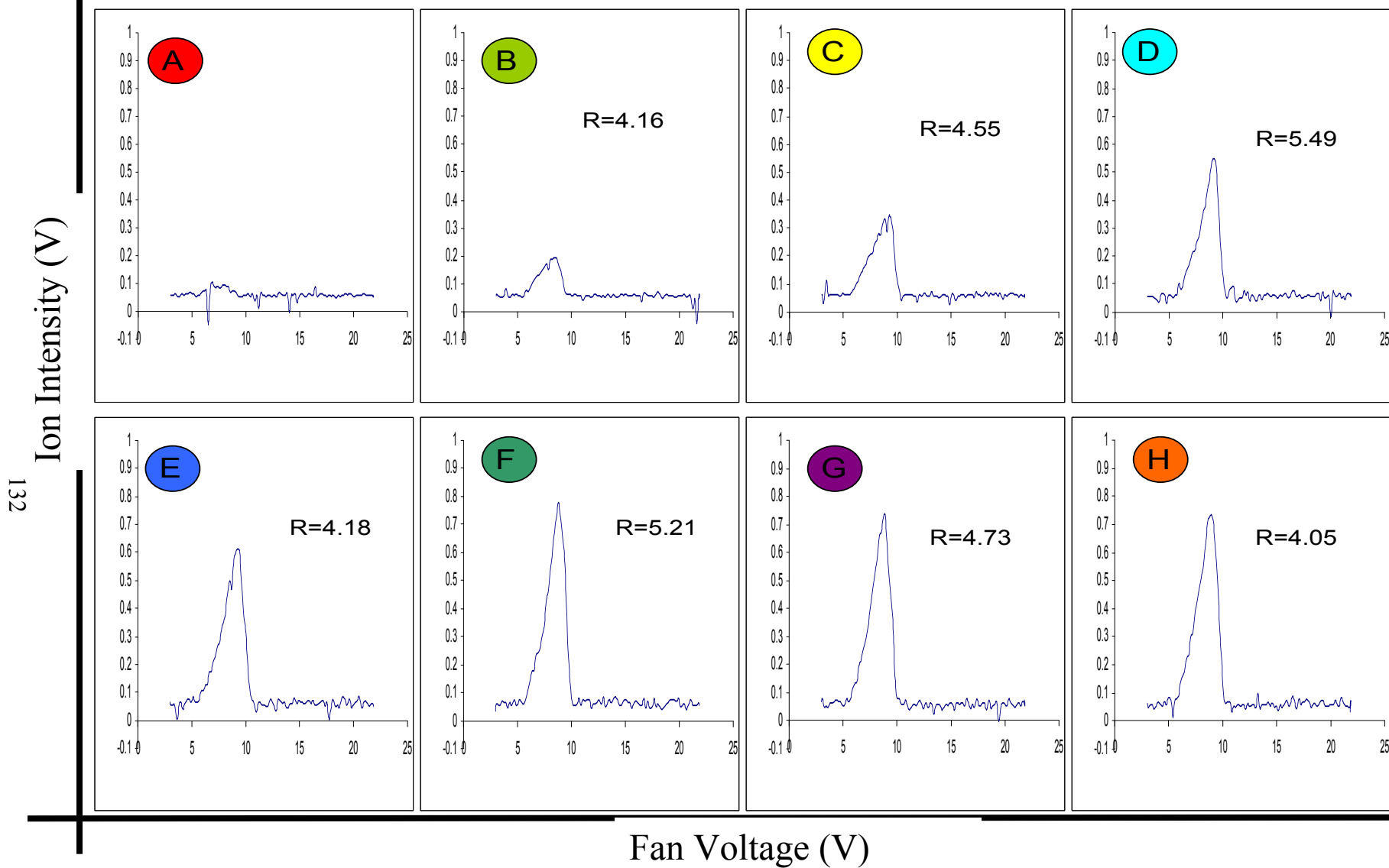


Figure 10.20 Ion mobility spectra for 30 V potential difference across electrodes for electric field configurations depicted in Figure 4.18. The resolution value for (A) was not determined because the peak was too small.

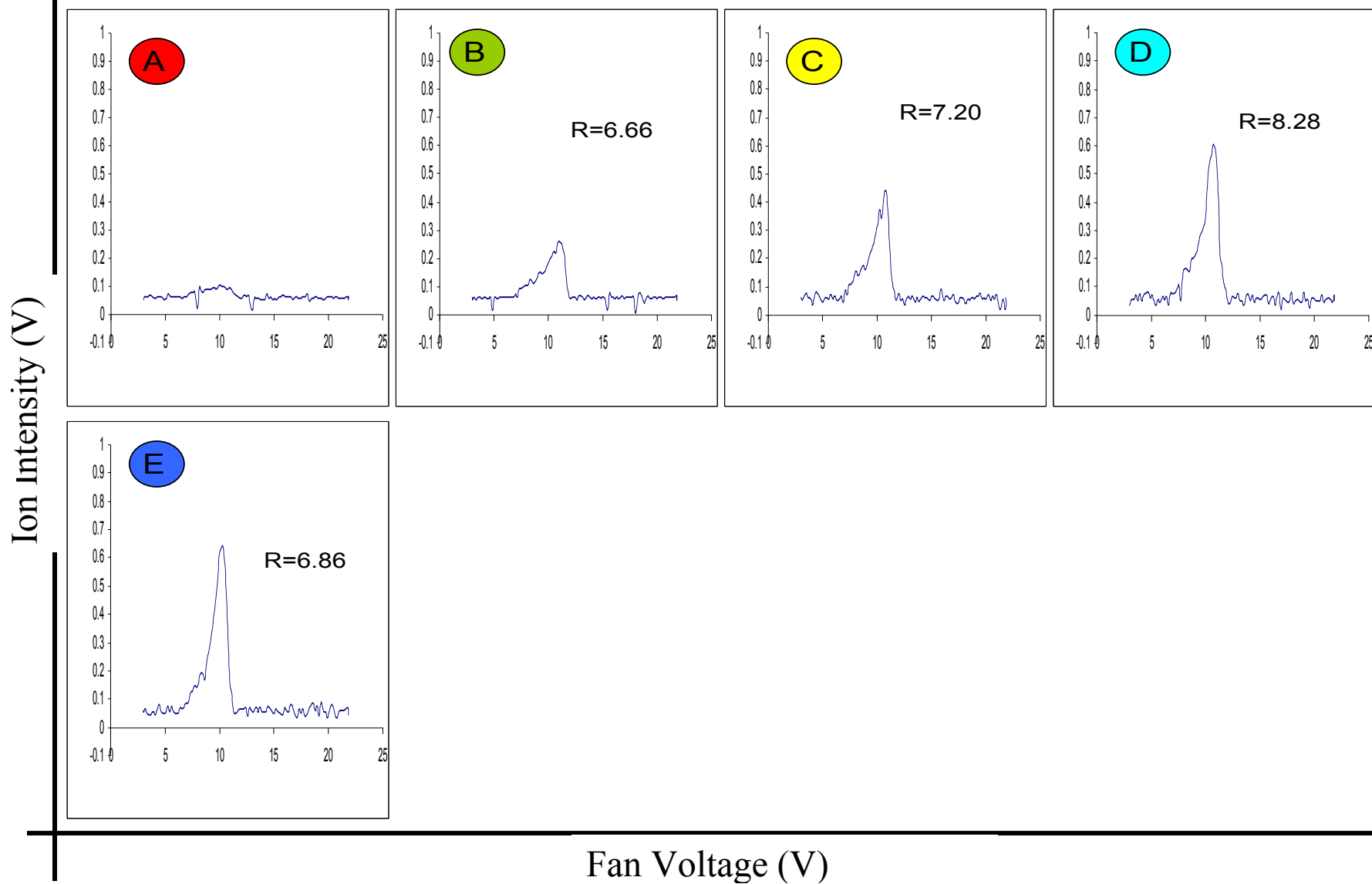


Figure 10.21 Ion mobility spectra for 40 V potential difference across electrodes for electric field configurations depicted in Figure 4.18. The resolution value for (A) was not determined because the peak was too small.

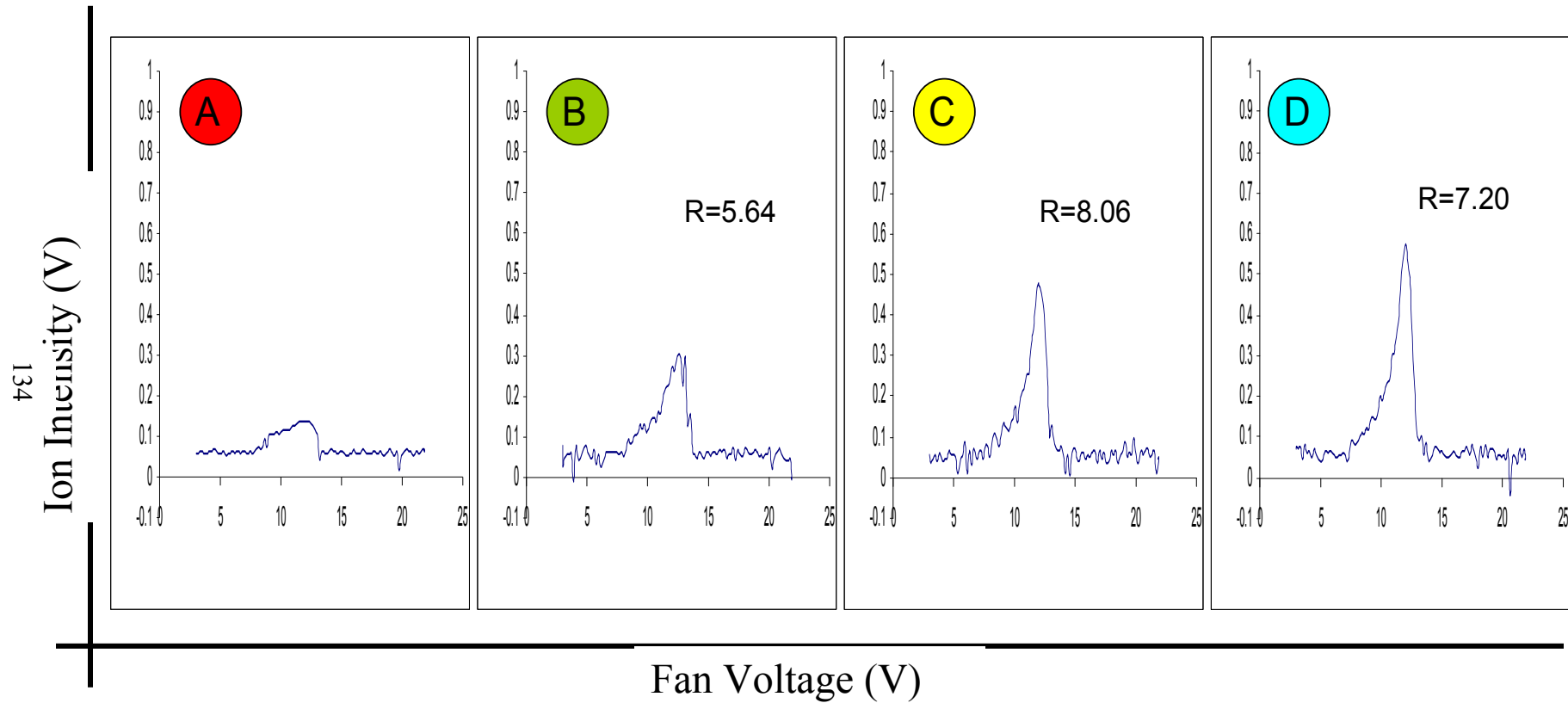


Figure 10.22 Ion mobility spectra for 50 V potential difference across electrodes for electric field configurations depicted in Figure 4.18. The resolution value for (A) was not determined because the peak was too small.

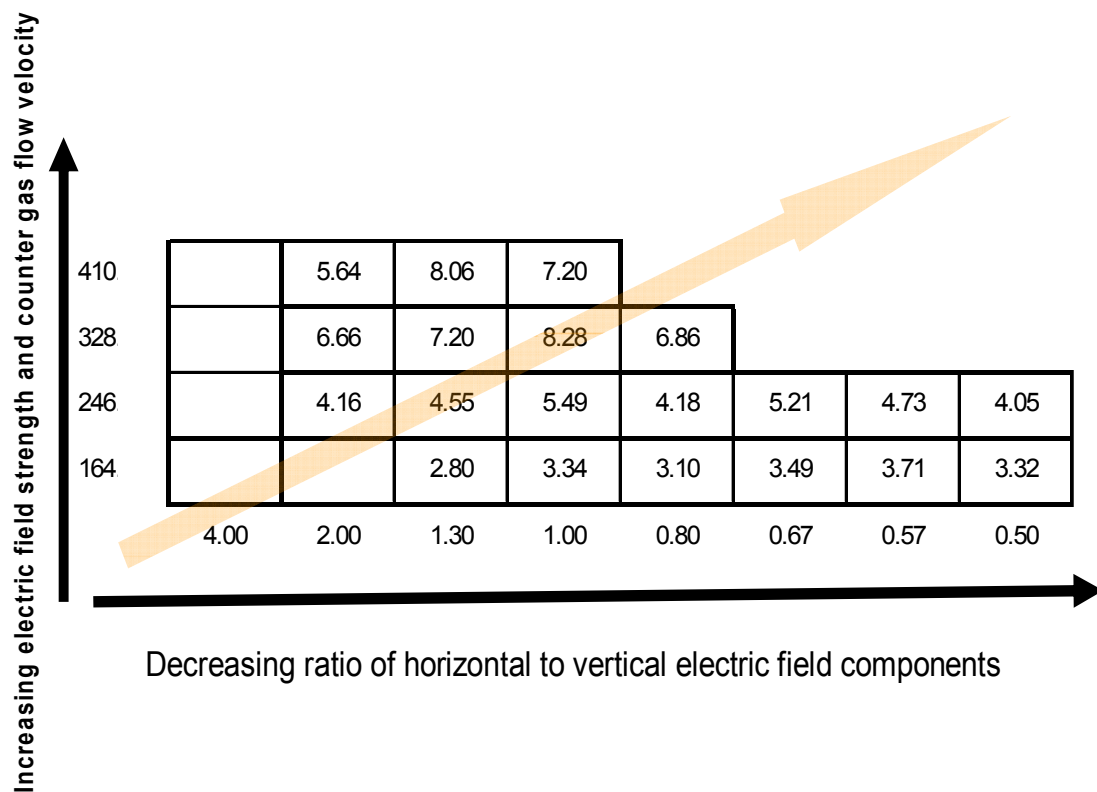


Figure 10.23 Graph showing the trend toward increasing resolution as the electric field and counter gas flow increased with decreasing ratio of horizontal to vertical electrical field.

The results from the simulation work discussed in Chapter 2 show that conditions for high resolution require a field strength of about 3000 V cm^{-1} and a counter-flow gas velocity of approximately 10 m s^{-1} —much higher than the achieved field strengths of 159 to 325 V cm^{-1} and counter gas flow velocities of 2.47 to 6.83 m s^{-1} . The gas flow will always be limited by the electric field, suggesting that the principal requirement for high resolution is high electric field strength.

The high resolution that is potentially achievable in CIMA requires high electric field strength. This high field strength would generate high ion velocity, which would reduce the time available for diffusion. High electric field and high gas flow would also aid resolution by filtering away ions with mobility constants close to those of the ions of interest. In traditional IMS, separating ions of interest from others with similar mobilities is difficult, and a single broad peak often appears. The CIMA process narrows the different ion bands (see Figure 4.24)

Conclusion. When the wind tunnel CIMA was operated with an electric field horizontal-to-vertical component ratio between 2 to 0.5, the resolution of the spectral peaks moderately increased. Resolution should increase with an increase in electric field and a concomitant increase in counter-gas flow velocity.

4.8 Effects of Different Counter Flow Gases and Test Samples

Objectives. The effect of using helium gas as the counter-flow gas on CIMA performance for the various test compounds listed below was evaluated.

Materials and Samples. The same instrumentation and experimental setup were used as previously described except that helium was used as the counter-flow gas. The organic test compounds used included trichloroethane (Fisher Scientific, Fair Lawn, NJ), toluene

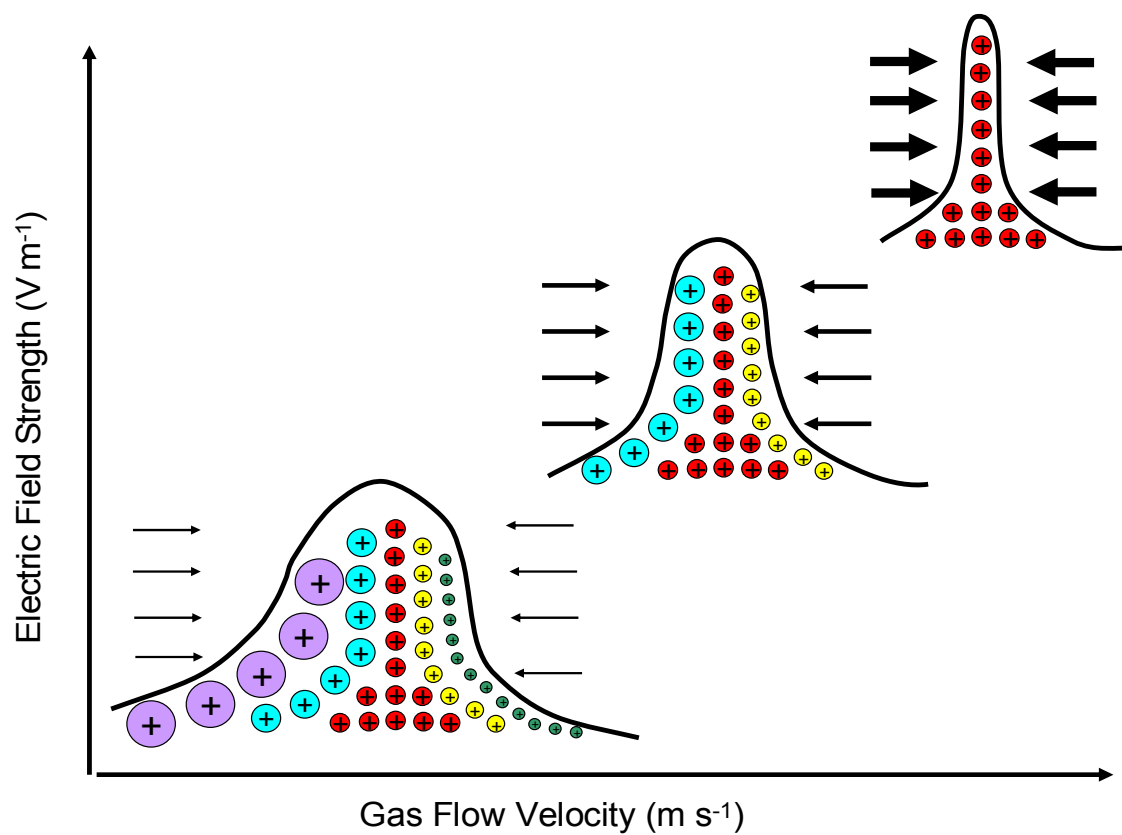


Figure 10.24 Representation of the effect of electric field and counter-gas flow on spectral peak width and ion volume. As values of the electric field strength and gas flow velocity increase, the ion volume shrinks, leading to narrower peak width and higher resolution.

(Mallinckrodt Baker, Paris, KY), ethylbenzene (Fisher Scientific, Fair Lawn, NJ), pyridine (Aldrich Chemical, Milwaukee, WI), chlorobenzene (Mallinckrodt), ethylene chloride (Fisher Scientific), and benzyl alcohol (Fisher Scientific).

Experimental Procedure. The experimental procedure was identical to that used previously. Samples (80 mL) of chlorobenzene, ethylene chloride, and benzyl alcohol were each introduced into 100 mL bottles for testing. In addition, a mixed sample containing 20 mL each of trichloroethane, toluene, and ethylbenzene was prepared. Furthermore, an even more complex test sample was prepared by adding 20 mL each of pyridine, chlorobenzene, trichloroethane, toluene, and ethylbenzene in a 200 mL bottle.

Results and Discussion. Figures 4.25 to 4.29 show the results obtained from these experiments. Use of nitrogen as counter-flow gas produced only one peak, regardless of the number of analytes present in the sample; however, there is a subtle difference in the position of the centroid of the peak (Figures 4.19 to 4.22 and Figure 4.30). Figure 4.30 is used to generalize the shape of the peak recorded, not to represent the spectrum of each and every situation. In contrast, the use of helium as counter-flow gas produced separation (Figures 4.25 to 4.29) since multiple peaks were recorded by the detector. The peak that appeared at a fan voltage of approximately 12 volts appears to be due to reactant ions (RIP) that were formed during the process of ionization. When nitrogen was used as the counter-flow gas, the RIP peak seemed to mask the peaks of the sample ions because it appeared around 5 V (the actual voltage differed depending on the sample). Figure 4.30 shows the appearance of the peak for a specific sample tested.

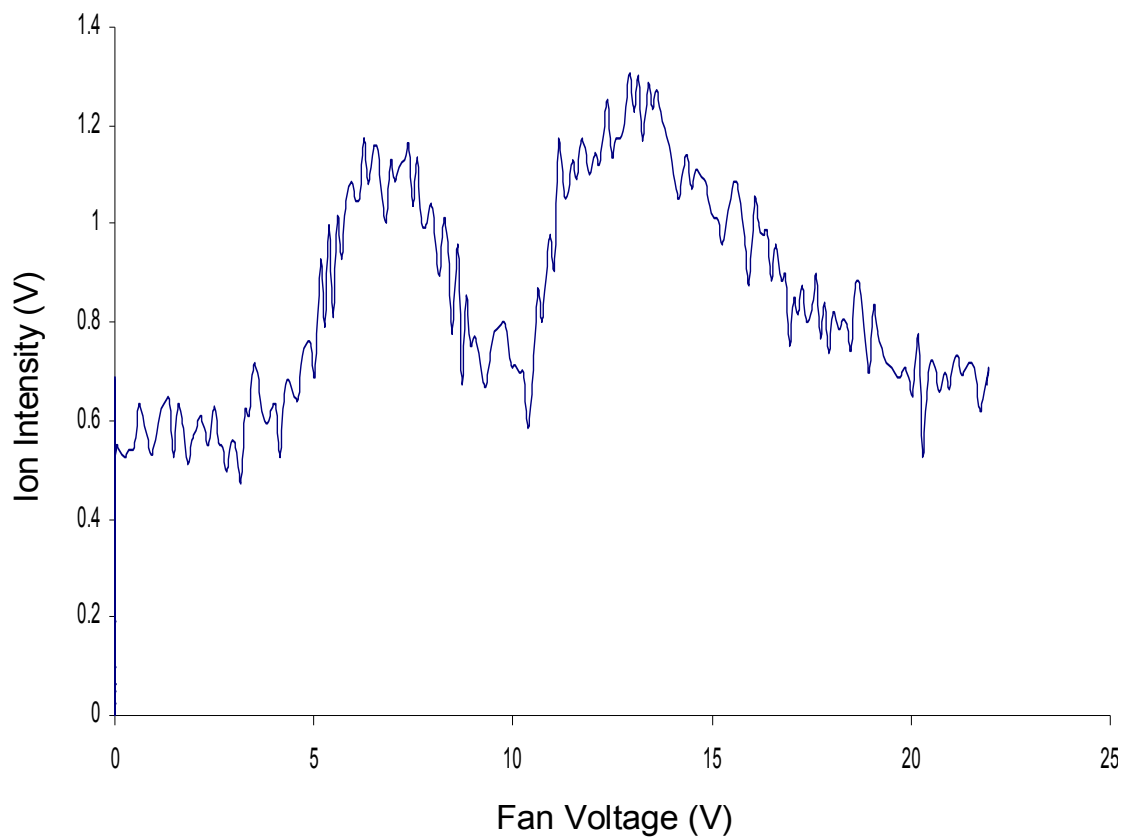


Figure 10.25 Spectrum of benzyl alcohol obtained using nitrogen as carrier gas and helium as counter-flow gas.

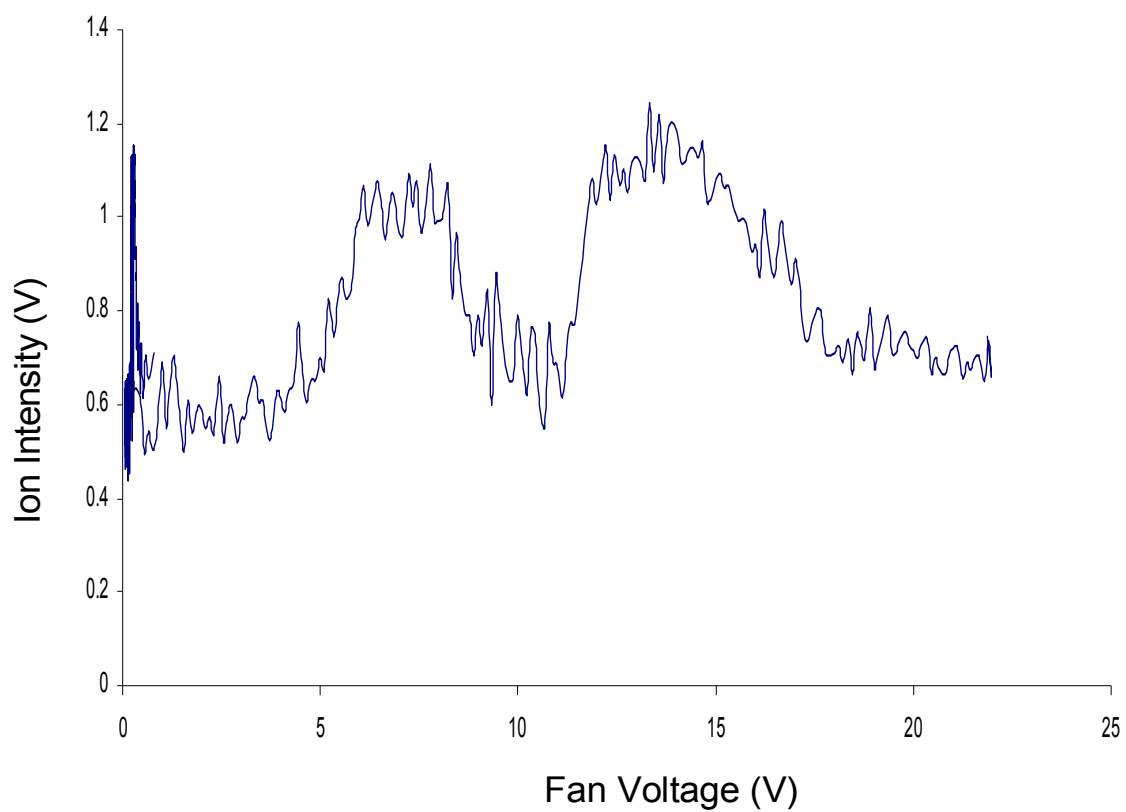


Figure 10.26 Spectrum of methylene chloride obtained using nitrogen as carrier gas and helium as counter-flow gas.

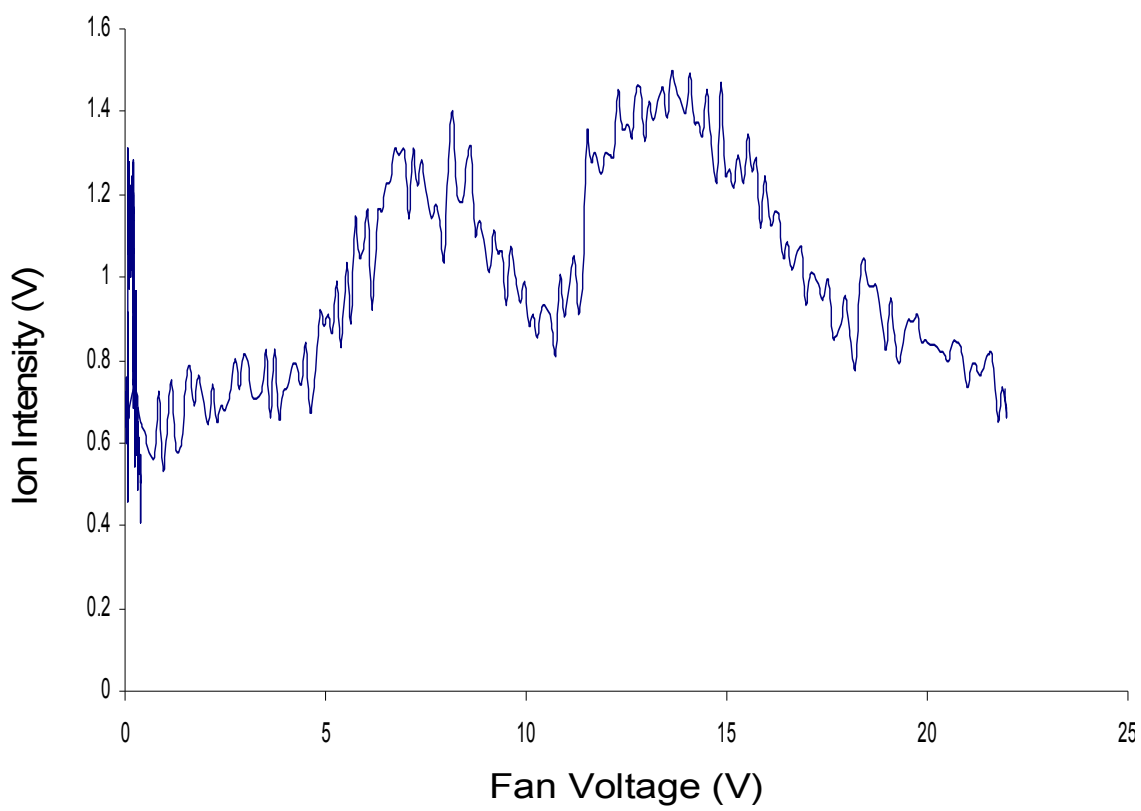


Figure 10.27 Spectrum of chlorobenzene obtained using nitrogen as the carrier gas and helium as counter-flow gas.

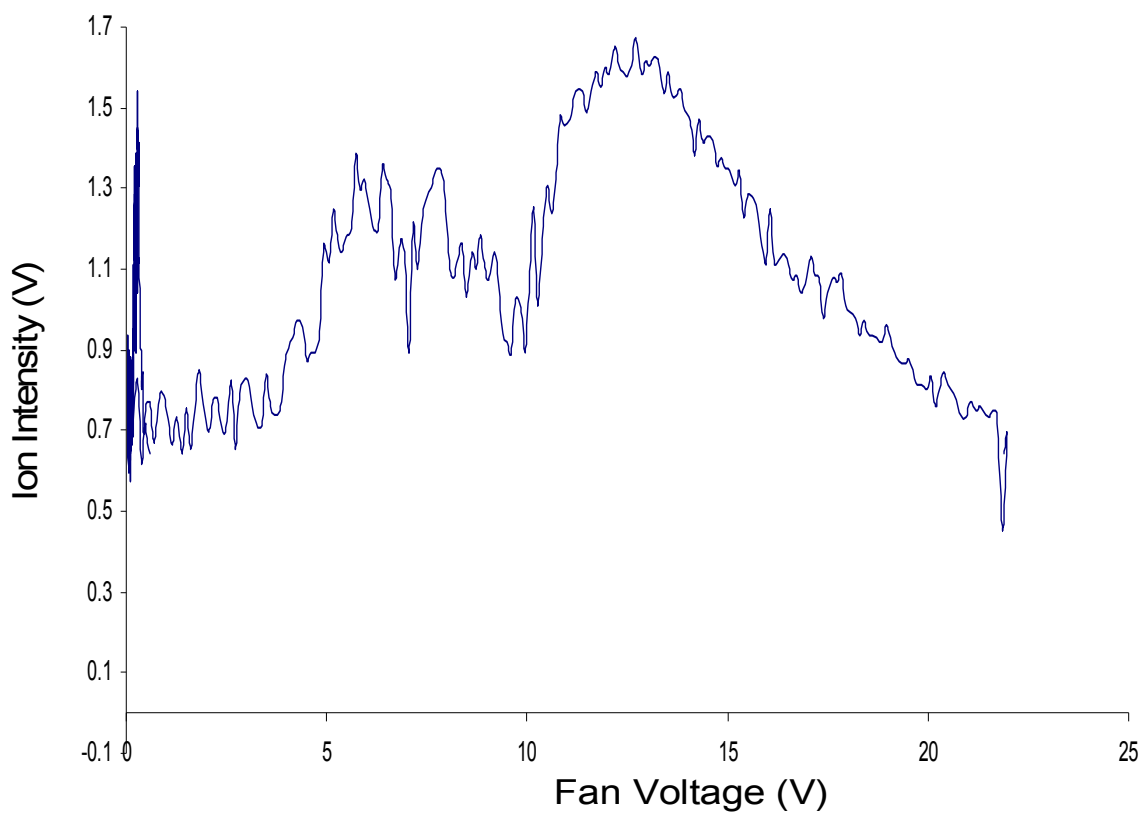


Figure 10.28 Spectrum of trichloroethane, toluene and ethylbenzene using nitrogen as carrier gas and helium as counter-flow gas.

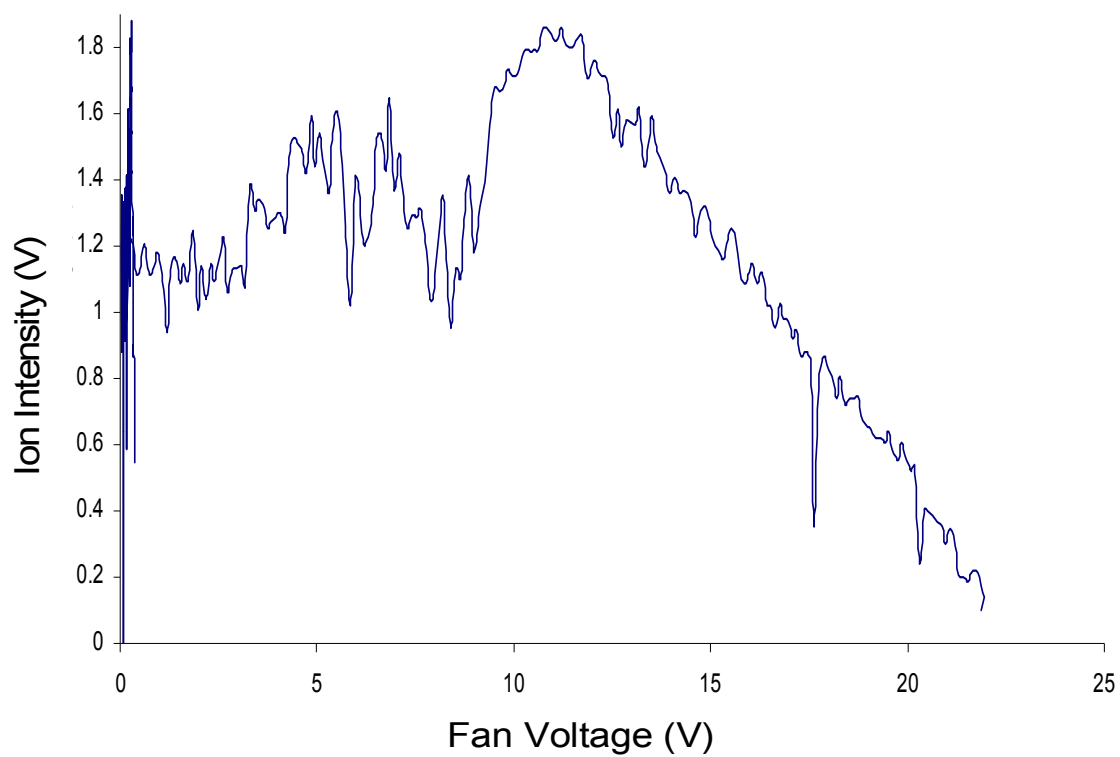


Figure 10.29 Spectrum of trichloroethane, toluene, pyridine, ethylbenzene and chlorobenzene obtained using nitrogen as carrier gas and helium as counter-flow gas.

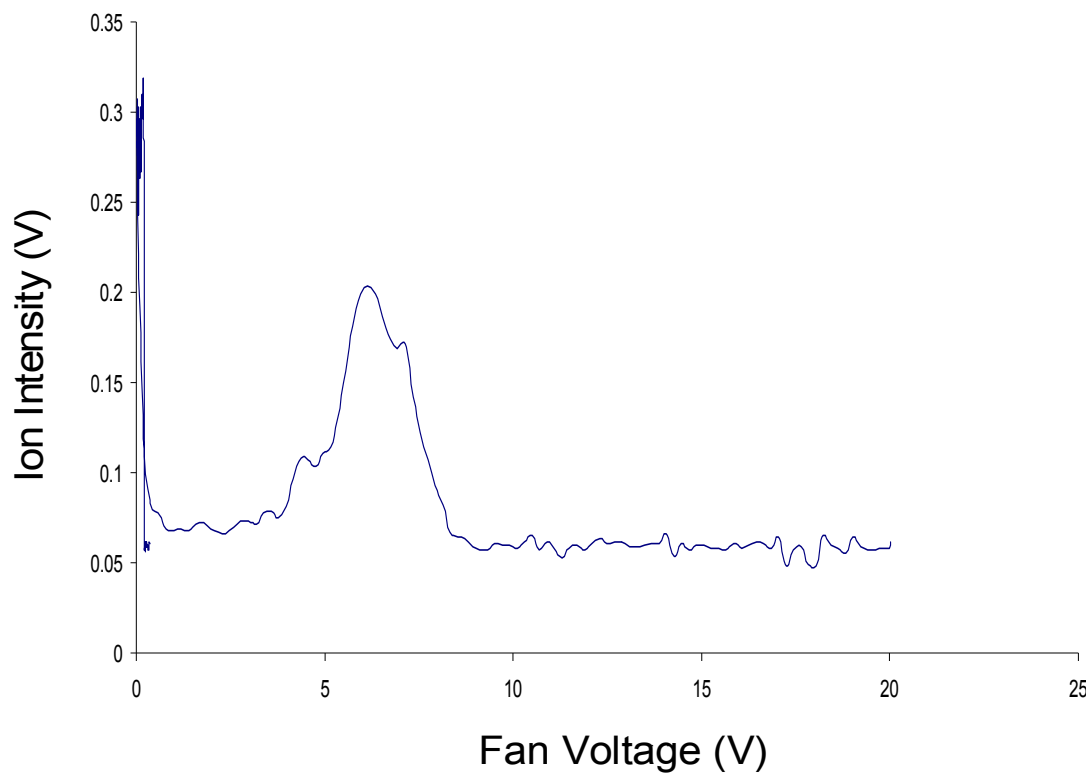


Figure 10.30 Example of the peak that appeared when any of the test samples, either singly or in a mixture, was used in the presence of nitrogen as the counter flow gas.

When helium was used as the counter-flow gas, chlorobenzene, trichloroethane, benzyl alcohol, pyridine, ethylene chloride, ethylbenzene, and toluene were detected when the fan voltage was between 7 to 8 V. After that, the RIP peak dominated. Higher (or stronger) electric field strength and gas flow rate helps to expand the separation window, and allowed other ions to be detected and resolved. In Figures 4.28 and 4.29, it appears as if all ions in the sample mixture were stacked in a small separation window. Methods to reduce the high concentration of reactant ions should be explored. The reason that helium allowed the compounds above to be detected as separate peaks and nitrogen did not is not fully understood. The test compound ions were able to move faster because of the lower flow resistance from helium compared to nitrogen. This might also explain why acetone was not detected as a separate peak when helium was used.

Conclusions. These experiments indicate partial separation of test analyte mixtures, although much additional work is needed to fully understand the results.

4.9 Simulation of CIMA Performance Using Actual Experimental Parameters

Objectives. In an effort to better understand the CIMA instrument performance, a numerical analysis was performed using actual experimental conditions to compare with the optimum performance modeled in Chapter 2. This modeling provides a comparison between ideal conditions and actual experimental conditions, and should provide ideas to improve the experimental design.

Numerical Experimental Procedure. The numerical analysis procedure used was the same as that described in Chapter 2. This time, however, the input parameters were changed to actual experimental parameters used (see Table 4.7).

Results and Discussion. The original simulation input parameters were very different from what was achievable with the present CIMA system. The most obvious difference was the

Table 10.7 Input parameters used in the modeling to simulate the actual experimental conditions.

Parameters	Numerical Modeling	Experimental Conditions Modeled
Length of analyzer	10 cm	5.08 cm
Counter-gas flow velocity	10 m s ⁻¹	5 m s ⁻¹
Electric field	3333 V cm ⁻¹	187 V cm ⁻¹
Analysis time	1 s	20 s
Test samples used with their reduced mobility constants	Methylamine	2.65 cm ² V ⁻¹ s ⁻¹
	Ethylamine	2.36 cm ² V ⁻¹ s ⁻¹
	Formamide	2.45 cm ² V ⁻¹ s ⁻¹
	Dimethylamine	2.46 cm ² V ⁻¹ s ⁻¹
	Isopropylamine	2.20 cm ² V ⁻¹ s ⁻¹

electric field strength. As discussed earlier, the present design was limited to lower electric field strength than desired. To use an electric field strength near that used in the simulation, a smaller instrument would have to be built. The size of the present design was determined by three factors. First, the analyzer region was designed to minimize wall effects, hence, the 2:1 ratio discussed earlier. Second, although 10 kV power supply was desired, it would have required more than a 3 month waiting period to receive this power supply after ordering, so we decided to use a power supply that was available in the laboratory that had a 5 kV output. The third factor was related to the previous two factors. The design of the analyzer unit at that time was a “vectorial” electrode design. This design made use of 12 electrodes that were 0.250” wide and 4.00” long, with 2 other electrodes that were 0.500” wide. Of the 12 electrodes, 6 were placed on the top wall or plate and the other 6 were placed at the bottom, while the 0.500” electrodes were placed near the end of the analyzer region and were called the end electrodes (see Figure 4.31). The 6 upper and bottom electrodes were further separated into two sets of 3, which were 3.00” apart. Within the sets of 3, the electrodes were further separated 0.500” apart. As indicated in Figure 4.31, the four electrodes in the middle of the analyzer were the “defining” electrodes that defined the area where analysis and separation would take place (“defining” electrodes). The other two “vectorial” electrodes and the “end” electrodes (also called “compensating” electrodes) were used to straighten the electric field lines in the analyzer region. The spacing of the electrodes was dictated by the maximum output of the available power supply. All electrodes on one half were positive and electrodes on the other half were negative. By changing the values of the top and bottom electrodes proportionally, applying lower voltages on the lower electrodes compared to the upper electrodes, and then fine-tuning the end electrodes to straighten the field lines, an inclined electric field was expected.

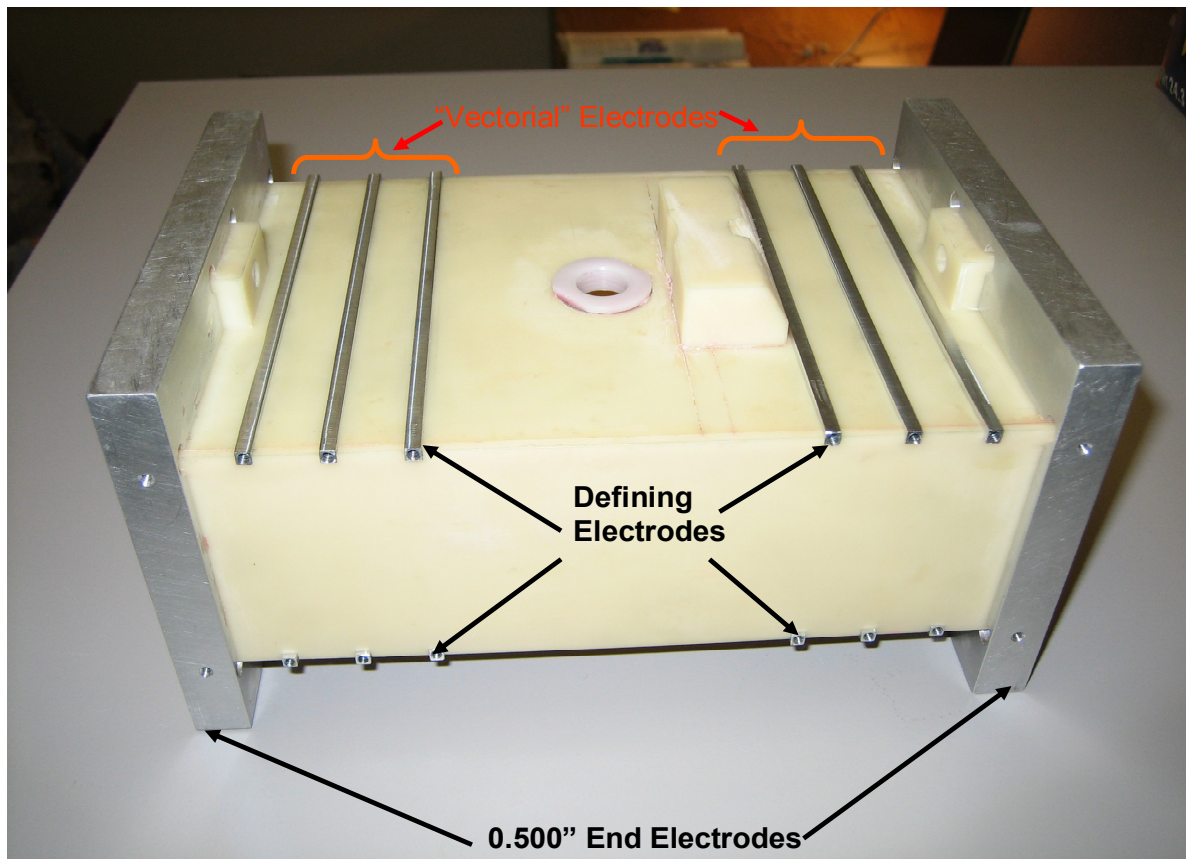


Figure 10.31 Photograph of the "original" analyzer region design showing the vectorial electrodes and compensating end electrodes.

The “vectorial” electrode design, unfortunately, was unable to produce the desired inclined electric field. When the design was tested, ions could not be detected. Electric field modeling using Comsol revealed that the electric field lines were horizontal instead of on an incline, clarifying why ions could not reach the detector (see Figure 4.32). Further analysis indicated that the end compensating electrodes dominated the vectorial electrodes, which led to a horizontal field.

The analysis time was another parameter for which the original simulation and actual experiment were very different. Even though our CIMA analyzer length (i.e., distance from ion injection to detection) was shorter than the hypothetical one used in the original simulation, the analysis time was 20 times longer. As stated before, shorter analysis times were not possible with the present instrument because the field strength was too low.

Figure 4.33 compares side-by-side the construction of the actual wind tunnel CIMA and the hypothetical CIMA used in the simulation presented in Chapter 2. In the modeled design, perforated walls were used to introduce the counter-flow gas and define the analyzer region. However, in the actual wind tunnel CIMA, no such walls existed. The analyzer region was defined purely by the electric field. In the modeled system, the ions moved from front to back along the analyzer in the z-axis direction, while in the wind tunnel CIMA, they moved from top to bottom along the y-axis. Figures 4.34-4.36 give a side-by-side comparison of the modeling results for (A) the original, ideal simulation and (B) the actual experimental set-up and parameters. The only similarity between the results is the narrow peaks in both spectra.

The modeling results of the ion transport process in the analyzer are given in Figure 4.34. The figure shows the initial sample concentration distribution at time $t = 0$, and how the concentration changes as it travels along the analyzer length. While (A) shows that the sample

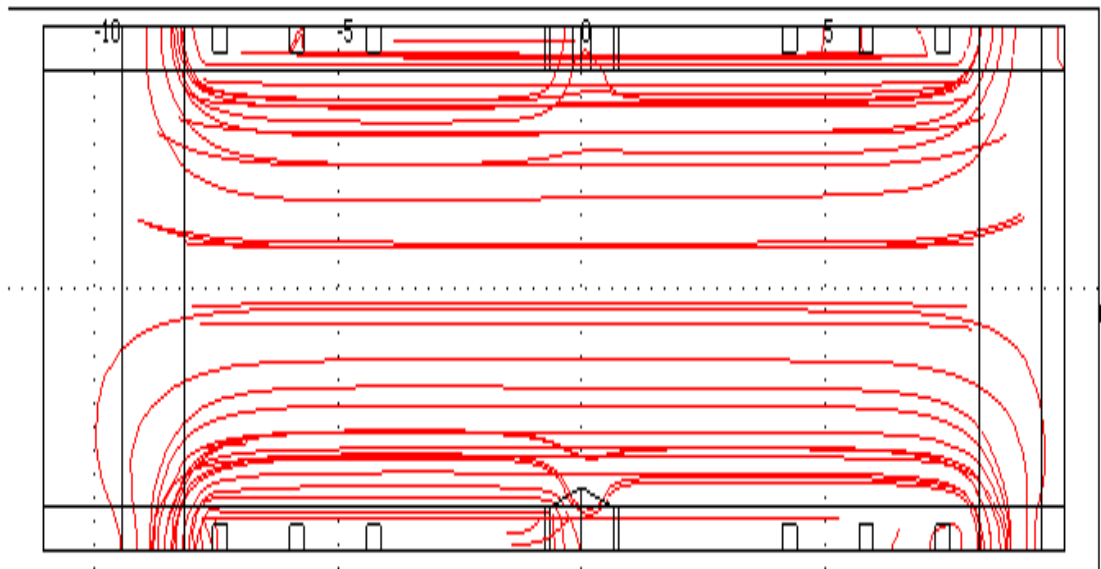


Figure 10.32 Electric field lines generated by the vectorial electrodes. Unexpectedly, the field lines were horizontal instead of inclined.

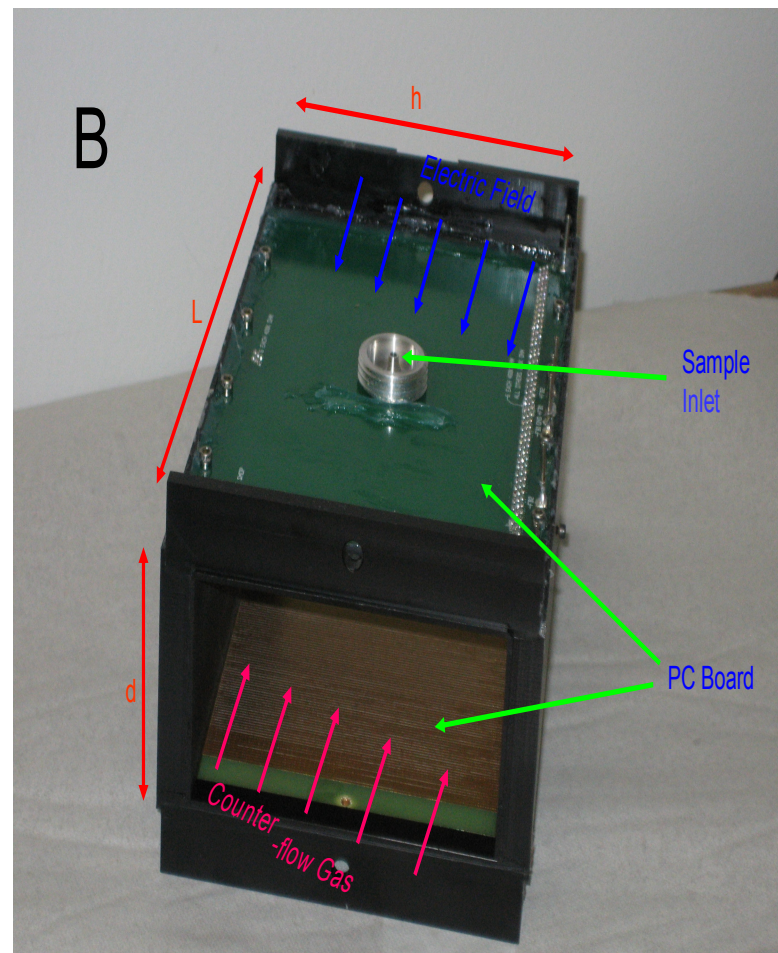
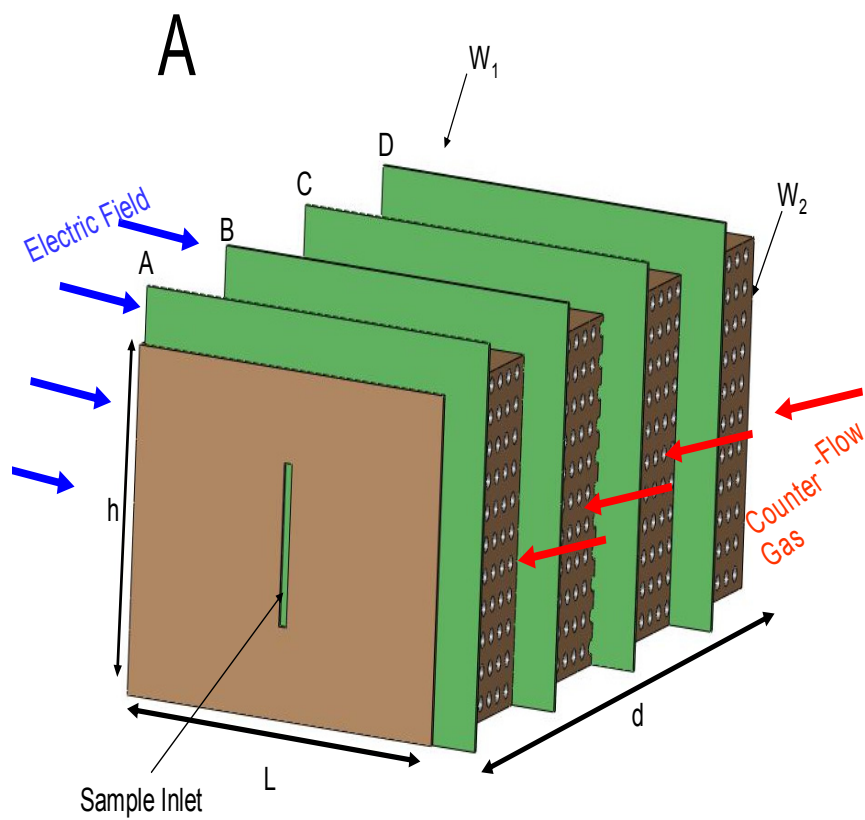


Figure 10.33 (A) Drawing of the hypothetical analyzer used in the original CIMA simulation and (B) photograph of the wind tunnel CIMA

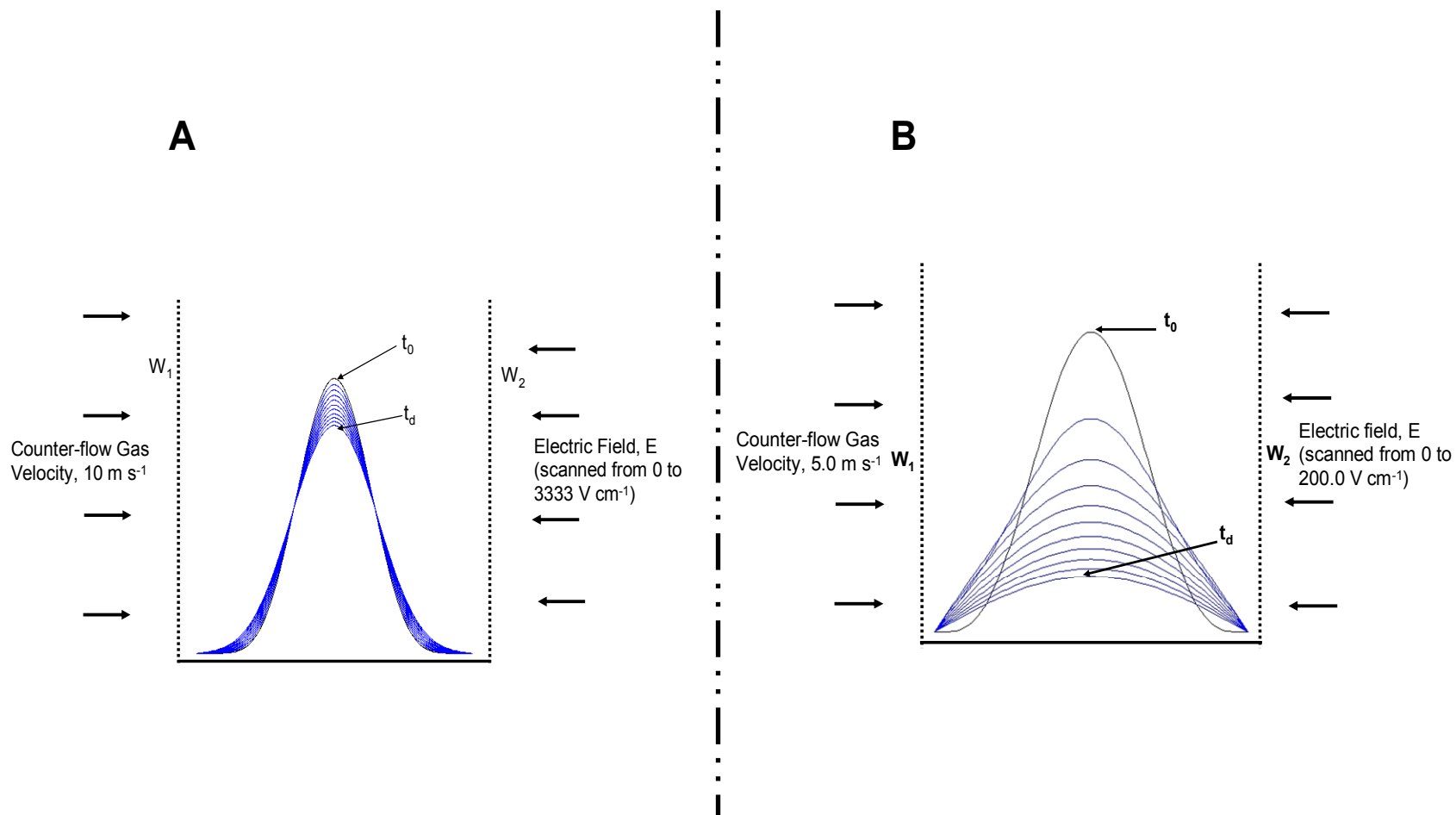


Figure 10.34 (A) Model of the initial simulation using the ideal conditions discussed in Chapter 2, which shows the concentration of the sample from the time it is injected at t_0 to when it is detected at t_d and (B) model of the same process, but using the experimental parameters discussed in this chapter.

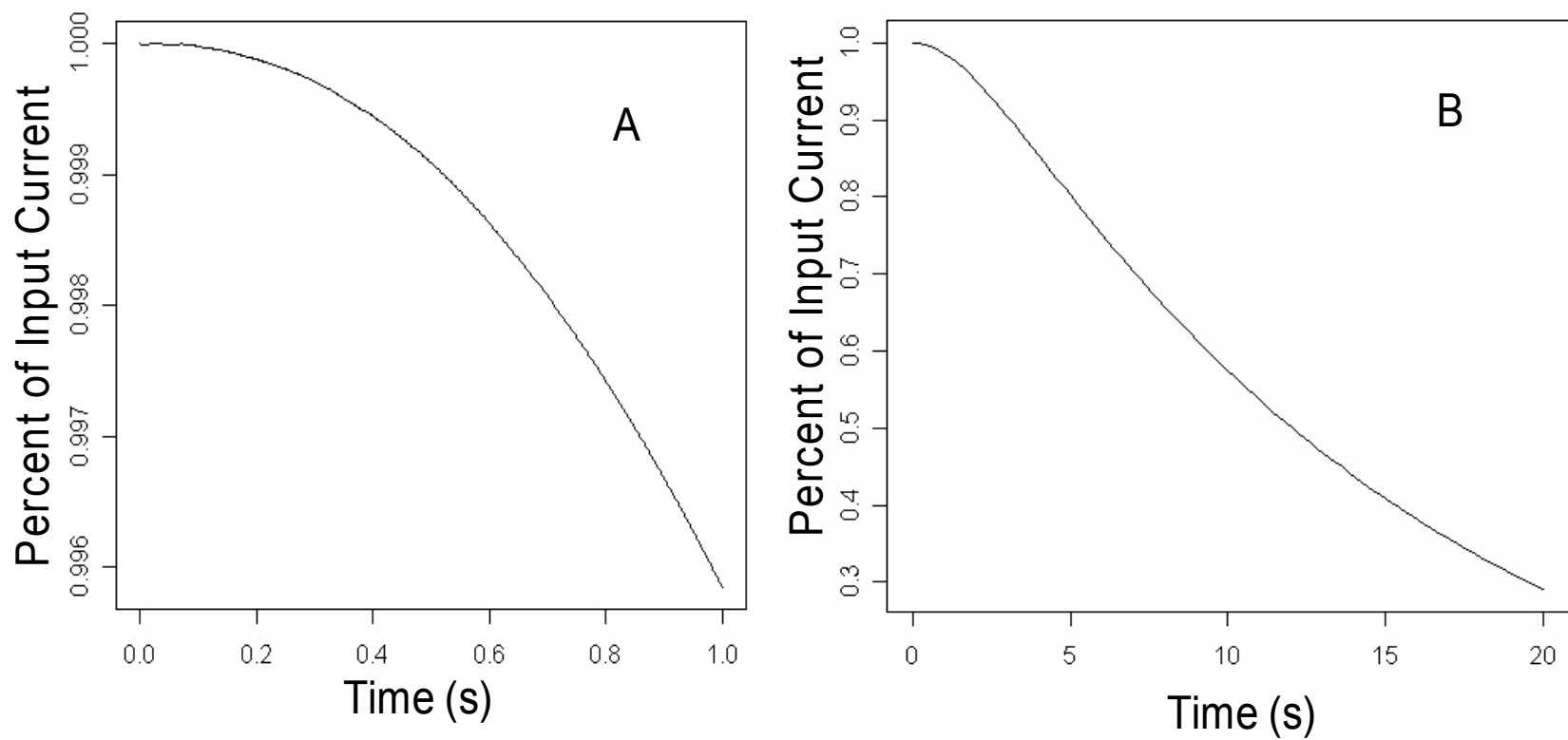


Figure 10.35 Amount of initial concentration of sample that reaches the detector as a function of input current. While (A) takes 1 s to carry out the analysis, (B) takes 20 s. The results of this time difference is that diffusion is allowed to take place in (B) and most of the sample is lost before it reaches the detector, while in (A) less than 1% of the sample is lost.

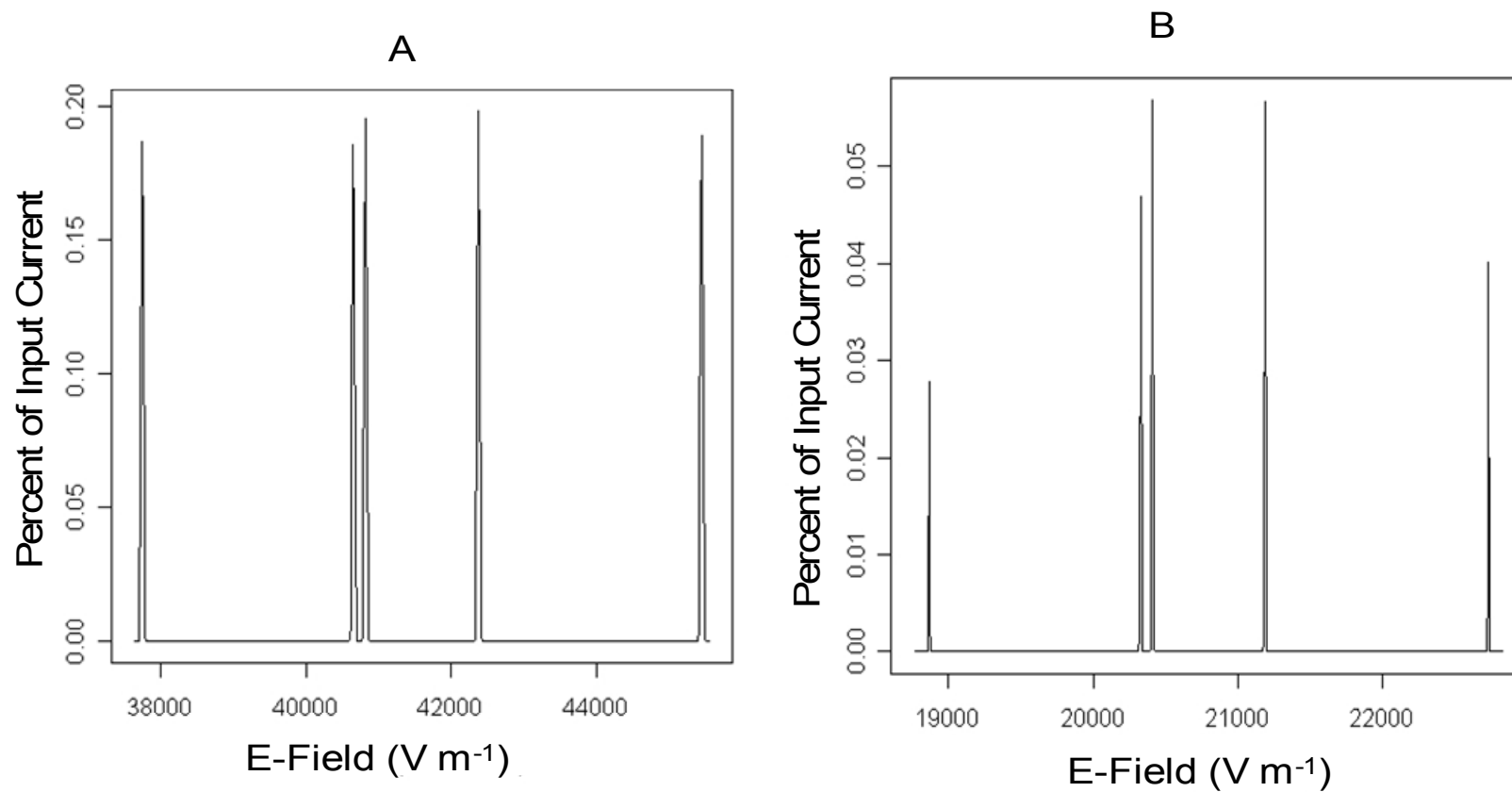


Figure 10.36 CIMA spectra from (A) original simulation using ideal conditions, and (B) simulation using experimental conditions. Both reveal narrow peaks and thus high resolution. However, the intensities of the peaks in (B) relative to (A) are smaller, indicating that while almost all of the sample introduced in (A) arrives at the detector, only approximately 5% in (B) reaches the detector.

remains near the volume of the initial sample concentration during the travel time through the analyzer, (B) shows spreading of the sample with time, primarily due to diffusion. While the analysis time for (A) was 1 s, it was 20 s for (B). This longer analysis time for (B) allows diffusion to take place which leads to loss of sample. Figure 4.35 shows the percentage of the initial amount of sample that reaches the detector. This plot records the amount of sample that remains within the analyzer not lost due to diffusion. This plot supports the need for faster analysis time in CIMA. Shorter analysis time means less time for diffusion and less sample loss; longer analysis time leads to more time for diffusion and more loss of sample ions to the walls of the analyzer.

Figure 4.36 shows the modeled CIMA spectra for (A) the ideal simulation conditions and (B) the experimental conditions. The narrow peaks in both spectra suggest that high resolution is possible even with a low electric field. However, the resolution in (B) is less than half that in (A), which is quite significant. In (A), the calculated resolution was 1400 while in (B) the calculated resolution was 682. These results clearly suggest that attaining high resolution will require high electric field and high counter-gas flow velocity.

Assumptions used to simplify the model were presented in Chapter 2. However, the validity of these assumptions has not yet been addressed. It is anticipated that an examination of these assumptions will help to understand the actual experimental results. The difficulty in comparing the simulated results with actual experimental results arises from conditions in the actual experiment that are not easily simulated. From the results presented above, the reactant ion peak (RIP) was the most prominent feature of the recorded CIMA spectra. Although not modeled in the simulation, this peak was always present in CIMA as well as in traditional IMS spectra.

Another example is the noise that is present in real systems, which was not present in the modeled system. The effect of gas type on CIMA performance was not considered in the simulated system. Finally, under actual experimental conditions, ion clusters are real and present, but were not considered in the simulations.

In this simulation, samples were introduced as an injection plug similar to a pulsed ion injection process. In contrast, the actual experiment involved continuous sampling of ions. Furthermore, in the simulation, the analyzer volume was defined using walls, W_1 and W_2 (Chapter 2), however, in the actual CIMA design, there were no walls to define the analytical volume. How this affects the final experimental results vis-à-vis the modeled results must be investigated further.

Conclusions. The numerical analyses seems to suggest that narrow peaks and, hence, high resolution are possible even at low counter-gas flow velocity and weak electric field. Obviously, the simulations do not adequately represent what actually takes place in an experiment.

4.10 Ion Transient Time Determination

The ion transient time (also called the residence time) is the time it takes an ion to travel from the ion source to the detector. In conventional IMS, pulsing of the ions into the drift region makes it easy to determine this property. In the wind tunnel CIMA, continuous sampling of the ions makes direct determination difficult to do. However indirect calculation of this property can be done using the electric field strength in the vertical direction and the mobility constant of the analyte.

Ion drift velocities were determined from the electric field, E (in V cm^{-1}) and ion reduced mobility constants, K_0 ($\text{Cm}^2 \text{V}^{-1} \text{s}^{-1}$)

$$v_d = K_0 * E \quad (4.1)$$

The transient time, t (s), was then determined from the drift velocity, v_d (cm s^{-1}), and the analyzer height, d (cm), from

$$t = \frac{d}{v_d} \quad (4.2)$$

Determination of the transient time of an analyte in the wind tunnel CIMA enabled comparison with conventional IMS, to see if there is a trend or relationship between the resolution and the transit time. Table 4.8 lists the electric field strengths in the vertical direction, E_y (y-axis), of the wind tunnel CIMA. This is the field that is used to transport the analyte to the detector. As overall analyzer electric field becomes more inclined, the E_y component becomes greater. This greater field drives ions faster to the detector. Table 4.9 lists the velocities of the ions corresponding to the electric fields in Table 4.8. The ion velocity increases as the electric field becomes greater. Table 4.10 lists the transient times that correspond to the velocities in Table 4.9. As ion velocity increases, ion transient times becomes shorter, and it takes less time for the ions to reach the detector.

Figure 4.37 illustrates a trend to shorter transient time as the vertical electric field increases. This figure is comparable to Figure 4.23, which shows increasing resolution as the vertical field increases. Thus, shorter transient time leads to higher resolution. Shorter transient time requires a smaller analyzer and/or increased electric field. The need for shorter transient time again supports the need for a higher or stronger electric field. The transient times reported here are much longer than those of conventional IMS, i.e., 5-8 ms.

4.11 Ion Lifetime Determination

The spatial dispersion of ions by diffusion through gas to fill the analyzer volume is important in determining the relationship between ion diffusion and the transient time. The lifetime, τ , is the time it takes a diffusing ion packet to fill the analyzer volume or space. Thus, to have spatial resolution of component ions in a system, this lifetime must be longer than the transient time.

Table 4.11 lists the calculated lifetimes for four of the sample ions (acetone ethylbenzene, pyridine, and toluene) used in previous experiments. A comparison of the transient times and lifetimes of the ions shows that the transient times are considerably shorter than the lifetimes of the ions which should lead to good spatial resolution of the peaks. However, the lifetimes are close to the experimental analysis times, which were 20 and 25 s. Furthermore, the analytes in Table 4.11 have very close transient times, and should all arrive at the detector at approximately the same time. Reducing the analysis time as well as using higher electric field and counter-gas flow velocity should improve the resolution of the peaks.

For a rectangular cross-section like the analyzer region of the CIMA, the following equation was used to calculate the lifetimes of the ions

$$\tau = \left(D\pi^2 \left(\frac{1}{a^2} + \frac{1}{b^2} \right) \right)^{-1} \quad (4.3)$$

where D is the diffusion coefficient in $\text{cm}^2 \text{s}^{-1}$, and a and b are the height and width of the test region, which were 5.08 cm and 10.2 cm, respectively.

Table 10.8 Calculated electric field in the vertical y-axis of the wind tunnel CIMA as the ground common position is shifted and the field becomes more inclined.

ΔV Between Electrodes	Electric Field in the Vertical Direction (E_y) (V cm⁻¹)							
	0.500'' (C)	1.00'' (D)	1.50'' (E)	2.00'' (F)	2.50'' (G)	3.00'' (H)	3.50'' (I)	4.00'' (J)
10.0	18.8	35.3	46.2	54.3	59.7	63.6	66.5	68.4
20.0	37.7	70.7	93.7	107	118	126	132	135
30.0	56.5	107	141	165	182	191	210	210
40.0	75.3	142	188	220	242			
50.0	94.2	177	215	251				

Table 10.9 Calculated velocity of acetone corresponding to the electric field in Table 4.9. This is the velocity of the ions as they travel from the injector to the detector.

ΔV Between Electrodes	Velocity of Acetone Ions in the Vertical Direction (cm s^{-1})							
	0.500'' (C)	1.00'' (D)	1.50'' (E)	2.00'' (F)	2.50'' (G)	3.00'' (H)	3.50'' (I)	4.00'' (J)
10.0	40.1	75.3	98.4	116	127	136	142	146
20.0	80.2	151	200	229	251	268	280	288
30.0	120	227	299	352	387	408	426	448
40.0	160	301	399	469	516			
50.0	201	376	457	535				

Table 10.10 Calculated transient time of acetone. This is the time it takes for acetone ions to reach the detector from when they enter the analyzer.

ΔV between electrodes	Transient Time of Acetone in the Vertical (y-axis) Direction (ms)							
	0.500'' (C)	1.00'' (D)	1.50'' (E)	2.00'' (F)	2.50'' (G)	3.00'' (H)	3.50'' (I)	4.00'' (J)
10.0	127	67.0	52.0	44.0	40.0	27.0	36.0	35.0
20.0	63.0	34.0	25.0	22.0	20.0	19.0	18.0	18.0
30.0	42.0	22.0	17.0	14.0	13.0	12.0	12.0	11.0
40.0	32.0	17.0	13.0	11.0	10.0			
50.0	25.0	13.0	11.0	9.00				

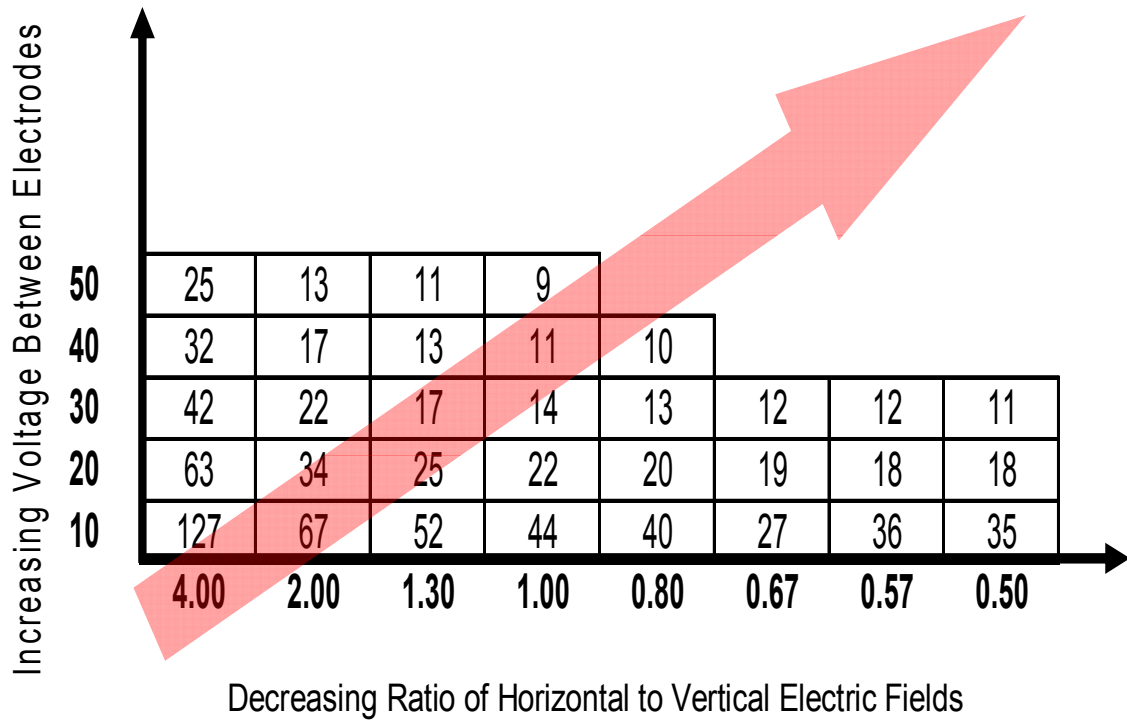


Figure 10.37 Graphical representation of the trend in transient time in ms as the ratio between the horizontal and vertical fields approaches 0.5 and the voltage is increased across the analyzer.

Table 10.11 Transient times, reduced mobilities, and lifetimes of analytes used in test experiments.

Compound	K_0 (cm ² V ⁻¹ s ⁻¹)	Transient Time (ms)	Lifetime, τ (s)
Acetone	2.13	13	24
Ethylbenzene	1.97	14	26
Pyridine	1.84	15	28
Toluene	1.87	15	28

4.12 References

1. Mathew, J.; Bahr, C.; Carroll, B.; Sheplak, M.; Cattafest, L. *26th AIAA Aeroacoustics Conf.*, Monterey, CA, May, 2005.
2. Mehta, R. D.; Bradshaw, P. *Aero. J.*, **1979**, 443-449
3. <http://www.sunon.com.tw/english/wealth/tech/tech-05.htm>
4. Giubbilini, P. *J. Appl. Phys.* **1988**, 64, 3730-3732.
5. www.fluent.com
6. www.comsol.com
7. www.ni.com/labview
8. Agbonkonkon, N.; Tolley, H. D.; Asplund, M. C.; Lee, E. D.; Lee, M. L. *Anal. Chem.* **2004**, 76, 5223-5229.
9. Wessel, M. D.; Sutter, J. M.; Jurs, P. C. *Anal. Chem.* **1996**, 68, 4237-4243.
10. Rosell-Llompарт, J.; Loscertales, I.G.; Bingham, D.; Fernandez de la Mora, J. *J. Aerosol Sci.* **1996**, 27, 695-719.
11. Loscertales, I. G. *J. Aerosol Sci.* **1998**, 29, 1117-1139.

Chapter 5

Prediction of Gas-phase Reduced Ion Mobility Constants (K_0)

5.1 Introduction

This chapter reports the development of a model for the prediction of reduced mobility constants, K_0 . As discussed in Chapter 1, the mobility constants of a gas is related to its molecular structure according to the equation

$$K = \frac{3q}{16N} \left(\frac{2\pi}{kT} \right)^{\frac{1}{2}} \left(\frac{m+M}{mM} \right)^{\frac{1}{2}} \frac{1}{\Omega_D} \quad 5.1$$

where q is the ion charge, N is the drift gas density, k is Boltzmann's constant, T is temperature in Kelvin, m is the mass of the ion, M is the drift gas mass, and Ω_D is the collision cross section. Since Ω_D is determined by the size, shape, and polarizability of an ion, it follows that a relationship between structure and K exists.¹

Since the introduction of IMS, there have been efforts to understand the physical and chemical processes that occur in the system,² especially the relationship between ion mobility and structure. Efforts to relate mobility to ion mass have been successful for some homologous series of organic compounds. Quantitative structure-property relationships (QSPRs) are now being employed to predict mobility constants from the structures of the ions.

We evaluated the possibility of predicting gas-phase reduced mobility values, K_0 , of ions based on multiple physical (e.g., topological and electronic) properties of the ions. The ability to predict K_0 values is important for several reasons. First, there are limited experimental K_0 values that have been published. Second, predicted K_0 values provide an initial value for algorithms

used to calibrate instrument-specific measurements. Finally, a prediction equation could provide valuable insight into the principle dynamics that have the greatest effects on ion mobilities.

There are two primary methods reported in the literature for determining or calculating gas-phase K_0 values: a fitting procedure³ and a neural network (neural net) computer model.^{1,4} The latter model, developed by Jurs *et al.*, was able to predict K_0 values with over 99% accuracy for a defined set of relatively simple compounds¹ and a somewhat lower (i.e., 91.1%) accuracy for an expanded set containing more diverse compounds.⁴ The regression step of Jurs fit to these data had an R^2 of 88.7%. The neural net adjustments were able to improve this fit to 91.1%. Despite this reasonably good level of predictability, the model has two shortcomings for practical use. First, because it is based on a trained neural network, it requires a training set of experimentally measured K_0 values to hone its predictive accuracy. This training optimizes the parameters used in future predictions but limits extrapolation to new molecule types.

A second shortcoming of neural nets, in general, is the difficulty often experienced in interpreting the prediction model. The weights and node links of neural nets are constructed to optimize predictions by specific criteria, however, without providing the user a method of relating inputs to predictions.

In constructing their neural net, Jurs *et al.*⁴ initially identified a set of six measures that had the greatest predictive capability for K_0 when used as regression variables in a fitted multiple regression. We used their regression equation as a starting point for our prediction model.

5.2 Prediction Model

The ion cross section, Ω_D , is related to K as given by the expression in Equation 5.1 above. The mobility of a polyatomic ion depends on its average collision cross section, Ω_D , which in turn depends on various characteristics of the ion (i.e., size, shape, and charge

distribution) and the neutral buffer gas molecules (i.e., size, shape, and dipole or quadrupole moments). Our prediction model is based on these cross-section characteristics.

Six parameters or “descriptors” used by Jurs *et al.* were also used by us in our model; five were topological and one was electronic. These indexes, which include KAPA-3, V1, Qneg, 2SP2, NO, and TPT-3, were manually calculated according to the equations reported by Jurs *et al.*,^{1,4} except for Qneg and WTPT-3, which are described below (see Appendix C for a detailed description of equations used to calculate these parameters).

According to Wessel and Jurs,¹ KAPA-3 is an index that describes the molecular shape of compounds corrected for the presence of heteroatoms. V1 is a valence connectivity index that describes the molecular connectivity of the compound, taking into account the type of bond that connects each atom.⁴ 2SP2 is a descriptor that accounts for the total number of sp²-hybridized carbon atoms that are attached to two other carbons and one hydrogen in the structure.⁴ NO is simply the number of oxygen atoms in the structure.

Qneg, the charge on the most negative atom, was calculated using a computer program (NWChem, version 4.5 on an IBM SP2 Power3).⁵ Computation of partial atomic charges is more difficult than other electrostatic quantities, such as dipole moment, because atomic charges could not be measured, leaving no basis for comparison to experiment. It is well known that simple methods for calculating charges, such as Milliken charges, are not reliable and are dependent on the basis set. A recent article compared methods of calculating partial charges.⁶ We were interested in selecting a method that would provide consistent results over a range of atom types and molecules, could be correlated with known ion mobility data, and would use a readily accessible code so others could easily perform similar calculations. Fitting tests showed that

electrostatic potential charges computed by the NWChem program provided consistent agreement with measured quantities.

The geometries of the ions were optimized according to the Hartree-Fock ab initio method, with either a 3-21G* basis set (for first-row elements) or a LANL2DZ ECP basis set (for transition metals). Calculation of the partial charges was then performed according to the ESP electrostatic potential fitting method using either 6-311G* or LANL2DZ basis sets. These results provided maximum negative charges, which led to the best agreement between calculated and measured K_0 values.

WTPT-3, the sum of weighted path lengths, accounts for the contribution of heteroatoms to the overall geometry and shape of the hydrocarbon skeleton of an ion. Following the lead of Jurs *et al.*, a pure hydrocarbon was assigned a value of zero. This was not entirely consistent with the original Randić index,⁷ which has a nonzero value for hydrocarbons. In this work, WTPT-3 was modified to follow the Randić algorithm⁷ more closely. Heteroatoms were assigned nonzero values, and the sum of weighted path calculations was carried out starting from the heteroatoms.

Initially, we tried a simple multiple regression model, which included the six variables plus an intercept on the data used by Jurs *et al.* This model worked well ($R^2 = 88.7\%$) for many organic ions, i.e., aliphatic hydrocarbons and certain aromatic and cyclic structures containing electronegative atoms such as O, N, halogens, and certain forms of S. However, the model in its current form is less predictive for mobilities of compounds containing P, As, and certain forms of S. Therefore, the ions of interest in this study (Table 5.1) were divided into eight groups, as listed in Table 5.2, and a specific index value was calculated for each of these groups.

Table 11.1 Experimental and predicted K_o values used in developing the prediction model^a

Compounds	Exptl K_o	Predicted K_o	Reference
Carbonic dichloride	2.77	2.72	11
Nitrochloroform (Chloropicin)	2.70	2.74	11
Chloroacetophenone	2.66	2.01	11
Hydrogen cyanide	2.50	2.39	11
Cyanogen chloride	2.50	2.59	11
3-Xylylbromide (3-Methyl benzyl bromide)	2.47	2.03	11
Acetone	2.13	2.06	4
Ethanol	2.06	2.04	4
Acetic acid	2.03	2.03	4
Pentane	2.02	2.05	4
2,2,3,3-Tetramethylbutane	2.02	1.93	4
n-Hexane	2.00	1.93	4
tert-Butylamine	2.00	1.92	4
2-Butanone	2.00	1.93	4
2-Propanol	1.98	1.97	4
Ethyl ester	1.98	1.95	4
1,2,4,5-Tetramethylbenzene	1.98	1.76	4
Glutaraldehyde	1.97	1.85	4
Ethylbenzene	1.97	1.95	4
Cycloheptane	1.96	1.95	4
o-Xylene	1.96	1.94	4
m-Xylene	1.96	1.88	4
Methylcyclohexane	1.95	1.95	4
Triethylamine	1.95	1.96	4
2,4-Lutidine	1.95	1.96	4
Ethylcyclopentane	1.94	1.95	4
Propionic acid	1.94	1.91	4
Benzene	1.94	2.12	4
Propanal	1.93	2.00	4
2-Methylpropanal	1.93	1.97	4
Propanol	1.93	1.91	4
Ethyl acetate	1.93	1.89	4
n-Butylamine	1.92	1.85	4
3-Methylhexane	1.91	1.88	4
Dimethyl methylphosphonate	1.91	1.67	4
2-Methylhexane	1.90	1.82	4
n-Heptane	1.90	1.87	
Diisopropylamine	1.90	1.79	4

Butylbenzene	1.89	1.79	4
2-Pentanone	1.88	1.84	4
3-Pentanone	1.88	1.91	4
1,3-Dimethylcyclohexane	1.87	1.82	4
1,2-Dimethylcyclohexane	1.87	1.85	4
Methyl isobutyrate	1.87	1.90	4
Propyl methanoate	1.87	1.91	4
Toluene	1.87	1.88	4
1,2,4-Trimethylbenzene	1.87	1.82	4
Ethylcyclohexane	1.86	1.89	4
Di-n-propylamine	1.86	1.80	4
Isobutyric acid	1.86	1.89	4
Methyl butanoate	1.86	1.87	4
Ethyl propanoate	1.86	1.84	4
2-Ethoxyethyl acetate	1.86	1.75	4
2-(2-Hydroxyethyl)pyridine	1.86	1.81	4
Aniline	1.86	1.87	4
Cumene	1.86	1.87	4
Napthalene	1.86	1.85	4
2-Butanol	1.85	1.84	4
Propylbenzene	1.85	1.86	4
Benzaldehyde	1.85	1.93	4
2-Ethyl-1-hexane	1.84	1.67	4
Isoamylamine	1.84	1.78	4
2-Methyl-1-propanol	1.84	1.88	4
3,3-Dimethyl-2-butanol	1.84	1.77	4
2,4,6-Trimethylpyridine	1.84	1.87	4
Cyclohexanone	1.84	1.85	4
Cyclohexene	1.83	1.98	4
Isopropyl acetate	1.83	1.83	4
Butanal	1.83	1.94	4,10
2-Methyl-2-propanol	1.83	1.91	4
Chlorobenzene	1.83	1.98	11
2,2,4-Trimethylpentane	1.82	1.74	4
2,2-Dimethylhexane	1.82	1.76	4
Methyl tert-valerate	1.82	1.86	4
Cyclohexylamine	1.82	1.71	4
2-Methylcyclohexanone	1.82	1.80	4
4-Methylheptane	1.81	1.78	4
3-Methylbutanal	1.81	1.87	4
2-Methylbutanal	1.81	1.92	4
N,N-Dimethylaniline	1.81	2.09	4

2-Methylheptane	1.80	1.74	4
n-Octane	1.80	1.77	4
Methyl anteisovalerate	1.80	1.81	4
Pentanal	1.80	1.85	4
o-Toluidine	1.80	1.85	4
Dicylopentadiene	1.79	1.72	4
2-Hexanone	1.79	1.76	4
2-Methyl-3-hexanone	1.79	1.76	4
Ethyl butanoate	1.79	1.76	4
n-Amylamine	1.79	1.76	4
2,5-Dimethyl-1,5-hexadiene	1.78	1.73	4
Isopropylcyclohexane	1.78	1.79	4
3-Pentanol	1.78	1.83	4
3,5,5-Trimethyl-1-hexene	1.77	1.69	4
Propylcyclohexane	1.77	1.79	4
Propyl propanoate	1.77	1.77	4
4-Heptanone	1.76	1.73	4
p-Cymene	1.76	1.74	4
3-Methylcyclohexanone	1.76	1.77	4
4-Methylcyclohexanone	1.76	1.78	4
Isobutylbenzene	1.75	1.81	4
tert-Butyl acetate	1.75	1.76	4
sec-Butyl acetate	1.75	1.77	4
3-Heptanone	1.75	1.71	4
sec-Butylbenzene	1.75	1.81	4
2-Ethylbutanoic acid methyl ester	1.74	1.77	4
Benzyamine	1.74	1.91	4
2-Methylpentanal	1.73	1.83	4
n-Nonane	1.72	1.70	4
Isobutyl acetate	1.72	1.76	4
2-Methylpentanoic acid methyl ester	1.72	1.75	4
2-Methyl-1-butanol	1.72	1.81	4
Isoamyl alcohol	1.72	1.78	4
3-Methyl-5-hexanone	1.72	1.73	4
Biphenylene	1.72	1.80	4
Propyl butanoate	1.71	1.68	4
3-Hexanol	1.71	1.73	4
Diisobutylamine	1.70	1.75	4
5-Methyl-2-hexanone	1.70	1.70	4
3-Octanone	1.70	1.64	4
N,N-Diethylaniline	1.70	1.88	4
Hexanal	1.69	1.78	4

Tri-n-propylamine	1.69	1.68	4
2-Hexanol	1.69	1.67	4
2-Heptanone	1.69	1.61	4
Butylcyclohexane	1.68	1.70	4
3-Amyl acetate	1.68	1.71	4
n-Hexamine	1.68	1.68	4
Butyl propanoate	1.68	1.69	4
Methyl hexanoate	1.68	1.69	4
Isopropyl methylphosphonofluoridate	1.68	1.66	11
Methyl isocaproate	1.67	1.71	4
Di-n-butylamine	1.67	1.66	4
tert-Amyl alcohol	1.67	1.76	4
sec-Amyl acetate	1.66	1.70	4
2-Ethyl-1-butanol	1.66	1.84	4
Isoamyl acetate	1.64	1.66	4
n-Decane	1.63	1.61	4
Ethyl hexanoate	1.63	1.60	4
Hexanol	1.62	1.68	4
Dichloro-(2-chlorovinyl) arsine	1.62	1.59	11
Heptanal	1.60	1.69	4
2-Octanone	1.60	1.60	4
Methyl heptanoate	1.60	1.61	4
Mesitylene	1.60	1.80	4
p-Diisopropylbenzene	1.59	1.67	4
n-Heptylamine	1.58	1.60	4
Ethyl N, N-dimethylphosphoroamidocyanidate	1.57	1.74	11
Heptanol	1.54	1.59	4
Pinacolyl methylphosphonofluoridate	1.52	1.61	12
Octanal	1.51	1.61	4
Diethyl phthalate	1.49	1.60	4
Octanol	1.47	1.51	4
Ethyl octanoate	1.47	1.43	4
Tri-n-butylamine	1.46	1.54	4
Nonanal	1.44	1.52	4
Nonanol	1.40	1.43	4
Decanal	1.38	1.44	4
Decanol	1.34	1.35	4
Parathion	1.27	1.10	13
o-Ethyl-S-(2-diisopropylaminoethyl) methylphosphonothiolate	1.23	1.38	12

^aThis list of compounds includes those used by Jurs and coworkers,⁴ plus a number of others of current interest to the authors

Table 11.2 Grouping of compounds according to structure.

Alkanes

Alkanes with heteroatoms (mainly O and N)

Cyclic alkanes

Cyclic alkanes with heteroatoms (mainly O and N)

Aromatic compounds

Compounds containing As and Cl

Compounds containing halogens, N, and O

Compounds containing S, Cl, and O

Compounds containing P, S, O, F, and N

5.3 Results and Discussion

Although, there is a reciprocal relationship between ion cross section and K_0 , as shown in Equation 5.1, we modeled the relationship between the various topological parameters representing ion cross section and observed K_0 values as a linear relationship in order to gain insight into the principle dynamics that have the greatest effects on K_0 . The measured parameter values were multiplied individually by the coefficients listed in Tables 5.3 and 5.4 to derive a predicted value of the inverse of the cross section. The R^2 value (80.1%) reported at the bottom of Table 5.3 is a measure of the goodness of fit of the model. The square root of this value (i.e., 0.895) is the correlation between the predicted and observed K_0 values.

Nearly the same level of predictability as attained by Jurs *et al.* was obtained in this study. However, we included a more extensive and diverse list of 162 ions. We observed that two compounds, i.e., chloroacetophenone and 3-xylyl bromide (3-methylbenzyl bromide) have very large residuals and, when they were taken out of the pool (Figure 5.2; see Figures 5.1-5.6), the predictability improved to an R^2 value of 87.4%. As noted earlier, Jurs *et al.* attained a regression line with an R^2 value of 88.7%, albeit for a less diverse set of ions.

The less than perfect predictability of K_0 values is due to the limitations in the descriptors that are available for use in the model. The topological indexes used here were originally designed for hydrocarbons and only later corrected to account for the addition of halogens and heteroatoms such as O, N, P, and S. Thus, use of the same descriptors for compounds for which they were not designed would be expected to exhibit some limitations. In the predictions of Jurs *et al.*, the Randić index was modified from its original form. This modification was a data centric adjustment, which means that the modification was based on actual ion mobility data

Table 11.3 Estimated coefficients of parameters from regression analysis. ^{a,b}

Predictor	Coefficient	Standaard Error	Number of Compounds
Constant	2.464	0.041	all
V1	-0.131	0.011	all
NO	-0.131	0.014	all
2SP2	-0.003	0.005	all
QNEG	0.401	0.040	all
Kappa 3a ^c	-0.016	0.004	154
Kappa 3b ^c	-0.253	0.027	8
WTPT 1 ^d	0.090	0.009	114
WTPT-PSO ^d	0.031	0.006	6
WTPT 2 ^d	0.128	0.016	42

^aCoefficient in column 1 implicitly define $\frac{1}{\Omega_D}$ as given in equation 5.1.

^b $R^2 = 80.1\%$

^cKappa 3a are Kappa 3 values for hydrocarbons, cyclic hydrocarbons, hydrocarbons with heteroatoms, cyclic hydrocarbons with heteroatoms, aromatics and other compounds containing, P, S, O, F, and N atoms. Kappa 3b are Kappa 3 values for all others.

^dWTPT 1 are WTPT index values for hydrocarbons with heteroatoms, cyclic hydrocarbons with heteroatoms and aromatics.

WTPT-PSO is WTPT index for compounds containing P, S, O, F, and N atoms.

WTPT 2 includes the WTPT index values for all other compounds.

Table 11.4 Estimated coefficients of parameters from regression analysis of the data used in Table 5.3 after elimination of data for chloroacetophenone and 3-xylyl bromide^a

Predictor	Coefficient	Standard Error	Numbers of Compounds
Constant	2.457	0.030	all
V1	-0.130	0.008	all
NO	-0.114	0.011	all
2SP2	-0.010	0.004	all
QNEG	0.368	0.030	all
KAPA 3a ^b	-0.016	0.003	152
KAPA 3b ^b	-0.248	0.20	8
WTPT 1 ^c	0.073	0.006	112
WTPT-PSO ^c	0.025	0.005	6
WTPT 2 ^c	0.125	0.012	42

^aR² = 87.4%

^bKAPA 3a are KAPA 3 values for hydrocarbons, cyclic hydrocarbons, hydrocarbons with heteroatoms, cyclic hydrocarbons with heteroatoms, aromatics, and other compounds containing P, S, O, F, and N atoms.

KAPA 3b are KAPA 3 values for all other compounds.

^cWTPT 1 are WTPT values for hydrocarbons with heteroatoms, cyclic hydrocarbons with heteroatoms, and aromatics.

WTPT-PSO are the WTPT values for compounds containing P, S, O, F, and N atoms.

WTPT 2 are WTPT values for all other compounds.

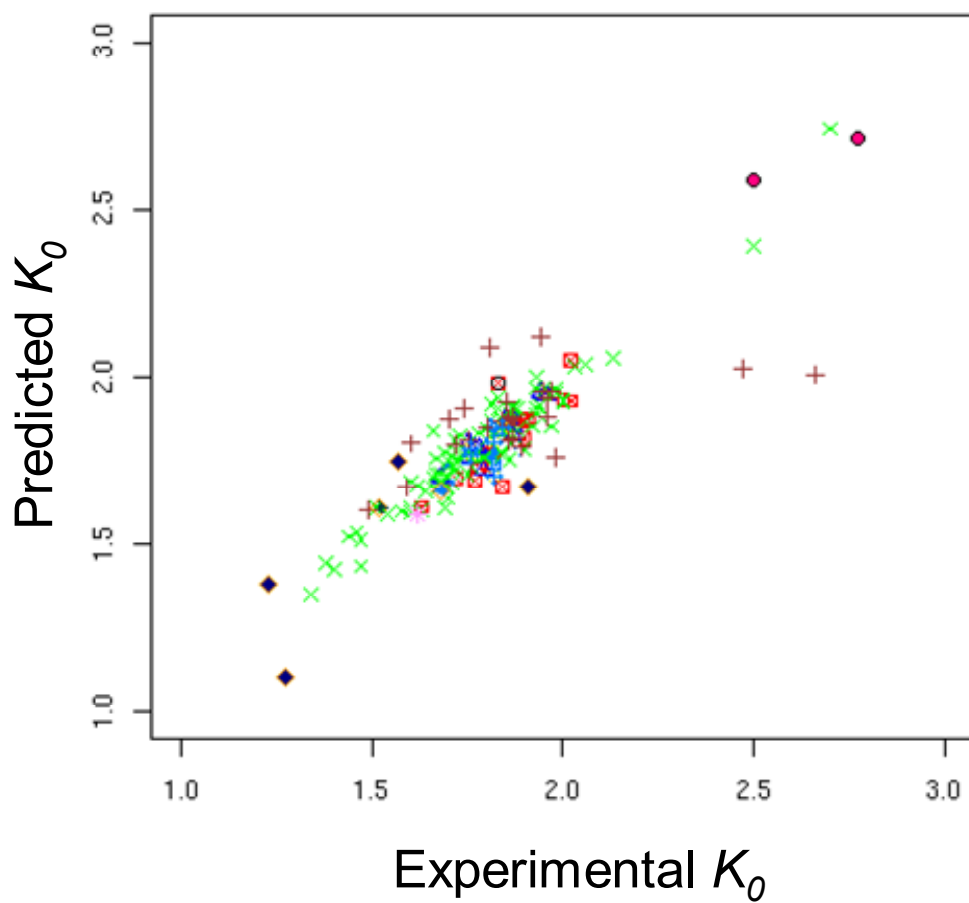


Figure 11.1 Plot of predicted K_0 vs experimental K_0 values using all compounds (Table 5.4 coefficients).

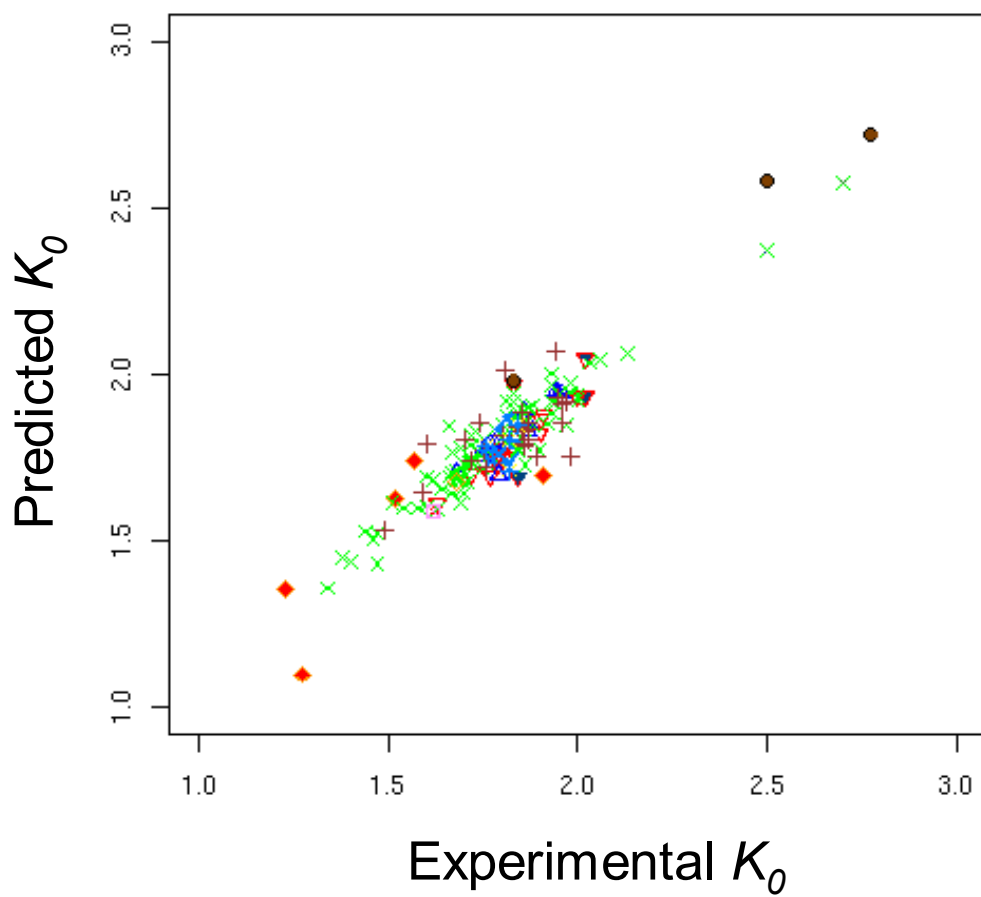


Figure 11.2 Plot of predicted K_0 vs experimental K_0 values after omitting data for chloroacetophenone and 3-xylylbromide (Table 5.5 coefficients).

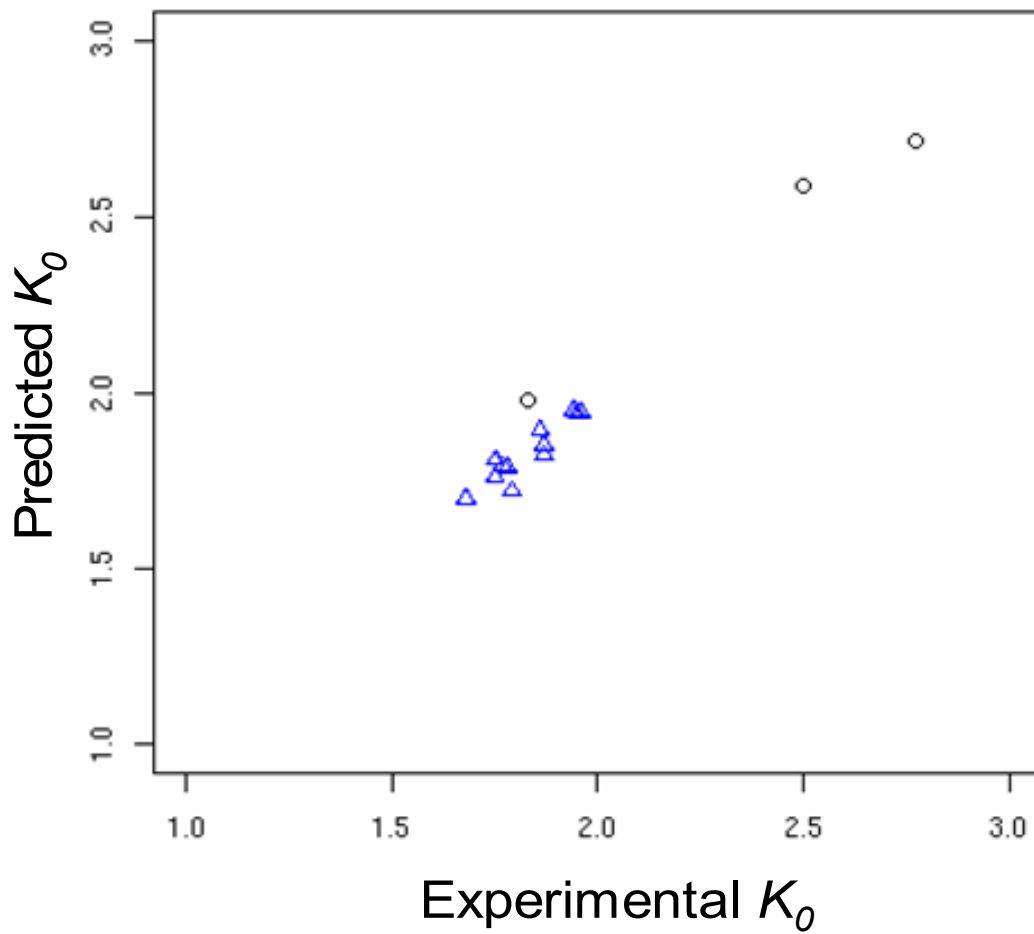


Figure 11.3 Plot of predicted K_0 vs experimental K_0 values for groups 1 and 2 of Table 5.2.

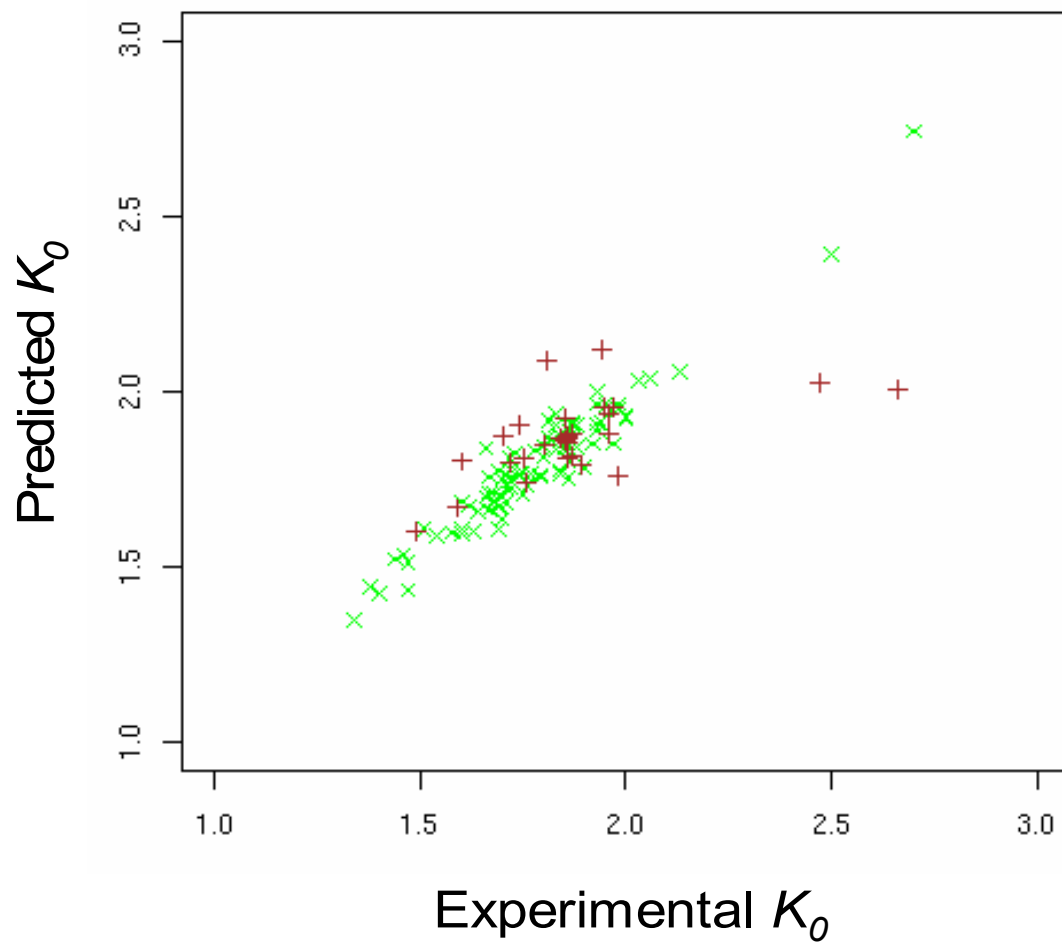


Figure 11.4 Plot of predicted K_0 vs experimental K_0 values for groups 3 and 4 of Table 5.2.

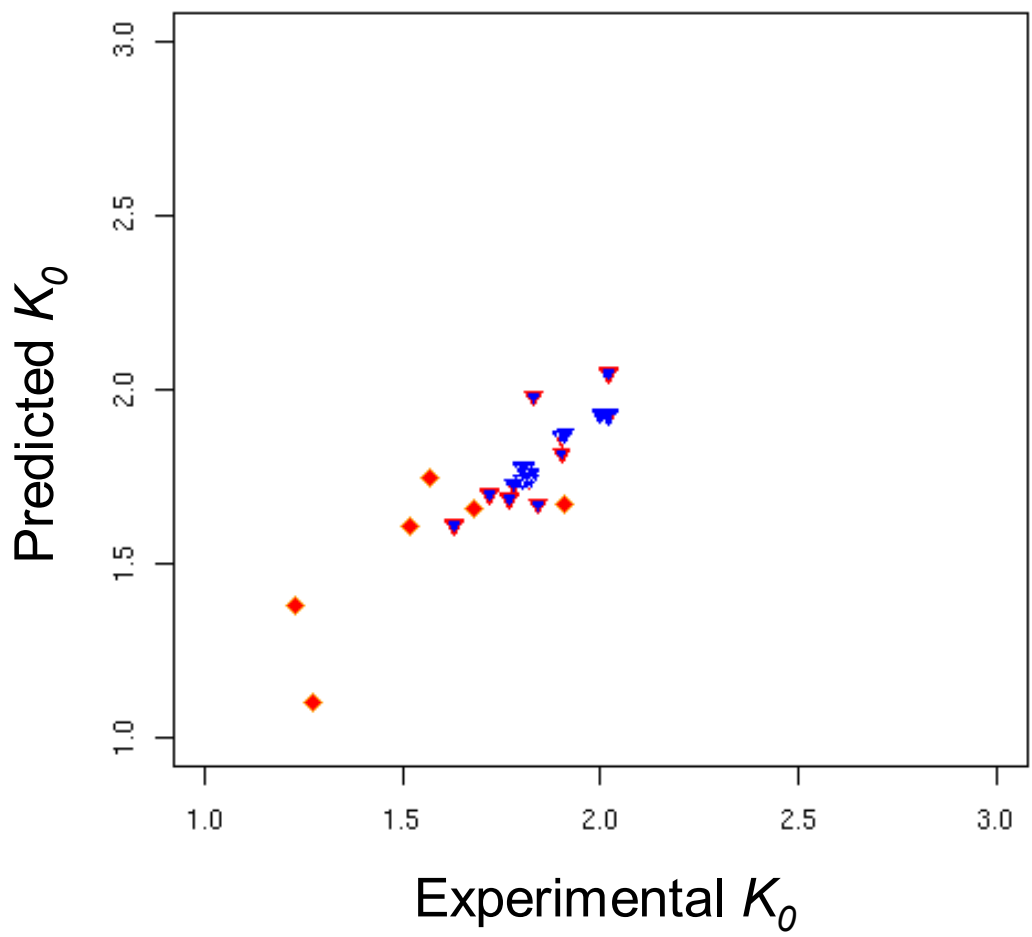


Figure 11.5 Plot of predicted K_0 vs experimental K_0 values for groups 5 and 6 of Table 5.2.

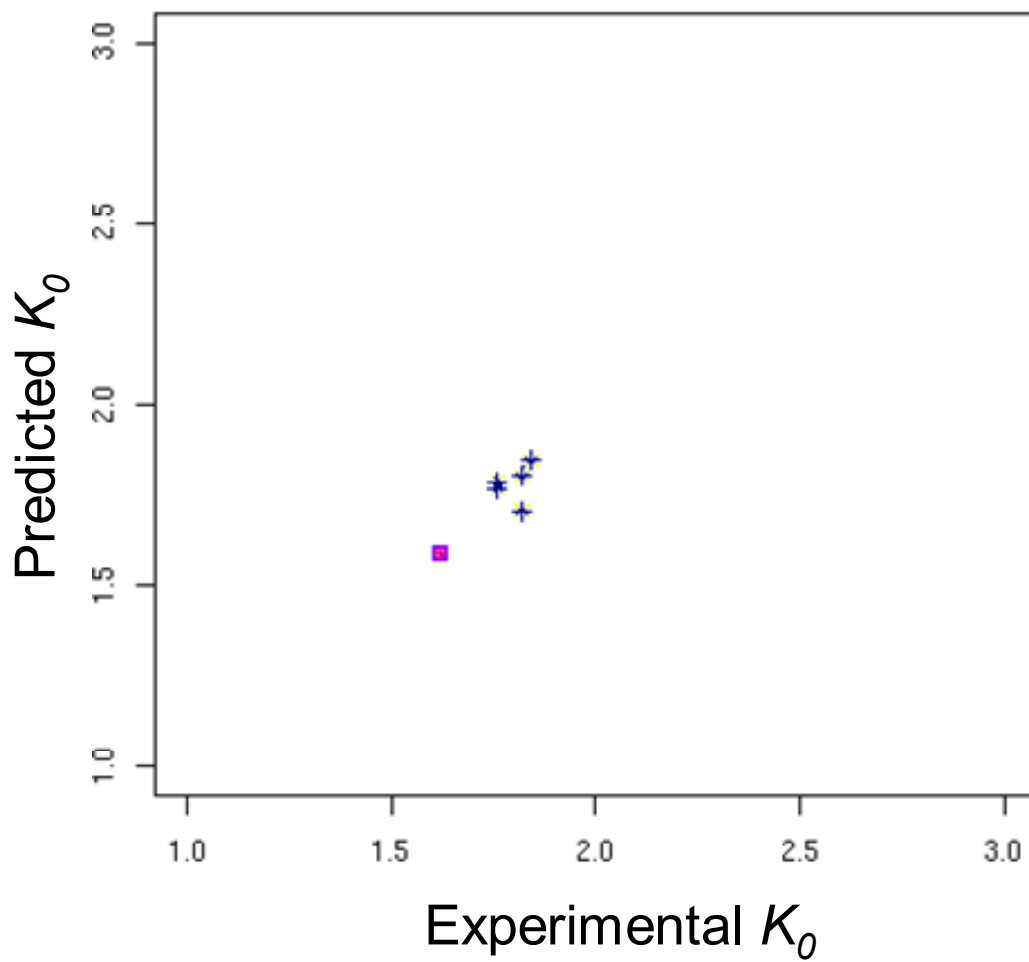


Figure 11.6 Plot of predicted K_0 vs experimental K_0 values for groups 7 and 9 of Table 5.2.

and not entirely on topological considerations. This gave the index more predictive power but made it difficult to predict mobilities for compounds for which the training set was not applicable. The version of the Randić index used in this work is readily obtainable for new compounds.

In this study, we allowed the descriptors KAPA 3 and WTPT to be different for the eight different groups of compounds (Table 5.2). In the analyses, we discovered that the eight groups could empirically regroup into two clusters with respect to KAPA 3. The groups in the same clusters showed the same KAPA 3 effect on mobility. These clusters are identified in Tables 5.3 and 5.4. For a molecule in a particular cluster, the KAPA 3 values are as specified in Tables 5.3 and 5.4. The same is true for the WTPT index, which this time has three clusters. Again the groups may be grouped into three clusters, although different from the clusters identified for KAPA 3. Groups in the same cluster show the same effect of WTPT on mobility as described in Tables 5.3 and 5.4.

The estimate of the standard error, $SE = 0.028$, indicates that there is a significant level of uncertainty in the predictions. Note that this is not the standard error of prediction, but the standard error of the fit. The standard error of prediction depends on the value of the index of the compound for which the mobility is to be predicted. Table 5.1 gives the observed and fitted values for each compound and also the standardized difference in fit. This standardized difference is the number of standard deviations for the particular values of the regression variables by which the predicted and observed values differ. For a few of these cases, values of this standardized difference that are much greater than 2 in absolute value indicate a very poor prediction.

Table 5.5 shows the R^2 values for the first six groups of Table 5.2; calculation of the R^2 values for the remaining three groups was not possible as experimental K_0 values for the compounds in these groups were not available. As the table shows, our model is quite good for compounds in group 3, i.e., hydrocarbons with a heteroatom. Group 5 gave an R^2 value of zero. The R^2 value could have resulted from five compounds in Table 5.6 that gave high residual values, which could partially explain the low R^2 value. Groups 1, 3, and 6 of Table 5.5 have 16, 12, and 6 compounds; this could explain why they have low R^2 values.

However, the true predictive power of this model could only be tested with more experimentally determined K_0 values for compounds in the groups. Group 3 has a high R^2 value, where there are 95 compounds in this group.

Accuracy of measured K_0 values depends greatly on the experimental conditions, instrumentation, and reproducibility of measurements. Until recently, adequate care was not taken to ensure that mobilities were accurately measured. This is evident in the data in the literature, as there is considerable variability in K_0 values even for frequently measured compounds. Although, the variation may appear small to the casual observer, the observed level of uncertainty is too large for prediction with high certainty.

A high level of variation can be seen from Table 5.7 using data for benzene, toluene, aniline, and 1-octanol taken at the same temperature.⁸ Some of these measurements were reported in the same publication. What is not apparent in these studies are the experimental conditions with the exception of temperature. Ionization method and vapor pressure also play key roles in this regard. Clustering of primary product ions may also lead to variation in these measurements. Thus, introducing a chemical to standardize K_0 measurements as proposed by Eiceman *et al.*⁹ will help to resolve some of these problems.

Table 11.5 R^2 Values for different groups^a.

Group	R^2
Hydrocarbon	0.562
Cyclic hydrocarbon	0.569
Hydrocarbons with heteroatom	0.920
Aromatic compounds	0.342
Cyclic hydrocarbons with heteroatom	0.000
Compounds containing P, S, O, F, and N	0.448

^aExperimental measured K_0 values were not available for compounds in three of the groups; thus, R^2 values could not be calculated for them.

Table 11.6 Unusual observations (residual for outliers).

Compound	Residual
N,N-Dimethylaniline	-2.83
Mesitylene	-2.02
1,2,4,5-Tetramethylbenzene	2.24
Chloroacetophenone	6.71
3-Xylyl bromide	4.57
Parathion	2.23
Dimethyl methylphosphonate	2.52

Table 11.7 Data for some compounds that show variation in measured K_0 values

Compound	K_0 ($\text{cm}^2 \text{V}^{-1} \text{s}^{-1}$)	Temp ($^{\circ}\text{C}$)
Benzene	2.00	50
Benzene	2.22	50
Benzene	2.22	50
Benzene	2.22	50
Benzene	2.33	150
Benzene	2.45	150
Benzene	2.48	150
Benzene	2.26	150
Benzene	2.08	150
1-Octanol	0.98	22
1-Octanol	1.12	22
1-Octanol	1.21	22
1-Octanol	1.46	22
1-Octanol	1.53	22
1-Octanol	1.88	22
Aniline	1.93	200
Aniline	2.00	200
Aniline	2.07	200
Aniline	1.95	200
Aniline	1.83	140
Aniline	2.00	140
Aniline	2.06	140

One other topological characteristic that would likely improve our ability to predict K_0 is compound symmetry. From a physical and, perhaps, chemical point of view, the symmetry of a compound would affect its mobility and its ability to polarize the buffer gas.

5.4 Conclusions

A simple model for calculating and predicting reduced mobility constants was described. Unlike methods that use neural networks, this model relies solely on the structure of the compounds with a predictability that is as good as those that use neural networks when applied to a more diverse set of compounds than others have reported.

5.5 References

1. Wessel, M. D.; Jurs, P. C. *Anal. Chem.* **1994**, 66, 2480-2487.
2. Hill, H. H., Jr.; Siems, W. F.; St. Louis, R. H.; McMinn, D. G. *Anal. Chem.* **1990**, 1201A-1209A.
3. Eiceman, G. A.; Karpas, Z. *Ion Mobility Spectrometry*, CRC Press: Boca Raton, Fl, 1994.
4. Wessel, M. D.; Sutter, J. M.; Jurs, P. C. *Anal. Chem.* **1996**, 68, 4237-4243.
5. High Performance Computational Chemistry Group. NWChem, A Computational Chemistry
6. Package for Parallel Computers, Version 4.5, Pacific Northwest National Laboratory, Richland, WA 99352, 2003.
7. Proft, F. De; Alsenoy, Van C.; Peeters, A; Langenaeker, W.; Geerlings, P. *J. Comput. Chem.* **2002**, 23, 1198-1209.
8. Randić. M. *J. Chem. Inf. Comput. Sci.* **1984**, 24, 164-175.
9. Shumate, C; St. Louis, R. H.; Hill, H. H., Jr. *J. Chromatogr.* **1986**, 373, 141-173.
10. Eiceman, G. A.; Nazarov, E. G.; Stone, J. A. *Anal. Chim. Acta* **2003**, 493, 185-194.
11. Steiner, W. E.; Clowers, B. H.; Matz, L. M.; Siems, W. F.; Hill, H. H., Jr. *Anal. Chem* **2002**, 74, 4343-4352.
12. Sohn, H.; Steinhanses, J. *IJIMS* **1998**, 1, 1-14.
13. Alder, J.; Döring, H. R.; Starrock, V.; Wülfing, E. *Proc. 4th Int. Symp. Protection Against Chemical Warfare Agents*, Stockholm, Sweden, 8-12 June, 1992; pp 175-180.
14. Shumate, C.; St. Louis, R. H.; Hill, H. H., Jr. *J. Chromatogr.* **1986**, 373, 141-173.

Chapter 6

Conclusions and Recommendations for Future Work

6.1 Conclusions

Efforts to improve the resolution of IMS are on-going. This is necessary for IMS to reach its full potential, even though it has other attractive features such as high sensitivity, excellent detection limits, simplicity of instrumentation, miniaturizability, and simplicity of interfacing. While others have tried to increase the resolution by improving the instrumentation and electronics, this dissertation describes a different approach called counter flow ion mobility analysis (CIMA) which uses a high velocity counter-flow gas as an opposing force to the electric field driving force.

A partial differential equation was used to represent the CIMA operation, and numerical analysis was employed to solve the equation, choosing parameters that made the flow velocity component the dominant process. Results of this analysis predicted a resolution of over 1000.

A prototype CIMA using a wind tunnel design was fabricated and tested. The results indicated that high gas flows of uniform velocity (plug flow) and high electric fields were needed for the high resolution predicted from CIMA modeling. A plug gas flow profile as well as an inclined electric field were also required. The inclined field served a dual purpose; when resolved into horizontal and vertical components, the horizontal field was used to counter the effect of the gas flow, while the vertical field was used to transport ions from the point of injection to the detector.

The results indicated that resolution increased when (1) the ratio of the horizontal to vertical electric fields approached 0.5 and (2) very high electric fields close to those used in the modeling were employed. The modeling field was over 3000 V cm^{-1} . The resolution should be

further increased as the power supply scan rate increased. The power supplies used were made for static mode operation, and attempts to use them in the scanning mode were not very successful.

Preliminary results using volatile organic compounds (VOC) such as acetone in a nitrogen counter-flow gas showed that ions could be detected. When analyzing organic compounds such as trichloroethane, toluene, ethylbenzene, pyridine, chlorobenzene, ethylene chloride, and benzyl alcohol with a counter-flow gas of helium, two peaks appeared, the first peak being the analyte and the second the reactant ion (RIP). When a mixture of these volatile organics was prepared and tested, multiple peaks were seen in the ion mobility spectrum showing that separation is possible with the CIMA instrumentation.

6.2 Recommendations for Future Work

Wind Tunnel Analyzer Size. The prototype CIMA wind tunnel analyzer used in this work was quite large. Thus, the first obvious challenge is to reduce its size, so it can compete with other conventional bench-top analyzers. The current size was dictated by the first analyzer region design that employed vectorial electrodes discussed in Chapter 4. In that design, two electrodes 3.00” apart were used to determine the effective analyzer volume, but additional evenly spaced electrodes were needed to help straighten the electric field lines. This led to the rather large size of our prototype instrument.

Since the analyzer size is determined by the test region, the new PC board configuration makes it possible to significantly reduce the size. This reduction in size should provide significant improvements. The current length of the test region can be reduced to half its size for better functionality.

Effect of Size Reduction. Reducing the size of the wind tunnel will affect two core features that determine the analyzer resolution: gas flow velocity and electric field. Using the same fan volumetric flow, a reduction in the area of the analyzer will lead to an increase in linear velocity of gas flowing through the analyzer region, which is needed to produce higher resolution. The electric field will be affected in the same manner; a shorter length with the same voltage will lead to a higher electric field. A shorter drift distance will further give diffusion less time to occur, thereby increasing the resolution.

Another consequence of higher electric field that should be explored is the spacing of the conductive electrode traces on the PC board. There is a limit on how much voltage can be applied to the electrodes the way they are presently configured. The upper limit is approximately 140 V, since any voltage higher than that will lead to arcing and breakdown of the insulation between the electrodes. Thus, there must be a balance between the electrode spacing and sustained applied voltage. To circumvent this problem, a groove was created between the electrodes by milling out part of the material. This essentially increased the distance between the electrodes and, thus, enabled a sustained voltage of over 500 V. However, this led to some gas flow disturbances close to the PC board surface. Fortunately, these disturbances did not penetrate or propagate deep into the analyzer. More studies need to be carried out to determine the full effect of the grooves, especially as they affect the sample inlet and the detector.

6.3 Recommended Dimensions for a New Wind Tunnel CIMA Design

Dimensions that allow the conditions used in the simulation are highly recommended. An analyzer region that is 2.00" x 1.00" and approximately 3.15" long would be ideal (a short analyzer region will reduce boundary layer separation that leads to the development of laminar flow in the region). An applied voltage of approximately 24,000 V would provide an electric

field of approximately 3000 V cm^{-1} which is close to that used in the modeling. These dimensions would allow the use of a single fan. The recommended fan is the Sunon MagLev axial DC fan (model number KDE2412PMV1). This fan, with the new analyzer region dimensions, would produce a gas flow velocity of approximately 50 m s^{-1} . Figure 6.1 is a schematic of the proposed new design.

In this new design, a honeycomb that has a 1/16" cell width and is 3/8" long is recommended. Meshes with open areas of 64.8%, 62.7%, and 59.1% are recommended. The length of the contraction region should be 6.14" with front end dimensions of 4.00" x 5.00" and back end dimensions of 1.00" x 2.00" to give a contraction ratio of 10:1.

To sustain 24,000 V across the analyzer PCB boards, two approaches are recommended. One approach is to separate the electrodes by 0.00800" grooves milled 0.0200" deep into the board to increase the effective distance between the electrodes. In this configuration, there will be 242 electrodes along the PCB plate. In the second approach, the spacing between the electrodes would be increased by approximately 16 times to about 0.128", which could sustain approximately 3000 V between the electrodes. This would affect the static dissipative ability of the plates, which would be compensated for by the very high linear velocity of the counter-flow gas that would move the ions quickly away from the analyzer. A clean plate surface would help prevent breakdown and charge leakage between electrodes. With this configuration, there would be 23 electrodes along the PCB plate with the middle electrode grounded.

The diffuser region would be 11.76" long. This is much shorter than the present design. The cone shaped diffuser would have angles of 6.6° and 9.0° , respectively. The entire length would be 21.1". This new design should minimize the volume of counter-flow gas used and achieve much better results than the current design.

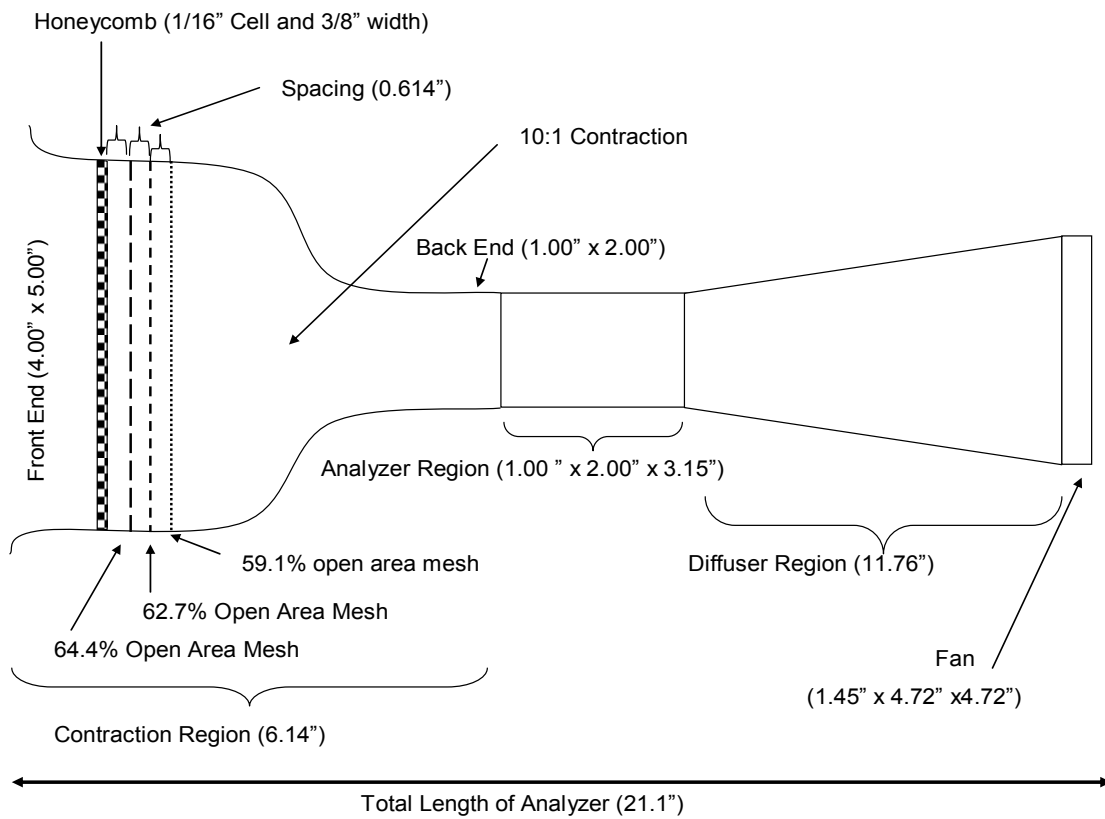


Figure 12.1 Schematic showing the recommended analyzer design. This figure shows details including dimensions of the various components.

6.4 Diffuser and Fan

The rectangular nature of the analyzer region affects the shape and perhaps the performance of the diffuser region. A rectangular shape requires steeper diffuser angles than a square shape for the same analyzer length. Although the reason for a rectangular shape has been well articulated, it is recommended that a square design also be tested to determine the wall effects, if any, on the performance of the analyzer. This will help determine which shape provides the best performance and minimum size

The stability of the gas flow, or instantaneous variation, is affected by the stability of the fan motor and the overall stability of the blades during operation. In this work, slight variations in the gas flow profile hurt the performance. The fan is an open-loop device, thus any variation in voltage or load applied to the motor will adjust the speed. It is recommended that a feedback system be incorporated into the fan circuitry to stabilize the rotational speed of the motor. The problem with commercially available fans is that they are not built for CIMA operation.

6.5 Number of Meshes

When the wind tunnel analyzer was first tested, the contraction region had three meshes. However, two additional meshes were added, with two sandwiching the honeycomb. The five mesh arrangement produced a more stable gas flow and improved the linearity of the flow velocity versus the fan operating voltage. Unfortunately, more meshes required the use of fans with larger volume flow and back pressure. In optimizing the analyzer, the minimum number of meshes that would aid in stabilizing the flow in the analyzer region will have to be determined.

6.6 Materials and Machining

As was discussed in Chapter 4, aluminum was used in the contraction region, plastic and fiber glass in the analyzer region, and sheet metal in the diffuser region. While the fiber glass and sheet metal were smooth, the plastic and aluminum surfaces did not have a smooth enough surface finish. This affected the flow as little disturbances were generated from the rough surfaces. Therefore, it is suggested that the contraction region be made from perhaps a molded plastic material with smoother surface. The same would be true for the plastic material used in the test region.

6.7 Ionization Source Chamber

In this work a corona discharge was used. However, for non-volatile compounds, other forms of ionization will be needed. A design change that utilizes an electric field to inject ions into the system is recommended. By using an electric field to transport the ionized sample instead of a carrier gas, reaction product ion peaks (RIP) will be significantly reduced if not eliminated. However, if a carrier gas is to be used, it must be a dry gas. Investigating the use of a membrane inlet sampling system is recommended. Use of a membrane would reduce the concentration of sample available to the ionization source as well as reduce moisture which would reduce the incidence of ion clustering. The present ionization chamber design should be retained but with slight modification. The modified version should have the discharge needle closer to the ion entrance opening in the analyzer region.

6.8 Detection System

The detector is currently exposed to both the gas flow and changing electric field, and tests have shown that this exposure leads to detector noise. In conventional IMS, there is a grid

before the faraday detector as discussed in Chapter 1. This grid is used to prevent capacitive coupling of the ions with the detector, thus forcing the ions to reach the detector in one packet. A similar approach is needed in this wind tunnel design. The detector should also be shielded better from the effects of the gas flow and the electric field. Similar to aperture grids used in traditional IMS, a dome shaped wire mesh with an applied voltage could be used to enclose the detector. This should help decouple the ions from the detector, so that the ions detected arrive as a narrow band.

6.9 Electrical Parts and Electronics

Power supplies with better stability when the voltage is scanned are required. Variations that result from this instability create perturbations of both gas flow and electric field. Commercial DC power supplies are built for static mode operation, and are not suited for CIMA operation. A custom built dedicated power supply that takes into consideration the requirements for fast scan response time, voltage stability, and very little or no hysteresis, and can output up to ± 15 kV is needed to help with noise reduction. This built power supply should be equipped with effective filters to reduce noise.

Appendix A

List of Acronyms and Symbols

IMS	Ion mobility spectrometry
ppm	Parts per million
ppb	Parts per billion
K	Mobility constant
K_0	Reduced mobility constant
E	Electric field
v_d	Ion drift velocity
pA	Pico-ampere
nA	Nano-ampere
ms	Millisecond
t_d	Ion drift time
T	Temperature in Kelvin
P	Pressure in torr
PDMS	Polydimethylsiloxane
keV	Kilo electron volts
^{63}Ni	Nickel-63
mCi	Millicurie
CD	Corona discharge
DC	Direct current
kV	Kilo volts
mm	Millimeters
ESI	Electrospray ionization
H	Hydrogen
R	Alkyl group
MALDI	Matrix assisted laser desorption ionization
q	Charge on ion
N	Number density of buffer gas
μ	Reduced mass of colliding ion-molecule pair
k	Boltzman's constant
Ω_D	Ion collision cross section
M	Mass of buffer gas ion
m	Mass of sample ion
α	Separation factor
S/N	Signal-to-noise ratio
FT	Fourier transform
W	Ion spectral width at half maximum intensity of peak
$R(R_s)$	Resolution
l_d	Length of drift tube
GC	Gas chromatography

MS	Mass spectrometry
VOA	Volatile organic analyzer
LC	Liquid chromatography
SFC	Supercritical fluid chromatography
EVM	Environmental vapor monitor
μm	Micrometer
CAD	Chemical agent detector
CAM	Chemical agent monitor
CWA	Chemical warfare agent
FAIMS	High field asymmetric ion mobility spectrometry
FIS	Field ion spectrometry
TFC	Transverse field compensation sensor
$V_{dis}(t)$	Dispersion voltage
CV	Compensation voltage
VOC	Volatile organic compounds
DMA	Differential mobility analyzer
Z	Mobility constant
CIMA	Counter or cross flow ion mobility analysis
D	diffusion constant
V	Flow velocity
e	Charge on ion
c	Sample ion concentration
DDMA	Drift differential mobility analyzer
E_x	Electric field in the x direction
E_y	Electric field in the y direction
OMAC	Opposed migration aerosol classifier
FFF	Field flow fractionation
τ	Average lifetime of ions in containing vessel

Appendix B

Definitions of Boundarys and Other Parameters Used in Fluent and Comsol Modeling

Pressure Outlet. Pressure outlet boundary conditions require the specification of a static (gauge) pressure at the outlet boundary. The value of static pressure specified is used only while flow is subsonic.

Pressure Inlet. Pressure inlet boundary conditions are used to define the fluid pressure at flow inlets, along with all other scalar properties of the flow. They are suitable for both incompressible and compressible flow calculations. Pressure inlet boundary conditions can be used when the inlet pressure is known, but flow rate and/or velocity is not known.

Superficial Velocity. Superficial velocity is a solver parameter that fluent uses in calculations, it is based on the volumetric flow rate and is used inside porous media (in the modeling reported here, it was one of the default parameter used by the program).

Gradient Option (Cell Based) Solver Parameter. The gradient option function allows you to mark cells or adapt the grid based on the gradient (undivided Laplacian) of the selected field variables.

Wall Boundary Conditions. Wall boundary conditions allow you to specify the type of wall. It is used to bound fluid and solid regions. In viscous flow, no-slip is enforced at walls by default.

Laminar Viscous Model. Laminar viscosity of fluid (molecular viscosity), μ , is defined by the ratio of shear stress to the rate of shear.

Segregated Solver Parameter. The segregated solver traditionally has been used for incompressible and mildly compressible flow. By default, Fluent uses the segregated solver. The segregated solver solves the flow equation sequentially.

Implicit Formulation Solver Parameters. Implicit solver option linearizes implicitly the coupled set of governing equations with respect to all dependent variables in the set. This results in a system of linear equations with N equations for each cell in the domain, where n is the number of coupled equations in the set. The implicit approach solves for all variables in a cell at the same time.

Face Zone Boundary Condition. The face zone allows you to define the property of that face as either a fluid or a solid.

Space (Dimension). This specifies the dimensions used; in this case, 2-D was used.

Time. Time specifies whether or not the calculation is carried out in a steady state or in a continuous mode.

Inward Current Flow. Inward current flow boundary conditions specify the normal component of the current density rather than the complete vector. When the normal component is positive, the current flows inward through the boundary.

Electric Potential. The electric potential boundary condition specifies the voltage at the boundary condition.

Appendix C

Equations Used to Calculate Topological Descriptors

KAPA 3 (Kier shape index)

$${}^3\kappa = \frac{(A-3)(A-2)^2}{({}^3P_i)^2} \quad A \text{ is even}$$

$${}^3\kappa = \frac{(A-1)(A-3)^2}{({}^3P_i)^2} \quad A \text{ is odd}$$

For heteroatom correction, the equation above was modified as follows

$${}^3\kappa = \frac{(A+\alpha-3)(A+\alpha-2)^2}{({}^3P_i+\alpha)^2} \quad A \text{ is even}$$

$${}^3\kappa = \frac{(A+\alpha-1)(A+\alpha-3)^2}{({}^3P_i+\alpha)^2} \quad A \text{ is odd}$$

where A is the number of atoms in the molecule, 3P_i is the count of contiguous 3-bond fragment derived from molecule and α heteroatom modifier, i.e., non-carbon atom(s) in the molecule (see Table 1).

V1 (Path 1 Valence Connectivity)

V1 is calculated from a graph theory representation of the molecule. For each vertex of the graph there is a vertex valence (number of bonds of the atom at the vertex), denoted ∂_i for the i th vertex and a set of connecting segments between the vertex and other vertexes, called edges. The variable V1, denoted ${}^1\chi$ in the literature, is given for hydrocarbons by

Table 1. α based on covalent radius.

Atom (valence state)	$\alpha_x = (r_x / rc_{sp^3}) - 1$	
	$r_x (A^0)^a$	α_x
C sp3	0.77	0
C sp2	0.67	-0.13
C sp	0.60	-0.22
N sp3	0.74	-0.04
N sp2	0.62	-0.20
N sp	0.55	-0.29
O sp3	0.74	-0.04
O sp2	0.62	-0.20
F	0.72	-0.07
P sp3	1.10	0.43
P sp2	1.00	0.30
S sp3	1.04	0.35
S sp2	0.94	0.22
Cl	0.99	0.29
Br	1.14	0.48
I	1.33	0.73

^aSchomaker, V.; Stevenson, D. P. *J. Am. Chem. Soc.* **1961**, 63, 37.

$${}^1\chi = \sum_{s=1}^{N_e} (\delta_i \delta_j)_s^{-1/2}$$

where the sum is over all edges linking vertexes v_1 and v_2 . The number of edges in the graph of the molecule is N_e .

For heteroatoms, the above formula is modified by changing δ_i to δ_i^v where

$$\delta_i^v = Z^v - h_i$$

and where Z^v is the valence of the atom in the molecule backbone structure and h_i is the number of hydrogen atoms surrounding that atom. For all other molecules, the V1 value is zero (See Table 2).

WTPT (Randić Connectivity ID Number)

The Randić' connectivity ID number is a measure of connectivity. It is formed by summing the connectivity weights. These weights are given by

$$w(pl) = \prod_{i=1}^l w(e_i)$$

where $w(e_i)$ is the connectivity weight of the i th edge of the graph representation of the molecule.

The Randić index is given by

$$ID = N + (\frac{1}{2}) \sum_{pl} w(pl)$$

where N is the number of atoms in the molecule, pl is the weighted path length corrected for heteroatoms using Table 5.2, and e_i ($i = 1, 2, \dots, l$) represents a set of weighted atoms making up the path.

Table 2. Heteroatom valence δ values

Group	δ^v	Group	δ^v
NH_4^+	1	H_3O^+	3
NH_3	2	H_2O	4
$-\text{NH}_2$	3	$-\text{OH}$	5
$-\text{NH}-$	4	$-\text{O}-$	6
$=\text{NH}$	4	$=\text{O}$	6
$\begin{array}{c} \\ -\text{N}- \end{array}$	5	O (both nitro)	6
$\equiv\text{N}$	5	O (both carboxylate)	6
$=\text{N}-$ (pyridine)	5	$-\text{F}$	(-)20
$\begin{array}{c} \\ -\text{N}- \end{array}$ (quaternary)	6	$-\text{Cl}$	0.690
$\begin{array}{c} \\ -\text{N}=\end{array}$ (nitro)	6	$-\text{Br}$	0.254
$\begin{array}{c} \\ -\text{S}- \end{array}$	0.994	$-\text{I}$	0.085
$\begin{array}{c} \\ =\text{S}= \\ \end{array}$	3.58		

Equation Used for Mobility Calculations

The regression equation for linear mobility is

$$\begin{aligned} \text{Exptl Ko} = & 2.46 - 0.131 \text{ V1} - 0.132 \text{ NO} - 0.00267 \text{ 2SP2} + 0.401 \text{ QNEG} \\ & - 0.253 \text{ KAPA} * \text{Kbar} + 0.0905 \text{ NsumW} + 0.0315 \text{ WTPT-PSOFN} - 0.0162 \text{ NsumK} \\ & + 0.129 \text{ WTPT} * \text{Wbar} \end{aligned}$$

The regression equation for linear mobility with outliers 154 and 157 removed is

$$\begin{aligned} \text{Mobility w/o out} = & 2.46 - 0.130 \text{ V1} - 0.115 \text{ NO} - 0.0107 \text{ 2SP2} + 0.368 \text{ QNEG} \\ & - 0.248 \text{ KAPA} * \text{Kbar} + 0.0730 \text{ NsumW} + 0.0250 \text{ WTPT-PSOFN} - 0.0163 \text{ NsumK} \\ & + 0.125 \text{ WTPT} * \text{Wbar} \end{aligned}$$